Progress in Mathematical Physics
60

Bertrand Duplantier
Vincent Rivasseau
Editors

Biological Physics

Poincaré Seminar 2009

Birkhäuser

Biological Physics

Poincaré Seminar 2009

Bertrand Duplantier
Vincent Rivasseau
Editors

Birkhäuser

Editors
Bertrand Duplantier
Service de Physique Théorique
Orme des Merisiers
CEA – Saclay
91191 Gif-sur-Yvette Cedex
France
e-mail: bertrand.duplantier@cea fr

Vincent Rivasseau
Laboratoire de Physique Théorique
Université Paris-Sud
Campus d'Orsay
91405 Orsay Cedex
France
e-mail: Vincent.Rivasseau@th.u-psud fr

ISBN 978-3-0346-0427-7 e-ISBN 978-3-0346-0428-4
DOI 10.1007/978-3-0346-0428-4

Library of Congress Control Number: 2010937783

2000 Mathematics Subject Classification: 76-xx, 80-xx, 35-xx, 37-xx, 60-xx

Cover design deblik, Berlin

Printed on acid-free paper

Springer Basel AG is part of Springer Science+Business Media

www.birkhauser-science.com

Contents

Séminaire Poincaré XII

Bio-Physique

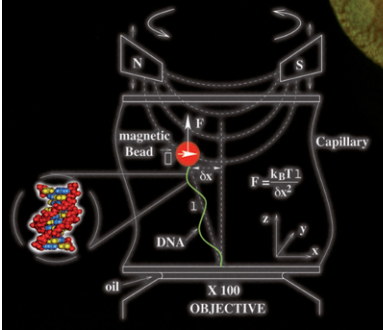

Samedi 31 janvier 2009

J. Prost : Gels actifs *(avec J.-F. Joanny)* • *10h*

J. Howard : Motor Proteins as Nanomachines • *11h*

V. Croquette : Réplication en molécules uniques • *14h*

R.E. Goldstein : Evolution of Biological Complexity • *15h*

S. Dehaene : Brain Mechanisms for Conscious Access • *16h*

INSTITUT HENRI POINCARÉ • Amphi Hermite
11, rue Pierre et Marie Curie • 75005 Paris

www.bourbaphy.fr

ÉCOLE POLYTECHNIQUE • CPM • imago : R.E. Goldstein - DAMTP - Université de Cambridge

Foreword

This book is the ninth in a series of Proceedings for the *Séminaire Poincaré*, which is directed towards a broad audience of physicists, mathematicians, and biologists.

The goal of this Seminar is to provide up-to-date information about general topics of great interest in physics at-large. Both the theoretical and experimental aspects are covered, with some historical background. Inspired by the Nicolas Bourbaki seminar in mathematics, hence nicknamed "Bourbaphy", the Poincaré Seminar is held twice a year at the Institut Henri Poincaré in Paris, with written contributions prepared in advance. Particular care is devoted to the pedagogical nature of the presentations, so as to fulfill the goal of being accessible to a broad audience of scientists.

This new volume of the Poincaré Seminar Series, entitled *"Biological Physics"*, corresponds to the twelfth such seminar, held on January 31, 2009. It describes recent developments at the interface between physics and biology. This field of science has recently undergone spectacular developments, and entire departments devoted to this interdisciplinary activity, as well as to the interface between mathematics and biology, have been created worldwide in the last fifteen years.

The first survey article, by Jean-François Joanny and Jacques Prost, *"Constructing Tools for the Description of Cell Dynamics"*, describes the theoretical advances made in the study of "active gels", where cross-links are moved around by active elements constantly consuming energy. They give applications to the materials science of liquid crystals as well as to the understanding of cell motility.

This article is followed by *"A Physical Model of Cellular Symmetry Breaking"*, where Jasper van der Gucht and Cécile Sykes report on recent advances in the understanding of cell polarization, such as in cytokinesis, via the spontaneous symmetry breaking of the cortical actin network which underlies the plasma membrane. Actin gel layers grown around beads are shown to provide relevant biomimetic model systems helping to understand the nature of these fundamental cellular instabilities.

The next article, by Jonathon Howard, entitled *"Motor Proteins as Nanomachines: The Roles of Thermal Fluctuations in Generating Force and Motion"*, deals with the central role played by thermal fluctuations and Brownian motion in the direct transduction of chemical energy into mechanical work in motor proteins. Several molecular models for these proteins, including so-called ratchet models,

are presented and compared with experimental results for the microtubule-based motor protein kinesin.

In *"Fluctuation Relations for Molecular Motors"*, David Lacoste and Kirone Mallick show theoretically that ratchet models of motor proteins, such as those introduced by J. Howard in his contribution to describe the kinesin motor protein, naturally satisfy the so-called Gallavotti-Cohen fluctuation relation. This fundamental time-reversal symmetry appears because of thermo-kinetic constraints which are inherent in the definition of these models, and requires considering jointly mechanical and chemical variables, such as the ATP molecule consumption.

The team led in Paris by Jean-François Allemand, David Bensimon and Vincent Croquette is famous for its work on micromanipulation of single DNA molecules. In their contribution *"Studies of DNA-Replication at the Single Molecule Level Using Magnetic Tweezers"*, written with Maria Manosas, Timothée Lionnet, Élise Praly and Ding Fangyuan, they describe the latest advances made in the real-time study of the enzymes involved in DNA replication, at the replication fork or in the torsional state of the DNA molecule.

In *"Evolution of Biological Complexity"*, Raymond E. Goldstein addresses the problem of understanding, from a physics perspective, the driving forces behind the biological evolution of multicellularity. For a class of model organisms, the Volvocine green algae, he proposes several theoretical and experimental probes of the fascinating emerging hypothesis, that the transition from organisms with totipotent cells to those with differentiation might be due to the competition between diffusion and fluid advection created by beating flagella in these multicellular organisms.

Stanislas Dehaene addresses a major challenge of cognitive neuroscience, that of understanding the neuronal mechanism of consciousness. In *"Conscious and Nonconscious Processes: Distinct Forms of Evidence Accumulation?"*, he reviews the recent progress achieved by contrasting behavior and brain activation in minimally different experimental conditions, which can lead to conscious perception or not, and speculates on their possible theoretical explanations.

We hope that the publication of this Series will continue to serve the community of scientists, both at professional and graduate levels.

We thank the Commissariat à l'Énergie Atomique (Division des Sciences de la Matière), the Daniel Iagolnitzer Foundation, and the École polytechnique for sponsoring this Seminar. Special thanks are due to Chantal Delongeas for the preparation of the manuscript.

Bertrand Duplantier & Vincent Rivasseau
Saclay & Orsay, April 2010

Constructing Tools for the Description of Cell Dynamics

Jean-François Joanny and Jacques Prost

Abstract. We give a survey of the work which we and others have done over the last years on "active gels". In particular, we show how one can construct a set of equations describing gels in which the cross-links can be moved around by active elements constantly consuming energy. This situation corresponds to the cell cytoskeleton, which is thought to control most of cell dynamics. We illustrate the potential usefulness of the equations, first by giving material science types of applications, second by discussing cell behavior such as motility, oscillations, wound healing and cytokinesis.

1. Introduction

Our knowledge in Biology has improved significantly over the last fifty years, with impressive successes in molecular biology, genetics, developmental and cell biology. The wealth of information is such that it is hard to make use of all of them. Although it is clear that details matter in biological systems, it is also clear that one currently needs to develop a global picture taking into account the main features and recognizing what is universal. Cell biology provides a good example of this need: with exactly the same genome, cells can differentiate in about three hundred different types in complex animals such as vertebrates [1]. Physicists would say that they can go to three hundred stable attractors depending on external conditions. Considering that cell phase space is controlled among other things by the expression of a few out of 10^4 genes, three hundred is a very small number. A possible explanation for this small number of cell types is that they are not only controlled by gene expression, but that they are also constrained by generic physical laws. We are far from being able to discuss this problem in its generality, but in the following we address a simpler problem which illustrates how physics could provide generic tools for solving these questions. Namely we investigate what can be learned from using symmetry arguments and conservation laws in describing cell morphology and dynamics. In view of the acknowledged

B. Duplantier and V. Rivasseau (eds.), *Biological Physics*, Progress in Mathematical Physics 60,
DOI 10.1007/978-3-0346-0428-4_1, © Springer Basel AG 2011

specificity of biology such an endeavor may seem futile. We hope to convince the reader that it is on the contrary helpful. Indeed we will discuss in the last three sections of this review:

- one simple aspect of cell motility, namely the shape and speed of a lamellipodium, thin protrusion leading the cell motion on a substrate,
- cell oscillations which are observed when cells are suspended in a physiological serum,
- wound healing of xenopus eggs and the onset of cytokinesis.

For all these examples we use the same theoretical framework.

In order to do so, one needs to construct some tools. It is nowadays textbook knowledge that the shape of cells is maintained by a network of cross-linked biofilaments: the cytoskeleton [2]. At this stage, all we need to know is that the network constitutes a physical gel which would be rather conventional in the absence of molecular motors. At short time scales, it behaves like a conventional solid, at long time scales like a liquid. There are in fact some added complexities which will be discussed in the conclusion. The essential novelty comes from molecular motors. They consume continuously ATP (Adenosine Triphosphate) and are able to exert stresses on the cross-links of the gel. The question is then how to describe such a gel, which we call "active". Using conservation laws and symmetry arguments only we derive the relevant equations in Section 2. Since they result from general considerations, these equations can describe many different situations and are very similar to those derived in different contexts such as motions of bacterial colonies, fish shoals and bird flocks [3, 4, 5]. Active gels could also be made artificially, leading to original material properties [6]. In the third section, we discuss some of these expected original properties, such as the spontaneous transition to a moving state of a thin slab and the rotation of disclinations.

In the fourth, fifth and sixth sections we discuss the already mentioned biologically relevant questions, showing how quantitative information can be obtained and how connection with molecular details can be made. In the last section, we discuss the limitations and merits of the present construction.

2. Hydrodynamic theory of active gels

A common attitude for dealing with the cytoskeletal system in the presence of motors is to simulate ensembles of semi-flexible filaments on which motor bundles can exert force dipoles [7, 8]. Although this is perfectly licit and useful, it does not help much to extract generic behaviors. Another possibility is to start from a molecular picture and get from a statistical description the long wavelength, long time scale equations [9, 10, 11, 12]. This task is difficult: the low density limit has been worked out, without keeping track of the embedding solvent. Taking a pragmatic attitude, one can directly write equations including all terms allowed by symmetry as has been done for bacterial colonies and bird flocks [3, 4] but it is not guaranteed that one can expand equations around an existing state [13].

We have chosen to use generalized hydrodynamics. Hydrodynamic theories have been very successful in the description of systems such as superfluids, liquid crystals, polymers and of course simple fluids. They are valid close to equilibrium. The advantage is that the equations are expanded around a well-defined state. The drawback is that biological systems are not close to equilibrium: one might miss biologically relevant terms. We will discuss such a candidate in the following. In order to build a hydrodynamic theory, one has to identify conserved quantities, and continuous broken symmetries. From there on, the procedure is well defined and systematic. We will not go here through all the steps, referring the reader to references [14, 15, 16].

Conserved quantities are fairly easy to identify: the solvent, the cytoskeleton (actin in practice), the motors and most importantly momentum. However there are two complexities. First, actin units are either in the solvent as monomers or belong to polymerized filaments. There is, a priori, a chemical exchange between the two states, described by rates of polymerization and depolymerization. The corresponding biochemistry is well documented and original. We postpone its description to the discussion of biological examples. Second, the motors can be either bound to the filaments or unbound. This means that in principle the minimal description is that of a five-component system! One has to further identify continuous broken symmetries: actin filaments are polar, and most of the time even though their directions are widely statistically distributed they define a common polar direction. This means that on long time scales the system behaves like a polar active nematic as described first by [3]. One has thus to keep a polar order parameter as well. Deep into the ordered phase it can be chosen as a unit vector $\mathbf{p}$.

In the following, we discuss a simplified version of the equations, in which we keep only the gel velocity field $\mathbf{v}$ and the polarization field $\mathbf{p}$. The validity range and limits of this approximation are currently being investigated.

Constitutive equations are obtained by first identifying the fluxes and the corresponding conjugate generalized forces. Constitutive relations are obtained by a general linear expansion of fluxes in terms of forces, writing all terms that are consistent with the symmetries of the system. For the conventional terms we follow the so-called "Harvard choice", taking as flux the symmetric part of the stress tensor $\sigma_{\alpha\beta}$ and the "objective" polarization rate of change

$$P_\alpha = \frac{\partial p_\alpha}{\partial t} + v_\gamma \partial_\gamma p_\alpha + \frac{1}{2}(\partial_\alpha v_\beta - \partial_\beta v_\alpha) p_\beta, \tag{1}$$

and for forces, the symmetric strain rate

$$u_{\alpha\beta} = \frac{1}{2}(\partial_\alpha v_\beta + \partial_\beta v_\alpha), \tag{2}$$

and the orientational field defined as the functional derivative of the free energy F with respect to the polarization $\mathbf{p}$.

$$h_\alpha = -\frac{\delta F}{\delta p_\alpha} \ . \tag{3}$$

The relevant part of the energy is the polarization free energy given by the standard expression for a polar liquid crystal [18]:

$$F = \int d\vec{x} \left[\frac{K_1}{2}(\nabla \cdot \mathbf{p})^2 + \frac{K_2}{2}(\mathbf{p}.(\nabla \times \mathbf{p}))^2 + \frac{K_3}{2}(\mathbf{p} \times (\nabla \times \mathbf{p}))^2 - \frac{1}{2}h_{\|}\mathbf{p}^2 \right] \quad (4)$$

where $K_1 = K$, K_2 and K_3 are the splay, twist and bend elastic moduli. We have introduced here a Lagrange multiplier $h_{||}$ in order to satisfy the constraint $\mathbf{p}^2 = 1$ and we have omitted surface terms such as the linear splay term which is specific to polar systems.

Of particular significance for our theory is the existence of active processes mediated by molecular motors. In general, a chemical fuel, such as Adenosine Triphosphate (ATP), provides the energy source. Motor molecules consume ATP by catalyzing the hydrolysis to Adenosine Diphosphate (ADP) and inorganic phosphate and transduce the free energy of this reaction to generate forces and motion along filaments. The energy of ATP is also used in order to polymerize and depolymerize filaments. The presence of the fuel represents a chemical "force" acting on the system. We characterize this generalized force by the chemical potential difference $\Delta\mu$ of ATP and its hydrolysis products, ADP and inorganic phosphate. The corresponding flux is the ATP consumption rate r. We thus have the following set of fluxes and forces:

$$\begin{array}{rcl} \text{flux} & \leftrightarrow & \text{force}, \\ \sigma_{\alpha\beta} & \leftrightarrow & u_{\alpha\beta}, \\ P_\alpha & \leftrightarrow & h_\alpha, \\ r & \leftrightarrow & \Delta\mu \ . \end{array} \quad (5)$$

After some manipulations we obtain the following constitutive equations [16]:

$$2\eta u_{\alpha\beta} = \left(1 + \tau\frac{D}{Dt}\right)\left\{\sigma_{\alpha\beta} + \zeta\Delta\mu\left(p_\alpha p_\beta - \frac{\delta_{\alpha\beta}}{3}\right) + \frac{\nu_1}{2}\left(p_\alpha h_\beta + p_\beta h_\alpha - \frac{2}{3}\delta_{\alpha\beta}p_\gamma h_\gamma\right)\right\}, \quad (6)$$

$$\frac{dp_\alpha}{dt} = -(v_\gamma\partial_\gamma)p_\alpha - \omega_{\alpha\beta}p_\beta - \nu_1 u_{\alpha\beta}p_\beta + \frac{1}{\gamma_1}h_\alpha + \lambda_1 p_\alpha\Delta\mu, \quad (7)$$

$$r = \zeta p_\alpha p_\beta u_{\alpha\beta} + \Lambda\Delta\mu + \lambda_1 p_\alpha h_\alpha \ . \quad (8)$$

where $\omega_{\alpha\beta} = \frac{1}{2}(\partial_\alpha v_\beta - \partial_\beta v_\alpha)$. Here we have included geometric non-linearities but we have restricted other terms to linear order in the logic of the expansion. Also, we have neglected chiral terms which in principle exist in cytoskeletal systems, and assumed an incompressible gel. Eq. (6) generalizes the expression of the stress tensor of a visco-elastic Maxwell gel to active systems with polarity. Indeed, if we first look at passive terms, i.e., those which survive when $\Delta\mu = 0$, it is straightforward to check that the equation describes an elastic medium at short time scales, and an anisotropic fluid at long time scales, i.e., a nematic liquid. For the sake of simplicity we have introduced only one viscosity coefficient η and $\sigma_{\alpha\beta}$ is the traceless symmetric stress. The elastic modulus of the short time gel is $E = \frac{\eta}{\tau}$.

The term proportional to $\Delta\mu$ is the only novel term compared to passive systems. If all flows are suppressed, for instance by suitable boundary conditions (which is possible), the active terms generate a nonzero stress tensor. A contractile stress corresponds to $\zeta\Delta\mu < 0$, and a dilative stress to $\zeta\Delta\mu > 0$. In view of the fact that experiments show that the stress is contractile in the case of the actin-myosin system, [19, 20] we call $\zeta\Delta\mu$ the contractility of the system; it has the dimensions of an elastic modulus. If by another choice of suitable boundary conditions, the stress is maintained to zero, the active term generates spontaneous motion. We illustrate both these situations in the following. Thus, ATP hydrolysis can generate forces and material flow in the gel via the action of active elements such as motors. These effects are characterized by one coefficient ζ. Similarly, Eq. (7) describes the dynamics of a nematic liquid, with just one added term weighted by the coefficient λ_1. This term plays a role only if the degree of order is not fixed, since it is a longitudinal term. If the polarization field can be taken as a unit vector, then this term does not change the physics. Another term implying gradients of the polarization is allowed by symmetry in Eq. (7), namely $p_\beta\partial_\beta p_\alpha$. Since this term does not appear in a passive system, the coefficient characterizing it must be proportional to $\Delta\mu$. It is thus a second-order term, which should not be retained in the logic of a linear expansion. It appears however naturally in gradient expansions far from equilibrium [9, 21]. It is easy to realize that it favors sharp polarization gradients. In cases where this term is important, interesting structures are expected [22].

Furthermore, material flow couples to the polarization dynamics via the coefficients ν_1. The rate of ATP consumption r is primarily driven by $\Delta\mu$ and characterized by Λ. However, it is also coupled to the fluid flow and to the field $\mathbf{h}$ acting on $\mathbf{p}$.

These equations are complemented by the force balance condition:

$$\partial_\beta\sigma^{\mathrm{tot}}_{\alpha\beta} = \partial_\beta\Pi \tag{9}$$

where Π is the pressure and $\sigma^{\mathrm{tot}}_{\alpha\beta} = \sigma_{\alpha\beta} + \frac{1}{2}(p_\alpha h_\beta - p_\beta h_\alpha)$. This last relation is familiar to liquid crystal physics and results from rotational invariance.

3. Material science aspects

If one specializes Eq. (7), to steady state in the passive case of a nematic liquid submitted to the action of a simple shear $\frac{\partial v_x}{\partial y}$ one finds that, in the absence of any other orienting field or boundary effect, the nematic director picks a well-defined and stable direction making an angle θ with the y-axis such that $\cos(2\theta) = \frac{1}{\nu_1}$ whenever $-1 < \frac{1}{\nu_1} < 1$ (Fig. 1). This means that the shear flow exerts a torque on the nematic director until it reaches that direction. This flow alignment has been well characterized in nematics (it plays often an unwanted role in display devices). This term is still present in the active polar case and the same shear will have the same tendency to orient the polarization direction (see Figs. 1 and 2).

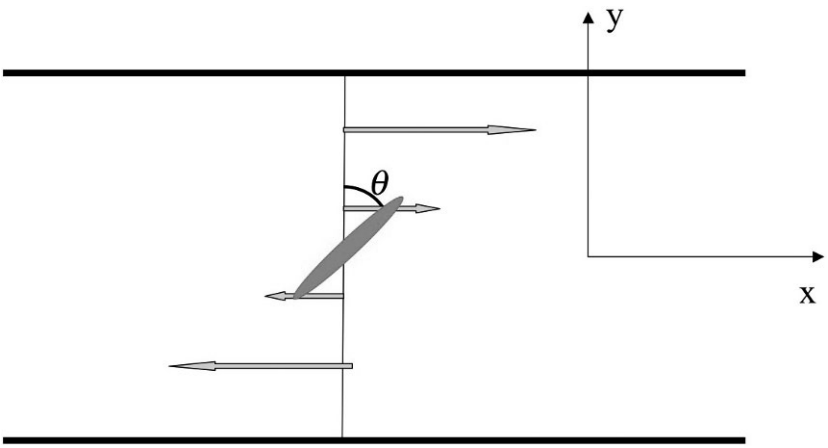

FIGURE 1. Alignment of a nematic director in a simple shear, as described in the text.

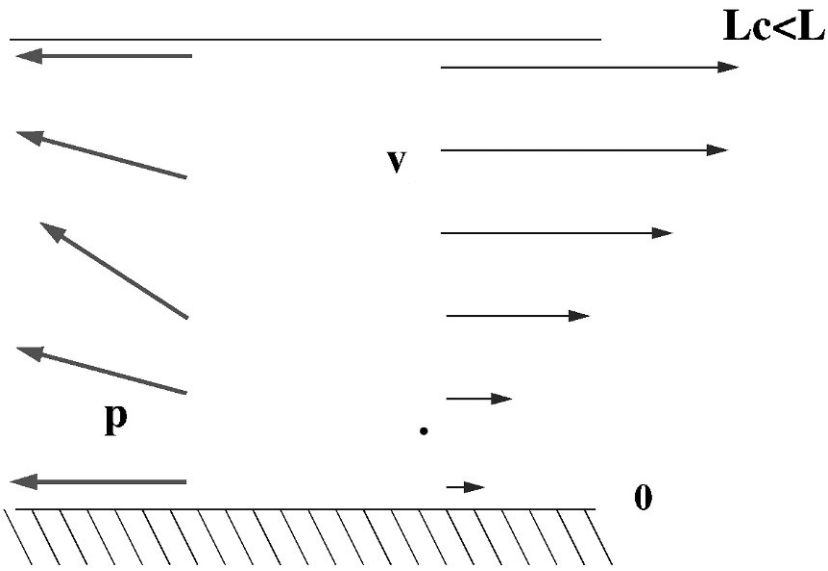

FIGURE 2. Spontaneous distortion (left) and flow field (right) of an initially homogeneous slab, with a free upper surface and parallel boundary conditions for the polarization.

Conversely, Eq. (6) shows that in the absence of stress, a polarization tilt tends to result in a shear. One can thus understand that with appropriate signs of the coupling terms, a possibility for a dynamical instability exists.

One can for instance look at a slab geometry with a free surface, and in which the polarization field is oriented parallel to the surfaces in a direction which we call y. We call x the normal to the slab surface. The free surface guarantees that, for any perturbation with zero wave vector parallel to the slab, the σ_{yx} stress vanishes. In the absence of activity, $\zeta\Delta\mu = 0$, we know from thermodynamics that the homogeneous state with polarization parallel to the faces of the slab is the lowest energy state. It is thus stable. Now, let us slowly increase activity. For small activity, the system is still stable. However, for a well-defined critical activity threshold, simultaneously the polarization field becomes inhomogeneous and a shearing motion sets in. This situation is reminiscent of the Frederiks transition: when a nematic liquid initially homogeneously aligned in direction y is submitted to the action of a magnetic field oriented in direction x, it starts to distort under the action of the field only after a well-defined threshold has been reached [18]. This is the basis for some display devices. There are two important differences: in nematics, flows are only transient, and the distortion sets in because of the action of an external orienting field. In active polar systems the distortion arises spontaneously without any externally orienting field and permanent flow results. Yet instability conditions, the polarization distortion and flow field above threshold, can be calculated in a way fairly similar to that of the Frederiks transition [23]. The activity threshold reads:

$$\zeta\Delta\mu_c = \frac{\pi^2 K(4\eta/\gamma_1 + (\nu_1+1)^2)}{-2L^2(\nu_1+1)}. \tag{10}$$

The minus sign shows that the instability exists only if the gel is contractile. L is the thickness of the slab and the other coefficients are defined in Eq. (6). The threshold value tends to zero for large enough thickness, at constant contractility: infinite size homogeneous active gels do not exist. There is always an instability, which can be at finite wave vector depending on boundary conditions for large enough systems. The stability of fluctuating modes have been worked out for thin and bulk compressible systems [21, 24, 25].

Note that we have discussed here a simple shear since it is rather easy to realize in the lab. A pure elongational shear orients the nematic director either parallel or perpendicular to it. This geometry cannot be obtained in any clean way with liquid crystals: we will show in Section 6 that it occurs spontaneously in biological systems and that it is physiologically important.

Topological singularities provide nice signatures of the phase symmetries. It is thus natural to characterize the topological singularities of active gels. In nematic liquid crystals such singularities are called disclinations. They can be classified with homotopy groups [26]. Defining a contour around the singularity point one counts the number of angular rotations of the nematic director; obtained in one rotation around the contour it can be integer or half-integer. For polar nematics, this number is necessarily an integer, positive if the rotation of the polar vector is in the sense of the contour and negative if it is in the opposite sense. It is called the topological charge of the disclination. We give on Fig. 3 the three possibilities

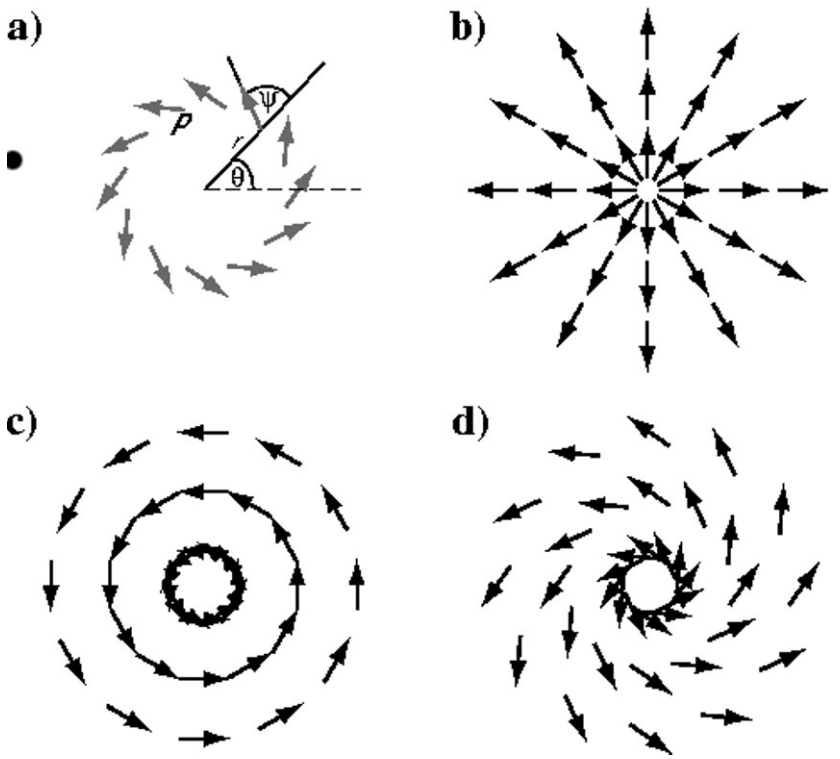

FIGURE 3. Disclinations of topological charge 1 in polar nematics.
a) Definition of the angles.
b) Stable structure when $K_1 < K_3$.
c) Stable structure when $K_1 > K_3$.
d) When $K_1 = K_3$ all spirals with indeterminate ψ are are stable. From Ref. [14].

corresponding to disclinations of topological charge 1. Since active gels behave like active polar nematics on long time scales, one expects the same geometrical aspects for the disclinations. However, the temporal symmetry is different: equilibrium systems are invariant upon time reversal (changing t in $-t$), whereas active systems are not. On general grounds one thus expects differences in the dynamical behavior of the disclinations. The case d) of Fig. 3 is particularly interesting: the spatial symmetry is such that the positive and negative rotations are not equivalent. Combined with the absence of time reversal symmetry, one concludes that such spirals should rotate permanently. Eqs. (6), (7) can be solved analytically, if we choose boundary conditions such that at a radius R from the singularity center, the angle ψ takes on the value such that $\cos(2\psi_0) = \frac{1}{\nu_1}$. Indeed, we expect a shear

flow to exist and thus the flow alignment to impose this orientation in the bulk of the disclination, breaking the passive degeneracy. Choosing the same orientation at the boundary suppresses the boundary layer and leads to simple results.

With these values of ψ_0, we find for the shear rate $u_{r\theta}$:

$$u_{r\theta} = \frac{\sin 2\psi_0}{4\eta + \gamma_1 \nu_1^2 \sin^2 2\psi_0} \tilde{\zeta} \Delta\mu \quad . \tag{11}$$

The velocity is ortho-radial, along the θ direction; it is obtained from (11)

$$v_\theta \quad = \quad 2r \left(\int_0^r \frac{u_{r\theta}}{r'} dr' + v_\theta^0 \right) \tag{12}$$

where v_θ^0 is an integration constant. For a finite system with radius R and with the boundary condition that no motion occurs at the boundary,

$$v_\theta = 2u_{r\theta} r \log \frac{r}{R} \quad . \tag{13}$$

In the cases a) and b) for "small" $\zeta\Delta\mu$, we find that there is no motion. Strictly speaking this result holds for the barycentric velocity only. The absence of motion is obvious for case a). For case c) there are constant fluxes indicating rotating motion, for instance of the motors around the singularity center; the term describing them appears in the densities conservation equations. For larger $\zeta\Delta\mu$, beyond a critical value depending on the elastic moduli anisotropy $K_1 - K_3$, we find that the immobile disclinations become unstable with respect to the onset of a rotating state [14, 15]. Strength one disclinations of type b), c), and d) are called respectively asters, vortices and spirals. Biological systems which follow the general definition of active gel, have shown the existence of both immobile asters and rotating spirals [7]. A detailed comparison with our results cannot be made though, because the experiments do not correspond to the long wavelength limit. Eventually, the existence of moving spirals provides a paradigm for what is called low Reynolds number turbulence [5, 24, 21].

4. Cell motility

In Section 2 we have derived generic hydrodynamic equations for active gels and in Section 3 we have discussed simple experimental situations which, except for the last one, have a priori little connection with Biology. In this section we discuss some features of a Keratocyte lamellipodium. Fish keratocytes are eukaryotic cells which can easily be obtained by pulling out a fish scale and dipping it in an appropriate physiological serum. If one squeezes a drop of the obtained suspension under a microscope, one observes after sedimentation, cells moving steadily on the lower coverslip. The velocity is of the order of $10\,\mu$m/min, which for a cell is fast. The reason for this high speed is probably a function of keratocyte cells in wound healing: they dash to the wound. They draw sizable attention because their motion is steady and their shape is smooth and invariant during the motion: it looks like a good start for understanding cell motility. The top image that one

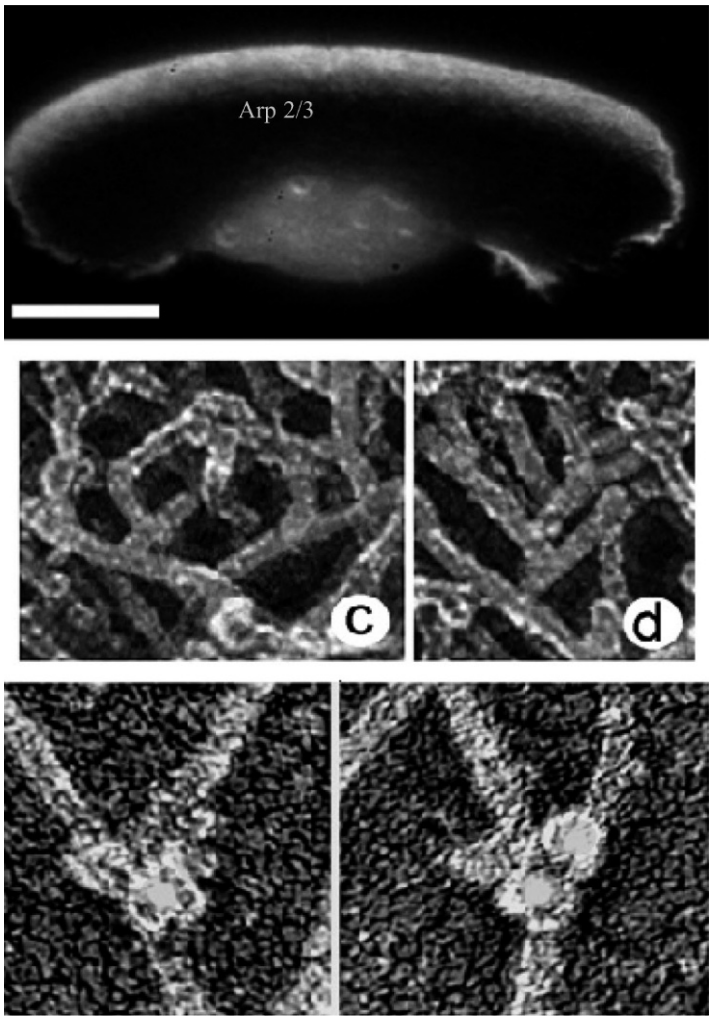

FIGURE 4. Top image: keratocyte crawling on a substrate towards the top of the image. Bar = 5μm. Middle images: actin network viewed with electron microscopy (the width of the filaments is 5 nanometers). Bottom image: close up view on a protein complex (Arp2/Arp3) known to play an important role in the assembling process of the network. Figure from [17].

sees on Fig. 4 shows a keratocyte moving upwards. Aside from the nucleus which builds a protuberance of the order of ten microns in the central rear region of the cell, the rest is fairly thin, of the order of a micron or less. The flat region in front

of the nucleus is called the lamellipodium, it extends from the leading edge to the vicinity of the nucleus. This region is filled with an actin gel, cross-linked by several proteins or protein complexes which are displayed on the middle and bottom of Fig. 4. Since the cross-links have a finite life time (of order tens of seconds), it is a physical gel. In addition, myosin motor bundles can grab two filaments at a time and exert a stress on the structure. Since the motor activity requires ATP hydrolysis, the lamellipodium acto-myosin system obeys exactly our definition of an active gel.

The biochemistry involved in the motion is well documented. We give here a minimal description. At the leading edge or very close to it, the actin network is assembled by polymerization and cross-linking. Further into the cell, in the vicinity of the nucleus, actin depolymerizes. This process is also typically out of equilibrium. The assembling units are ATP-monomers, whereas the disassembling ones are ADP-monomers: the filaments have been hydrolyzed along the way. It is known from molecular biology that this polymerization/depolymerization process is the main mechanism responsible for motion. This is not true of all types of motility, for instance it does not hold for ameoboid motion.

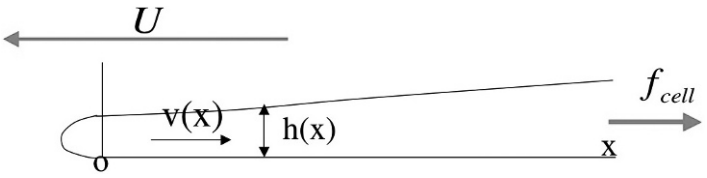

FIGURE 5. Sketch of an advancing lamellipodium.

Ideally one would like to be able to describe the three-dimensional cell shape, how it relates to speed and what is its response to external forces. We are not yet able to achieve such a task. We will just describe the lamellipodium profile perpendicular to the leading edge, in the central region of the keratocyte. In this region, in general, the leading edge is fairly straight and one can consider that the problem is translationally invariant in the direction parallel to the leading edge. A typical shape is sketched on Fig. 5. The lamellipodium moves globally to the left with velocity U keeping its shape constant. By definition U is taken to be positive. The gel moves with respect to the substrate with velocity $\mathbf{v}$, essentially oriented along the x direction. We call v this x component, omitting the subscript; it is positive if the gel motion is to the right. To find the motion characteristics and the shape of the lamellipodium, we must solve Eqs. (6), (7), with appropriate boundary conditions, keeping track of the polymerization process at the leading edge and of the interaction between the gel and the phospholipid membrane which surrounds the cell (plasma membrane). We take as an experimental input the fact that the filament orientation does not seem to vary significantly in these regions of the lamellipodium. We thus take $\mathbf{p}$ parallel to the x direction everywhere which solves Eq. (7) trivially. We treat separately a proximal region where the membrane

is not in contact with the substrate (i.e., to the left of the origin labeled O), and a distal one where it is in contact with the substrate (to the right of the origin).

4.1. Proximal region

In this region, the main challenge is to describe the interaction of the polymerizing gel and the plasma membrane [27]. The gel velocity field varies over a length scale which is larger than that of the proximal region: thus it can safely be considered as constant there. Once we have described the interaction with the membrane, all we have to do is match the velocity field and conserve forces in the plane of the origin O.

The velocities that we are considering are tens of microns per minute and for steady state shapes, the hydrodynamic forces on the membrane are totally negligible. Thus for all practical purposes the membrane is in mechanical equilibrium:

$$0 = \frac{\delta F^{\rm tot}}{\delta r_n}. \tag{14}$$

For a fluid membrane, the variation has to be taken with respect to displacements r_n normal to it. $F^{\rm tot}$ is the sum of the energy of the bare membrane F_m and the gel-membrane interaction energy. Its variation is easy to express in terms of the gel stress normal to the membrane and the bare membrane free energy:

$$\delta F^{\rm tot} = \delta F_m + \int ds \delta r_n (\sigma_{n,n} - \delta P) \ . \tag{15}$$

In this equation, the variations are taken again with respect to displacements δr_n; $\sigma_{n,n}$ is the normal-normal component of the gel stress tensor and δP the hydrostatic pressure difference between interior and exterior of the cell and ds the surface element on the membrane. The membrane bare free energy is that of a membrane under tension, with curvature rigidity and possibly spontaneous curvature as first introduced by Helfrich [28]:

$$F_m = \int ds \left(\sigma + \frac{K}{2} \left(H - C_0 \right)^2 \right) \ . \tag{16}$$

where H is the total curvature. The question of the membrane shape at the tip is a well-posed problem if one knows $\sigma_{n,n}$. The way it enters Eq. (15) shows that it provides an effective pressure difference. $\sigma_{n,n}$ can be obtained in an implicit way, by imposing that the polymerization rate parallel to the x direction must lead to a uniform displacement of the structure with velocity U to the left. Indeed the polymerization rate V_p is a function of the stress $V_p(\sigma_{n,n})$, and the continuity of the structure requires:

$$V_p(\sigma_{n,n}) = U + v \ . \tag{17}$$

Thus for a given U, extracting v from our hydrodynamic equations one can invert Eq. (17) to obtain $\sigma_{n,n}$. Microscopic theories relating polymerization rate and stress come into this relation [29, 30]. It is important to understand that the stress value depends on v which involves solving the hydrodynamic equations in the distal region: the effective pressure exerted by the polymerizing gel is not a local

property. One can illustrate the argument further by considering a "small" stress regime:

$$V_p(\sigma_{n,n}) = V_{p0} + \lambda\sigma_{n,n} \ . \tag{18}$$

The effective pressure then reads:

$$\delta P^{\text{eff}} = \delta P + \frac{V_{p0} - (v+U)}{\lambda} \ . \tag{19}$$

The shape of a membrane submitted to a pressure difference is a well-known problem. One can immediately infer that, provided the length $\sqrt{(\frac{K}{\sigma})}$ is small compared to the lamellipodium thickness, the radius of curvature at the leading edge is given by Laplace's law $R_l = \frac{\sigma}{\delta P^{\text{eff}}}$ and that the global shape is as sketched on Fig. 5. Conversely, taking the curvature radius of the order of the thickness and typical membrane tension values, we can estimate the value of the effective pressure to be of the order of 10^3Pa.

Force balance imposes that the integrated effective pressure difference matches exactly the pulling forces due to membrane tension together with external forces applied in the proximal region:

$$P^{\text{eff}} h(x=0) = \sigma + \sigma\prime + f_p^{\text{ext}}; \tag{20}$$

σ is the tension of the membrane in the presence of the gel as already introduced and $\sigma\prime$ is the tension "dressed" by the interaction of the membrane with the substrate. It could be negative and help the motion if the membrane tends to wet the substrate.f_p^{ext} is the integrated external force on the proximal region. Replacing P^{eff} by its expression Eq. (19) one can express the polymerization velocity as a function of applied force and membrane tensions:

$$V_p = U + v = V_{p0} - \lambda \frac{\sigma + \sigma\prime + f_p^{\text{ext}}}{h(x=0)} \ . \tag{21}$$

This expression shows that for a given tension there is a minimum thickness below which lamellipodia cannot grow. One sees also that an external force can either speed up or halt polymerization at constant thickness. In order to get a complete picture, we now need to calculate the gel velocity field v and the height profile h in the distal region.

4.2. Distal region

The gel dynamics is ruled by Eq. (6). Taking as boundary condition that both the normal and tangential stresses must vanish at the free surface of the lamellipodium, in a lubrication approximation we can recast the equation in a form involving only the thickness-averaged velocity field $h(x)v(x) = \int dz v(x,z)$ and the force $f(x) = \int dz \sigma_{x,x}(x,z)$:

$$4\eta \frac{dv}{dx} = \left(1 + \tau U \frac{d}{dx}\right) \frac{f}{h} + \zeta \Delta\mu \ . \tag{22}$$

An important point concerns the dynamical interaction of the gel and the substrate. The actin network is connected to the substrate by binding proteins. One

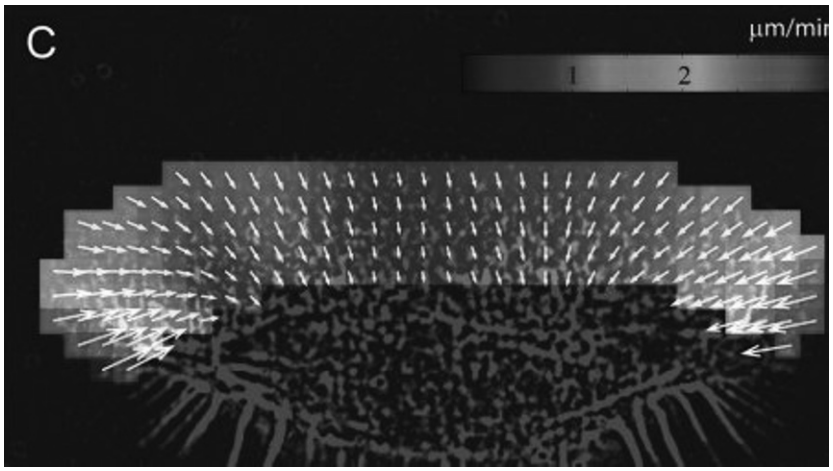

FIGURE 6. Velocity field determined by speckle microscopy in a lamellipodium. Figure from Ref. [31]

could believe that the correct boundary condition is a no-slip boundary condition. This is not the correct choice, because the bound state has a finite lifetime. For the slow motion that we consider the average force transmitted to the substrate can be shown to be proportional to the slip velocity [32, 33]. For large rates one can reach stick-slip regimes which have been observed in the Listeria motility [32]. This last regime may correspond to fibroblast motion and in some cases to keratocytes but most of the time a linear friction is sufficient. Expressing the global conservation of force reads:

$$\frac{df}{dx} = \xi v \ . \tag{23}$$

Eventually, global volume conservation leads to the relation:

$$h(x)(U + v(x)) = \text{const} \ . \tag{24}$$

With proper boundary conditions this set of equations is complete and can provide both the gel velocity field and the height profile. At the origin, one has to match distal and proximal solutions. In particular, forces must be conserved. At the rear of the lamellipodium, which we will also call the trailing edge, the boundary conditions are less well defined. The depolymerization process being rather well localized in space we take as a first attempt a depolymerization occurring in a well-defined plane $x = L$. In the case of cell fragments, we have discussed spatially distributed depolymerization [34], but for the case at hand, this simplification will be sufficient. At the trailing edge $x = L$ forces must be matched. We call f_L^{ext} the force that the rest of the cell is exerting on the lamellipodium (a genuine external force could be added as well). With these "rules" everything can be calculated [35]. One can get further insight by noting that the thickness variations are small.

If one linearizes the equations around the average thickness $\bar{h}$, one can solve the equations analytically. An important point comes from the comparison of Eqs. (22) and (23): eliminating the velocity in (22) with its value obtained from (23) one sees the emergence of the length scale $d = 2\sqrt{\frac{\eta\bar{h}}{\xi}}$. Forces and velocities are screened over a length scale d. In the regime where $L \gg d$ we find:

$$f(x) = \left(\zeta\Delta\mu\bar{h} - (\sigma+\sigma\prime) + \xi\tau v(0)[U+v(0)] - f_p^{\text{ext}}\right)\exp\left(-\frac{x}{d}\right) + (f_L^{\text{ext}} + \zeta\Delta\mu\bar{h}) \times \exp\left(\frac{x-L}{d}\right) - \zeta\Delta\mu\bar{h} \quad (25)$$

and

$$v(x) = \frac{1}{\xi d}\Bigg\{-(\zeta\Delta\mu\bar{h} - (\sigma+\sigma\prime) + \xi\tau v(0)[U+v(0)] - f_p^{\text{ext}})\exp\left(-\frac{x}{d}\right) + (f_L^{\text{ext}} + \zeta\Delta\mu\bar{h})\exp\left(\frac{x-L}{d}\right)\Bigg\} \quad (26)$$

with

$$v(0) \simeq \frac{-\zeta\Delta\mu\bar{h} + (\sigma+\sigma\prime) + f_p^{\text{ext}}}{\xi(d+\tau U)} \quad (27)$$

and

$$v(L) \simeq \frac{f_L^{\text{ext}} + \zeta\Delta\mu\bar{h}}{\xi d} \quad (28)$$

and eventually

$$U = v_{dp} - v(L) \simeq v_{dp}(f_L^{\text{ext}}) - \frac{f_L^{\text{ext}} + \zeta\Delta\mu\bar{h}}{\xi d}\ . \quad (29)$$

In this last equation v_{dp} is the depolymerization velocity. It can depend on stress but not on monomer concentration. The values of the gel velocities at the leading edge and at the trailing edge are completely decoupled. Note that $v(0)$ in the absence of external force is positive since $\zeta\Delta\mu$ is negative and the tensions' sum is in general positive. Thus, even though the motion of the lamellipodium is to the left, the gel moves to the right: this motion, called retrograde motion, is indeed found by biologists (Fig. 6) [31]. The measured profiles of both velocity and force exerted on the substrate can be compared to the results of Eqs. (26), (25), in the case when there is no applied force at the leading edge $f_p^{\text{ext}} = 0$, and the force at L is entirely due to the cell $f_L^{\text{ext}} = f^{\text{cell}}$. One can extract both the contractility and the friction coefficients. One finds for the contractility $\zeta\Delta\mu \simeq -10^3\,\text{Pa}$ and for the substrate friction $\xi \simeq 3\ 10^{10}\,\text{Pa}\cdot\text{s}\cdot\text{m}^{-1}$. The contractility is about one tenth of the short time shear modulus and the friction is of the same order of magnitude as that found experimentally in vitro for a passive actin gel/polystyrene interface [36].

Note that the steady state velocity U depends on the external force at the trailing edge f_L^{ext} but not on the force at the leading edge. This may seem surprising at first sight, but results from the steady-state conditions. The predicted effect

of forces is non-trivial and results from the fact that at steady state, monomer conservation imposes $h(0)V_p = h(L)v_{dp}$. Since the polymerization rate $V_p = k_p C(0)$ depends on the actin monomer concentration at the leading edge $C(0)$, and the monomers diffuse from the cell body to the leading edge, the length of the lamellipodium adjusts in such a way that the monomer concentration drops enough for the former equality to hold. It is thus the depolymerization rate which fixes the speed.

Suppose first that, starting from steady state, we turn on and maintain a force opposing the motion $f_L^{\rm ext}$ at the trailing edge. The explicit dependence of U on $f_L^{\rm ext}$ suggests that one should observe a slowing down of the lamellipodium. This will hold if v_{dp} does not depend on force. However, biochemistry, tells us that v_{dp} should increase exponentially with $f_L^{\rm ext}$. Then applying an opposing force at the trailing edge could result in a speeding of the lamellipodium, at steady state!

Suppose now that, starting from a steady state we turn on a force $f_p^{\rm ext}$ opposing the motion and which we maintain constant. The leading edge naturally slows down (k_p decreases), but as it slows down the length L of the lamellipodium decreases and the actin monomer concentration increases. This process goes on until the concentration is high enough for the steady state to be restored. For not too large forces, the inequality $L \gg d$ still holds and U is still given by Eq. (29)! If the force is larger, one may get to a regime where $L < d$, in which the gel velocity is constant:

$$v \simeq \frac{1}{\xi(L+\tau U)}(f_L^{\rm ext} + f_p^{\rm ext} + \sigma + \sigma\prime) \tag{30}$$

and the lamellipodium velocity now depends on all forces:

$$U \simeq v_{dp} - \frac{1}{\xi(L+\tau U)}(f_L^{\rm ext} + f_p^{\rm ext} + \sigma + \sigma\prime)\ . \tag{31}$$

Thus the predicted response of a lamellipodium to an opposing force applied at the leading edge is that the lamellipodium first shrinks without slowing down and only when it is "small" does it slow down.

5. Cell oscillations

There are several instances where the shape of a cell shows periodic oscillations. When the microtubules in a cell are depolymerized using a drug, the cell oscillates by forming a bleb which is a protrusion where the membrane is detached from the cytoskeleton [37]. Due to the contractility of the cortical actin layer in the cell body, the pressure in the cell body is larger than that in the bleb and the cytoplasm flows into the bleb. In an oscillating cell, the bleb is unstable and the whole cytoplasm empties in the bleb. The cortical layer then repolymerizes and the oscillation occurs by successive formation of unstable blebs. An example of an oscillating cell is shown in Fig. 7. The period of the oscillation is of the order of 10 minutes and the oscillation disappears when either actin or myosins are inhibited, which is a clear indication that the contractility of the cortical layer

drives the oscillation. Cell fragments which are formed by extraction of the nucleus show similar oscillations with a smaller period of the order of 2 minutes. These oscillations have been observed with several cell types.

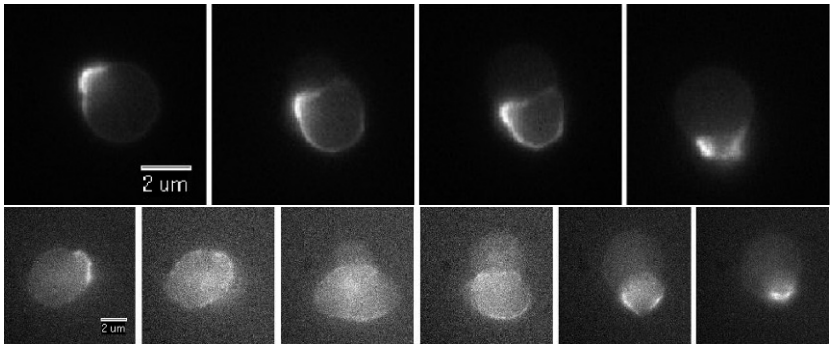

FIGURE 7. Shape oscillations after microtubule depolymerization of mice fibroblasts: in the first frame actin is fluorescently labeled; in the second frame myosin is fluorescently labeled. The labeling clearly shows the cortical layer in the cell body and the growth of a bleb which has no cortical layer and which invades the whole cell. After one oscillation, a new bleb appears Courtesy C. Sykes, E. Paluch.

Another type of shape oscillations is observed for fibroblast cells floating in solution when adhesion on any surface is prevented as shown on Fig. 8 [38]. The period of the oscillation is very well defined and of the order of 30s. As in the previous example, disruption of the cortical actin layer and inhibition of the myosin stops the oscillation. Myosin activity in a cell can be modulated by introducing various drugs. These experiments show that the oscillation period decreases when myosin activity increases. Another key component for the oscillation is the presence of extracellular calcium. The oscillation disappears if the medium is depleted in calcium. This suggests that calcium channels play an important role. Although the nature of calcium channels in these cells is not known, the addition of an inhibitor of ion channels stops the oscillations. Similar oscillations have been observed after depolymerization of the microtubules in Ref. [39].

In order to study the oscillations of suspended cells we assume that the membrane in these cells contains calcium channels and that these channels are gated by the deformation of the actin cortical layer x defined as the relative change in local area of the cortical layer [38]. If the deformation is large, the channels are open and if the deformation is small the channels are closed. For an incompressible layer of thickness e any change in the deformation is related to a relative change in thickness $\delta x = -\delta e/e$. The precise mathematical form of the opening probability $p_o(x)$ of the channels is not known but it is a sigmoidal function varying between 0 and 1 with a sharp variation around a critical value x_c that we suppose to be small.

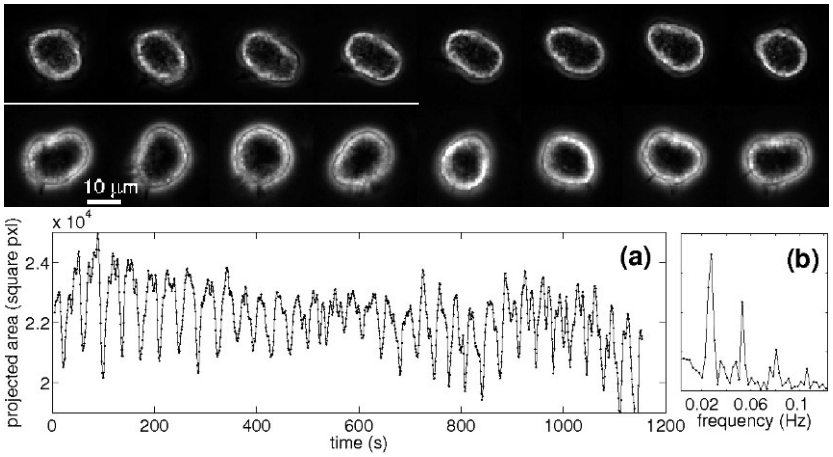

FIGURE 8. Shape oscillations of non-adhering fibroblasts. The second frame shows the periodic oscillation of the projected area of the cell and the associated Fourier spectrum. Figure from Ref. [38].

When calcium enters the cell, it undergoes a cascade of chemical reactions with calmodulin and the myosin light chain kinase which eventually leads to a phosphorylation of the myosins light chains and an increase in activity. A detailed study of the chemical reactions involved leads to a variation of the free calcium concentration in the cell as

$$\frac{d[Ca]}{dt} = \left[-k_{[Ca]}([Ca] - [Ca]_{\rm cell}) + \lambda p_0(x)\right] \ . \tag{32}$$

The first term describes the effect of calcium pumps which tend to drive the concentration back to its equilibrium value $[Ca]_{\rm cell}$ and the second term describe calcium penetration through the channel; the coefficient λ is proportional to the difference of the calcium chemical potentials inside and outside the cell and therefore depends on the calcium concentration in the external medium. We will assume here that the calcium concentration in the cell is not uniform and that the local opening of the calcium channels only modifies the local calcium concentration. This is justified by the fact that most of the calcium in the cell is sequestered by calmodulin and diffuses very slowly.

For the sake of simplicity, we assume that a small change in the calcium concentration $\delta[Ca]$ induces a small change in the local myosin activity $\delta\zeta\Delta\mu$ proportional to $\delta[Ca]$. This leads to an equation for the local variation of the myosin activity of the form

$$\frac{d(\delta\zeta\Delta\mu)}{dt} = -k_{[Ca]}\delta\zeta\Delta\mu - k_f\delta e/e \tag{33}$$

where k_f is a retroaction coefficient proportional to both λ and to the variation of the opening probability with the deformation $\frac{dp_o(x)}{dx}$.

The mechanism of the instability is sketched on Fig. 9. If the cortical layer is stretched on one side of the cell and compressed on the other, the calcium channels are open on the side where the membrane is stretched and calcium enters the cell on this side. The local increase of contractility provokes a local compression of the cortical layer and a closure of the channels. On the opposite side, the cortex is stretched and the channels open. The oscillation can then proceed.

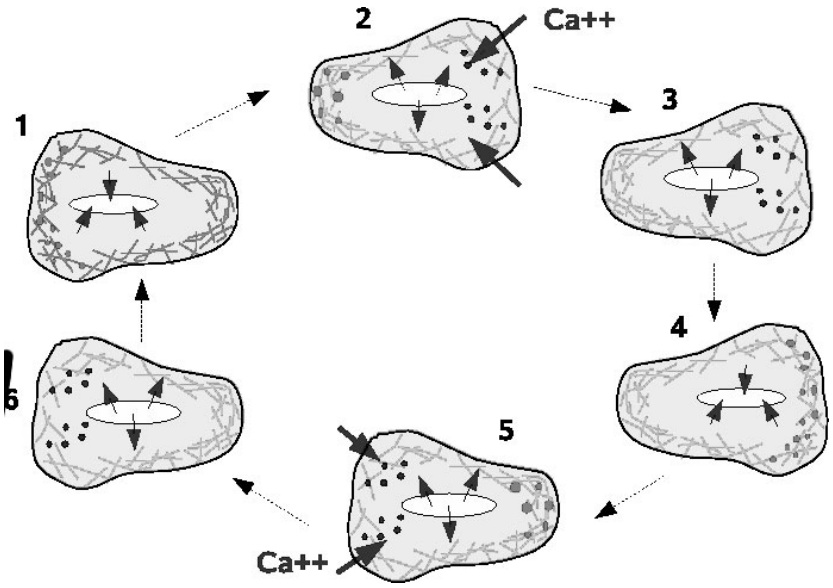

FIGURE 9. Sketch of the oscillation mechanism. Figure from Ref. [38].

The change in the cortical layer thickness is due both to a lateral flow of actin along the cortical layer and to the constant polymerization and depolymerization of the filaments (the so-called treadmilling process). We study the instability here ignoring treadmilling that we consider as very slow and we only consider the lateral actin flow. This flow obeys Eqs. (9), (6) since the cortical actin network obeys again our definition of an active gel. It is similar to the lamellipodium gel, but different in that the filament directions are on average parallel to the plasma membrane and thus perpendicular to the local symmetry axis, which is also the **p** axis. As a result, the gel is contractile in the plane parallel to the membrane.

In the absence of interaction with a substrate, cells are on average spherical. Thus we consider a spherical cell and perform a linear perturbation analysis expanding the shape in Legendre polynomials (assuming azimuthal symmetry). It

turns out that the most unstable mode always corresponds to a Legendre polynomial $n = 1$. This mode is somewhat peculiar since a perturbation of a sphere with a mode $n = 1$ gives a translation of the sphere. The radius of the cell R is therefore not changed by such a perturbation. The thickness of the cortical layer e however is proportional to $\cos\theta$, corresponding to a thinning of the cortical layer at one pole and a thickening at the other pole. The amplitude of the $n = 1$ mode for the thickness of the cortical layer can be calculated from the active gel theory. This leads to

$$\tau \frac{d\delta e/e}{dt} = \frac{\zeta \Delta\mu}{6E} \delta e/e + \left(1 + \tau \frac{d}{dt}\right) \frac{\delta\zeta \Delta\mu}{6E}. \tag{34}$$

The stability of the cortical layer can be studied from the dynamical system formed by Eq. (33), (34). The results are summarized in the stability diagram of Fig. 10. There are three regions in this diagram. At low activity and large enough value of

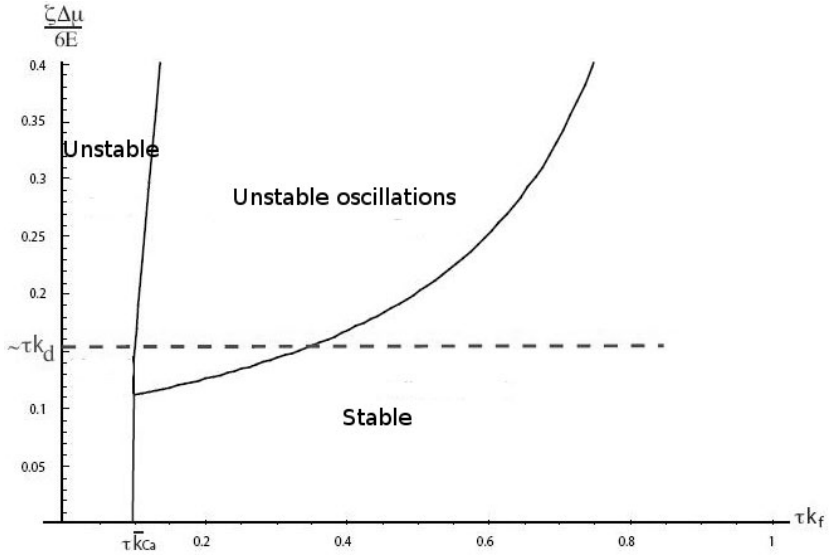

FIGURE 10. Stability diagram for a non-adhering cell. The vertical axis is proportional to the activity and the horizontal axis to $k_f\tau$ where k_f is the retroaction coefficient associated to the channels and τ the Maxwell viscoelastic relaxation time

$k_f\tau$ the spherical cell shape is stable. At small values of $k_f\tau$, the cell is unstable but there is no oscillation. As the instability grows the thickness decreases on one side of the cell and eventually a hole forms in the cortex. In this range of parameters, one expects either large blebbing oscillations of Paluch et al. or the apparition of simple blebs. In the central region of the stability diagram, the cell is unstable with respect to an oscillatory mode with the symmetry of a mode $n = 1$. The shape of the cell does not change in the linearized theory that we present here. However if

the parameters are not too close to the instability threshold, there are couplings between the $n = 1$ mode and higher-order modes which leads to an oscillation of the cell shape. The period of the oscillations is given by

$$\tau_{osc} = \frac{2\pi\tau}{\sqrt{\frac{\zeta\delta\mu}{6E}(4\tau k_f - (1-\tau k_f)^2 \frac{\zeta\delta\mu}{3E})}} \,. \tag{35}$$

As shown on Fig. 11 the period decreases with the activity as observed experimentally. Finally the horizontal line on Fig. 10 corresponds to the limit of validity

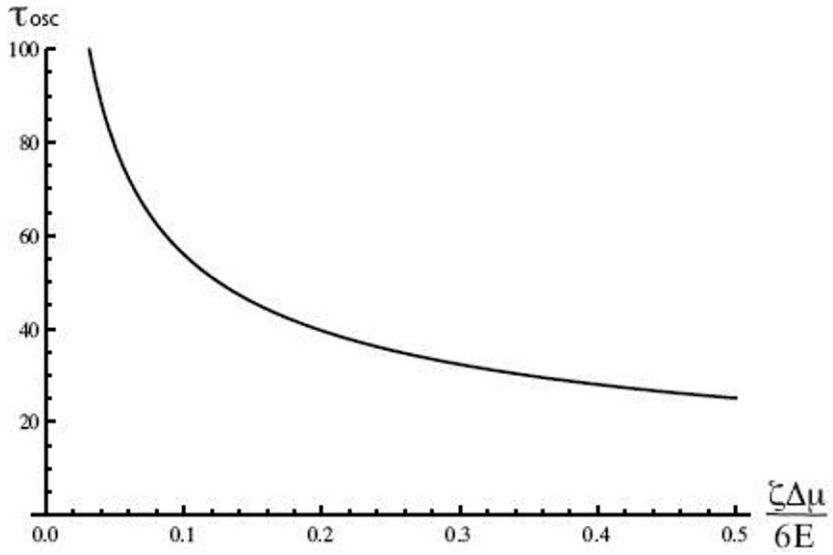

FIGURE 11. Variation of the oscillation period with the myosin activity.

of the theory. If the activity is smaller than $E\tau k_f$, treadmilling is important and stabilizes the cortical layer.

6. Wound healing and cytokinesis

Cell division proceeds by successive steps. In a first step, the S phase, the cell duplicates its biological material. During mitosis, the chromosomes of the two daughter cells separate and form two nuclei precursors to the two daughter cells [2]. After mitosis the two cells separate in a process called cytokinesis. At the beginning of mitosis the cells are roughly spherical: the actin cortical layer discussed in the previous section recruits myosin motors and becomes more active, leading to an increase of the cortical tension. After mitosis, the activity of the cortical layer is non-homogeneous, there is an excess of myosins at the equator of the cell and the activity is larger at the equator than at the poles [40]. The gradient in

activity drives a cortical flow from the pole to the equator, which has recently been experimentally studied in detail [41]. When the flow develops, an actin ring appears along the equator as shown on Fig. 12 [42]. The ring is contractile and pinches the

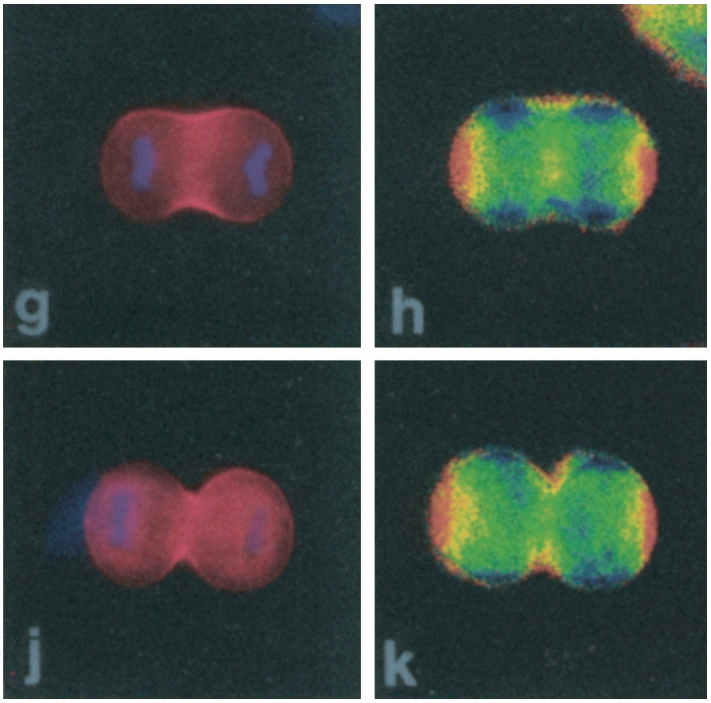

FIGURE 12. Cytokinesis and formation of the cleavage furrow. On the left panel the cell nuclei are labeled in blue. On the right panel, the actin filaments are labeled in blue, red or yellow. A blue or red color corresponds to an orientation of the filaments from the pole to the equator and a yellow color to an orientation around the equator. Figure from Ref. [42].

cell to create a so-called cleavage furrow. Eventually the cleavage furrow shrinks and leads to the formation of a bridge and to the separation of the two daughter cells when the bridge ruptures.

The aim of this section is to study quantitatively the onset of the cortical flow and the formation of the contractile ring appearing during cytokinesis. There are several instances in cellular biology where contractile rings form. A spectacular example is that of wound healing in a xenopus egg. The authors of Ref. [43] make a wound in a xenopus egg by laser ablation. As shown on Fig. 13, the wound is a circular hole in the cortex with a size of the order of 50μm. Just after the wound formation, myosins are recruited around the hole in a rim with a width

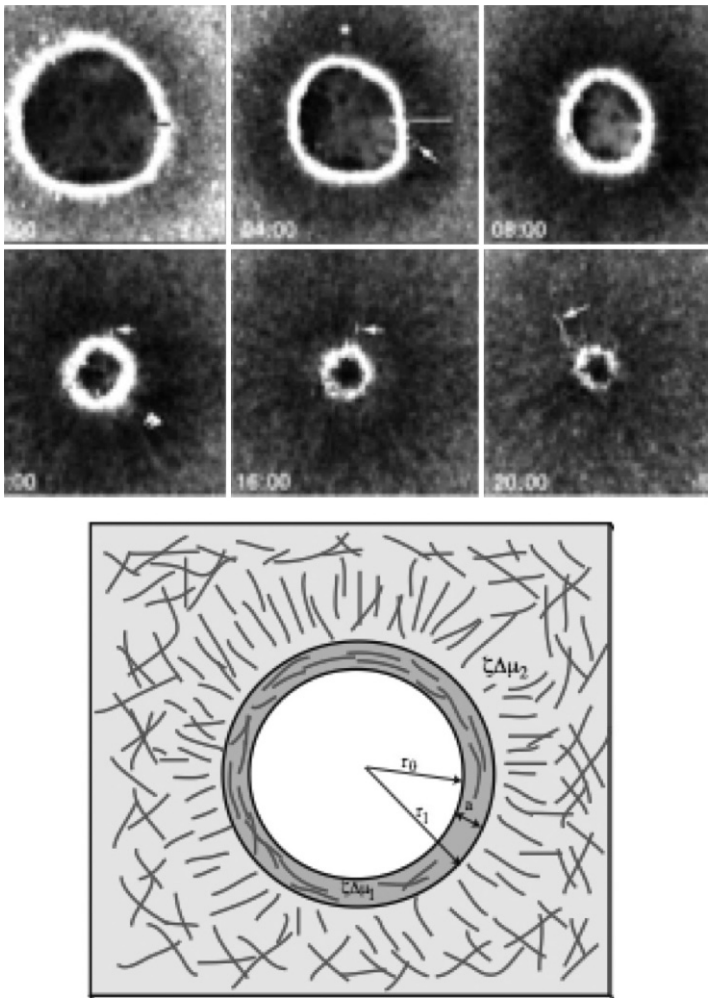

FIGURE 13. Wound healing in a xenopus egg. Upper figure: time laps picture of wound healing after hole punching in a xenopus egg cortex. Figure from Ref. [44]. Lower figure: schematic representation of the actin filaments distribution, and definition of the symbols used in the text. Figure from Ref. [38].

of the order of 5μm. There is thus in this rim an increase in activity [44]. As for cytokinesis, the gradient in activity induces a flow towards the rim which heals the wound at a constant radial velocity of the order of 0.04μm/s. Before the wound formation the actin filaments in the cortical layer are randomly oriented in the tangent plane to the embryo. When the wound heals, the actin filaments

are oriented radially towards the center of the wound outside the rim of increased activity and tangent to the wound edge inside the rim. They thus form a contractile ring around the wound. Another similarity with cytokinesis is that the recruitment of myosin motors around the wound is independent of actin, in the early stages, but it seems due to an increase of microtubule concentration around the wound. Other contractile rings are observed during the first division of C.Elegans embryos or in the dorsal closure of drosophila. In this last case the actin ring is not observed in a single cell but rather in a tissue. It spans over all the cells surrounding the closing hole.

The geometry of wound healing in a xenopus egg which is almost planar with a rotational symmetry is far simpler that that of the dividing cells. We therefore first discuss wound healing and then present very briefly our results on cytokinesis [45]. The closure of the wound is due to a competition between the contractile active stress away from the wound which tends to open the hole and the increased activity in the rim around the wound which tends to close the wound. In the absence of any activity around the hole, the group of F. Brochard [46] has shown that a hole in a visco-elastic film opens with a radius increasing exponentially with time. The increased activity in the rim increases locally the cortical tension and the local increase of the cortical tension drives the closure of the wound. In order to use the active gel theory for a film with randomly oriented filaments, it first must be generalized to systems with pretransitional nematic order. The nematic order parameter is defined in two dimensions as $Q_{ij} = \langle n_i n_j - \delta_{ij}/2 \rangle$ where n_i is the ith component of the local orientation of the actin filament. It is a traceless tensor and in a system with rotational symmetry it has a single independent parameter $\tilde{Q}$ which is positive if the actin filaments are pointing radially towards the center of the wound and negative if the actin filaments are pointing tangentially around the wound. In polar coordinates, the generalization of the active gel theory to gels in two dimensions with a nematic order leads to the two following equations for the order parameter $\tilde{Q}$ and the radial velocity v_r.

$$\begin{aligned} 4\eta\partial_r \left(\partial_r + \frac{1}{r}\right) v_r + (\partial_r + \frac{2}{r})(\zeta\Delta\mu + \beta_1\chi)\tilde{Q} = 0 \ , \\ \frac{\partial\tilde{Q}}{\partial t} = -\frac{\chi}{\beta_2}\tilde{Q} + \frac{\beta_1}{2}\left(\partial_r - \frac{1}{r}\right) v_r \ . \end{aligned} \tag{36}$$

The first equation is the force balance equation and the second equation is the equation for the relaxation of the order parameter. The first term on the left-hand side of the force balance equation is the gradient of the viscous stress, the second term is due to the gradient of the active stress where in this section the activity coefficient ζ is positive and the last term is the coupling to the order parameter. As already mentioned, contractility is in the plane of the cortex and perpendicular to the polarization axis. The reactive coefficient β_1 is proportional to the coupling coefficient ν_1 introduced in Eq. (6). The sign of β_1 is not imposed by the theory. We only consider here the case where β_1 is positive which corresponds

to an orientation of the actin filaments in the direction of an elongation (i.e., that of a positive velocity gradient). The nematic susceptibility χ is positive. In the second equation, the dissipative coefficient β_2 is positive and it is related to the rotational viscosity by $\gamma_1 = 2\beta_2 S$.

We consider now the wound as a circular hole in the cortex of a xenopus egg with a radius r_0. In the rim of size $a = r_1 - r_0$ around the wound where the myosins are recruited, the active stress is $\zeta_1 \Delta\mu$. Outside the rim, the myosin density is lower and the active stress is $\zeta\Delta\mu$ with $\zeta_1 > \zeta$. The dynamic equations can be solved easily in the limit where the relaxation of the order parameter is fast, i.e., in the limit where the $\frac{\partial \tilde{Q}}{\partial t}$ term is negligible in Eq. (36). The hole closes only if the activity is large enough, namely when $\zeta\Delta\mu_1 > \left(\frac{8\zeta\Delta\mu\eta\chi r_0}{a\beta_1\beta_2}\right)^{1/2}$. For $\zeta\Delta\mu$ above the threshold activity, we give in Fig. 14 a plot of both the order parameter and the radial velocity v_r.

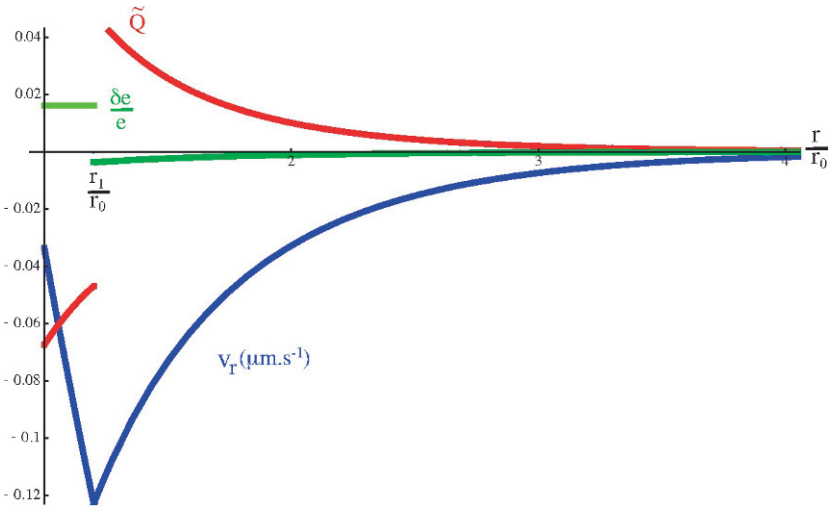

FIGURE 14. Radial actin velocity (blue curve) and nematic order parameter (red curve) during the wound healing of a xenopus egg.

Outside the rim $r > r_1$, the velocity modulus obtained from Eq. (36) decreases with increasing r as $1/r$ slower than the observed velocity which decays exponentially to zero. This is accounted for in Fig. 14 by adding in the equation of motion (36) a viscous friction between the cortex and the membrane. Outside the rim, the velocity gradient drives the order parameter $\tilde{Q}$ to a positive value corresponding to a radial orientation of the filaments. The gradient in the active stress thus drives a radial flow which itself orients the actin filaments. Inside the rim $r_0 < r < r_1$, the velocity gradient has the opposite sign, the order parameter

is negative and the actin filaments are oriented in the tangential direction. The velocity modulus decreases with decreasing r and the maximal velocity is reached at the edge of the rim $r = r_1$. The variation of the radius of the wound r_0 is equal to the velocity at r_0. If we assume, as seems to be the case experimentally, that the size of the active rim a is constant, we find a constant closing velocity

$$v_r(r_0) = -\frac{\zeta \Delta\mu_1^2 \beta_1 \beta_2}{16\eta^2\chi} a + \frac{\zeta \Delta\mu r_0}{2\eta} \ . \tag{37}$$

A direct comparison of the ring velocity with the experiments using $a = 2\mu$m, $\beta_1 = 2$ and $\beta_2 = \eta$, leads to the values $\zeta\Delta\mu_1/\eta = 0.5\text{s}^{-1}$ and $\zeta\Delta\mu_1/\chi = 0.3$ which are used in Fig. 14.

We now turn to the study of the formation of the contractile ring during cytokinesis [45]. Prior to the formation of the contractile ring, the cell is a sphere of radius R. The direction of the poles is perpendicular to the plane of division of the chromosomes during mitosis. We use here spherical coordinates with the pole direction as a reference axis. The angle θ vanishes at one of the poles and is equal to π at the other pole. The equator of the cell is the circle corresponding to $\theta = \pi/2$. At the beginning of cytokinesis, an excess of myosin motors is recruited along the equator in the region where the contractile ring will form. It has been shown experimentally that the recruitment of myosins is not connected to actin but it is rather related to an increase in the density of microtubule end points along the equator [40]. Myosin motors are carried on microtubules toward the equator by other molecular motors. The increase of the myosin density induces an increase of the active stress $\delta\zeta\Delta\mu(\theta)$. We describe this increase by the mathematical form $\delta\zeta(\theta) = \zeta_m \exp\left(-\frac{R^2\cos^2\theta}{a^2}\right)$. The size of the region around the equator where the myosins are recruited is a. Away from the equator, the active stress $\zeta\Delta\mu$ is constant and it is equivalent to a cortical tension $T = e\zeta\Delta\mu/2$ where e is the thickness of the actin cortex. This tension maintains the cell spherical. The increased activity along the equator of the cell tends to pinch the cell. It is the competition between these two effects which monitors the formation of the cleavage furrow. The dynamic equations for the formation of the contractile ring and the cleavage furrow are obtained along the lines followed to obtain the dynamic equations for wound healing in the xenopus egg. They must however be written on the surface of the spherical cell in spherical coordinates for the velocity field along the cell surface and the nematic order parameter. When the actin ring forms, the spherical cell is deformed and contracted at the equator. There is therefore a third dynamical equation associated to force balance in the radial direction which determines the cell deformation. The actual solution of these equations requires an expansion of all quantities in Legendre polynomials. These equations have been solved numerically and the results are displayed on Fig. 15. As in the case of wound healing, there is a cortical flow from the pole to the equator. If the increase in activity is switched on at time $t = 0$, the velocity is first located in the vicinity of the equator and then spreads towards the pole. At long times, a steady state is reached. The orientation

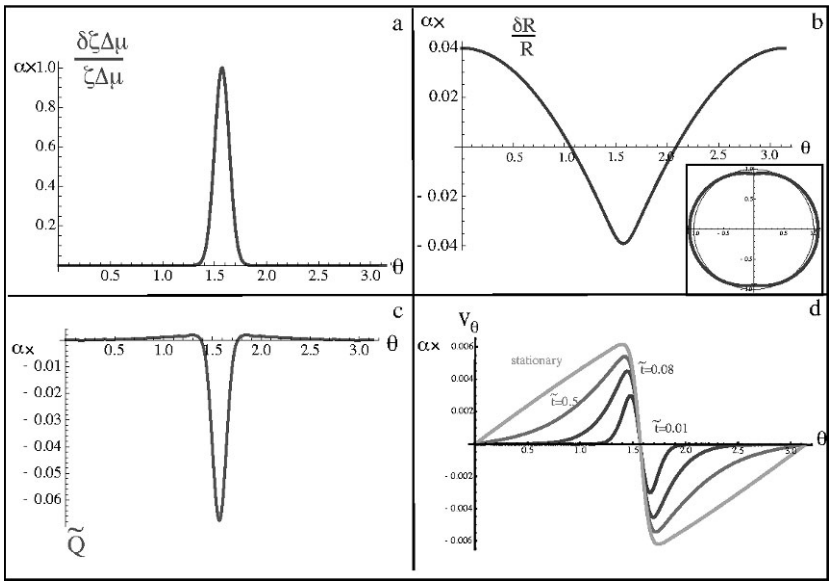

FIGURE 15. Formation of a contractile ring during cytokinesis.
a) Active stress profile.
b) Deformation of the cell around a spherical shape.
c) Nematic order parameter.
d) Velocity profile.
All the curves are plotted as a function of the angle θ.

of the actin filaments is again coupled to the flow. Away from the equator, the nematic order parameter is positive and the actin filaments are oriented from the pole to the equator. In the vicinity of the equator, the velocity gradient changes sign and the orientation of the actin filament changes: the nematic order parameter $\tilde{Q}$ is negative and the filaments are oriented in the ϕ direction along the equator forming thus a contractile ring. The figure also shows the cell deformation. The deformation reaches a steady state resulting from a balance between the average activity which favors a spherical shape and the increase in activity close to the equator which tends to develop the cleavage furrow.

This steady state is not observed in cell division where the cleavage furrow develops and leads to the separation of the two cells. The development of the cleavage furrow is due to non-linear effects that we have not included in the theory and which drive an instability of the steady state. One of the possible non-linearities that could be introduced is a coupling between the activity along the equator and the orientation of the filaments. It is known experimentally that the recruitment of myosin motors is larger on parallel filaments. The activity increases then with the alignment of the filaments and this clearly makes the weakly perturbed steady

state that we calculated unstable. A full non-linear theory for the formation of the contractile ring is however very complex and has not been performed.

The appearance of a cortical flow and the orientation of the actin filaments during cytokinesis has been recently studied in detail by the group of Y. Wang [41]. The application of the active gel theory to the cortical actin layer that we have done here clearly shows that once there is a region of enhanced activity along the equator, the pure mechanical effects taken into account by the theory are sufficient to explain the existence of a cortical flow, the orientation of the actin filaments and the formation of a cleavage furrow.

7. Conclusion

The linear theory which we have constructed has limitations. First we have not discussed fluctuations. Fluctuations have a thermal and a non-thermal component. The thermal component can be written in a systematic, well-controlled procedure from the current theory Ref. [25]. There are no added parameters. The non-thermal part can either be inferred by educated guesses or measured Refs. [25, 47]. The non-thermal fluctuations are again not universal and depend on molecular details. Related theories, written for bacterial colonies, predict giant density fluctuations observed in simulations Refs. [3, 13]. The importance of active gel fluctuations in cell behavior remains to be assessed. They could for example have a strong influence on endosome diffusion.

Second, the linear hydrodynamic theory that we have presented is a "gradient expansion" valid at long length scale. It is probably relevant to the actin-myosin system involved in the biological phenomena discussed here, but it does not apply to the microtubule system since individual microtubules span basically half of the cell. This is not a problem since microtubules are thought to play very little mechanical role. They are important signaling players for which we have no generic description so far.

The last limitation, is that we have described an active gel close to equilibrium. We have already pointed out that by doing so we miss a term in the dynamical equation for the polarization which can be added easily [22]. There are other consequences: far from equilibrium the tension induced by motors renormalizes the value of the short-time elastic modulus together with the contractility in a spectacular way [20, 48], $E \sim (f_s)^{\frac{3}{2}}$, $\zeta\Delta\mu \sim f_s$, where f_s is the motor stall force [48]. As a result, the ratio $\frac{\zeta\Delta\mu}{E}$ decreases like the inverse square root of the motors stall force even though both E and $\zeta\Delta\mu$ increase significantly! Thus increasing motor activity results in a decrease of the relative contractility. Furthermore, general barrier crossing theories tell us that the Maxwell time should decrease exponentially with the same stall force. These features help reconcile contradictory observations: some reports claim that calcium fluidifies the gel, others that it rigidifies it and increases activity. Indeed it does all of that depending on the observation time scale. At "short" time scale it rigidifies the structure, but it

shortens exponentially the Maxwell time, which results in a decrease in the long time viscosity $\eta = \tau E$! Such a remark is important if one wants to understand how increasing motor activity helps us move in a dynamical diagram such as the one of Fig. 10. More generally, which non-linearity should be kept in a non-linear theory is model dependent and needs close comparison with experiments.

We have shown in this review that the "active gel" theory has two virtues. First it can help extract the relevant physics involved in important biological processes such as cell motility, wound healing, cytokinesis and help getting at quantitative biology. It is interesting to remark that the orders of magnitude that we obtain for the contractility from cell motility experiments are useful to understand cell oscillations, wound healing and cytokinesis. Since the equations were obtained essentially from conservation laws and symmetry arguments, they are robust and do not depend on molecular details. What depends on the protein details is the value of the parameters such as viscosity, friction coefficient and contractility. One of the main findings is that thin active gel layers such as the cortical layer, are unstable without proper feedback. It has been known since the work of Hodgkin and Huxley that neural cells are electrically excitable media. We now know that most eukaryotic cells are almost mechanically excitable systems, prone to strong shape responses since they are sitting "close" to mechanical instabilities. This is probably the main reason for the observed cell plasticity. Getting to quantitative biology will require measuring the parameters that we have introduced in this macroscopic theory. Their number may look large at first sight, but there are only a few additional terms as compared to liquid crystals for which all coefficients have been measured and for which the theory has been very successful. One could also get a profound insight by studying artificial systems for which it would be easier to vary parameters. For instance it would be very useful to replace ATP by photons.

However, though the tool is useful it is not sufficient as it stands. We have already seen in the example of the oscillations that signaling comes into the game and is important. The second messenger, calcium, stabilizes the cortical layer and the feedback efficiency compared to the Maxwell time is the key feature controlling the oscillations. This feedback is not universal and depends on many details, so that even though one starts with a rather universal description the outcome depends on biological details. This is in a sense reassuring since we knew from the start that it had to, but it tells us that these details control the dynamical state of the cell, in a prescribed generic diagram. It also tells us that only a close collaboration between experiment and theory will allow us to construct a quantitative description of cell behavior.

Acknowledgement

It is a pleasure to thank F. Julicher, K. Kruse, C. Marchetti, P. Pullarkat, S. Ramaswamy, G. Salbreux, R. Voituriez and all our friends of the IHP session "Statistical physics of active matter". We also acknowledge the support of the Indo-French Center CEFIPRA under project No. 3504-2.

References

[1] M. Kirshner, J. Gerhart, *The Plausibility of Life: Resolving Darwin's dilemma*, Yale University Press, 2007.

[2] B. Alberts *et al.*, *Molecular Biology of the Cell*, Garland, 2002.

[3] R. Simha, S. Ramaswamy, *Hydrodynamic fluctuations and instabilities in ordered suspensions of self-propelled particles*, Phys. Rev. Lett. **89** (2002), 058101.

[4] J. Toner, Y. Tu, *Long range order in a two-dimensional dynamical xy model: how birds fly together?*, Phys. Rev. Lett. **75** (1995), 4326–4329.

[5] I. Tuval, L. Cisneros, C. Dombrowski, C.W. Wolgemuth, J.O. Kessler, R.E. Goldstein, *Bacterial swimming and oxygen transport near contact lines*, Proc Natl Acad Sci U S A **102** (7) (2005), 2277–2282.
URL http://dx.doi.org/10.1073/pnas.0406724102

[6] J. Prost, Conference solvay, in: Chemistry of molecular motors, 2007.

[7] F.J. Nedelec, T. Surrey, A.C. Maggs, S. Leibler, *Self-organization of microtubules and motors*, Nature **389** (6648) (1997), 305–308.
URL http://dx.doi.org/10.1038/38532

[8] A. Mogilner, G. Oster, *The physics of lamellipodial protrusion*, Eur. Biophys. J. **25** (1996), 47–53.

[9] T.B. Liverpool, M.C. Marchetti, *Instabilities of isotropic solutions of active polar filaments*, Phys. Rev. Lett. **90** (2003), 138102.

[10] A. Ahmadi, T. Liverpool, M. Marchetti, *Nematic and polar order in active filament solutions*, Phys. Rev. E **72** (2005), 060901.

[11] I. Aranson, L.S. Tsimring, *Pattern formation of microtubules and motors: Inelastic interaction of polar rods*, Phys. Rev. E **71** (2005), 050901 (R).

[12] K. Kruse, F. Julicher, *Actively contracting bundles of polar filaments*, Phys. Rev. Lett. **85** (8) (2000), 1778–1781.

[13] H. Chate, F. Ginelli, R. Montagne, *Simple model for active nematics: quasi-long-range order and giant fluctuations*, Phys. Rev. Lett. **96** (18) (2006), 180602.

[14] K. Kruse, J.F. Joanny, F. Julicher, J. Prost, K. Sekimoto, *Asters, vortices, and rotating spirals in active gels of polar filaments*, Phys. Rev. Lett. **92** (7) (2004), 078101.

[15] K. Kruse, J. Joanny, F. Julicher, J. Prost, K. Sekimoto, *Generic theory of active polar gels: a paradigm for cytoskeletal dynamics*, Eur. Phys. J. E **16** (2005), 5–16.

[16] F. Julicher, K. Kruse, J. Prost, J.F. Joanny, *Active behavior of the cytoskeleton*, Physics Reports **449** (2007), 3–28.

[17] T. Svitkina, G.G. Borisi, *Correlative light and electron microscopy of the cytoskeleton of cultured cells*, Methods Enzymol. **298** (1998), 570–592.

[18] P.-G. de Gennes, J. Prost, *The Physics of Liquid crystals*, Oxford University Press, 1993.

[19] K. Takiguchi, *Heavy meromyosin induces sliding movements between antiparallel actin filaments*, J. Biochem. **109** (4) (1991), 520–527.

[20] P.M. Bendix, G.H. Koenderink, D. Cuvelier, Z. Dogic, B.N. Koeleman, W.M. Brieher, C.M. Field, L. Mahadevan, D.A. Weitz, *A quantitative analysis of contractility in active cytoskeletal protein networks*, Biophys. J. **94** (8) (2008), 3126–3136.
URL http://dx.doi.org/10.1529/biophysj.107.117960

[21] Y. Hatwalne, S. Ramaswamy, M. Rao, R. Simha, *Rheology of active-particle suspensions*, Phys. Rev. Lett. **92** (2004), 118101.

[22] L. Giomi, M.C. Marchetti, T. Liverpool, *Complex spontaneous flows and concentration banding in active polar films*, Phys. Rev. Lett. **101** (2008), 198101.

[23] R. Voituriez, J. Joanny, J.J. Prost, *Spontaneous flow transitions in active polar gels*, Europhys. Lett. **70** (2005), 404–410.

[24] R. Voituriez, J.F. Joanny, J. Prost, *Generic phase diagram of active polar films*, Phys. Rev. Lett. **96** (2) (2006), 028102.

[25] A. Basu, J. Joanny, F. Julicher, J.J. Prost, *Thermal and non-thermal fluctuations in active polar gels*, Eur. Phys. J. E **27** (2008), 149–160.

[26] G. Toulouse, M. Kleman, *Principles of a classification of defects in ordered media*, J. Phys. Lett. **37** (1976), 149–151.

[27] J. Prost, C. Barbetta, J.-F. Joanny, *Dynamical control of the shape and size of stereocilia and microvilli*, Biophys. J. **93** (4) (2007), 1124–1133.
URL http://dx.doi.org/10.1529/biophysj.106.098038

[28] W. Helfrich, *Elastic properties of lipid bilayers: theory and possible experiments*, Zeitschrift fur Naturforschung C **28** (11–1) (1973), 693–703.

[29] A. Mogilner, G. Oster, *The polymerization ratchet model explains the force-velocity relation for growing microtubules*, Eur. Biophys. J. **28** (1999), 235–242.

[30] A.E. Carlsson, *Growth velocities of branched actin networks*, Biophys. J. **84** (5) (2003), 2907–2918.

[31] P. Vallotton, G. Danuser, S. Bohnet, J.-J. Meister, A.B. Verkhovsky, *Tracking retrograde flow in keratocytes: news from the front*, Mol. Biol. Cell. **16** (3) (2005), 1223–1231.
URL http://dx.doi.org/10.1091/mbc.E04-07-0615

[32] F. Gerbal, P. Chaikin, Y. Rabin, J. Prost, *An elastic analysis of listeria monocytogenes propulsion*, Biophys. J. **79** (5) (2000), 2259–2275.

[33] K. Sekimoto, K. Tawada, *Fluctuations in sliding motion generated by independent and random actions of protein motors*, Biophys. Chem. **89** (1) (2001), 95–99.

[34] A.C. Callan-Jones, J.-F. Joanny, J. Prost, *Viscous-fingering-like instability of cell fragments*, Phys. Rev. Lett. **100** (25) (2008), 258106.

[35] K. Kruse, J.F. Joanny, F. Julicher, J. Prost, *Contractility and retrograde flow in lamellipodium motion*, Phys. Biol. **3** (2) (2006), 130–137.
URL http://dx.doi.org/10.1088/1478-3975/3/2/005

[36] Y. Marcy, J. Prost, M.-F. Carlier, C. Sykes, *Forces generated during actin-based propulsion: a direct measurement by micromanipulation*, Proc. Natl. Acad. Sci. USA **101** (16) (2004), 5992–5997.
URL http://dx.doi.org/10.1073/pnas.0307704101

[37] E. Paluch, M. Piel, J. Prost, M. Bornens, C. Sykes, *Cortical actomyosin breakage triggers shape oscillations in cells and cell fragments*, Biophys. J. **89** (1) (2005), 724–733.
URL http://dx.doi.org/10.1529/biophysj.105.060590

[38] G. Salbreux, J.F. Joanny, J. Prost, P. Pullarkat, *Shape oscillations of non-adhering fibroblast cells*, Phys. Biol. **4** (4) (2007), 268–284.
URL http://dx.doi.org/10.1088/1478-3975/4/4/004

[39] I. Pletjushkina, Z. Rajfur, P. Pomorski, T. Oliver, J. Vasiliev, K. Jacobson, *Induction of cortical oscillations in spreading cells by depolymerization of microtubules*, Cell Motility and the Cytoskeleton **48** (2001), 235–244.

[40] J.H. Zang, J.A. Spudich, *Myosin II localization during cytokinesis occurs by a mechanism that does not require its motor domain*, Proc. Natl. Acad. Sci. USA **95** (23) (1998), 13652–13657.

[41] M. Zhou, Y.-L. Wang, *Distinct pathways for the early recruitment of myosin ii and actin to the cytokinetic furrow*, Mol. Biol. Cell. **19** (1) (2008), 318–326.
URL http://dx.doi.org/10.1091/mbc.E07-08-0783

[42] D.J. Fishkind, Y.L. Wang, *Orientation and three-dimensional organization of actin filaments in dividing cultured cells*, J. Cell. Biol. **123** (4) (1993), 837–848.

[43] C. Mandato, W. Bement, *Contraction and polymerization cooperate to assemble and close actomyosin rings around xenopus oocyte wounds*, J. Cell. Biol. **154** (2001), 785–797.

[44] C.A. Mandato, W.M. Bement, *Actomyosin transports microtubules and microtubules control actomyosin recruitment during xenopus oocyte wound healing*, Curr. Biol. **13** (13) (2003), 1096–1105.

[45] G. Salbreux, J. Prost, J.F. Joanny, *Hydrodynamics of cellular cortical flows and formation of contractile rings*, Phys. Rev. Lett. **103** (2009), 058102.

[46] G. Debregeas, P. Martin, F. Brochard-Wyart, *Viscous bursting of suspended films*, Phys. Rev. Lett. **75** (21) (1995), 3886–38.

[47] D. Mizuno, C. Tardin, C. Schmidt, F. MacKintosh, *Nonequilibrium Mechanics of Active Cytoskeletal Networks*, Science **315** (2007), 370–373.

[48] T. Liverpool, C. Marchetti, J.-F. Joanny, J. Prost, *Mechanical Response of Active Gels*, Europhys. Lett. **85** (2009), 18007.

Jean-François Joanny
Institut Curie, CNRS UMR 168, UPMC
26, rue d'Ulm, F-75248 Paris Cedex 05, France
e-mail: jean-francois.joanny@curie.fr

Jacques Prost
Physicochimie Curie, CNRS UMR 168, UPMC
Institut Curie, Section de Recherche
26, rue d'Ulm, F-75248 Paris Cedex 05, France

and

E.S.P.C.I, 10, rue Vauquelin, F-75231 Paris Cedex 05, France
e-mail: jacques.prost@curie.fr

A Physical Model of Cellular Symmetry Breaking

Jasper van der Gucht and Cécile Sykes

Abstract. Cells can polarize in response to external signals, such as chemical gradients, cell-cell contacts, and electromagnetic fields. However, cells can also polarize in the absence of an external cue. For example, a motile cell that initially has a more or less round shape can lose its symmetry spontaneously even in a homogeneous environment and start moving in random directions. One of the principal determinants of cell polarity is the cortical actin network that underlies the plasma membrane. Tension in this network generated by myosin motors can be relaxed by rupture of the shell, leading to polarization. In this chapter, we discuss how simplified model systems can help us to understand the physics that underlies the mechanics of symmetry breaking.

1. Introduction

Symmetry breaking in physics is an old well-known concept. It is based on energy considerations: a symmetrical system can lose its symmetry if an asymmetrical state has a lower energy. The initial symmetrical state can be either unstable or metastable. In the latter case, there is an energy barrier to be overcome before symmetry breaking occurs. An external trigger can drive the system from its symmetrical to its asymmetrical state, but simple noise can also do so if its amplitude is sufficiently high.

Symmetry breaking is ubiquitous in physics, and can lead to phase transitions or pattern formation. It is also an important theme in cell biology, where polarization is crucial for proper functioning of the cell, as recently reviewed (Li and Bowerman 2009). Cell polarization typically occurs in response to certain external or internal triggers. A well-known example is chemotaxis, where a chemical gradient leads to polarization and directed movement of bacterium cells. Polarization also occurs during cytokinesis, where intracellular stimuli triggered by the mitotic spindle determine the position of the cleavage furrow (Burgess and Chang 2005). Interestingly, cells conserve the ability to polarize even in the absence of an asymmetric signal (Devreotes and Zigmond 1988). For example, chemotactic

B. Duplantier and V. Rivasseau (eds.), *Biological Physics*, Progress in Mathematical Physics 60,
DOI 10.1007/978-3-0346-0428-4_2, © Springer Basel AG 2011

cells that are presented as a uniform concentration of chemoattractant polarize and move in random directions. Another example is blebbing, the spontaneous appearance of bare membrane bulges in some cells.

Symmetry breaking in biological systems is a complex phenomenon, because biological systems are always out of equilibrium. Hence, symmetry breaking is not just a transition to a state of lower potential energy. Instead, active, dynamic processes must be considered that feed energy into the system. A biochemical explanation for symmetry breaking was given by Alan Turing. In a seminal paper in 1952 (Turing 1952), he showed that patterns can be generated by simple chemical reactions if the reactants have different diffusion rates. To make this clear, he considered the hypothetical situation where the morphology of a cell (or cell clump) is determined by two chemical substances (called morphogens). These morphogens also control their own production rate: one enhances morphogen production (the activator) and the other inhibits morphogen production (the inhibitor). It was shown that a spatially homogeneous distribution of morphogens is unstable if the activator diffuses more slowly than the inhibitor. In this case, small stochastic concentration fluctuations are amplified, leading to a chemical instability (a "Turing instability") and the formation of concentration gradients (or patterns). Reaction-diffusion models of the Turing type have been widely explored to explain polarization and biological development (Gierer and Meinhardt 1972; Sohrmann and Peter 2003; Wedlich-Soldner and Li 2003).

Although reaction-diffusion models have proven to be very successful, there is increasing evidence that cell polarization is not only a matter of biochemistry; mechanical aspects play an important role, too. Recent work suggests that spontaneous polarization can also be driven by a mechanical instability of the actomyosin cortex of cells. In the remainder of this review we will focus on such mechanical instabilities.

2. The actin cortex and polarization

A key role in animal cell polarization is played by the cortical actin network. This is a thin shell of cross-linked actin filaments, myosin motors and actin-binding proteins, between 100 nm and 1 μm thick, that underlies and supports the plasma membrane (Fig. 1). The spatial organization and dynamics of the actin cortex are only beginning to be resolved. The myosin motors that are present in the cortex generate contractile forces that result in a tensile stress in the actin network (Dai, Ting-Beall et al. 1999). A stress is a force per unit area whereas a tension is a force per unit length. Thus, the tension in the cortex is roughly equal to the stress multiplied by the thickness of the cortex. In fact, the exact tension is given by the integral of the stress over the cortex thickness. Due to these stresses, the cell cortex is metastable: the elastic energy that is stored in the stressed actin shell can be released by rupture of the network or by detachment of the membrane from the cortex, as seen in fibroblasts and lymphoblasts (Paluch, Piel et al. 2005).

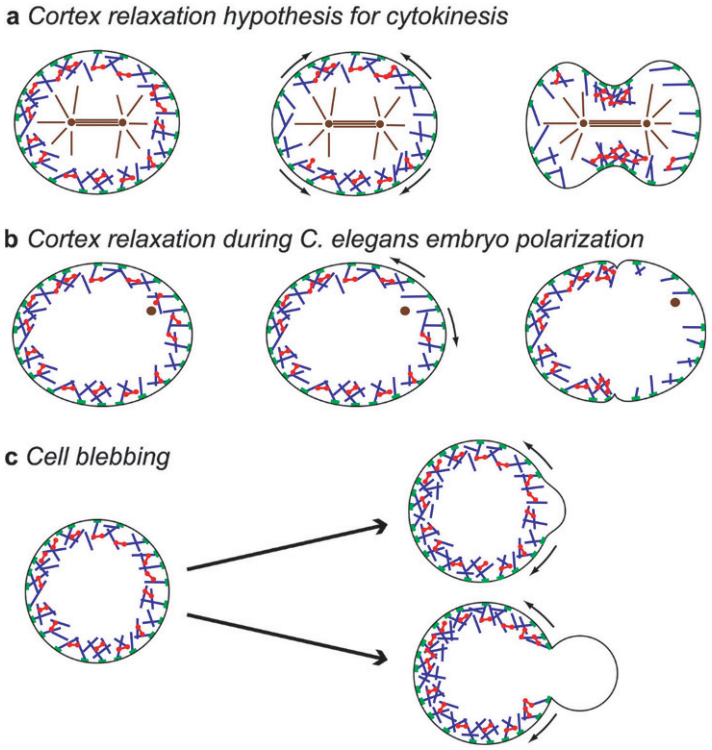

FIGURE 1. Scheme for different cases of cortex relaxation in cellular events. Blue rods, actin filaments; red dumbbells, myosin fibers; green patches, membrane attachments; brown rods, microtubules; brown dots, centrosomes. Curved arrows indicate the direction of cortex flows.

(a) At the onset of cytokinesis, spindle microtubules have been proposed to cause cortex relaxation at the poles of the cell. The relaxed regions expand, leading to cleavage furrow formation.

(b) In the *Caenohabditis elegans* embryo, shortly after meiosis II, the sperm centrosome triggers cortex relaxation. The cortex then flows away from the relaxed region, leading to polarity protein segregation and pseudocleavage furrow formation.

(c) Blebs form at sites of local detachment of the membrane from the cortex (top) or at sites of local cortex rupture (bottom). Cortex detachment from the membrane is sometimes followed by local cortex disassembly at the base of the bleb. Note that under certain conditions, multiple blebs can form.

Expansion of the relaxed region, due to pulling forces from the adjacent regions can lead to large cortical organizations, known as cortical flows (Bray and White 1988; Munro, Nance et al. 2004) or to the growth of membrane protrusions called

blebs (Keller, Rentsch et al. 2002; Charras, Yarrow et al. 2005; Paluch, Piel et al. 2005).

Cells can use this instability of the actin-myosin cortex by biasing it with intracellular or extracellular cues. For example, flows of the actomyosin cortex have been observed in various cell lines at the onset of cytokinesis, where they presumably contribute to formation of the cleavage furrow (Cao and Wang 1990; DeBiasio, LaRocca et al. 1996) (Fig. 1a). One possible mechanism that has been proposed to cause these cortical flows is a local relaxation of the cortex at the cell poles by astral microtubules (Bray and White 1988). Another process that is thought to depend on local cortex relaxation is the polarization of the one-cell *C. elegans* embryo. Here, the sperm provides the external cue: after fertilization, the point of sperm entry defines where cortical contractility locally relaxes (Cowan and Hyman 2004). As during cytokinesis, actin and myosin flow away from the relaxed region, transporting polarity proteins and shaping the pseudo-cleavage furrow (Munro, Nance et al. 2004) (Fig. 1b). Polarization by cortex relaxation may also, in some cells, precede cell migration (Paluch, Sykes et al. 2006; Yoshida and Soldati 2006).

In the examples mentioned above, cortex instabilities and polarization are triggered by a spatial cue that presumably relaxes the cortex locally. However, the cortical tension can also relax spontaneously. This is observed, for example, in blebbing cells, where spontaneous rupture or detachment from the membrane leads to the expulsion of membrane bulges in the weakened regions, driven by the pressure generated by contraction of the actomyosin cortex (Jungbluth, von Arnim et al. 1994; Keller, Rentsch et al. 2002; Paluch, Piel et al. 2005) (Charras, Yarrow et al. 2005; Sheetz, Sable et al. 2006) (Fig. 1c). Interestingly, blebbing cells can form one single large bleb (Paluch, Piel et al. 2005; Yoshida and Soldati 2006) or multiple smaller blebs over the cell surface (Cunningham 1995; Charras, Yarrow et al. 2005) (Fig. 2e, f; see below).

3. Build-up and release of tension in actin cortices grown around beads

A much simpler system for studying cortex symmetry breaking consists of actin gel layers growing around beads that are coated with an activator of actin polymerization and placed in a medium that reconstitutes actin assembly (Bernheim-Groswasser, Wiesner et al. 2002; van der Gucht, Paluch et al. 2005). Such beads have been used widely in the last ten years as a model system for studying actin-based movement of intracellular objects and lamellipodium extension (van der Gucht, Paluch et al. 2005; Mogilner 2006). Actin polymerization is activated at the surface of the bead, resulting in the growth of an actin gel around the bead. During gel growth, new monomers are incorporated at the bead surface underneath the pre-existing gel, which is thus pushed outward and stretched due to the curved surface (Noireaux, Golsteyn et al. 2000). As a consequence, stresses build

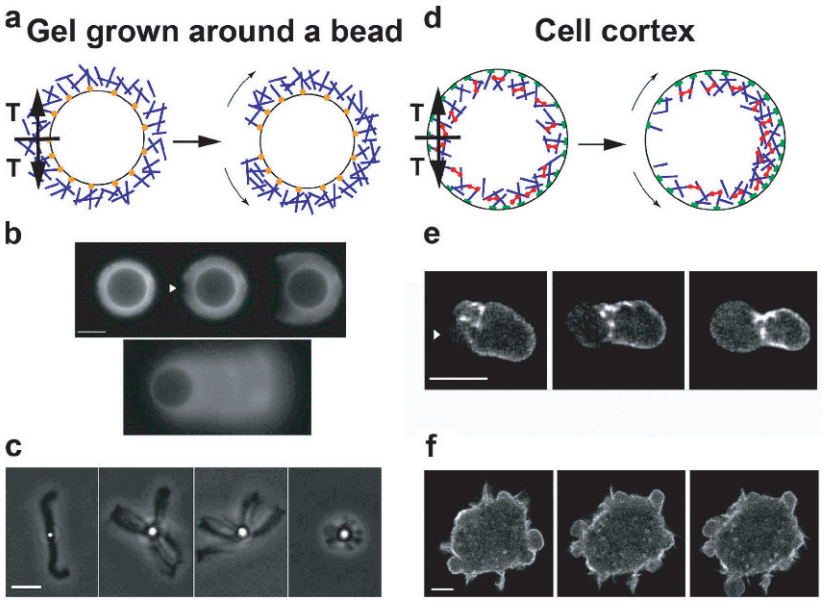

FIGURE 2. Analogy of the tension state in an actin gel growing from a bead surface and in the cell cortex. (a–c) Growing from a bead surface; (d–f) in the cell cortex. (a and d) Schematic view of the symmetry breaking of an actin gel growing from the surface of a bead (a) or the breakage of the cell cortex (d). Blue rods, actin filaments; red dumbbells, myosin fibers; green patches, membrane attachments; orange dots, actin polymerization activators. In both cases, a tension (T) builds up because of polymerization in curved geometry for the gel on the bead, and because of the presence of myosin motors in the cortex. Rupture of the gel leads to actin shell or cortical movement (curved arrows). (b) Time lapse of a symmetry breaking event (arrowhead) preceding the actin-based movement of a bead (epifluorescence microscopy with actin-AlexaFluor594). The first three images were taken 21, 24, and 40 min after the start of incubation, respectively. The last image shows the comet that develops eventually. Images are reprinted from van der Gucht et al. (2005). (c) Phase-contrast images of beads of different diameters (1 μm for the left image and 2.8 μm for the three other images) at low gelsolin concentration. Images were provided by M. Courtois (Institut Curie, Paris, France). (e) Time lapse of cortex breakage (arrowhead) and bleb growth in an L929 fibroblast fragment expressing actin-GFP. Fluorescence images are projections from a three-dimension reconstruction (time between images is 20 s). Images are reprinted from Paluch et al. (2005) (f) Time lapse of a cell displaying multiple blebs. Confocal images of an L929 fibroblast expressing actin-GFP were taken at 0, 25, and 35 s. Images were provided by J.-Y. Tinevez and E. Paluch (Max Planck Institute of Molecular Cell Biology and Genetics, Dresden, Germany). Bars (b and c), 10 μm; (e and f), 5 μm.

up and the actin shell is under tension (Fig. 2a). Initially, the shell grows homogeneously around the bead, but after some time the shell breaks spontaneously: a notch appears at the external surface of the actin gel (arrowhead in Fig. 2a), which grows inward and expands laterally with a velocity of a few micrometers per minute. After several minutes, the hole is big enough for the bead to escape from the gel, and the bead starts to move, trailing an actin comet (Fig. 2c). This symmetry breaking can also be triggered by a local disruption of the actin gel. Altogether, these observations strongly suggest that symmetry breaking is driven by the release of elastic energy stored in the actin gel (Noireaux, Golsteyn et al. 2000; Bernheim-Groswasser, Wiesner et al. 2002).

4. Modeling of actin shell growth and rupture around beads

Let us consider the growth of a homogeneous crosslinked actin gel around a bead in more detail. Polymerization occurs at the surface of the bead (where filaments are nucleated), while depolymerization occurs at the pointed ends that are assumed to be mostly situated near the exterior of the gel (Noireaux, Golsteyn et al. 2000; Sekimoto, Prost et al. 2004). Thus, the growth velocity of the gel can be described as follows:

$$\frac{dh}{dt} = a(k^b_{\rm on} C_a - k^{\rm off}_p) \tag{1}$$

where $k^b_{\rm on}$ and $k^{\rm off}_p$ are the rate constants for monomer addition at the inner surface (barbed ends) and monomer loss at the outer surface (pointed ends), respectively, C_a is the concentration of monomeric (G-)actin available for polymerization, and $a = 2.7$ nm is the gained filament length per monomer (Holmes, Popp et al. 1990). Note that we neglect here depolymerization at the barbed end and polymerization at the pointed end. The rate parameters $k^b_{\rm on}$ and $k^{\rm off}_p$ depend on the stress in the gel, because forces pushing or pulling on a filament can change the rate constants (Hill and Kirschner 1982). However, in the early stages of gel growth, the stresses in the gel are still small, and the rate constants are approximately equal to those of free barbed and pointed ends. Experimentally, the optimum initial polymerization rate ν^0_p is 0.6 μm/min, in accordance with an estimate of Eq. 1 using reported values for the rate constants (Pollard 1986): $k^b_{\rm on} = 12\mu M^{-1}s^{-1}, k^{\rm off}_p = 0.8s^{-1}$, and $C_a = 0.6\mu M$ (close to the critical concentration of pointed ends, because all barbed ends are capped). Note that $k^b_{\rm on}$, $k^{\rm off}_p$, and thus ν^0_p, depend on the concentrations of the various actin binding proteins (van der Gucht, Paluch et al. 2005).

As the gel grows thicker, the tensile stress in the gel also becomes higher. Assuming that the actin layer can be considered as an isotropic, linearly elastic gel, the tangential stress can be evaluated as (Noireaux, Golsteyn et al. 2000)

$$\sigma_{\theta\theta}(h) \approx \frac{Eh}{R} \tag{2}$$

where E is the elastic modulus of the gel and R is the radius of the bead. If the tensile stress becomes too high, the gel may rupture spontaneously. As suggested

by Griffith (Griffith 1920) rupture of a gel starts at the weakest spot in the gel, that is at a defect or flaw. The resistance of a material to fracture can be estimated by considering (i) the energy that is needed for breaking bonds to make this defect larger and (ii) the elastic energy that is released when the defect grows. As shown in (van der Gucht, Paluch et al. 2005), spontaneous fracture occurs as soon as the stress exceeds a critical value $\sigma^f \approx (E\Gamma/d)^{1/2}$, which corresponds to a critical gel thickness

$$h^f = R\,(\Gamma/Ed)^{1/2}\,. \tag{3}$$

Here, Γ is the fracture energy per unit area, which depends on the density and the strength of the crosslinks in the gel, and d is the typical size of the defects in the gel. As soon as the gel reaches this critical thickness, it becomes unstable and ruptures spontaneously. The value of the critical thickness and the time needed for symmetry breaking depend on the radius and on the presence of actin-binding proteins and crosslinkers that affect the growth rate and the gel properties (van der Gucht, Paluch et al. 2005).

The spontaneous fracture mechanism sketched above occurs only under appropriate conditions, when the concentrations of the various actin-binding proteins are in the proper range. If this is not so, the symmetry breaking process is delayed. The gel thickness first reaches a stable value and it may take a very (sometimes infinitely) long time before gel rupture occurs. The occurrence of a steady gel thickness is caused by the influence of the stress on the polymerization rate. As the gel grows thicker, the polymerization rate is reduced and at some point it may become equal to the rate of depolymerization at the external surface. If that happens, the thickness reaches a steady state value. Assuming that only the polymerization rate is affected by the stress, the following equation has been derived for the steady-state gel thickness (Noireaux, Golsteyn et al. 2000):

$$h^s = R\left(\frac{\Delta\,\widehat{\mu}}{E\xi^2 a}\right)^{1/2} \tag{4}$$

where $\Delta\,\widehat{\mu} = kT\ln\left(k^b_{\rm on}C_a/\,k^p_{\rm off}\right)$ is a measure for the energy of the polymerization process, and ξ is the mesh size of the actin network. For very large beads, the gel may become so thick that diffusion of actin monomers through the gel becomes the growth-limiting factor (Paluch, van der Gucht et al. 2006).

It is clear that if $h_s < h_f$, the gel will stop growing before the critical thickness for fracture is reached. The gel is now in a metastable state: it is stable towards small fluctuations (because the stress is below the threshold), but large fluctuations can still lead to gel rupture. The delay in symmetry breaking is due to an energy barrier that must be overcome. The height of the barrier is related to the difference between h_f and h_s. Such a nucleation mechanism process is also characterized by a much larger variation in symmetry breaking rates among different beads (van der Gucht, Paluch et al. 2005). As discussed in (Sekimoto, Prost et al. 2004), symmetry breaking could be enhanced in this case if the depolymerization rate is also affected by the stresses in the gel.

5. Comparison of symmetry breaking in cells and around beads

At a microscopic scale, the actin gels around the bead and the cell cortex appear to differ in several ways: the origin of the tension is different in the two systems and the orientation of the actin filaments and the direction of network growth are different as well. Yet, at a mesoscopic scale, the two networks are very similar: both are cross-linked actin meshworks where stresses develop tangentially to the actin layer (Fig. 2a and 2d). In both cases, relaxation of these stresses by rupture lead to polarization. Such a rupture occurs spontaneously if the stress exceeds a critical threshold, or it is delayed by an energy barrier.

This implies that symmetry breaking can be enhanced either by lowering the threshold (the strength of the network) or by increasing the global tension (the driving force). Observations of symmetry breaking in both the bead system and the cell cortex support this idea.

In both systems, the instability threshold can be lowered by lowering the density of crosslinkers in the actin gel, like filamin or α-actinin, which leads to a softer and weaker network. Indeed, depletion of filamin or degradation of α-actinin in cells enhances blebbing, probably due to cortical breakage, or at least a local release in the cortical tension (Cunningham 1995; Miyoshi, Umeshita et al. 1996). Conversely, shell breakage in the bead system is slowed down by the presence of filamin or α-actinin (van der Gucht, Paluch et al. 2005). In both systems, actin gel rupture is thus facilitated by the depletion of cross-linkers.

The driving force for cortex breakage in cells can be enhanced by increasing the activity of myosin II, leading to an increased contractility of the cortex and a larger cortical tension. Indeed, blebbing in cells is enhanced when the global contractility of the cortex is increased (Sahai and Marshall 2003) and, conversely, blebbing is reduced when contractility is decreased (Mills, Stone et al. 1998). In the bead system, the tension is related to the thickness of the gel layer. Hence, the analogous effect of decreased contractility (leading to a lower tension) is a decrease in gel thickness. This can be achieved, for example, by adding ADF (Actin depolymerizing factor)/cofilin, which enhances depolymerization of filaments in the outer regions of the actin gel. Indeed, at high ADF/cofilin concentrations the gel thickness remains small and no symmetry breaking is observed, indicating that the threshold tension for gel rupture can never be reached (van der Gucht, Paluch et al. 2005).

A growing actin shell in spherical geometry can break spontaneously and form a propelling comet at the opposite side of the breakage point, although the original breakage and therefore direction of the comet is random. If gel growth stops before the instability threshold is reached, then symmetry breaking can still be triggered by an external perturbation, for example by a local disruption of the actin network by photo-damage (van der Gucht, Paluch et al. 2005). Likewise, a local alteration of the actin cortex in cells, either by locally applying drugs that affect actin or by increasing the local stress mechanically, induces cortex rupture and bleb formation (Paluch, Piel et al. 2005).

We can compare the forces necessary for shell breakage around beads and for cortex breakage in cells. The stresses in the gel around beads can be estimated from the elastic modulus of the actin gel and the thickness of the gel (Noireaux, Golsteyn et al. 2000). This gives a value of 10^3-10^4 Pa for the critical tensile stress for gel rupture (van der Gucht, Paluch et al. 2005). The cell cortical tension has been estimated in different cell types and is on the order of 10^{-3} N/m for *Dictyostelium discoideum* (Pasternak, Spudich et al. 1989; Dai, Ting-Beall et al. 1999), lymphocytes (Pasternak and Elson 1985) or fibroblasts (Matzke, Jacobson et al. 2001), while it is about 20–30 times smaller for neutrophils (Evans and Yeung 1989). This gives, with a cortical thickness of a few hundred nm, a value of 10^3–10^4 Pa for the tensile stress in the cortex, very similar to the stress in the bead system. Interestingly, in *Dictyostelium discoideum*, deletion of either myosin II or of two myosins I, leads to a decrease of the tension by about 50%, suggesting that most of the cortex tension is due to myosin motors (Dai, Ting-Beall et al. 1999). Note that the cortical tension in these cells is very close to the threshold for cortex breakage, as breakage can be induced by applying pressures as small as 100 Pa, which is only 10% of the cortical stress (Paluch, Piel et al. 2005). However, in the case of *C. elegans* zygote, spontaneous symmetry breaking has never been observed: polarization always requires a cue from sperm entry. This indicates that the symmetric state in this case is far from the threshold. This could be due, for example, to a specific acto-myosin organization, to a high degree of cross-linking, or to rapid acto-myosin dynamics that would allow for effective reparation of the cortex.

6. Symmetry can break from one point or from multiple points

Cortex instabilities can occur at multiple sites along the cell periphery, leading to multiple blebs, or it can be a single event leading to a global polarization of the cell (as during polarization of the *C. elegans* embryo or the formation of large blebs) (Fig. 1 e,f). Similarly, the gel growing around a bead can rupture once, leading to the formation of a single comet tail, or it can break at multiple sites, leading to several comets (Fig. 1 b,c). The factors that determine whether a rupture leads to a global or to a local symmetry breaking are not well understood, but an analogy with the break-up of a liquid film on a surface by a nucleation and growth mechanism may provide insight. If nucleation of dry zones is fast compared to their growth, then dewetting will start independently from many different locations. By contrast, if nucleation is slow then dewetting will start from one single hole that expands. Similarly, if nucleation of new holes in the stressed actin shell is fast compared to growth of existing holes, then the actin network is likely to break at multiple sites. In contrast, if nucleation is slow compared to growth of a hole, then the formation of a single hole will probably lead to global polarization. Indeed, multiple comet tails around beads are observed when gel growth proceeds slowly (e.g., at low gelsolin concentration, J.v.d.G. unpublished results) and there is more

time for new holes to appear in the gel. The biochemical factors that regulate the nucleation and growth rates of holes in the cell cortex remain to be explored, but we can nevertheless speculate about factors that affect these rates. The nucleation rate in cells depends on how far the cortical tension is from the instability threshold. Obviously, in cases where spontaneous nucleation of instabilities does not occur but needs to be induced, there is usually only one rupture. In blebbing cells, on the other hand, nucleation is faster and blebs form spontaneously and rapidly. Multiple blebs tend to form when cells adhere to the substrate (Cunningham 1995; Sahai and Marshall 2003), whereas one single, large bleb is rather formed when cells are in suspension (Paluch, Piel et al. 2005). This might indicate that adhesion to the substrate could restrict membrane extension, and thus bleb growth.

The understanding of symmetry breaking in biomimetic systems can provide essential insight into spontaneous cortex rupture in cells. Therefore, reconstituting a cortex inside a liposome (Pontani, van der Gucht et al. 2009) provides an interesting artificial system that paves the way to a controlled study of symmetry breaking mechanisms in cells.

7. Stress-induced polarization in other systems

The concept of polarization driven by a global driving force that can locally exceed a mechanical threshold is not restricted to actin gels under tension, but can be applied more generally. For example, in plant cells, fungi, or bacteria, the force that drives cell deformation and growth comes from the internal osmotic pressure, while the mechanical strength that resists deformation is provided by the cell wall. Since the pressure in the cell is homogeneous, the polarized growth of walled cells requires an inhomogeneous extensibility of the cell wall (Cosgrove 2005). For example, root hairs and pollen tubes in plants, and buds in budding yeast are all initiated as small bulges growing at the cell periphery in regions where the cell wall is locally softened (Harold 2002). In order to achieve such a local wall softening, a cell needs to direct vesicles that contain cell-wall-loosening enzymes to specific sites at the cell periphery. This directed transport requires a polarized cytoskeleton, which may, in turn, be achieved by a biochemical instability (Wedlich-Soldner and Li 2003). Similarly, neuritogenesis starts by the growth of small buds at the initially spherical neuron surface. Buds are thought to result from pushing forces exerted by microtubules at spots where the actin network underlying the membrane is locally relaxed (Da Silva and Dotti 2002). This relaxation could be tension-driven, since the implication of the Rho/ROCK pathway, which activates myosin II, the molecular motor involved in contraction, has been reported (Da Silva, Medina et al. 2003). It could also result from some other kind of instability triggered by external signals (Da Silva and Dotti 2002).

On a larger scale, a mechanical instability has been proposed to explain the shape and size oscillations observed during regeneration of fresh-water polyp *Hydra Vulgaris*. At the initial stages, *Hydra* cells form a hollow sphere consisting

of a cell bilayer. This sphere inflates by uptake of fluid and builds up pressure due to stretching of the cells, analogous to the accumulation of stress in the actin gel growing around a bead. It has been proposed that this stress is released by rupture of the cell layer, followed by rapid shrinkage of the cell ball and re-swelling, thus generating an oscillation mechanism (Fütterer, Colombo et al. 2003). Interestingly, it has been suggested in a recent paper (Soriano, Rudiger et al. 2009) that *Hydra* symmetry breaking is a combination of a mechanical and a biochemical (Turing) instability: mechanical stresses in the cell aggregate affect the diffusion rates of proteins and thereby provide the biochemical conditions necessary for a Turing instability.

8. Conclusion

Cell polarization is a complex process that involves many factors, including the cytoskeleton, soluble cytoplasmic proteins and intra- and extracellular signals. The fact that cells can polarize even without external cues implies that they are operating close to an instability threshold. This increases their sensitivity to small stimuli, but also makes them sensitive to fluctuations. The nature of the symmetry-breaking instability can be mechanical, based on a release of stored elastic energy, or biochemical, based on reaction-diffusion processes. This suggests that cells could have redundant mechanisms for their polarization that can be triggered by different signals. It is very likely, however, that the two types of instabilities are strongly intertwined. In the case of *Hydra*, for example, biochemical instability seems to be triggered by a mechanical instability that precedes it. Conversely, it is well possible that in other cells a Turing-instability can lead to local cortex relaxations, and thus precede a mechanical instability.

References

A. Bernheim-Groswasser, S. Wiesner, et al., *The dynamics of actin-based motility depend on surface parameters*, Nature **417** (2002), 308–311.

D. Bray and J.G. White, *Cortical Flow in Animal Cells*, Science **239** (1988), 883–888.

D.R. Burgess and F. Chang, *Site selection for the cleavage furrow at cytokinesis*, Trends in Cell Biology **15**(3) (2005), 156–62.

L.-g. Cao and Y.-l. Wang, *Mechanism of the formation of contractile ring in dividing cultured animal cells. II. Cortical movement of microinjected actin filaments*, The Journal of Cell Biology **111**(5) (1990), 1905–1911.

G.T. Charras, J.C. Yarrow, et al., *Non-equilibration of hydrostatic pressure in blebbing cells*, Nature **435**(7040) (2005), 365–369.

D.J. Cosgrove, *Growth of the plant cell wall*, Nature Reviews, Molecular Cell Biology **6** (2005), 850–861.

C.R. Cowan and A.A. Hyman, *Cetrosomes direct polarity independently of microtubule assembly in C. elegans embryos*, Nature **431** (2004), 92–96.

C.C. Cunningham, *Actin Polymerization and Intracellular Solvent Flow in Cell Surface Blebbing*, The Journal of Cell Biology **129**(6) (1995), 1589–1599.

J.S. Da Silva and C.G. Dotti, *Breaking the neuronal sphere: regulation of the actin cytoskeleton in neuritogenesis*, Nature Reviews in Neuroscience **3**(9) (2002), 694–704.

J.S. Da Silva, M. Medina, et al., *RhoA/ROCK regulation of neuritogenesis via profilin IIa-mediated control of actin stability*, The Journal of Cell Biology **162**(7) (2003), 1267–1279.

J. Dai, H.P. Ting-Beall, et al., *Myosin I contributes to the generation of resting cortical tension*, Biophysical Journal **77**(2) (1999), 1168–76.

R.L. DeBiasio, G.M. LaRocca, et al., *Myosin II Transport, Organization, and Phosphorylation: Evidence for Cortical Flow/Solation-Contraction Coupling during Cytokinesis and Cell Locomotion*, Molecular Biology of the Cell **7** (1996), 1259–1282.

P.N. Devreotes and S. Zigmond, *Chemotaxis in Eukaryotic Cells: A Focus on Leukocytes and Dictyostelium*, Annual Review of Cell Biology **4** (1988), 649–686.

E. Evans and A. Yeung, *Apparent viscosity and cortical tension of blood granulocytes determined by micropipet aspiration*, Biophysical Journal **56**(1) (1989), 151–160.

C. Fütterer, C. Colombo, et al., *Morphogenetic oscillations during symmetry breaking of regenerating Hydra vulgaris cells*, Europhysics Letters **64**(1) (2003), 137–143.

A. Gierer and H. Meinhardt, *A theory of biological pattern formation*, Kybernetik **12**(1) (1972), 30–9.

A.A. Griffith, *The phenomenon of rupture and flow in solids*, Philosophical Transactions of the Royal Society A **221** (1920), 163–198.

F.M. Harold, *Force and compliance: rethinking morphogenesis in walled cells*, Fungal Genetics Biology **37** (2002), 271–282.

T.L. Hill and M.W. Kirschner, *Subunit treadmilling of microtubules or actin in the presence of cellular barriers: possible conversion of chemical free energy into mechanical work*, Proceedings of the National Academy of Sciences of the United States of America **79**(2) (1982), 490–4.

K.C. Holmes, D. Popp, et al., *Atomic model of the actin filament*, Nature **347** (6288) (1990), 44–9.

A. Jungbluth, V. von Arnim, et al., *Strong increase in the tyrosine phosphorylation of actin upon inhibition of oxidative phosphorylation: correlation with reversible rearrangements in the actin skeleton of Dictyostelium cells*, Journal of Cell Science **107**(1) (1994), 117–125.

H. Keller, P. Rentsch, et al., *Differences in Cortical Actin Structure and Dynamics Document that Different Types of Blebs are Formed by Distinct Mechanisms*, Experimental Cell Research **277** (2002), 161–172.

R. Li and B.A. Bowerman, Symmetry breaking in biology, Cold Spring Harbour perspectives, (2009).

R. Matzke, K.A. Jacobson, et al., *Direct, high-resolution measurement of furrow stiffening during division of adherent cells*, Nature Cell Biology **3** (2001), 607–610.

J.C. Mills, N.L. Stone, et al., "Apoptotic Membrane Blebbing Is Regulated by Myosin Light Chain Phosphorylation." The Journal of Cell Biology 140(3) (1998), 627–636.

Miyoshi, H., K. Umeshita, et al., *Calpain activation in plasma membrane bleb formation during tert-butyl hydroperoxide-induced rat hepatocyte injury*, Gastroenterology **110**(6) (1996), 1897–904.

A. Mogilner, *On the edge: modeling protrusion*, Current Opinion in Cell Biology **18**(1) (2006), 32–9.

E. Munro, J. Nance, et al., *Cortical Flows Powered by Asymmetrical Contraction Transport PAR Proteins to Establish and Maintain Anterior-Posterior Polarity in the Early C. elegans Embryo*, Developmental Cell **7** (2004), 413–424.

V. Noireaux, R.M. Golsteyn, et al., *Growing an actin gel on spherical surfaces*, Biophysical Journal **78** (2000), 1643–1654.

E. Paluch, M. Piel, et al., *Cortical actomyosin breakage triggers shape oscillations in cells and cell fragments*, Biophysical Journal **89** (1) (2005), 724–733.

E. Paluch, C. Sykes, et al., *Dynamic modes of the cortical actomyosin gel during cell locomotion and division*, Trends in Cell Biology **16** (2006), 5–10.

E. Paluch, J. van der Gucht, et al., *Deformations in actin comets from rocketing beads*, Biophysical Journal **91** (8) (2006), 3113–3122.

C. Pasternak and E.L. Elson, *Lymphocyte Mechanical Response Triggered by Cross-linking Surface Receptors*, The Journal of Cell Biology **100** (1985), 860–872.

C. Pasternak, J.A. Spudich, et al., *Capping of surface receptors and concomitant cortical tension are generated by conventional myosin*, Nature **341** (1989), 549–551.

T.D. Pollard, *Rate Constants for the Reactions of ATP- and ADP-Actin with the Ends of Actin Filaments*, The Journal of Cell Biology **103** (1986), 2747–2754.

L.L. Pontani, J. van der Gucht, et al., *Reconstitution of an actin cortex inside a liposome*, Biophysical Journal **96** (1) (2009), 192–8.

E. Sahai and C.J. Marshall, *Differing modes of tumour cell invasion have distinct requirements for Rho/ROCK signalling and extracellular proteolysis*, Nature Cell Biology **5** (8) (2003), 711–719.

K. Sekimoto, J. Prost, et al., *Role of tensile stress in actin gels and a symmetry-breaking instability*, European Physical Journal E **13** (3) (2004), 247–259.

M.P. Sheetz, J.E. Sable, et al., *Continuous Membrane-Cytoskeleton Adhesion Requires Continuous Accommodation to Lipid and Cytoskeleton Dynamics*, Annual Reviews of Biophysics and Biomolecular Structure **35** (2006), 417–434.

M. Sohrmann and M. Peter, *Polarizing without a C(l)ue*, Trends in Cell Biology **13** (10) (2003), 526–533.

J. Soriano, S. Rudiger, et al., *Mechanogenetic coupling of Hydra symmetry breaking and driven Turing instability model*, Biophysical Journal **96** (4) (2009), 1649–60.

A.M. Turing, *The chemical basis of morphogenesis*, Philosophical Transactions of the Royal Society of London. Series B, Biological Sciences **237** (641) (1952), 37–72.

J. van der Gucht, E. Paluch, et al., *Stress release drives symmetry breaking for actin-based movement*, Proceedings of the National Academy of Sciences of the United States of America **102** (22) (2005), 7847–7852.

R. Wedlich-Soldner and R. Li, *Spontaneous cell polarization: undetermining determinism*, Nature Cell Biology **5** (2003), 267–270.

K. Yoshida and T. Soldati, *Dissection of amoeboid movement into two mechanically distinct modes*, Journal of Cell Science **119** (Pt 18) (2006), 3833–44.

Jasper van der Gucht
Laboratory of Physical Chemistry and Colloid Science
Wageningen University
Wageningen, The Netherlands
e-mail: jasper.vandergucht@wur.nl

Cécile Sykes
Biomimetism of cellular movement
UMR 168
CNRS/Institut Curie/Universités Paris 6 et 7
11, rue Pierre et Marie Curie
F-75231 Paris Cedex 05, France
e-mail: cecile.sykes@curie.fr

Motor Proteins as Nanomachines: The Roles of Thermal Fluctuations in Generating Force and Motion

Jonathon Howard

Abstract. Motor proteins are enzymes that convert chemical energy derived from the hydrolysis of a small molecule called ATP into mechanical work used to power directed movement along cytoskeletal filaments inside cells. Motor proteins have essential biological functions such as driving the contraction of muscle, the beating of sperm and cilia, and the transport of intracellular cargoes. Motor proteins are also interesting from a physical point of view because they do what no man-made engines do: they transduce chemical energy directly to mechanical work without using heat or electrical energy as an intermediate. A central issue in the mechanism of this chemomechanical transduction by motor proteins concerns the roles played by thermal fluctuations, diffusion and Brownian motion. In this lecture I discuss several molecular models for motor proteins, including so-called ratchet models, and compare predictions of these models to experimental results for the microtubule-based motor protein kinesin. I argue that kinesin, which has two motor domains or "heads," walks using a "hand-over-hand" mechanism such that at least one head is bound to the microtubule. Diffusion likely plays an essential role by facilitating the search of the unbound head for the next binding site, a distance 8 nm away. During this diffusive phase, the bound head supports the load ensuring that forward motion can still take place even against loads up to several piconewtons.

The force-generation problem

The structures of both kinesin-1 (Kozielski *et al.*, 1997), the first member of the kinesin family to be discovered, and the microtubule (Nogales et al., 1998; Nogales *et al.*, 1999) have both been solved with atomic resolution (Fig. 1). Using lower resolution electron microscopy images, the approximate location and orientation of the motor relative to the microtubule has been deduced (Hirose and Amos, 2007;

B. Duplantier and V. Rivasseau (eds.), *Biological Physics*, Progress in Mathematical Physics 60,
DOI 10.1007/978-3-0346-0428-4_3, © Springer Basel AG 2011

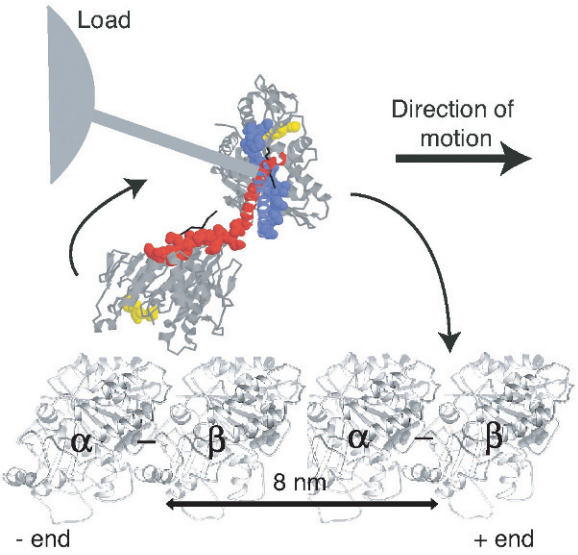

FIGURE 1. **Structure of kinesin-1 docked onto the surface of the microtubule.** The red and blue regions highlight the amino acids that form the region where the two motor domains come together to form the dimer. Cellular cargoes attach to the motor via additional amino acids not shown in the structure but denoted by the thick grey line. The yellow regions are where the ATP binds. Associated with the hydrolysis of ATP in the bound head, the free head moves to the next binding site, as indicated by the downward arrow; the bound head then becomes free.

Sindelar and Downing, 2007). In the absence of ATP, one of the motor domains, also called a "head," binds strongly in the crevice between the α and β subunits of the tubulin dimer, the building block of the microtubule. The other motor domain is not strongly bound to the microtubule.

Kinesin-1, also sometimes called simply kinesin, moves towards the fast-growing end of the microtubule, termed the plus end, which is capped by the β-subunit. Single-molecule techniques (e.g., Howard *et al.*, 1989) have shown that kinesin-1 moves at 800 nm/s at high ATP concentration and in the absence of load. This corresponds to about one hundred 8-nm steps (from one tubulin dimer to the next) per second. On average, kinesin takes about 100 steps along a microtubule before dissociating; it is therefore said to be a processive motor.

A load force slows down the motion. Several techniques have been used to apply loads to a single motor: hydrodynamic loads by increasing the viscosity of the aqueous medium through which the motor moves, and elastic loads from a flexible fiber or an optical trap. The motor stops at a load of $\approx 7\ pN$ (reviewed in

Howard, 2001). Larger loads cause motion in the opposite direction (Carter and Cross, 2005).

Despite 20 years of structural and single-molecule studies, how kinesin translates the 8 nm to the next tubulin dimer is not well understood. The force-generation problem is a difficult one.

Rectified-diffusion model

An early idea was that the motor diffuses along the microtubule surface (Fig. 2). The nucleotide binding and hydrolysis would then somehow rectify the diffusion such that the motor would let go at the starting site and then bind again when it reached the next subunit (Braxton and Yount, 1989; Vale and Oosawa, 1990). Note that several kinesins have been shown to be held electrostatically to the surface of the microtubule and to diffuse along the surface in the absence of ATP (Okada and Hirokawa, 2000; Helenius *et al.*, 2006; Bormuth *et al.*, 2009).

If diffusion plays a primary role in translocating the motor to the next binding site, then the speed is expected to depend on the viscous damping from the solution. By solving the diffusion equation, the first-passage time for a particle released at a reflecting boundary (the starting position in Fig. 2) to reach at absorbing boundary (the finishing position), a distance d away is

$$t = d^2/2D = d^2\gamma/2kT$$

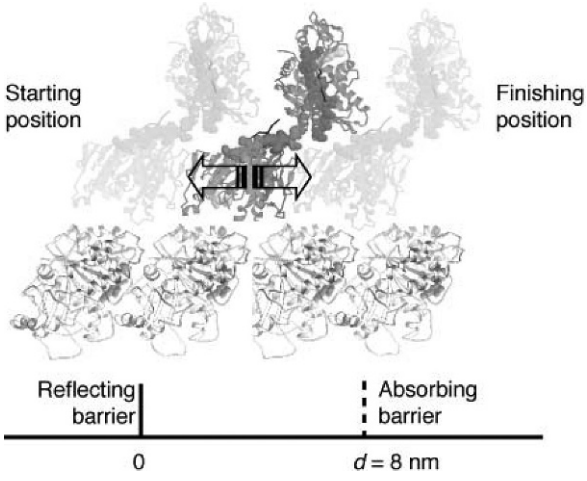

FIGURE 2. **The rectified-diffusion model.** The motor releases from its starting binding site, diffuses along the surface of the microtubule, and is then captured by the next binding site. The release and capture are coupled, in some unspecified way, to the hydrolysis of ATP and the release of products.

(Howard, 2001) where D is the diffusion coefficient, γ is the corresponding friction coefficient associated with the diffusion coefficient via the Einstein relation, k is the Boltzmann constant and T the absolute temperature. The maximum force exerted against a viscous load is therefore

$$f_{\max} = \gamma v_{\max} = \gamma d/t = 2kT/d \approx 1pN$$

where $v_{\max}$ is the maximum velocity and we have taken $d = 8\ nm$ (Hunt *et al.*, 1994).

The maximum force against a viscous load was measured by Hunt *et al.* (Hunt *et al.*, 1994) using the assay shown in Fig. 3a. In this "upside-down" assay, the motor is held at the surface of a chamber viewed under a microscope. When the motor attaches to and moves along the microtubule, the microtubule glides across the surface. The viscosity of the surrounding aqueous medium was increased by addition of solutes. The drag on a long microtubule is much greater than that on a single motor; drag forces of up to several piconewtons were applied. Analysis

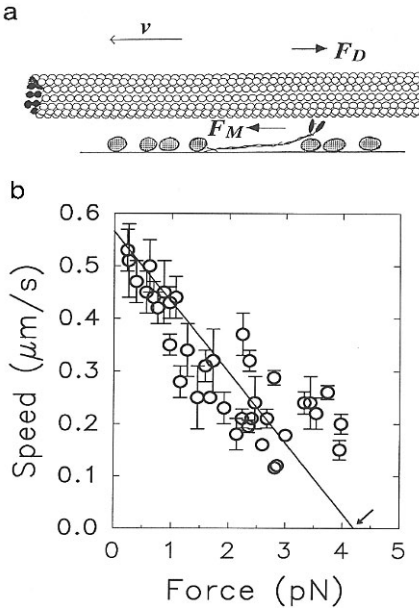

FIGURE 3. **Force exerted by kinesin-1 against a viscous load.** (a) In the "up-side down" assay, the kinesin is attached to the surface of the microscope slide and drives the gliding of the microtubule across the surface. The drag force increases with the viscosity of the aqueous medium and the length of the microtubule. (b) The force-velocity curve. The drag coefficient is estimated using the hydrodynamic theory of slender rods near surfaces (Hunt *et al.*, 1994). The drag force can then be calculated as the drag coefficient times the velocity.

of microtubule gliding speeds over a range of viscosities and microtubule lengths indicate that a single kinesin molecule can generate a force of up to 4 pN against this viscous load (Fig. 3b).

Because the measured force is much larger than the $1pN$ predicted from the first-passage-time analysis, the rectified diffusion model can be rejected.

Flashing-ratchet model

According to the flashing ratchet model shown in Fig. 4, the surface potential felt by the motor alternates between an asymmetric sawtooth energy profile, the ratchet (Fig. 4a, lower), and a flat profile (Fig. 4a, upper) along which the motor can diffuse freely. The switching from one profile to the other is controlled by ATP hydrolysis and product release. As in the rectified diffusion model, it is assumed the motor is constrained to the surface of the microtubule.

When the profile is sawtoothed, the motors concentrate in the valleys where the energy is lowest (Fig. 4b). When the profile switches to flat, the motor is

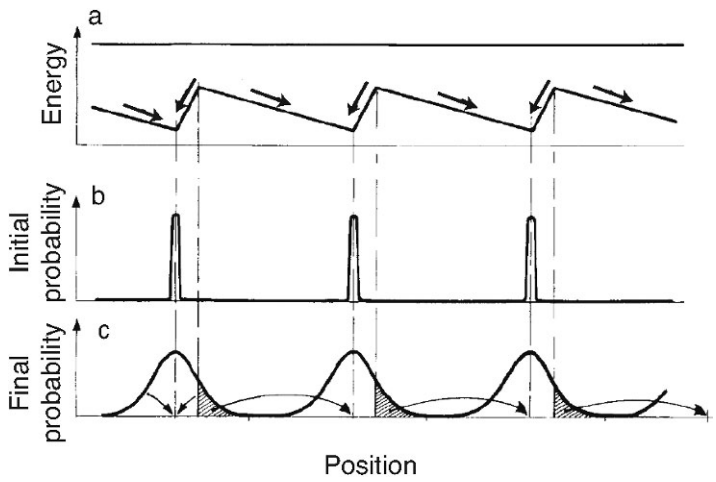

FIGURE 4. **Flashing-ratchet model.** (a) Sawtooth potential energy profile in the "on" state (lower) and flat energy profile in the "off" state (upper). (b) After equilibration in the on state, there is a high probability of finding the motor bound at the bottom of the valley. (c) During the off state, the motor diffuses; when the system enters the on state again, the particle will move to the right if it has diffused into the shaded region; otherwise it will diffuse back to the initial state. Alternation between on and off states leads to net motion to the right. After Ajdari and Prost, 1992; Magnasco, 1993; Rousselet et al., 1994; Astumian and Bier, 1994.

equally likely to diffuse in either direction. When the sawtooth profile returns, the direction of movement of the motor depends on its current position. If it diffuses only a small distance, then most of the time the motor will return to its initial position. However, if it diffuses past the position of the peak in the sawtooth, then it will move to a different valley. If and only if the potential is asymmetric, there will be a net movement in one direction.

This model can be ruled out definitively. A key prediction of the model is that on average the motor requires at least two switching processes per step because half the time the net diffusion is in the wrong direction (the greatest economy is when the sawtooth is most asymmetric). If the switching is driven by ATP hydrolysis, then this requires two ATP per step (on average). The stoichiometry of the movement of kinesin (steps per ATP) has been measured using a number of different approaches in different laboratories. For example, Coy et al. measured the speed of kinesin and the rate of ATP hydrolysis under identical conditions: dividing the speed by the ATPase gave 9 nm/ATP (Table 1). Similar results were obtained in other laboratories (Iwatani et al., 1999). Other measurements have shown that the step size is 8 nm (Ray *et al.*, 1993; Svoboda *et al.*, 1993; Carter and Cross, 2005). Thus there is ≈ 1 step per ATP. 1 step per 2 ATPs can be ruled out.

Table 1. (Kinesin-1 takes just one 8-nm step per ATP hydrolyzed (Coy *et al.*, 1999). Mean ± SE)

Speed (nm/s)	ATPase (s^{-1})	Distance/ATP (nm/ATP)	Stoichiometry (steps/ATP)
772 ± 29	88 ± 6	8.7 ± 0.7	1.08 ± 0.09

Huxley 1957 and powerstroke models

Two models have been extensively discussed in the muscle literature. According to the Huxley 1957 model (Fig. 5a) (Huxley, 1957), the motor domain contains an elastic element (i.e., a spring) that undergoes thermal fluctuations. The motor domain can only bind to its site on the filament when the spring is strained. The force due to the strain in the spring then drives motion. Following relief of the strain, the motor domain unbinds. The binding and unbinding are position dependent and are coupled to the hydrolysis of ATP. This model has also been called a thermal ratchet model (Cordova *et al.*, 1992) after Feynman's pawl and ratchet (Feynman *et al.*, 1963).

An early criticism of this model was that it would take too long for the strain to be built up through a thermal fluctuation alone (Eisenberg and Hill, 1978). However, this is not the case: the dynamical properties of a damped spring undergoing thermal fluctuations has been solved (Kramers, 1940), and it can be shown (Hunt *et al.*, 1994) that for the dimension of the motor domain and the

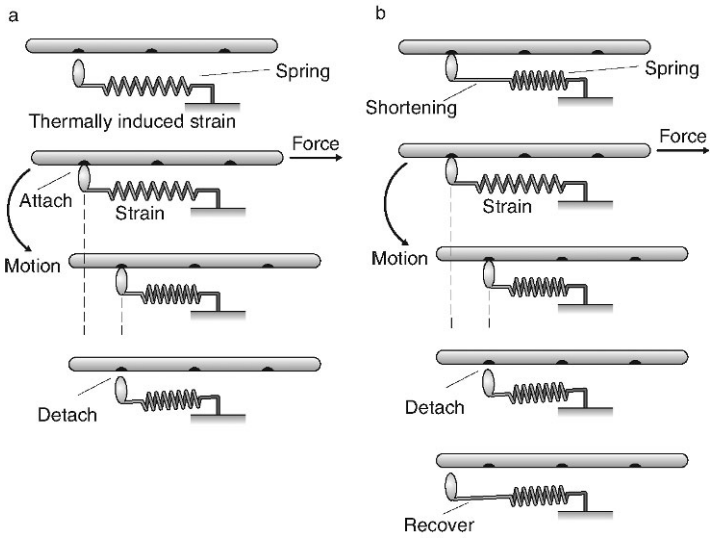

FIGURE 5. **Huxley 1957 (left) and powerstroke models.** These models were initially developed for myosin, with the thermal ratchet model following Huxley (1957) and the powerstroke model following Eisenberg and Hill. See text for details.

viscosity of the aqueous solution in which it is bathed, the time is not prohibitive (at least at low loads). Nevertheless, this criticism led to the development of *powerstroke* models (Fig. 5b) (and also Huxley and Simmons, 1971). The key difference between the models is that rather than a thermal fluctuation leading to strain (Huxley), the powerstroke model envisages that strain is developed by a conformational change in the motor domain. In Fig. 5b the strain is shown as a lengthening; a rotation is now favored given the structure of the myosin head (Howard, 2001). The conformational change is coupled to the ATP hydrolysis cycle. Detailed powerstroke models have been developed (Eisenberg *et al.*, 1980). In addition, the flashing ratchet model can be converted to a powerstroke model by replacing the flat profile with another ratchet that is phase shifted relative to the original sawtooth landscape. Alternation of these profiles will lead to directed motion (Parmeggiani *et al.*, 1999).

The Huxley and powerstroke models are actually closely related (Howard, 2006). Both can be understood in terms of a transition-state model (Fig. 6). The difference between them comes down to the location of the transition state along the reaction coordinate defined as the position of the load carried by the motor (e.g., a bead held in an optical trap) projected onto the axis of the filament.

In the Huxley model, the transition state is near the final state so that the motor domain must diffuse through a large distance with respect to the step size. In the powerstroke model, the transition state is close to the initial state, so that

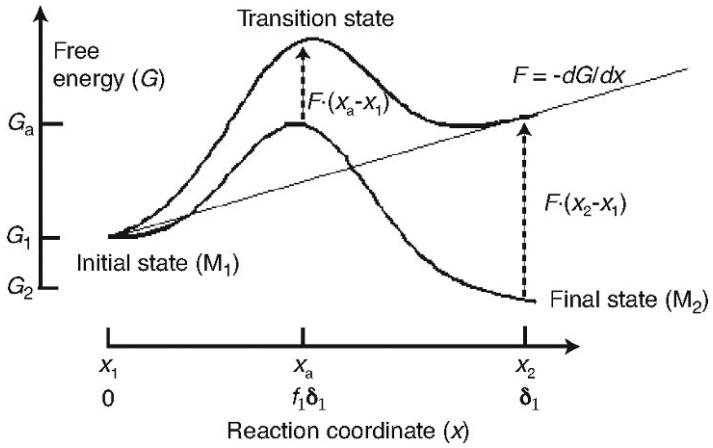

FIGURE 6. **Transition-state model.** To move from the initial state to the final state, an energy barrier has to be crossed. The reaction coordinate is the position of the load carried by the motor, projected onto the axis of the microtubule. The energy barrier is reached as a result of thermal fluctuations. A load force tilts the energy profile upwards, making it more difficult to cross the barrier and, as a consequence, slowing down the speed of the motor.

thermal motion of the motor domain is not required to reach it. However, it is important to realize that even in the powerstroke mechanism, energy is still required to reach the transition state and the energy must come from thermal fluctuations; in the powerstroke mechanism the fluctuations occur along a reaction pathway that is orthogonal to the axis of the microtubule and therefore requires no physical motion of the load in the direction of motion.

The two models behave quite differently in the presence of a load force. A load force tilts the energy diagram as shown in Fig. 6 and changes the height of the activation barrier. If the transition state is close to the final state (Huxley model), then the activation barrier is increased considerably compared to the case where the transition state is near the initial state (powerstroke). Thus a load force will lead to a large decrease in speed for the Huxley model but have little effect on speed for the powerstoke model. This suggests that the models can be distinguished based on the load-dependence of the motor speed.

For a single activation barrier, the forward transition rate is expected to depend exponentially on the load force F according to

$$k_+ = k_0 \exp\left(-\frac{F x_a}{kT}\right)$$

where k_0 is the transition rate in the absence of load, and x_a is the distance to the transition state. For kinesin, the velocity (which is proportional to the transition

rate), decreases e-fold per $\approx 4\ pN$ (Fig. 7). This implies that the distance to the transition state is only ≈ 1 nm ($kT/4\ pN$). Comparing this distance to the 8 nm step size, we conclude that the transition state lies close to the initial state. Thus the powerstroke-type models are more compatible with the experimental data. Another way to view this is that Huxley-type models, in which a load-bearing element has to undergo considerable diffusion along the microtubule axis, will result in a very strong force dependence of the motor's speed on the load force. For example, diffusion through 8 nm to reach the transition state would lead to an 85% reduction in speed at a load of only 1 pN, not consistent with the experimental data. In other words, by reducing the distance to the transition state, powerstroke mechanisms enable motors to generate large forces.

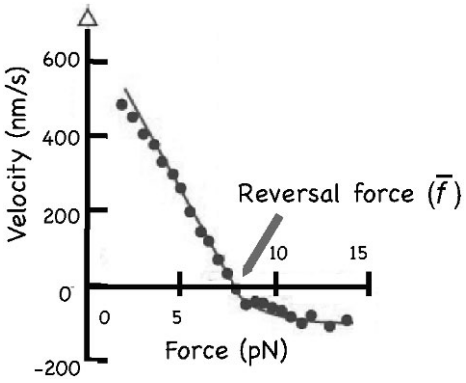

FIGURE 7. **Force-velocity curve for kinesin measured using an optical trap** (after Carter and Cross 2005).

Hand-over-hand models

Does the rejection of the Huxley 1957 model for kinesin rule out a role for diffusion in the motor mechanism? Absolutely not! The reason is that processive motors like kinesin-1 (and also myosin-5) have two motor domains. The two motor domains alternate their binding to the microtubule: they walk hand-over-hand (Hackney, 1994; Hancock and Howard, 1998; Hancock and Howard, 1999; Asbury *et al.*, 2003; Kaseda *et al.*, 2003; Yildiz *et al.*, 2003; Warshaw *et al.*, 2005; Schief *et al.*, 2004). Thus, while one motor domain can support the load, the other is free to diffusively search for and bind to the next binding site (Fig. 8). After binding, the load can be transferred to the forward head. In this way the kinetic slowing of the motor by the load force is reduced and a large stall force can be attained.

There are several lines of evidence that the free head does indeed use a diffusive search for the next binding site. The most convincing data are from myosin-5. (i) The powerstroke is 25 nm, leaving a shortfall of ~ 11 nm (the step

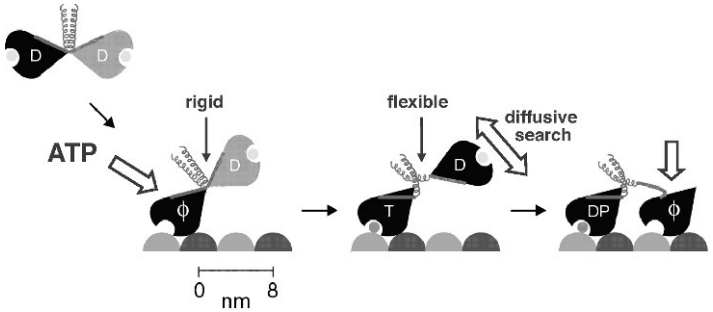

FIGURE 8. **Hand-over-hand model** (after Schief and Howard, 2001).

size in this case is 36 nm) (Veigel *et al.*, 2002). (ii) In an ingenious "chop-sticks" experiment Shiroguchi and Kinosita, (2007), attached microtubules to the motor domains of myosin-5 and observed large-scale diffusive motions. For kinesin-1, the evidence is not as clear. Early experiments showed that increasing the viscosity of the medium slowed down the motion, consistent with reducing the diffusive mobility of the free head (Hunt *et al.*, 1994). On the other hand, according to a popular model, the forward motion of the free head is driven by a directed conformational change involving the docking of the neck-linker domain (Rice *et al.*, 1999), rather than a diffusional motion. However, several lines of evidence suggest that the linking region between the two heads is highly flexible: for example, at high loads, kinesin-1 can move backwards or forwards, suggesting that there is considerable flexibility (Carter and Cross, 2005; Yildiz *et al.*, 2008). Thus, it is quite possible that the free kinesin-1, like that of myosin-V, also uses a diffusional search to find the next binding site.

Open questions

The force-generation problem has proven to be a very challenging one. The simple question "how do motor proteins work?" does not have a simple answer. Several key questions are still open:

(i) Are both motor domains bound to the filament in the "waiting state" (when the motor is yet to bind ATP)? Fig. 8 shows the waiting state (the first bound state) to have one of the heads free, but is that right?

(ii) What is the nature of the communication between the motor domains? It is clear that their activities are highly coordinated – e.g., the binding of one motor domain greatly accelerates the unbinding of the other (Hancock and Howard, 1998; Hancock and Howard, 1999), but how can strain between the heads modulate the binding?

(iii) To what extent do macroscopic concepts such as friction help us to understand the performance of molecular engines (Bormuth *et al.*, 2009)?

(iv) What structural changes occur during translocation, and in particular how are structural changes in the nucleotide-binding pocket, the motor-filament interface, and the region between the motor domains coupled?

References

A. Ajdari and J. Prost, C.R. Acad. Sci. Paris II **315** (1992), 1635.

C.L. Asbury, A.N. Fehr and S.M. Block, *Kinesin moves by an asymmetric hand-over-hand mechanism*, Science **302** (2003), 2130–34.

R.D. Astumian and M. Bier, *Fluctuation driven ratchets: Molecular motors*, Phys. Rev. Lett. **72** (1994), 1766–69.

V. Bormuth, V. Varga, J. Howard, and E. Schäffer, *Protein friction limits diffusive and directed movements of kinesin motors on microtubules*, Science **325** (2009), 870–873.

S.M. Braxton and R.G. Yount, *A ratchet diffusion model for directed motion in muscle*, Biophys. J. **55** (1989), 12a.

N.J. Carter and R.A. Cross, *Mechanics of the kinesin step*, Nature **435** (2005), 308–312.

N.J. Cordova, B. Ermentrout and G.F. Oster, *Dynamics of single-motor molecules: the thermal ratchet model*, Proc. Natl. Acad. Sci. USA **89** (1992), 339–343.

D.L. Coy, M. Wagenbach and J. Howard, *Kinesin takes one 8-nm step for each ATP that it hydrolyzes*, J. Biol. Chem. **274** (1999), 3667–671.

E. Eisenberg and T.L. Hill, *A cross-bridge model of muscle contraction*, Prog. Biophys. Mol. Biol. **33** (1978), 55–82.

E. Eisenberg, T.L. Hill and Y. Chen, *Cross-bridge model of muscle contraction. Quantitative analysis*, Biophys. J. **29** (1980), 195–227.

R.P. Feynman, R.B. Leighton and M.L. Sands, *The Feynman lectures on physics* (Reading, Mass., Addison-Wesley Pub. Co.), (1963).

D.D. Hackney, *Evidence for alternating head catalysis by kinesin during microtubule-stimulated ATP hydrolysis*, Proc. Natl. Acad. Sci. USA **91** (1994), 6865–69.

W.O. Hancock and J. Howard, *Processivity of the motor protein kinesin requires two heads*, J. Cell. Biol. **140** (1998), 1395–1405.

W.O. Hancock and J. Howard, *Kinesin's processivity results from mechanical and chemical coordination between the ATP hydrolysis cycles of the two motor domains*, Proc. Natl. Acad. Sci. USA **96** (1999), 13147–152.

J. Helenius, G. Brouhard, Y. Kalaidzidis, S. Diez and J. Howard, *The depolymerizing kinesin MCAK uses lattice diffusion to rapidly target microtubule ends*, Nature **441** (2006), 115–19.

K. Hirose and L.A. Amos, *High-resolution structural analysis of the kinesin-microtubule complex by electron cryo-microscopy*, Methods Mol. Biol. **392** (2007), 213–230.

J. Howard, *Protein power strokes*, Curr. Biol. **16** (2006), R517–19.

J. Howard, A.J. Hudspeth and R.D. Vale, *Movement of microtubules by single kinesin molecules*, Nature **342** (1989), 154–58.

J. Howard, *Mechanics of Motor Proteins and the Cytoskeleton*, (Sunderland, MA: Sinauer Associates) (2001).

A.J. Hunt, F. Gittes and J. Howard, *The force exerted by a single kinesin molecule against a viscous load*, Biophys. J **67** (1994), 766–781.

A.F. Huxley, *Muscle structure and theories of contraction*, Prog. Biophys. Chem. **7** (1957), 255–318.

A.F. Huxley and R.M. Simmons, *Proposed mechanism of force generation in striated muscle*, Nature **233** (1971), 533–38.

S. Iwatani, A.H. Iwane, H. Higuchi, Y. Ishii and T. Yanagida, *Mechanical and chemical properties of cysteine-modified kinesin molecules*, Biochemistry **38** (1999), 10318–323.

K. Kaseda, H. Higuchi and K. Hirose, *Alternate fast and slow stepping of a heterodimeric kinesin molecule*, Nat. Cell. Biol. **5** (2003), 1079–082.

F. Kozielski, S. Sack, A. Marx, M. Thormahlen, E. Schonbrunn, V. Biou, A. Thompson, E.M. Mandelkow and E. Mandelkow, *The crystal structure of dimeric kinesin and implications for microtubule-dependent motility*, Cell **91** (1997), 985–994.

H.A. Kramers, *Brownian motion in a field of force and the diffusion model of chemical reactions*, Physica **7** (1940), 284–304.

M.O. Magnasco, *Forced thermal ratchets*, Phys. Rev. Lett. **71** (1993), 1477–1481.

E. Nogales, M. Whittaker, R.A. Milligan and K.H. Downing, *High-resolution model of the microtubule*, Cell **96** (1999), 79–88.

E. Nogales, S.G. Wolf and K.H. Downing, *Structure of the alpha beta tubulin dimer by electron crystallography*, [see comments] [published erratum appears in Nature 1998 May 14;393(6681):191]. Nature **391** (1998), 199–203.

Y. Okada and N. Hirokawa, *Mechanism of the single-headed processivity: diffusional anchoring between the K-loop of kinesin and the C terminus of tubulin*, Proc. Natl. Acad. Sci. U S A **97** (2000), 640–45.

A. Parmeggiani, F. Julicher, A. Ajdari and J. Prost, *Energy transduction of isothermal ratchets: generic aspects and specific examples close to and far from equilibrium*, Phys. Rev. E Stat. Phys. Plasmas Fluids Relat. Interdiscip. Topics **60** (1999), 2127–140.

S. Ray, E. Meyhöfer, R.A. Milligan and J. Howard, *Kinesin follows the microtubule's protofilament axis*, J. Cell. Biol. **121** (1993), 1083–093.

S. Rice, A.W. Lin, D. Safer, C.L. Hart, N. Naber, B.O. Carragher, S.M. Cain, E. Pechatnikova, E.M. Wilson-Kubalek, et al., *A structural change in the kinesin motor protein that drives motility*, Nature **402** (1999), 778–784.

J. Rousselet, L. Salome, A. Ajdari and J. Prost, *Directional motion of Brownian particles induced by a periodic asymmetric potential [see comments]*, Nature **370** (1994), 446–48.

W.R. Schief and J. Howard, *Conformational changes during kinesin motility*, Curr. Opin. Cell. Biol. **13** (2001), 19–28.

W.R. Schief, R.H. Clark, A.H. Crevenna and J. Howard, *Inhibition of kinesin motility by ADP and phosphate supports a hand-over-hand mechanism*, Proc. Natl. Acad. Sci. USA (2004).

K. Shiroguchi and K. Kinosita, *Myosin V walks by lever action and Brownian motion*, Science **316** (2007), 1208–212.

C.V. Sindelar and K.H. Downing, *The beginning of kinesin's force-generating cycle visualized at* 9*-A resolution*, J. Cell. Biol. **177** (2007), 377–385.

K. Svoboda, C.F. Schmidt, B.J. Schnapp and S.M. Block, *Direct observation of kinesin stepping by optical trapping interferometry* [see comments], Nature **365** (1993), 721–27.

R.D. Vale and F. Oosawa, *Protein motors and Maxwell's demons: does mechano-chemical transduction involve a thermal ratchet?*, Adv. Biophys. **26** (1990), 97–134.

C. Veigel, F. Wang, M.L. Bartoo, J.R. Sellers and J.E. Molloy, *The gated gait of the processive molecular motor*, myosin V. Nat. Cell. Biol. **4** (2002), 59–65.

D.M. Warshaw, G.G. Kennedy, S.S. Work, E.B. Krementsova, S. Beck and K.M. Trybus, *Differential labeling of myosin V heads with quantum dots allows direct visualization of hand-over-hand processivity*, Biophys. J. **88** (2005), L30–32.

A. Yildiz, J.N. Forkey, S.A. McKinney, T. Ha, Y.E. Goldman and P.R. Selvin, *Myosin V walks hand-over-hand: single fluorophore imaging with* 1.5-nm *localization*, Science **300** (2003), 2061–65.

A. Yildiz, M. Tomishige, A. Gennerich and R.D.Vale, *Intramolecular strain coordinates kinesin stepping behavior along microtubules*, Cell **134** (2008), 1030–041.

Jonathon Howard
Max Planck Institute of
Molecular Cell Biology and Genetics
Pfotenhauerstrasse108
D-01309 Dresden, Germany
e-mail: howard@mpi-cbg.de

Fluctuation Relations for Molecular Motors

David Lacoste and Kirone Mallick

Abstract. This review is focused on the application of specific fluctuation relations, such as the Gallavotti-Cohen relation, to ratchet models of a molecular motor. A special emphasis is placed on two-state models such as the flashing ratchet model. We derive the Gallavotti-Cohen fluctuation relation for these models and we discuss some of its implications.

1. Introduction

The macroscopic observables of a system at mechanical and thermal equilibrium do not vary with time and can be characterized by a finite number of state variables. Thermodynamics imposes *a priori* constraints on the average values of these state variables that are satisfied regardless of the specific nature of the system. Because of this property of time-invariance, equilibrium is often imagined as being associated with stillness and frozen dynamics. This, of course, is not true: a system, even at thermodynamic equilibrium, is constantly evolving from one micro-configuration to another. This endless motion at the microscopic level can be probed macroscopically by measuring the fluctuations of some physical observables, the most famous example being Brownian Motion. Equilibrium fluctuations are perfectly well explained by the classical laws of statistical mechanics.

Brownian motion, its nature, its origins, have been a puzzle to physicists during the XIXth century [1]. One paradoxical issue was the following: can one rectify this random fluctuating motion and use it to perform some work ? If such a rectifying device could be constructed then work would be extracted from a single heat reservoir, contradicting the second law of thermodynamics. The most famous example of a mechanical system that may play the role of such a Maxwell's demon is the ratchet and pawl system, presented by Feynman in Chapter 46 of the first volume of his Physics Lectures [2]. A related paradox was proposed in 1950 by Brillouin [3]: consider an electrical circuit composed of a diode and a resistor at temperature T. The current in the circuit has a zero average value, but because of thermal noise, it exhibits non-vanishing fluctuations (known as Johnson-Nyquist

B. Duplantier and V. Rivasseau (eds.), *Biological Physics*, Progress in Mathematical Physics 60,
DOI 10.1007/978-3-0346-0428-4_4, © Springer Basel AG 2011

noise). Can the diode be used to rectify the current, allowing us to use it to perform work? The solutions of these paradoxes are now well known: thermal fluctuations are a universal phenomenon and all systems at a given temperature are subject to it. The rectifying device, whatever it is, is also subject to Brownian motion and undergoes some unavoidable fluctuations. If the signal to be rectified is produced at temperature T and the rectifier is at the same temperature, then the thermal fluctuations of the rectifier render it totally ineffective and the second law is saved. If the rectifier is at a lower temperature then this apparatus can indeed generate work: but now there are two heat sources at different temperatures, in accordance with the second law.

In recent years, a renewed interest has arisen in ratchet models in the context of non-equilibrium statistical physics. Many ratchet models exist (for a review see [4]). In one kind of ratchet called brownian motors, an association of two particles, one asymmetric and another one symmetric, can rectify thermal fluctuations provided that the two particles are in contact with heat baths at different temperatures [5]. In another family of ratchet models, the need of two heat baths is removed by coupling the ratchet to some external 'agent' (e.g., a chemical reaction) that continuously drives the system out of equilibrium. In this case too, under certain conditions, work can be extracted [6, 7, 8]. Again, there is no contradiction with thermodynamics here: the system is far from equilibrium and the ratchet plays simply the role of a transducer between the energy put in by the agent (e.g., chemical energy) and the mechanical work extracted. The analysis of the energetics of such devices far from equilibrium requires concepts that go beyond the classical laws of thermodynamics and this remains a very challenging and important open issue [9, 10].

Biophysics provides numerous examples of systems far from equilibrium. For example, a significant part of the eukaryotic cellular traffic relies on 'motor' proteins that move along filaments similar in function to railway tracks or freeways (kinesins and dyneins move along tubulin filaments; myosins move along actin filaments) [11]. The filaments are periodic (of period $\sim$ 10nm) and have a fairly rigid structure; they are also polar: a given motor always moves in the same direction. These molecular motors appear in a variety of biological contexts: muscular contraction, cell division, cellular traffic, material transport along the axons of nerve cells... A biological cell forms a crowded environment in which molecular motors work together and with other proteins. In these conditions, collective effects arise due to interactions between motors [12]. In many cases, these interactions can be modeled as excluded volume interactions, and for this reason, the behavior of an ensemble of motors in a low dimension space can be described by dynamical models similar to the ones developed for traffic problems [13, 14]. In the following, we focus on single molecular motor properties, in order to clarify in this simpler situation, the dynamics and the energetics of this system far from equilibrium.

Recently, a general organizing principle for non-equilibrium systems has emerged which is known under the name of fluctuation relations [15, 16, 17, 18, 19, 20, 21]. These relations, hold for non-equilibrium steady states but arbitrarily far

from equilibrium [22, 23, 24, 25], they can be seen as macroscopic consequences of the invariance under time reversal of the dynamics at the microscopic scale [26]. It is interesting to apply these concepts to small systems which can either be mechanically driven as biopolymers [27] or chemically driven as enzymes [28].

Molecular motors are enzymes which operate stochastically at the level of a few molecules, and for this reason they typically undergo large thermal fluctuations. Generically, single molecular motors have been described theoretically either by continuous ratchet models (see, e.g., review by Jülicher et al. [29]) or by models based on master equations on a discrete space [30, 31]. It is possible to give a thermodynamic interpretation of the elementary chemical reactions, which occur in a discrete and stochastic way in a molecular motor [32]. Such a thermodynamic interpretation of chemical transitions has similarities with the thermodynamic interpretation of the Langevin equation at the single trajectory level [33]. At a macroscopic scale, constraints arise on the operation of these molecular motors, as a result of single reaction events occurring stochastically at the microscopic scale. These constraints take the form of a fluctuation relation [34, 32, 35, 36, 37, 38].

The aim of this review is to explain how recent theoretical results in non-equilibrium statistical mechanics, namely these fluctuation relations, provide a way to understand the non-equilibrium energetics of molecular motors. Note that the same framework apply to both biological molecular motors or artificially made nanomachines.

In the first part of this review, we present the two theoretical approaches of molecular motors mentioned above, namely the flashing ratchet model and the approach based on master equations on a discrete space. In the second part of the review, we derive the fluctuation relations for these specific models and discuss some consequences of these relations for molecular motors.

2. Stochastic models of molecular motors

Molecular motors are enzymes capable of converting chemical energy derived from the hydrolysis of adenosine triphosphate (ATP) into mechanical work. There is a large diversity of molecular motors, and correspondingly a large number of processes accomplished by these motors within a cell. There are linear motors such as kinesins, dyneins, myosins or the RNA polymerases, and rotating motors such as the F_1-ATPase motor or the bacterial flagellar motor. These motors drive not only intracellular movements, they are also key players in the motility of the cell itself. Although, traditionally, these machines were subjects of investigation in biology and biochemistry, increasing use of the concepts and techniques of physics in recent years have contributed to a quantitative understanding of the fundamental principles of operation of these motors. The possibility of exploiting these principles for the design of artificial nanomachines has opened up a new field in nanotechnology.

2.1. The basic principle

On the theoretical side, molecular motors have been described by ratchet devices, which are systems able to extract useful work out of unbiased random fluctuations [39]. A generic model of such a ratchet device is shown in Figure 1 where the motor is represented by a small particle that moves in a one-dimensional space. At the initial time $t = 0$, the motor is trapped in one of the wells of a periodic asymmetric potential of period a. Between time 0 and t_f, the asymmetric potential is erased and the particle diffuses freely and isotropically at temperature T. At the switching time t_f, the asymmetric potential is re-impressed, the motor slides down to the nearest potential valley and, because of damping, is trapped in one of the wells. The motor has maximal chance to end up in the same well where it was at time $t = 0$. However, it has a small probability to be trapped in the well located to the right and, because of the asymmetry of the potential, an even smaller probability to end up in the left well. Indeed, in order to be trapped in the right well after time t_f, the particle must have diffused between $t = 0$ and $t = t_f$ over a distance larger than A towards the right. However, to end up in the left well it has to diffuse (towards the left) a distance larger than B, which is much less probable because $B > A$. In other words, because the potential is asymmetric, the motor has more chances to slide down towards the right: this leads on average to a net total current. The particle has used thermal noise to overcome the potential barrier and thanks to the asymmetry of the potential it has moved in a well-defined direction.

In order to move, the motor consumes r ATP fuel molecules per unit time, which are hydrolyzed to ADP + P (see Figure 2):

$$ATP \rightleftharpoons ADP + P\,.$$

It is the chemical energy released by ATP-hydrolysis that allows the motor to detach itself from the filament it was bound to. This detachment process corresponds in the basic mechanism to erasing the potential, whereas re-attachment of the motor at the switching time t_f corresponds to re-impressing the potential. Hence the motor undergoes chemistry-driven changes between strongly and weakly bound states (attachments and detachments). It is the coupling between chemistry and the interaction with the filament that allows the motor to overcome energy barriers. Besides, because of the polarity of the filament, the interaction potential is asymmetric, allowing directed motion to set in.

In general, the motor is subject to an external force $f_{\rm ext}$ which tilts the potential. Besides, when ATP is in excess, the chemical potential difference of the reaction of ATP hydrolysis, $\Delta\widetilde{\mu} = \mu_{\rm ATP} - \mu_{\rm ADP} - \mu_{\rm P}$ becomes *positive*. More precisely, we denote $\Delta\widetilde{\mu} \equiv k_B T \Delta\mu$, where $\Delta\mu$ is the normalized chemical potential and

$$\Delta\tilde{\mu} = k_B T \ln\left(\frac{[ATP]\,[ADP]_{\rm eq}\,[P]_{\rm eq}}{[ATP]_{\rm eq}\,[ADP]\,[P]}\right), \tag{1}$$

where [..] denotes concentration under experimental conditions and $[..]_{\rm eq}$ denotes equilibrium concentrations.

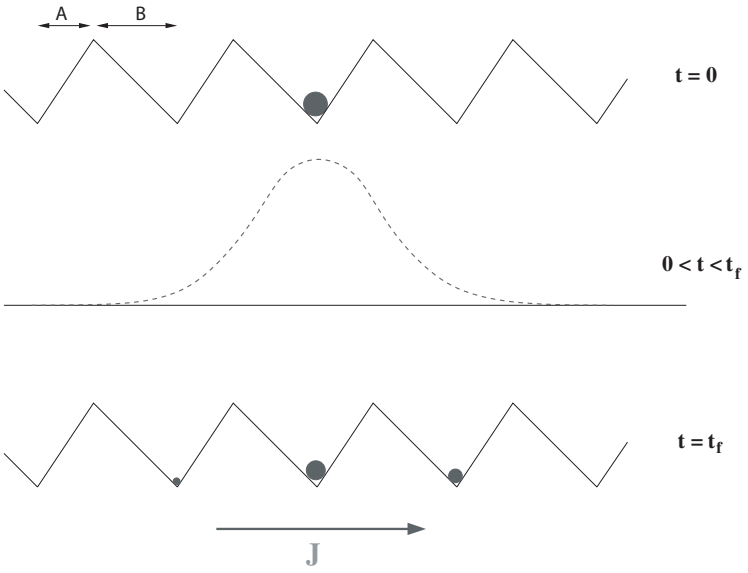

FIGURE 1. The principle of a Brownian ratchet: by inscribing and erasing periodically an asymmetric potential, a directed motion of the particle is induced. In this example, the potential is a saw-tooth function of period $a = A + B$. Since $B > A$, the potential is asymmetric. The relative sizes of the probabilities of ending in one of the wells are represented by the sizes of the disks in the lowest picture. The right and left probabilities being different, this leads on average to a net total current J.

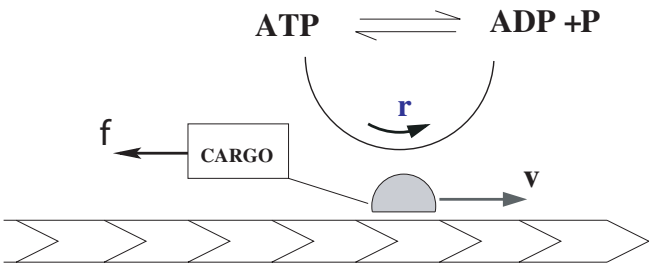

FIGURE 2. Schematic representation of a molecular motor: by hydrolyzing ATP, the motor proceeds along the polar filament and carries a 'cargo' molecule, which typically exerts a force f on the motor.

A basic problem is then to determine the velocity of the motor $v(f_{\text{ext}}, \Delta\mu)$ (mechanical current) and the ATP consumption rate $r(f_{\text{ext}}, \Delta\mu)$ (chemical current) as functions of the external mechanical and chemical loads.

To summarize, molecular motors move by using the ratchet effect, providing an example of a *rectification process* of Brownian motion. The two basic requirements for obtaining directed motion are:

(i) an external energy source, provided by the chemical reaction of ATP hydrolysis. During this process ATP is consumed and ADP is produced. This reaction therefore breaks time-reversal invariance (more technically, it breaks the detailed balance condition which holds at equilibrium, and introduces a bias in the dynamics of the motor).

(ii) The polarity of the filament which breaks spatial left-right symmetry and allows the motor to move in a well-defined direction.

2.2. The flashing ratchet model

In the simplified discussion above, we did not specify the characteristics of the switching time t_f. Different models are possible: one can consider a deterministically forced ratchet in which the binding potential of the motor switches periodically (and even smoothly) from strong-binding to weak-binding. Another possibility that we shall discuss here in detail is the flashing ratchet model [29, 4] in which the switching of potentials is sudden and occurs at random times generated by a Poisson Process. Then, we shall show how to construct a discrete version of the flashing ratchet model [30, 31].

In the flashing ratchet model [29, 40, 41], the state of the motor is described by a continuous position variable x and by discrete internal states $i = 1, 2$ corresponding to different chemical states of the motor. For instance, one could associate one state with a configuration where one motor head is bound to the filament (the high-energy state) and the other state to a configuration where both heads are bound (the low-energy state). The motor evolves in two time-independent periodic potentials $U_i(x)$, with $i = 1, 2$. Note that in the basic mechanism discussed in the previous section, $U_1(x)$ is a saw-tooth potential and $U_2(x)$ is taken to be zero. But one can consider the general case where both U_1 and U_2 are non-zero asymmetric potentials of arbitrary shape with a common period a. In Figure 3, we represent the often studied situation in which U_1 and U_2 are identical saw-tooth potentials but slightly shifted with respect to each other along the x axis.

The dynamics of the motor can be represented by a Langevin equation

$$\dot{x} = -\gamma F - \gamma \sum_{i=1,2} U_i(x)\delta_{\zeta(t),i} + \sqrt{D_0}\,\xi(t) \tag{2}$$

where $\xi(t)$ is a normalized white-noise and $\zeta(t)$ a dichotomous noise that can exist in two states 1 and 2. The switching-rates of $\zeta(t)$ are position dependent and are given by $\omega_1(x)$ (transition from 1 to 2) and $\omega_2(x)$ (transition from 2 to 1). The friction coefficient γ satisfies the Einstein relation $D_0 = k_B T/\gamma$ and F represents an external force acting on the motor. The function $\delta_{\zeta(t),i}$ is a Kronecker delta.

The probability density for the motor to be at position x at time t and in state i is denoted by $P_i(x,t)$, which obeys the equations

$$\frac{\partial P_1}{\partial t} + \frac{\partial J_1}{\partial x} = -\omega_1(x)P_1 + \omega_2(x)P_2, \tag{3}$$

$$\frac{\partial P_2}{\partial t} + \frac{\partial J_2}{\partial x} = \quad \omega_1(x)P_1 - \omega_2(x)P_2\,, \tag{4}$$

where $\omega_1(x)$ and $\omega_2(x)$ are space dependent transition rates, and the local currents J_i are defined by:

$$J_i = -D_0\left(\frac{\partial P_i}{\partial x} + \frac{1}{k_BT}\left(\frac{\partial U_i}{\partial x} - F\right)P_i\right), \tag{5}$$

with D_0 the diffusion coefficient of the motor and F a non-conservative force acting on the motor.

The transition rates can be modeled using standard kinetics for chemical reactions applied to each chemical pathway between the two states of the motor [40]:

$$\begin{aligned}\omega_1(x) &= [\omega(x) + \psi(x)e^{\Delta\mu}]e^{(U_1(x)-fx)/k_BT},\\ \omega_2(x) &= [\omega(x) + \psi(x)]e^{(U_2(x)-fx)/k_BT},\end{aligned} \tag{6}$$

where $f = Fa/k_BT$ is the normalized force acting on the motor. It is assumed that the rates can be decomposed into a contribution proportional to $\omega(x)$, which is associated with thermal transitions, and a contribution proportional to $\psi(x)$ corresponding to transitions induced by ATP hydrolysis. Note that the functions $\omega(x)$ and $\psi(x)$ have to be periodic functions but they are otherwise unspecified. The form of the rates in the absence of hydrolysis (*i.e.* when $\psi(x) = 0$) is chosen to satisfy the detailed balance condition

$$\frac{\omega_2(x)}{\omega_1(x)} = \exp\left(\frac{U_2(x) - U_1(x)}{k_BT}\right). \tag{7}$$

The form of the rates associated with the transitions induced by ATP hydrolysis (*i.e.* when $\omega(x) = 0$) is chosen to satisfy a generalized detailed balance condition, which is generalized in the sense that it accounts for the exchange of chemical energy [35, 28]. In this case, this leads to the condition

$$\frac{\omega_2(x)}{\omega_1(x)} = \exp\left(\frac{U_2(x) - U_1(x)}{k_BT} - \Delta\mu\right). \tag{8}$$

Note that the way the force enters the rates is unambiguous in continuous models as compared to discrete models, in which the force dependent rates must contain unknown load distribution factors [37, 30]. One could easily extend the model to introduce more chemical pathways [40] or more internal states; such extensions are possible but they have not been considered here since they are not essential for the present argument.

When $F = 0$ and $\Delta\mu = 0$, the system is in equilibrium since the detailed balance condition (7) holds. In this case, the steady state probabilities P_i obey

Boltzmann distribution, the currents J_i vanish and there is no average displacement of the motor. When F and $\Delta\mu$ are not simultaneously zero, the detailed balance condition (7) is broken, the system is out of equilibrium and currents are present.

2.3. A discrete ratchet model

From the continuous model, a simplified effective discrete model can be constructed as shown schematically in Figure 3 following the procedure outlined in [42]. We as-

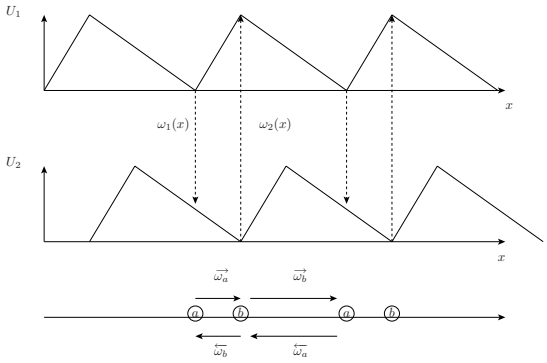

FIGURE 3. The top two curves represent the two time independent periodic potentials $U_1(x)$ and $U_2(x)$ of the flashing ratchet model. At any position x, vertical transitions are possible between the two internal states with rates $\omega_1(x)$ and $\omega_2(x)$. Below is represented the corresponding discrete model, which is obtained by considering effective transitions between the minimum of $U_1(x)$ (state a) to the minimum of the other potential (state b), with rates as shown in the lower part of the figure.

sume that the motor has a vanishingly small residence time in all states which are not minima of the potentials $U_1(x)$ or $U_2(x)$, i.e. the time taken to slide down towards a well is negligible. Switching between the potentials, represented as dashed lines in the figure, occurs at finite rates $\omega_1(x)$ and $\omega_2(x)$, but only between states that are at the same location x. Since downward sliding occurs instantly, the observable transitions are effectively from one minimum of one potential (state a) to the other minimum of the other potential (state b). In this way, a discrete hopping model on a 1D lattice is constructed in which transitions are allowed between even and odd sites called a and b. The dynamics of the motor on the linear discrete lattice is as follows: the motor hops from one site to neighboring sites, either consuming or producing ATP (see Figure 4). The position of the motor is denoted by $x = nd$, where $2d \approx 8\,\text{nm}$ is the step size of a kinesin. The even sites (denoted by a) are the low-energy state of the motor, whereas the odd sites (denoted by b) are its high-energy state; their energy difference is $\Delta E \equiv k_B T\epsilon$, where k_B is the Boltzmann constant and T is the temperature. Because of the periodicity of the

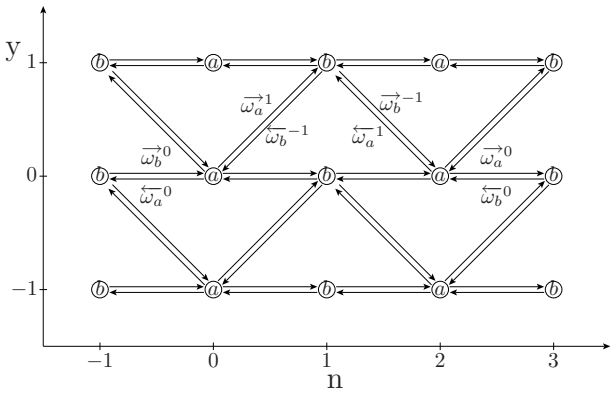

FIGURE 4. A schematic of the evolution of the motor in a plane (n, y), where n represents the position of the motor on the filament and y is the number of ATP molecules consumed. The even and odd sublattices are denoted by a and b, respectively. Note that the lattices of a and b sites extend infinitely in both directions along the n and y axis. The possible transitions are represented with arrows on a particular section of the lattice.

filament, all the even (a) sites and all the odd (b) sites are equivalent. The dynamics of the motor is governed by a master equation for the probability, $P_n(y,t)$, that the motor has consumed y units of ATP and is at site n at time t:

$$\begin{aligned}\partial_t P_n(y,t) = & -(\overleftarrow{\omega}_n + \overrightarrow{\omega}_n)\, P_n(y,t) \\ & + \sum_{l=-1,0,1} \left[\, \overleftarrow{\omega}_{n+1}^{\,l}\, P_{n+1}(y-l,t) + \overrightarrow{\omega}_{n-1}^{\,l}\, P_{n-1}(y-l,t) \,\right], \end{aligned} \tag{9}$$

where $\overleftarrow{\omega}_n \equiv \sum_l \overleftarrow{\omega}_n^{\,l}$ and $\overrightarrow{\omega}_n \equiv \sum_l \overrightarrow{\omega}_n^{\,l}$. Denoted by $\overleftarrow{\omega}_n^{\,l}$ and $\overrightarrow{\omega}_n^{\,l}$ are the transition rates for the motor to jump from site n to $n-1$ or to $n+1$, respectively, with $l\,(=-1,0,1)$ ATP molecules consumed.

As we show below, this discrete stochastic model contains the essential features of the original ratchet model while being more amenable to precise mathematical analysis [43, 44, 45, 31]. In this sense, the discrete model may be regarded as a *minimal* ratchet model.

2.4. Application of the model to experiments

2.4.1. Modes of operation and efficiency: From the master equation Eq. 9, one can obtain the average velocity of the motor $\bar{v}$ and its average ATP consumption rate, $\bar{r}$. One finds explicitly that

$$\bar{v} = 2\frac{\overrightarrow{\omega}_a\,\overrightarrow{\omega}_b - \overleftarrow{\omega}_a\,\overleftarrow{\omega}_b}{\overrightarrow{\omega}_a + \overrightarrow{\omega}_b + \overleftarrow{\omega}_a + \overleftarrow{\omega}_b}\,, \tag{10}$$

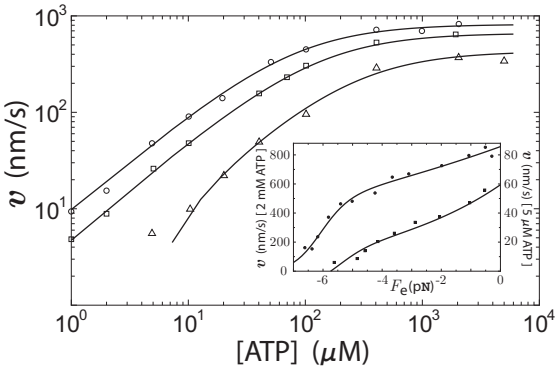

FIGURE 5. Kinesin velocity vs. ATP concentration under an external force [36]. The solid curves are the fits of our model to data from Ref. [46]. From top to down, the plots are for $F_e = -1.05, -3.59$, and -5.63 pN, respectively. Inset: Kinesin velocity vs. force under a fixed ATP concentration. The solid curves are fits to the data of Ref. [46]. From top to down, the plots are for [ATP] = 2 mM and 5 μM.

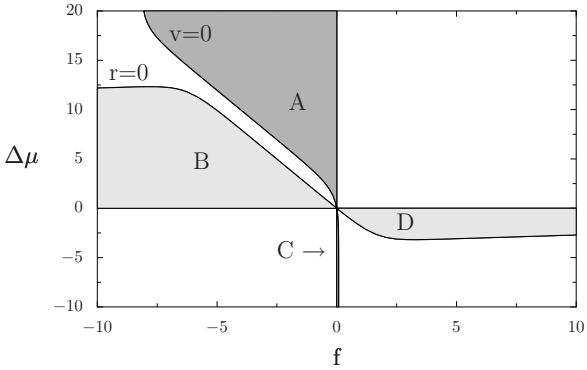

FIGURE 6. The four modes of operation of a molecular motor (such as kinesin) are delimited by $\bar{v} = 0$ and $r = 0$. The lines are generated with parameters that we have extracted by fitting the data for kinesin in Ref. [46] to our model, and this fit is shown in Figure 5.

$$r = \frac{\left(\overleftarrow{\omega}_a^1 + \overrightarrow{\omega}_a^1\right)\left(\overrightarrow{\omega}_b + \overleftarrow{\omega}_b\right) - \left(\overleftarrow{\omega}_b^{-1} + \overrightarrow{\omega}_b^{-1}\right)\left(\overrightarrow{\omega}_a + \overleftarrow{\omega}_a\right)}{\overrightarrow{\omega}_a + \overrightarrow{\omega}_b + \overleftarrow{\omega}_a + \overleftarrow{\omega}_b}\,. \tag{11}$$

By modelling the dependence of the rates on the force and on the chemical potential in a way similar to what was done in Eq. (6) for the flashing ratchet model, one obtains a theoretical prediction for the dependence of the velocity and

average ATP consumption rate on the force or the ATP concentration, that can be compared to experiments. Despite its simplicity, this discrete model can account quantitatively for such measurements as shown in Figure 5 in the case of a kinesin.

From the two currents $\bar{v}$ and r, a diagram of operation of the motor (see Figure 6) can be constructed, which summarizes the possible thermodynamic modes of operation of the motor [36]. This diagram is similar to that given in Ref. [29], except that the present diagram extends to the regime far from equilibrium rather than being limited to the linear response regime. Whenever $f\bar{v} < 0$, work is performed by the motor, whenever $r\Delta\mu < 0$, chemical energy is generated. The motor can work in eight different regimes. Four of them are passive and correspond to the white regions in Figure 6, in which there is no energy output from the system, since $f\bar{v} > 0$ and $r\Delta\mu > 0$. [1] The four remaining regimes are more interesting since $f\bar{v}$ and $r\Delta\mu$ are not of the same sign, which means that some form of transduction occurs between the mechanical and chemical forms of energy. More precisely:

- In region A of the diagram, where $r\Delta\mu > 0$ and $f\bar{v} < 0$, the motor uses the chemical energy of ATP to perform mechanical work. This can be understood by considering a point on the y-axis of Figure 6 with $\Delta\mu > 0$. There we expect that the motor drifts to the right with $\bar{v} > 0$. Now in the presence of a small load $f < 0$ on the motor, we expect that the motor is still going in the same direction although the drift is uphill and thus work is performed by the motor at a rate $\dot{W} = -f\bar{v} > 0$. This holds as long as f is smaller than the stalling force, which defines the other boundary of region A.
- Similarly, in region B, where $r\Delta\mu < 0$ and $f\bar{v} > 0$, the motor produces ATP already in excess from mechanical work.
- In region C, where $r\Delta\mu > 0$ and $f\bar{v} < 0$, the motor uses ADP in excess to perform mechanical work.
- In region D, where $r\Delta\mu < 0$ and $f\bar{v} > 0$, the motor produces ADP already in excess from mechanical work.

It is interesting to note that the large asymmetry between regions A and C in Figure 6 reflects the fact that kinesin is a unidirectional motor. The diagram also illustrates the fact that under usual conditions with $\Delta\mu \simeq 10 - 25$, a kinesin uses the chemical energy of ATP hydrolysis to produce mechanical work (region A of the figure), rather than operating in the other way to synthesize ATP (region B of the figure).

It is also possible to analyze the mechanical efficiency of this motor, defined as the ratio between the mechanical work delivered by the motor divided by the chemical energy supplied [37]. Other definitions of efficiency have been considered in the literature (such as the efficiency at maximum power [47] or the Stokes efficiency) but the advantage of this definition is that it holds arbitrarily far from

[1] The case where $f\bar{v} < 0$ and $r\Delta\mu < 0$ is forbidden by the second law of thermodynamics, because it would lead to a negative entropy production. For this reason, there is no point in Figure 6 which corresponds to this case.

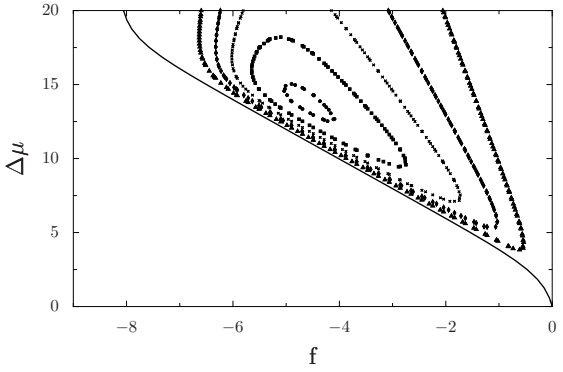

FIGURE 7. Curves of equal efficiency η within region A (which is delimited by the solid line and by the y axis). The parameters are those used in Figure 6 and obtained from the fit of Figure 5. From the outside to the inside the curves correspond to $\eta = 0.2$, $\eta = 0.3$, $\eta = 0.4$, $\eta = 0.5$ and $\eta = 0.58$. The absolute maximum efficiency for these parameters is about 59% and is located at $\Delta\mu \simeq 14$ and $f \simeq -4.9$.

equilibrium and it corresponds near to equilibrium to the definition used traditionally with heat engines. The kinesin operates most efficiently in a range of values of $\Delta\tilde{\mu}$ which corresponds well to the typical free energy delivered by the reaction of ATP hydrolysis (physiological conditions correspond to $\Delta\mu \simeq 10 - 25$). The maximum of efficiency is obtained around a single isolated point in the coordinates $(f, \Delta\mu)$ (rather than on a line as in the near equilibrium regime for instance) as shown in Figure 7. This suggests that kinesin is in fact optimized to operate under a load corresponding to a normalized force of about -4.9 in the conditions of Figure 7. The maximum of efficiency is around 40–60%, much higher than the typical efficiency in the near equilibrium regime (of the order of 0.03%). The value of the maximum efficiency of 40–60% agrees well with recent measurements for kinesin.

2.4.2. Violation of Onsager and Einstein relations: Away from equilibrium, we expect that Onsager and Einstein relations are no longer valid. To quantify their violations, we have introduced in Ref. [36] $\Delta\lambda \equiv \lambda_{12} - \lambda_{21}$ to quantify the violation of Onsager relations and four "temperature"-like quantities, $T_{ij} \equiv D_{ij}/\lambda_{ij}$ to quantify the violation of Einstein relations. All these quantities are defined using linear response theory in the vicinity of a non-equilibrium steady state rather than near an equilibrium state. Of course, these effective temperatures are not thermodynamic temperatures: they are merely one of many possible ways to quantify deviations of Einstein relations. These T_{ij} and $\Delta\lambda$ are shown in Figure 8 as functions of $\Delta\mu$ for the particular case of $f \ll 1$ within region A. We observe that all the T_{ij} start off at $T_{ij} = 1$ near equilibrium where $\Delta\lambda = 0$ as expected from

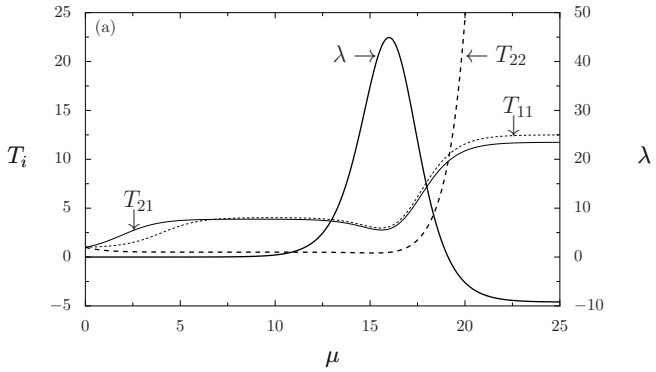

FIGURE 8. Effective temperatures T_{11} (dot-dashed), T_{21} (dotted), T_{22} (dashed), and $\Delta\lambda$ (solid) vs. $\Delta\mu$ in region A of Figure 6 for a small f. Note that T_{ij} characterizes the fluctuation-response ratios (see text), while $\Delta\lambda$ quantifies the breaking of Onsager symmetry.

Onsager relations, whereas for large $\Delta\mu$, T_{22} diverges exponentially while T_{21}, T_{11} and $\Delta\lambda$ approach constant values [36].

2.4.3. Beyond two states model of molecular motors. The discrete two-state model presented above describes many features of experiments on a single kinesin such as the average velocity versus force or versus ATP concentration, or the average ATP consumption rate. It does not describe however equally well the fluctuations of these quantities. As shown in [30], at least four internal states are necessary to describe the fluctuations of position of the motor, which are quantified by the so-called randomness parameter introduced and measured in Ref. [48]. For this reason, a more refined model of kinesin should contain more than two internal states to account for the way the motor walks on the filament, which is by a succession of binding and unbinding events of the two heads in a hand-over-hand fashion. To include that aspect, a model with nine states – which can be reduced to seven states for most cases – was proposed in Refs. [35, 49, 50], where the seven states describe the most significant chemical states of the two headed kinesin. The possible transitions between these states can be represented by a network, which describes the mechano-chemical coupling in this motor. In this network representation, several cycles can be identified just like in the discrete model presented above. The model successfully accounts for many experimental results known for kinesins [51]. Using this framework, a diagram summarizing the thermodynamic modes of operation of the motor has been constructed in Ref. [52]. This diagram has similarities with our Figure 6, but some differences are present due to the different role played by the mechanical and chemical cycles in the different models.

Many other works have used discrete or continuous stochastic models to analyze molecular motors: for instance a discrete model with seven states has been

developed for myosin V [53]. A discrete model with only three states has been used to describe the fluctuations of position of nucleosomes along DNA in Ref. [55]. In Ref. [54], the rotating motor F_1-ATPase is described by a stochastic process for the angle of rotation of the motor, which is treated as a continuous variable and for the chemical states, which are treated as discrete states. More recently, the authors of this reference have developed a discrete version corresponding to their continuous model, which is a two-state model very similar to the one discussed in this review [56].

3. Fluctuation relations in models of molecular motors

Fluctuation relations quantify the exchanges of energy between a system and its environment when the system is in a non-equilibrium state [17, 21]. These relations hold arbitrarily far from equilibrium in a regime where the usual thermodynamic laws – which hold only near equilibrium – do not apply. Since their discovery about a decade ago [15, 16, 17, 18, 19], there has been a growing interest in understanding their importance and implications. One reason for the popularity of this topic has to do with the fact that these relations provide a fresh look at old fundamental questions, such as the origin of irreversibility or the second law of thermodynamics.

For small systems (for which the fluctuations are large, in the sense that their magnitude can be of the same order as the average value), the fluctuation relations impose new constraints which go beyond the usual description of statistical fluctuations. Many fluctuation relations have been verified experimentally using biopolymers, in particular the Jarzynski's relation [57], the Crooks relation [58] and the Hatano-Sasa relation [59]. Complementary experimental verifications have been carried out with colloidal particles in optical traps [60, 61]. Recently, a modified Fluctuation-Dissipation relation, related to the Hatano-Sasa relation has been verified for a colloidal particle in a nonequilibrium steady state [62]. All these experiments represent remarkable achievements, which confirm the validity of the general framework of fluctuation relations in various experimental conditions. However, it may be worth pointing out that in all these examples, the experiments have been designed in order to verify the fluctuation relations. On the contrary, the case of molecular motors is particularly interesting since this is a system which was not designed for that objective. Molecular motors operate in a regime far from equilibrium, with fluctuation relations in some sense built-in in their natural mode of operation. For this reason, it is more appropriate to think about fluctuation relations as thermodynamic constraints on the operation of the motors, which presumably theoretical models of molecular motors should obey [34, 32]. That of course would assume that the fluctuation relations are obeyed exactly in experiments. To our knowledge, quantitative experimental tests of fluctuation relations have not been carried out on molecular motors yet, although there is some indication that, for instance, the data of [51] on single molecule experiments with kinesin is in agreement with the fluctuation relations.

The dynamics of a molecular motor breaks the detailed balance condition, and leads to a non-equilibrium steady state characterized by the presence of non-zero currents, which are independent of time. For each current, one can associate a cycle, also called an irreversible loop. The construction of these cycles and the way they can be associated with currents is explained by a general theory for systems governed by a master equation [63, 65, 64]. One central result of this theory is the relation

$$\frac{\Pi^+(\mathcal{L})}{\Pi^-(\mathcal{L})} = \frac{J^+}{J^-} = e^{A/k_BT}, \tag{12}$$

where $\Pi^+(\mathcal{L})$ denotes the product of reaction rates associated with the different transitions within the cycle $\mathcal{L}$ in the clockwise direction, whereas $\Pi^-(\mathcal{L})$ denotes the same product in the counter-clockwise direction. We have denoted by J^+ the number of cycles undergone by the motor per unit time in the clockwise direction, and J^- the number of cycles undergone per unit time in the counter-clockwise direction, so that overall the cycle flux is $J = J^+ - J^-$. The quantity A is called affinity or thermodynamic force. This affinity can be defined as the derivative of an effective potential, experienced by a biased random walker that would exhibit the same dynamics [37]. When the detailed balance condition is satisfied, $\Pi^+(\mathcal{L}) = \Pi^-(\mathcal{L})$, the effective potential is flat and $A = J = 0$.

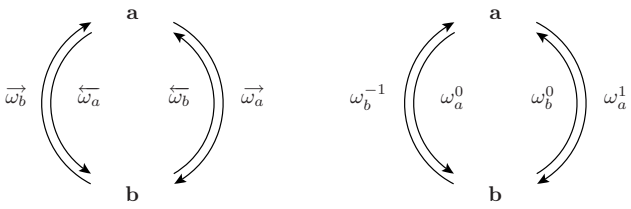

FIGURE 9. Cycles associated with the evolution of the motor in the discrete two-state model. Left: the cycle for the position variable n; the length n run by the motor corresponds to half the number of turns run around the cycle (the factor $1/2$ has to do with the period of the motor which is twice the unit length of the lattice on which the motor evolves). Right: the cycle for the chemical variable y.

In the simple case where the model contains a single cycle with only two states as in Figure 9, the relation (12) leads to the affinity $A/k_BT = -2\Psi$ where Ψ is defined by

$$\Psi = \frac{1}{2} \ln \left(\frac{\overleftarrow{\omega}_a \overleftarrow{\omega}_b}{\overrightarrow{\omega}_a \overrightarrow{\omega}_b} \right), \tag{13}$$

and the corresponding current J is the average motor velocity (see Eq. 10):

$$\bar{v} = 2 \frac{\overrightarrow{\omega}_a \overrightarrow{\omega}_b - \overleftarrow{\omega}_a \overleftarrow{\omega}_b}{\overrightarrow{\omega}_a + \overrightarrow{\omega}_b + \overleftarrow{\omega}_a + \overleftarrow{\omega}_b}. \tag{14}$$

In order to describe more precisely the dynamics of this system, let us consider $P_i(n,t)$, the probability that the motor at time t is on the site i $(= a, b)$ and at the position n (with $x = nd$ where d is distance between sites a and b). This probability can be obtained for instance by integrating over the variable y in the quantity $P_n(y,t)$, which satisfies the more general master equation of Eq. (9). Because of the periodicity of this problem, it is convenient to introduce generating functions $F_i(\lambda,t) \equiv \sum_n e^{-\lambda n} P_i(n,t)$, which evolve according to : $\partial_t F_i = \mathcal{M}_{ij}\, F_j$, where $\mathcal{M}[\lambda]$ is the following 2×2 matrix constructed from the master equation satisfied by $P_i(n,t)$:

$$\mathcal{M}[\lambda] = \begin{bmatrix} -\overrightarrow{\omega_a} - \overleftarrow{\omega_a} & e^{\lambda}\overleftarrow{\omega_b} + e^{-\lambda}\overrightarrow{\omega_b} \\ e^{\lambda}\overleftarrow{\omega_a} + e^{-\lambda}\overrightarrow{\omega_a} & -\overleftarrow{\omega_b} - \overrightarrow{\omega_b} \end{bmatrix}.$$

In the long time limit, the steady state properties of the motor can be obtained from the largest eigenvalue $\vartheta[\lambda]$ of this matrix. Indeed when $t \to \infty$,

$$\left\langle\, e^{-\lambda n} \,\right\rangle = \sum_i F_i(\lambda,t) \sim \exp\left(\vartheta\, t\right). \tag{15}$$

The first derivative of ϑ with respect to λ gives the average velocity $\bar{v}$ of the motor and the second derivative gives the diffusion coefficient of the motor.

From the explicit expression of this eigenvalue, the following property may be derived:

$$\vartheta(\lambda) = \vartheta(-\Psi - \lambda), \tag{16}$$

which is the Gallavotti-Cohen fluctuation theorem. Other equivalent forms of this relation can be obtained. One of them involves the large deviation function of the current v denoted $G(v)$, defined in the long time limit as

$$P(\frac{n}{t} = v) \sim e^{-G(v)t}\,. \tag{17}$$

The analytical expression of this function, obtained in Ref. [37], has a complicated non-linear expression in terms of the rates, but it satisfies a surprisingly simple relation:

$$G(v) - G(-v) = \Psi v. \tag{18}$$

This relation implies that the ratio of the probabilities to observe a velocity v or $-v$ after a time t satisfies the relation

$$\frac{\mathcal{P}(\frac{n}{t} = v)}{\mathcal{P}(\frac{n}{t} = -v)} = e^{-\Psi v t}. \tag{19}$$

Using Eq. (18), and the fact that $G(v)$ and $\vartheta(\lambda)$ are Legendre transforms of each other, one recovers indeed the relation (16).

The relations (16), (18) and (19) are equivalent forms of a constraint imposed on the system by the Gallavotti-Cohen fluctuation theorem. This theorem itself is a consequence of the time-reversal symmetry of the physical laws involved in this model. This symmetry is a fundamental property that does not depend on the details of the system and therefore, in this sense, the fluctuation theorem appears as a universal requirement, just as thermodynamic constraints are universal for

systems at equilibrium regardless of their microscopic structure. Of course, universality does not imply that the constraints are easy to find and to formulate explicitly for a given problem. Here, the relation (19) is an explicit prediction derived from the fluctuation theorem for molecular motors. It would be of great interest to verify this relation experimentally. Conversely, this equation can be used to measure the affinity Ψ, and therefore to access indirectly the microscopic rates, for a given molecular motor.

3.1. Modeling processivity at the single motor level

Experiments on single molecular motors depend on an important property of these motors called processivity. Molecular motors like kinesins, which can hydrolyze a large number of ATP molecules before detaching from microtubules, are called processive, whereas those like myosins II, which detach and reattach frequently from actin filaments are called non-processive. There are several ways to define processivity, either it can be defined as the average lifetime of the motor on the filament, or from the average length spanned by the motor or from the average number of ATP molecules consumed before detaching. In single molecule experiments [66, 51], the dependence of the run-length of a single kinesin on load and on the ATP concentration has been studied. On the theoretical side, the average lifetime of a molecular motor as a function of load has been studied in [67] using the flashing ratchet model. Here we focus on the run-length, for which we derive a simple expression within the discrete two-state model presented above. Using a similar theoretical approach, the average time before observing a backward step in a discrete model of a molecular motor has been studied in Ref. [34]. More generally, in a network of discrete chemical states, there are well-known methods to calculate the average lifetime of a random walker in the presence of absorbing states [65]. These methods can be used not only to calculate the lifetime of the motor on the filament, but also the dwell times associated with the motor steps as shown in Ref. [49].

The detachment of the motor from the filament can be represented by a detachment rate κ, which depends on the local site of the filament visited by the motor. Since in the discrete model presented above, the state b is the high-energy state and a a low-energy state, we assume for simplicity that detachment only occurs from site b, which corresponds to the maxima of $U_1(x)$ in Figure 3. Because of this detachment, the motor can be no longer only in states a or b, thus we need to modify the master equation in order to conserve probability at all times. This can be done by adding an extra state corresponding to the unbound motor state, which is an absorbing state. We define the generating functions $F_i(\lambda, t)$ as before, but now the matrix of evolution of these generating function is the following 3×3 matrix:

$$\mathcal{M}[\lambda] = \begin{bmatrix} -\overrightarrow{\omega_a} - \overleftarrow{\omega_a} & e^{\lambda}\overleftarrow{\omega_b} + e^{-\lambda}\overrightarrow{\omega_b} & 0 \\ e^{\lambda}\overleftarrow{\omega_a} + e^{-\lambda}\overrightarrow{\omega_a} & -\overleftarrow{\omega_b} - \overrightarrow{\omega_b} - \kappa & 0 \\ 0 & \kappa & 0 \end{bmatrix}.$$

This matrix has three eigenvalues μ_1, μ_2 and 0, which is associated with the absorbing state. The corresponding eigenvectors are $|\mu_1\rangle$, $|\mu_2\rangle$ and $|c\rangle$. If the initial state vector is $|F(\lambda,0)\rangle = A|\mu_1\rangle + B|\mu_2\rangle + C|c\rangle$, the state vector at time t is $|F(\lambda,t)\rangle = Ae^{\mu_1 t}|\mu_1\rangle + Be^{\mu_2 t}|\mu_2\rangle + C|c\rangle$. Since μ_1 and μ_2 are strictly negative, at time $t \to \infty$, $\langle e^{-\lambda n}\rangle = \langle 0|F(\lambda,\infty)\rangle = C(\lambda)$, with $\langle 0| = (1,1,1)$. Note that $C(\lambda)$ contains all the moments of the run length, and in particular the average run length, which is, in units of the lattice period,

$$\langle n\rangle = -\frac{\partial C(\lambda)}{\partial \lambda}|_{\lambda=0}. \tag{20}$$

The function $C(\lambda)$ can be calculated by projecting the left eigenvector associated with the eigenvalue 0, $\langle c|$, onto the initial state vector $|F(\lambda,0)\rangle$. If the initial state vector is along the unit vector $\mathbf{e}_x$, then one obtains

$$C(\lambda) = \frac{\overrightarrow{\omega}_a e^{\lambda} + \overleftarrow{\omega}_a e^{-\lambda}}{r\omega_a + \overrightarrow{\omega}_a \overrightarrow{\omega}_b (1-e^{2\lambda}) + \overleftarrow{\omega}_a \overleftarrow{\omega}_b (1-e^{-2\lambda})}. \tag{21}$$

If the initial state vector is along the unit vector $\mathbf{e}_x$, then

$$\langle n\rangle = \frac{\overrightarrow{\omega}_a - \overleftarrow{\omega}_a}{\omega_a + \omega_b} + 2\frac{\overrightarrow{\omega}_a \overrightarrow{\omega}_b - \overleftarrow{\omega}_a \overleftarrow{\omega}_b}{\kappa\omega_a}. \tag{22}$$

If the initial state vector is along the unit vector $\mathbf{e}_y$, then

$$\langle n\rangle = 2\frac{\overrightarrow{\omega}_a \overrightarrow{\omega}_b - \overleftarrow{\omega}_a \overleftarrow{\omega}_b}{\kappa\omega_a}. \tag{23}$$

Thus the part of the average length which is independent of the initial condition is

$$\langle \bar{n}\rangle = 2\frac{\overrightarrow{\omega}_a \overrightarrow{\omega}_b - \overleftarrow{\omega}_a \overleftarrow{\omega}_b}{\kappa\omega_a} = \frac{\bar{v}}{\kappa P_b}, \tag{24}$$

where $\bar{v}$ is the average motor velocity defined before and P_b the stationary probability to be in state b when $\kappa = 0$.

Note that it has been assumed implicitly that the motor runs in the positive direction so that by construction $\bar{v} > 0$, $\langle \bar{n}\rangle$ is positive and has the familiar form obtained above. The application of fluctuation relations to non-processive motors has not been discussed in the literature to our knowledge. We believe that a fluctuation relation will be obeyed only if a reattachment process is taken into account in the model. In this case, there is no longer an absorbing state.

3.2. Mechanochemical coupling for the discrete model

We have so far only discussed the form of fluctuation relations for models containing a single cycle. It is well known that models with at least two cycles must be introduced to account for experimental data such as those represented in Figure 5. In order to discuss more general fluctuation relations, and to compute in a simple way the chemical current, r, associated with the average ATP consumption rate, it is necessary to include in the description of the state of the motor, a chemical variable y associated with the average number of ATP consumed as done in

Eq. (9). With the notations, $\omega_a^l = \overrightarrow{\omega}_a^l + \overleftarrow{\omega}_a^l$ and $\omega_a = \overrightarrow{\omega}_a + \overleftarrow{\omega}_a$ (and similarly for site b), one obtains the chemical current

$$r = \frac{\omega_a^1 \omega_b - \omega_b^{-1} \omega_a}{\omega_a + \omega_b}, \tag{25}$$

in agreement with the cycle representation of Figure 9 and with the formula (11) above.

When the form of these rates is explicitly given in terms of the normalized force f and the normalized chemical potential $\Delta\mu$, a new reformulation of Eq. (12) is obtained:

$$k_B T \ln \frac{\overrightarrow{\omega}_b^{-l} \overrightarrow{\omega}_a^{l'}}{\overleftarrow{\omega}_a^{l} \overleftarrow{\omega}_b^{-l'}} = F_e(2d) - \Delta\tilde{\mu}\,(l - l')\,, \tag{26}$$

with $l, l' = 0, 1$. This equation can be understood as a statement of the first law of thermodynamics at the level of elementary transitions [35, 28]. Indeed, it is possible to associate the left-hand side of this equation with the heat released by the motor into the environment (treated as a reservoir at the same temperature) during transitions (l, l'). The right-hand side can then be interpreted as the difference between the mechanical work $-F_e(2d)$ and the variation of chemical energy $\Delta\tilde{\mu}\,(l - l')$ for these transitions. The variation of internal energy is zero in this case since only transitions involved in a cycle are considered. Note that similarly to this, the generalized detailed balance condition of Eq. (8) can be also interpreted as a statement of the first law at the level of elementary transitions.

Following the same steps that lead to the fluctuation relations for models with one cycle but now for a model with two cycles, one arrives at the following relation, similar to Eq. (16):

$$\vartheta(\lambda, \gamma) = \vartheta(-\tilde{\Psi} - \lambda, -\tilde{\chi} - \gamma), \tag{27}$$

with new affinities $-\tilde{\Psi}$ and $-\tilde{\chi}$ associated with the mechanical and chemical cycles. These affinities represent a part of the expression of the entropy production rate of the motor [37], which also satisfies a fluctuation relation different from that of the currents but very much related to it.

We emphasize that the relation (27) involves *both* the mechanical and the chemical activities and that, here, a symmetry relation of the type of Eq. (16) for the mechanical variable alone is not satisfied. It is therefore essential, in deriving fluctuation relations, to take into account and include all internal variables that are coupled with one another under time-reversal. Leaving aside some relevant degrees of freedom would manifest itself as an apparent violation of this symmetry and would wrongly be interpreted as a breakdown of the fluctuation theorem.

3.3. Flashing ratchet model on a continuous space

We show in this section how the ideas developed in the previous section for the discrete two-state model can now be extended to more general continuous models, such as the flashing ratchet. There are several reasons for considering continuous models as a substitute for discrete models: first of all, continuous models contain all

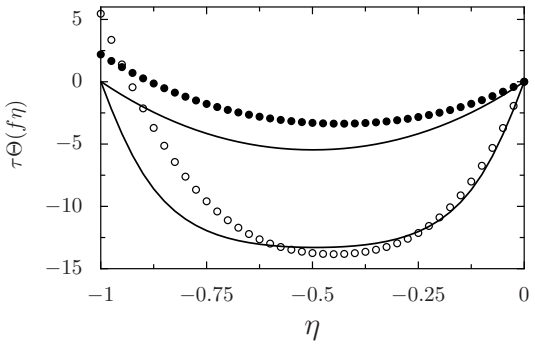

FIGURE 10. Normalized eigenvalue $\tau\Theta(f\eta)$ of the flashing ratchet model as a function of $\eta = \lambda/f$ (with $\tau = a^2/D_0$), for a normalized force $f = 5$ (top two curves) and $f = 10$ (bottom two curves). The solid curves correspond to the case where the transition rates between the internal states satisfy detailed balance, which leads to the Gallavotti-Cohen symmetry, *i.e.* to the symmetry with respect to $\eta = -1/2$. The curves with filled symbols ($f = 5$) and empty symbols ($f = 10$) correspond to the case where the detailed balance is broken with constant transition rates $\omega_1(x) = \omega_2(x) = 10\tau^{-1}$ and the same potentials.

the possible discrete models as limiting cases, second, the way to describe the effect of force on the motor is unambiguous for continuous models, and third, there are effects such as fluctuations which are not always well captured by discrete models.

We provide in this section an analytical proof that the flashing ratchet obeys a Gallavotti-Cohen symmetry [68], using a technique inspired by [17, 22]. We also analyze numerically this point by calculating the eigenvalue associated with the evolution matrix of the generating functions of the currents.

3.3.1. The purely mechanical ratchet. Before considering the case of the flashing ratchet with a mechanical and a chemical variable, it is helpful to look first at a purely mechanical ratchet, which has been used to describe in particular the translocation of a polymer through a pore [69]. In this model, one considers a random walker in a periodic potential subject to an external force F (model I) [70, 39]. The corresponding Fokker-Planck equation is

$$\frac{\partial P}{\partial t} = D_0 \frac{\partial}{\partial x}\left[\frac{\partial P}{\partial x} + \frac{U'(x) - F}{k_B T} P\right], \tag{28}$$

where $U(x)$ is a periodic potential $U(x + a) = U(x)$ and a is the period. This equation describes the stochastic dynamics of a particle in the effective potential $U_{eff}(x) = U(x) - Fx$. By solving Eq. (28) with periodic boundary conditions [69, 70], it can be readily proven that the system reaches a stationary state with

a uniform current J in the long time limit. This current is non-vanishing if a non-zero force is applied. When $F = 0$, there is no tilt in the potential, $J = 0$ and the stationary probability is given by the equilibrium Boltzmann-Gibbs factor.

Similarly to the discrete case, we introduce the generating function

$$F_\lambda(\zeta, t) = \sum_n \exp\left(\lambda(\zeta + n)\right) P((n + \zeta)a, t)\,. \tag{29}$$

The time evolution of this generating function F_λ is obtained by summing over Eq. (28). This leads to the equation

$$\frac{\partial F_\lambda(\zeta, t)}{\partial t} = \mathcal{L}(\lambda) F_\lambda(\zeta, t)\,, \tag{30}$$

where the deformed differential operator $\mathcal{L}(\lambda)$ acts on a periodic function $\Phi(\zeta, t)$ of period 1 as follows:

$$\frac{a^2}{D_0}\mathcal{L}(\lambda)\Phi = \frac{\partial^2\Phi}{\partial\zeta^2} + \frac{\partial}{\partial\zeta}\left(\tilde{U}'_{\text{eff}}\Phi\right) - 2\lambda\frac{\partial\Phi}{\partial\zeta} - \lambda\tilde{U}'_{\text{eff}}\Phi + \lambda^2\Phi\,, \tag{31}$$

where $\tilde{U}'_{\text{eff}} = a\partial_x U_{\text{eff}}/k_B T$ and the left-hand side of Eq. (31) is proportional to the inverse of the characteristic time $\tau = a^2/D_0$.

The operator $\mathcal{L}(\lambda)$ has the fundamental conjugation property

$$\mathrm{e}^{U(x)/k_B T}\mathcal{L}(\lambda)\left(\mathrm{e}^{-U(x)/k_B T}\Phi\right) = \mathcal{L}^\dagger\left(-f - \lambda\right)\Phi. \tag{32}$$

This property implies that the operators $\mathcal{L}(\lambda)$ and $\mathcal{L}^\dagger\left(-f - \lambda\right)$ are adjoint to each other, and thus have the same spectrum. If we call $\Theta(\lambda)$ the largest eigenvalue of $\mathcal{L}(\lambda)$, we obtain from Eq. (32) that $\Theta(\lambda)$ satisfies the Gallavotti-Cohen symmetry:

$$\Theta(\lambda) = \Theta(-f - \lambda). \tag{33}$$

In fact, this symmetry holds for all eigenvalues. For the special case $f = 0$, the conjugation relation (32) reduces to the *detailed balance* property [22]. One can note that this proof of the Gallavotti-Cohen symmetry does not require explicit knowledge of $\Theta(\lambda)$. In the discrete minimal ratchet model, an explicit analytical expression could be obtained for this quantity. In the continuous case, this is no longer the case but $\Theta(\lambda)$ can be calculated numerically. We have done this by first discretizing the operator $\mathcal{L}(\lambda)$ and then calculating its largest eigenvalue using the Ritz variational method [68]. A similar method has been used in Ref. [71] for the cosine potential. We note that our numerical approach can handle any form of potential.

3.3.2. The flashing ratchet. We now present the extension of the Gallavotti-Cohen symmetry to the case of the flashing ratchet model, which should include both the mechanical and chemical currents [36, 28]. When the switching rates satisfy a detailed balance condition, which is for instance the case when $\Delta\mu = 0$, the symmetry is indeed present as shown in the solid curves of Figure 10. In the general case however, where the normalized force f and chemical potential $\Delta\mu$ are both non-zero, the relation (7) is no longer satisfied and the Gallavotti-Cohen

relation (33) is not valid. This is shown in the curves with symbols in Figure 10 where for simplicity we took constant switching rates $\omega_1 = \omega_2 = 10\tau^{-1}$. For all the curves of this figure, a sawtooth potential U_1, and a potential U_2 constant in space have been chosen. The breaking of the symmetry of Eq. (33) can be interpreted as a result of the existence of internal degrees of freedom. Although other mechanisms exist which lead to violations of fluctuation relations as discussed in Ref. [74], this case appears to be rather generic.

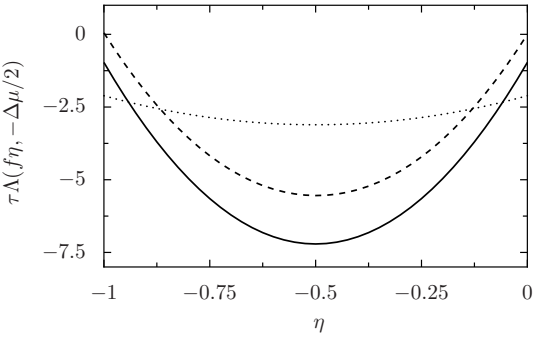

FIGURE 11. For the model described by Eqs. (34–35), the normalized eigenvalue $\tau\Lambda(f\eta, -\Delta\mu/2)$ is shown as function of η. The dashed curve corresponds to $f = 5$ and $\Delta\mu = 0$, the solid curve corresponds to $f = 5$ and $\Delta\mu = 10$, and the dotted curve corresponds to $f = 2$ and $\Delta\mu = 10$. The symmetry is recovered in all cases in this description which includes both the mechanical and chemical degrees of freedom.

Let us now introduce the probability density $P_i(x, q; t)$ associated with the probability that at time t the ratchet is in the internal state i, at position x and that q chemical units of ATP have been consumed. The evolution equations for this probability density is obtained by modifying Eqs. (3) after taking into account the dynamics of the discrete variable q. We have

$$\frac{\partial P_1(x,q,t)}{\partial t} = (\mathcal{L}_1 - \omega_1(x))\, P_1(x,q,t) + \omega_2^{-1}(x) P_2(x,q+1,t) + \omega_2^0(x) P_2(x,q,t), \tag{34}$$

$$\frac{\partial P_2(x,q,t)}{\partial t} = (\mathcal{L}_2 - \omega_2(x))\, P_2(x,q,t) + \omega_1^0(x) P_1(x,q,t) + \omega_1^1(x) P_1(x,q-1,t). \tag{35}$$

We use a notation similar to that of Ref. [37], where $\omega_i^l(x)$ denotes the transition rate at position x from the internal state i with $l(= -1, 0, 1)$ ATP molecules

consumed. This leads to

$$\omega_1^0(x) = \omega e^{(U_1 - fx)/k_B T}\,, \tag{36}$$

$$\omega_2^0(x) = \omega e^{(U_2 - fx)/k_B T}\,, \tag{37}$$

$$\omega_1^1(x) = \psi e^{(U_1 - fx)/k_B T + \Delta\mu}\,, \tag{38}$$

$$\omega_2^{-1}(x) = \psi e^{(U_2 - fx)/k_B T}\,. \tag{39}$$

We also have $\omega_1(x) = \omega_1^0(x) + \omega_1^1(x)$ and $\omega_2(x) = \omega_2^0(x) + \omega_2^{-1}(x)$. The operators $\mathcal{L}_1$ and $\mathcal{L}_2$ act on a function Φ as

$$\mathcal{L}_i = D_0 \frac{\partial^2 \Phi}{\partial x^2} + D_0 \frac{\partial}{\partial x}\left(\frac{U_i'(x) - F}{k_B T}\ \Phi \right) \qquad i = 1, 2\,. \tag{40}$$

As above, we introduce two generating functions $F_{1,\lambda,\gamma}$ and $F_{2,\lambda,\gamma}$, depending on two parameters λ and γ which are conjugate variables to the position of the ratchet and to the ATP counter q. We have for $i = 1, 2$,

$$F_{i,\lambda,\gamma}(\zeta, t) = \sum_q \mathrm{e}^{\gamma q} \sum_n \mathrm{e}^{\lambda(\zeta+n)} P_i(a(\zeta + n), q; t). \tag{41}$$

The evolution equation for these generating functions is obtained from Eq. (35) as

$$\frac{\partial}{\partial t}\begin{pmatrix} F_{1,\lambda,\gamma} \\ F_{2,\lambda,\gamma} \end{pmatrix} = \mathcal{L}(\lambda, \gamma) \begin{pmatrix} F_{1,\lambda,\gamma} \\ F_{2,\lambda,\gamma} \end{pmatrix}, \tag{42}$$

with the operator $\mathcal{L}(\lambda, \gamma)$ decomposed as

$$\mathcal{L}(\lambda, \gamma) = \mathcal{D}(\lambda) + \mathcal{N}(\gamma), \tag{43}$$

with $\mathcal{D}(\lambda)$ the diagonal matrix $\mathrm{diag}(\mathcal{L}_1(\lambda) - \omega_1, \mathcal{L}_2(\lambda) - \omega_2)$, where the deformed operators $\mathcal{L}_1(\lambda)$ and $\mathcal{L}_2(\lambda)$ have the form written in Eq. (31) with $U_{eff}(x)$ given by $U_i(x) - Fx$ for $i = 1, 2$, respectively. The operator $\mathcal{N}(\gamma)$ is defined as

$$\mathcal{N}(\gamma) = \begin{pmatrix} 0 & \omega_2^0 + \omega_2^{-1} e^{-\gamma} \\ \omega_1^0 + \omega_1^1 e^{\gamma} & 0 \end{pmatrix}. \tag{44}$$

Consider now the diagonal matrix Q defined by $\mathrm{diag}(e^{-U_1/k_B T}, e^{-U_2/k_B T})$. By direct calculation, one can verify that $Q^{-1}\mathcal{N}(\gamma)Q = \mathcal{N}^\dagger\left(-\Delta\mu - \gamma\right)$. From Eq. (32), one obtains $Q^{-1}\mathcal{D}(\gamma)Q = \mathcal{D}^\dagger\left(-\Delta\mu - \gamma\right)$. By combining these two equations, we conclude that

$$Q^{-1}\mathcal{L}(\lambda, \gamma)Q = \mathcal{L}^\dagger\left(-f - \lambda, -\Delta\mu - \gamma\right), \tag{45}$$

which leads to the Gallavotti-Cohen symmetry:

$$\Lambda(\lambda, \gamma) = \Lambda\left(-f - \lambda, -\Delta\mu - \gamma\right), \tag{46}$$

where $\Lambda(\lambda, \gamma)$ is the largest eigenvalue of $\mathcal{L}(\lambda, \gamma)$. This relation is the equivalent of Eq. (27), which was derived for the discrete model. If we consider only the mechanical displacement of the ratchet, the relevant eigenvalue $\Theta(\lambda)$ is given by $\Theta(\lambda) = \Lambda(\lambda, 0)$, which clearly does not satisfy the fluctuation relation of the form Eqs. (16–19) as shown in Figure 10. In Figure 11, we have computed $\Lambda(f\eta, -\Delta\mu/2)$ for the same potentials and with rates $\omega_i^l(x)$ of the form given above with $\omega(x) =$

$5\tau^{-1}$ and $\phi(x) = 10\tau^{-1}$. We have verified that in all cases the symmetry of Eq. (46) holds.

To conclude this section on the continuous flashing ratchet, we emphasize the following two points: (i) we have proved that the flashing ratchet satisfies the fluctuation theorem without having to adjust any parameter in the system to enforce the validity of this theorem. The only constraints on the switching rates were given *a priori* from thermodynamics and kinetic theory and these requirements are always taken into account in the very definition of the model (see, e.g., [40]). What we have shown is that these thermo-kinetic constraints are enough to imply the Gallavotti-Cohen symmetry, which itself has far-reaching consequences on the model. (ii) In order to derive the fluctuation theorem, all relevant microscopic degrees of freedom must be involved. For example, in the flashing rachet model, the position variable alone does not obey the fluctuation theorem and the chemical variable that counts how many ATP molecules have been consumed by the motor during its displacement has to be taken into account. The Gallavotti-Cohen symmetry thus leads to global mechano-chemical constraints on the modes of operation of the motor.

4. Conclusions

A first simple and useful message to take from this study is that the dynamics of a molecular motor can be described by the evolution of a random walker in an effective potential $U_{eff}(x, y)$ where x is the mechanical variable and y is the chemical variable [75]. The periodicity of the potential along x and y implies that the potential has an egg-carton shape.

The symmetry of the fluctuation relations for the currents is valid in general for the flashing ratchet model only when internal degrees of freedom are taken into account. This raises a fundamental question concerning the validity of fluctuation relations and their applicability to other types of ratchet models [72, 73, 4, 39]. More generally, other mechanisms exist which are known to produce deviations from fluctuation relations [74], and it would be valuable to know whether fluctuation relations can always be restored by enlarging the phase space and by modifying the dynamics accordingly.

On the experimental side, it would be very interesting to investigate fluctuation relations for molecular motors using single molecule experiments, in a way similar to what was achieved in colloidal beads or biopolymers experiments [57]-[62]. Using fluorescently labeled ATP molecules, recent experiments with myosin 5a and with the F_1-ATPase rotary motor, aim at simultaneous recording of the turnover of single fluorescent ATP molecules and the resulting mechanical steps of the molecular motor [76]. These exciting results indicate that a simultaneous measurement of the values of the mechanical and chemical variables of the motor is achievable in practice, and therefore from the statistics of such measurements it may be possible to obtain the distribution of probability to find the motor at a

specific position and with a specific number of molecules of ATP consumed. With enough statistics, one could thus in principle verify Eq. (27). Such an experimental verification would confirm that the Gallavotti-Cohen symmetry is a fundamental constraint that plays an essential role in the mechano-chemical coupling of molecular motors.

Finally, besides the Gallavotti-Cohen fluctuation theorem, many exact non-equilibrium relations have been discovered during the last decade, the most famous one being the Jarzynski identity [16] and its generalization by Crooks [19]. These identities, originally derived for systems being driven out of a state of thermodynamic equilibrium, have been extended by Hatano-Sasa to systems prepared in non-equilibrium stationary states and following Markovian dynamics [77]. This more general fluctuation relation leads with a proper choice of observables to generalizations of the well-known fluctuation-dissipation phenomenon known for systems close to equilibrium [78, 79, 80, 81]. These generalized fluctuation-response relations hold for systems prepared in non-equilibrium stationary states and following Markovian dynamics. The implications of the Crooks fluctuation theorem for kinesin has been analyzed in Ref. [82], while the implications of generalized fluctuation-response relations for molecular motors have been considered recently [83, 84].

All these various relations can be interpreted as universal constraints that have to be obeyed by systems far from equilibrium regardless of their detailed structure. It would be of great interest to explore the consequences of these relations in the field of ratchet models (both at the single motor level and at the level of many motors) and to draw from them some measurable predictions that could be verified experimentally on molecular motors.

Acknowledgment

D.L. acknowledges support from the Indo-French Center CEFIPRA (grant 3504-2), and the IIT Kanpur for hospitality during the 2010 Golden Jubilee.

References

[1] B. Duplantier, in *Einstein,* 1905–2005*: Poincaré Seminar* 2005, edited by T. Damour, O. Darrigol, B. Duplantier, and V. Rivasseau (Birkhäuser Verlag AG, 2006), Vol. 47 of *Prog. in Math. Physics*, pp. 201–293.

[2] R. P. Feynman, R. B. Leighton, and M. Sands, *The Feynman Lectures on Physics I* (Reading, MA, Addison-Wesley, 1963).

[3] L. Brillouin, J. Appl. Phys. **22** (1951), 334.

[4] P. Reimann, Phys. Rep. **361** (2002), 57.

[5] C. V. den Broek, P. Meurs, and R. Kawai, New J. of Phys. **7** (2005), 10.

[6] M. O. Magnasco, Phys. Rev. Lett. **71** (1993), 1477, *ibid* Phys. Rev. Lett. **72** (1994), 2656.

[7] A. Ajdari and J. Prost, C. R. Acad. Sci. Paris II **315** (1993), 1635.

[8] R. D. Astumian, Science **276** (1997), 917.

[9] K. Sekimoto, J. Phys. Soc. Jpn. **66** (1997), 1234, *ibid.* Phys. Rev. E, **76** (2007), 060103(R).

[10] J. M. R. Parrondo and B. J. D. Cisneros, Appl. Phys. A **75** (2002), 179.

[11] J. Howard, *Mechanics of Motor Proteins and the Cytoskeleton*, (Sinauer Associates, Sunderland, MA, 2001).

[12] Y. Aghababaie, G. Menon, and M. Plischke, Phys. Rev. E **59** (1999), 2578.

[13] D. Chowdhury, A. Basu, A. Garai, P. Greulich, K. Nishinari, A. Schadschneider, and T. Tripathi, Eur. Phys. J. B **64** (2008), 593.

[14] M. Müller, S. Klumpp, and R. Lipowsky, Proc. Natl. Acad. Sci. **105** (2008), 4609.

[15] G. Gallavotti and E. G. D. Cohen, Phys. Rev. Lett. **74** (1995), 2694.

[16] C. Jarzynski, Phys. Rev. Lett. **78** (1997), 2690.

[17] J. Kurchan, J. Phys. A: Math. Gen. **31** (1998), 3719, *ibid.* J. Stat. Mech. (2007) P07005.

[18] D. Evans and D. Searles, Adv. Phys. **51** (2002), 1529, *ibid.* Phys. Rev. E **50** (1994), 1645.

[19] G. E. Crooks, Phys. Rev. E **61** (2000), 2361.

[20] C. Jarzynski, Eur. Phys. J. B **64** (2008), 331.

[21] F. Ritort, Adv. Chem. Phys. **137** (2008), 31.

[22] J. L. Lebowitz and H. Spohn, J. Stat. Phys. **95** (1999), 333.

[23] B. Derrida, J. Stat. Mech. (2007), p. P07023.

[24] H. Qian, Phys. Rev. E **64** (2001), 022101.

[25] H. Qian, J. Phys.: Cond. Mat. **17** (2005), S3783.

[26] R. Chetrite and K. Gawedzki, Comm. Math. Phys. **282** (2008), 469.

[27] C. Bustamante, J. Liphardt, and F. Ritort, Phys. Today **58** (2005), 43.

[28] T. Schmiedl, T. Speck, and U. Seifert, J. Stat. Phys. **128** (2007), 77.

[29] F. Jülicher, A. Ajdari, and J. Prost, Rev. Mod. Phys. **69** (1997), 1269.

[30] A. Kolomeisky and M. Fisher, Annu. Rev. Phys. Chem. **58** (2006), 675.

[31] R. Lipowsky, Phys. Rev. Lett. **85** (2000), 4401.

[32] U. Seifert, Europhys. Lett. **70** (2005), 36.

[33] K. Sekimoto, Prog. of Theo. Phys. **130** (1998), 17.

[34] D. Andrieux and P. Gaspard, Phys. Rev. E **74** (2006), 011906.

[35] R. Lipowsky and S. Liepelt, J. Stat. Phys. **130** (2008), 39.

[36] A. W. C. Lau, D. Lacoste, and K. Mallick, Phys. Rev. Lett. **99** (2007), 158102.

[37] D. Lacoste, A.W.C. Lau, and K. Mallick, Phys. Rev. E **78** (2008), 011915.

[38] W. de Roeck and C. Maes, Phys. Rev. E **76** (2007), 051117.

[39] P. Hänggi and F. Marchesoni, Rev. Mod. Phys. **81** (2009), 387.

[40] A. Parmeggiani et al., Phys. Rev. E **60** (1999), 2127.

[41] H. Wang, C. S. Peskin, and T. C. Elston, J. Theor. Biol. **221** (2003), 491.

[42] A. Kolomeisky and B. Widom, J. Stat. Phys. **93** (1998), 633.

[43] M. Fisher and A. Kolomeisky, Proc. Natl. Acad. Sci. **96** (1999), 6597, *ibid.*, **98** (2001), 7748.

[44] Y. Kafri et al., Biophys. J.**86** (2004), 3373.

[45] C. Jarzynski and O. Mazonka, Phys. Rev. E **59** (1999), 6448.

[46] M. Schnitzer and S. Block, Nature **388** (1997), 386.

[47] T. Schmiedl and U. Seifert, Eur. Phys. Lett. **83** (2008), 30005.

[48] K. Visscher, M. J. Schnitzer, and S. M. Block, Nature **400** (1999), 189.

[49] A. Valleriani, S. Liepelt, and R. Lipowsky, Eur. Phys. Lett. **82** (2008), 28011.

[50] R. Lipowsky, S. Liepelt, and A. Valleriani, J. Stat. Phys. **135** (2009), 951.

[51] N. Carter and R. Cross, Nature **435** (2005), 308.

[52] S. Liepelt and R. Lipowsky, Phys. Rev. E **79** (2009), 011917.

[53] K. I. Skau, R. B. Hoyle, and M. S. Turner, Biophys. J. **91** (2006), 2475.

[54] P. Gaspard and E. Gerritsma, J. Theo. Biol. **247** (2007), 672.

[55] L. Mollazadeh-Beidokhti, J. Deseigne, D. Lacoste, F. Mohammad-Rafiee and H. Schiessel, Phys. Rev. E **79** (2009), 031922.

[56] E. Gerritsma and P. Gaspard, arXiv:0904.4218 (2009).

[57] J. Liphardt, S. Dumont, S. Smith, I. Tinoco, and C. Bustamante, Science **296** (2002), 1832.

[58] D. Collin, F. Ritort, C. Jarzynski, S. B. Smith, I. Tinoco, and C. Bustamante, Nature **437** (2005), 231.

[59] E. Trepagnier, C. Jarzynski, F. Ritort, G. Crooks, C. Bustamante, and J. Liphardt, Proc. Natl. Acad. Sci. USA **101** (2004), 15038.

[60] A. Imparato, L. Peliti, G. Pesce, G. Rusciano, and A. Sasso, Phys. Rev. E **76** (2007), 050101.

[61] V. Blickle, T. Speck, L. Helden, U. Seifert, and C. Bechinger, **96** (2006), 070603.

[62] J. R. Gomez-Solano, A. Petrosyan, S. Ciliberto, R. Chetrite, and K. Gawedzki, Phys. Rev. Lett. **103** (2009).

[63] J. Schnakenberg, Rev. Mod. Phys. **48** (1976), 571.

[64] D. Andrieux and P. Gaspard, J. Stat. Phys. **127** (2007), 107.

[65] T. Hill, *Free Energy Transduction and Biochemical Cycle Kinetics*, (Springer-Verlag, New York, 1989).

[66] M. J. Schnitzer, K. Visscher, and S. M. Block, Nature Cell Biol. **2** (2000), 718.

[67] A. Parmeggiani, F. Jülicher, L. Peliti, and J. Prost, Europhys. Lett. **56** (2001), 603.

[68] D. Lacoste and K. Mallick, Phys. Rev. E **80** (2009), 021923.

[69] D. K. Lubensky and D. R. Nelson, Biophys. J. **77** (1999), 1824.

[70] H. Risken, *The Fokker-Planck Equation* (Springer, Berlin, 1989).

[71] J. Mehl, T. Speck, and U. Seifert, Phys. Rev. E **78** (2008), 011123.

[72] G. Oshanin, J. Klafter and M. Urbakh, Europhys. Lett. **68** (2004), 26.

[73] F. Slanina, Europhys. Lett. **84** (2008), 50009.

[74] S. Rahav and C. Jarzynski, J. Stat. Mech-Theory E (2007), p. P09012.

[75] D. Keller and C. Bustamante, Biophys. J. **78** (2000), 541.

[76] Y. Ishii and T. Yanagida, HFSP J. **1** (2007), 15.

[77] T. Hatano and S.-I. Sasa, Phys. Rev. Lett. **86** (2001), 3463.

[78] J. Prost, J.-F. Joanny, and J. M. R. Parrondo, Phys. Rev. Lett. **103** (2009), 090601.
[79] R. Chetrite, G. Falkovich, and K. Gawedzki, J. Stat. Mech. (2008), p. P08005.
[80] T. Speck and U. Seifert, Europhys. Lett. **74** (2006), 391.
[81] M. Baiesi, C. Maes, and B. Wynants, Phys. Rev. Lett. **103** (2009), 010602.
[82] E. A. Calzetta, Eur. Phys. J. B. **68** (2009), 601.
[83] G. Verley, K. Mallick, and D. Lacoste, manuscript in preparation (2010).
[84] U. Seifert, Phys. Rev. Lett. **104** (2010) 138101.

David Lacoste
Laboratoire de Physico-Chimie Théorique
UMR 7083 CNRS
10, rue Vauquelin
F-75231 Paris Cedex 05, France
e-mail: david.lacoste@gmail.com

Kirone Mallick
Institut de Physique Théorique
CEA Saclay
F-91191 Gif sur Yvette, France
e-mail: Kirone.Mallick@cea.fr

Studies of DNA-Replication at the Single Molecule Level Using Magnetic Tweezers

Maria Manosas, Timothée Lionnet, Élise Praly, Ding Fangyuan, Jean-François Allemand, David Bensimon and Vincent Croquette

Abstract. The development of tools to manipulate single biomolecules has opened a new vista on the study of many cellular processes. In this review we will focus on the use of magnetic tweezers to study the behavior of enzymes involved in DNA replication. Depending on the DNA substrate used, magnetic tweezers give access either to the advancement in real time of the so-called replication fork or to the torsional state (the so-called supercoiled density) of the DNA molecule. We will show how the new tools at our disposal can be used to gain an unprecedented description of the kinetic properties of enzymes. The comparison of these results with theoretical models allows us to get insight into the mechanism used by the enzymes under study. This analysis is often out of reach of more classical, bulk techniques.

1. Introduction

Biophysics is currently undergoing an important transformation due to the development of tools for manipulating, visualizing and studying single molecules and their interactions. New tools such as optical or magnetic tweezers have allowed the manipulation of single DNA molecules and a detailed characterization of their elastic response (see [1] for review). These experiments have renewed theoretical interest in the mechanical properties of biomolecules. Consequently, we presently have a very good understanding of the response to tension and torsion of DNA over a large range of forces and torques [2]. Modification of these elastic properties induced by proteins that bind to DNA provides precious information about DNA-protein interactions and enzymatic kinetics. Proteins that alter the DNA's extension or the DNA's topological conformation can be studied at the single molecule level by using these tools. Moreover, whenever the time resolution of the measuring device is sufficient, these studies permit real-time monitoring of the DNA/protein interaction.

B. Duplantier and V. Rivasseau (eds.), *Biological Physics*, Progress in Mathematical Physics 60,

DOI 10.1007/978-3-0346-0428-4_5,

These micromanipulation experiments introduce force as a new thermodynamic parameter in *in vitro* experiments. Force can be used to alter the equilibrium of a reaction or modify its activation barriers, in addition to the temperature or buffer conditions, which are often the only control parameters in a conventional bulk assay [3, 4, 5]. Moreover, these single-molecule investigations avoid the ensemble averaging inherent in bulk measurements. Such averaging may hinder the observation of some dynamical properties of the enzyme or obscure the existence of an heterogeneous population. Single molecule assays only measure active enzymatic complexes, in contrast to conventional biochemical experiments where the intrinsic enzymatic activity is estimated by dividing the total activity by the concentration of enzymes, an estimate that often underestimates the real activity if a large portion of the enzymes are inactive or if the active complex is multimeric.

In the present review, after a short introduction to magnetic tweezers and a summary of the elastic properties of bare DNA molecules, we will present some of the results obtained in our group concerning the study of the DNA replication.

2. Magnetic tweezers

Most of the enzymes involved in DNA replication are molecular motors which convert the energy from NTP (or dNTP) hydrolysis into mechanical work. The hydrolysis of a single molecule of ATP, under physiological conditions, generates about 20 k_BT (i.e., $8 \cdot 10^{-20} J$) of energy (k_B is the Boltzmann constant and $T \sim 300°$K room temperature). Since the characteristic displacement of a biological motor is on the order of a few nanometers, the relevant forces for micromanipulation of biological molecules are on the order of: $8 \cdot 10^{-20} J / 10^{-8} m \sim 8 \cdot 10^{-12}$ N. To apply and detect such forces different techniques have been developed: Atomic Force Microscopy [6], Biomembrane Force Probe [7], glass micropipette manipulation [8], flow induced force [9], optical [10] and magnetic tweezers (see [2] and references therein). For the purpose of this review, we provide only a brief description of magnetic tweezers.

Magnetic tweezers are used to manipulate magnetic beads tethered to a surface by a DNA molecule (but potentially by any polymer). When placed in the magnetic field of permanent (or electro-) magnets (see Fig. 1), their magnetic dipole experiences both a force F (parallel to the magnetic field gradient) and a torque Γ (that tends to align its dipole with the magnetic field). A micron size bead at a distance of one millimeter of a pair of two NdFeB magnets separated by a half millimeter gap, is pulled by a force of a few pN towards the high magnetic field region. By varying the distance between the bead and the magnets we modulate the force between 20 pN to a few femtoNewtons. Interestingly, such force values fall in the range of biological forces. On the other hand, the torque applied to the bead can reach 10^5pN.nm, a value that exceeds any biological torque. Thus the bead magnetization follows closely that of the magnetic field.

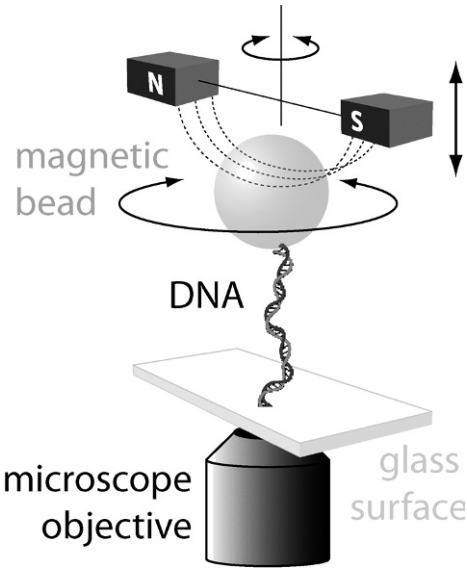

FIGURE 1. Magnetic tweezers set-up. A DNA molecule is anchored at one end to a micron sized magnetic bead and at the other to the bottom surface of a square capillary tube, placed on top of a microscope objective. Small magnets placed above the sample can be used to pull and twist the DNA molecule.

Since beads are not perfectly uniform in size and magnetization and the force is a very nonlinear function of the distance between the bead and the magnets, the exact value of the force applied by these tweezers must be calibrated. The latter is achieved by measuring the Brownian fluctuations. The beads are subject to Brownian fluctuations and exhibit random displacements transverse to the direction of the pulling force. The amplitude of such fluctuations is inversely proportional to F: the stronger the force the less the bead fluctuates. In fact, the bead tethered by a DNA molecule of extension l and pulled by the magnetic field is similar to a damped pendulum. Applying the dissipation-fluctuation theorem to this system yields a relation between the force and the amplitude of the transverse fluctuations $\langle \delta x^2 \rangle$: $F = k_B T l / \langle \delta x^2 \rangle$. Video microscopy allows measurement of the three-dimensional position of the bead with nanometer resolution [11] and thus of l and $\langle \delta x^2 \rangle$. Using this Brownian motion method, forces from a few femtoNewtons to a hundred of picoNewtons have been measured [11]. The magnetization of the bead presents no hysteresis. Therefore once the force versus magnet distance has been determined for several beads (see Fig. 2), we can use the average measured relation to predict the force according to the magnet distance. It turns out that the bead magnetization distribution is pretty narrow and the force acting on a

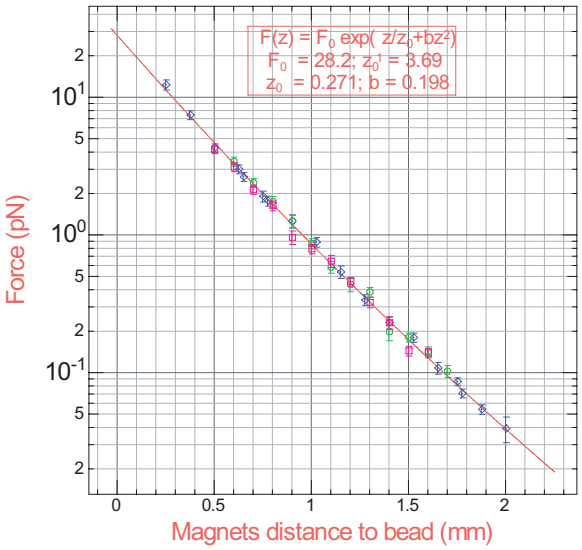

FIGURE 2. Force measured on a micron-sized bead versus the distance from the magnets. This calibration is done using the Brownian motion method. The curve may be fitted by a simple formula (full red line). Three different beads are compared on this graph (blue, magenta and green points). The force agrees for these three beads within the experimental error.

bead may be predicted without previous calibration with a typical error of 20% (see Fig. 2). This accuracy is sufficient for many experiments.

A distinct advantage of magnetic tweezers is that they are intrinsic force clamps: the force applied to the bead is controlled and the extension of the molecule is measured. Other micromanipulation systems (e.g., optical tweezers) are natural extension clamps, distances are imposed and the force is measured. In those systems the application of a constant force requires implementation of a feedback loop [12]. In addition, rotating the bead to impose a torque on the molecule is extremely simple using magnetic tweezers, thus permitting control over the topological state of the DNA under study.

2.1. Finding beads tethered by a single molecule

To prepare a single molecule assay, one usually mixes streptavidin coated beads with modified DNA molecules having biotin at one end and digoxigenin at the other end. The DNA molecule will diffuse until its biotinylated end links to the streptavidin coated bead. By gently flowing these beads in a microchannel coated with antidigoxigenin, the DNA molecule may tether a bead to the micro-channel glass plate. To work in the single molecule limit, we use a small number of DNA molecules compared with that of the magnetic beads. In general, this protocol

works very efficiently. Nevertheless, the probability of having one bead tethered to the glass substrate by two or more DNA molecules is not zero. Therefore, when we select a bead for further study our first task is to insure that it is indeed tethered by a single molecule.

Rotating the magnets offers a very convenient means to answer this critical question. The assay will depend on the exact molecule used. If we are dealing with single stranded DNA or nicked double stranded DNA, the molecule will be completely insensitive to torsion. In this latter case, if the bead is tethered by a single molecule its position (especially its vertical one) remains unchanged when we rotate the magnets by a significant number of turns. On the contrary, if it is tethered by two or more molecules, the bead rotation entangles the molecules inducing a reduction of the molecule extension. This test is quick and extremely simple. If we use a dsDNA molecule especially prepared to sustain torsion, the test is a little more complex since this time the molecule extension is sensitive to torsion. However, the occurrence of phase transitions such as DNA denaturation or PDNA [13] offers a mean to identify a possible single molecule tether. In any case, measuring the force extension curve of the tether is an ultimate single molecule test.

3. How stretching and twisting DNA helps to track replication process

3.1. Stretching a polymer model: dsDNA

The double stranded DNA (dsDNA) molecule is a long, double helical polymer. This particular secondary structure confers interesting mechanical properties to the molecule. Understanding such properties is crucial before studying the behavior of DNA bound motors as their action might induce changes in the DNA's extension and topology. Furthermore their activity might be controlled by the torque or the force on the molecule.

Like any polymer in solution, dsDNA adopts a random coil geometry that maximizes the number of accessible conformations and thus the entropy. As one starts to stretch dsDNA, the molecule tends to align along the force axis, which decreases the number of accessible conformations. Such decrease in entropy dictates the magnitude of the stretching force. This so-called entropic regime of forces lasts until the molecule is fully aligned (with a single conformation allowed) at a force $F \sim 10$pN. In that regime the elastic response of dsDNA is well described as a flexible tube with bending rigidity B (Worm-Like Chain (WLC) model). At any given force, the extension of the molecule l is determined by minimizing its free energy (*i.e.*, weighting the loss in bending energy against the gain in entropy [15, 16]).

The fit of the experimental force-extension data yields a persistence length (*i.e.*, the typical length over which thermal fluctuations can bend the DNA) $\xi = B/k_BT = 52$ nm [16] under physiological conditions, see Fig. 3. This value is

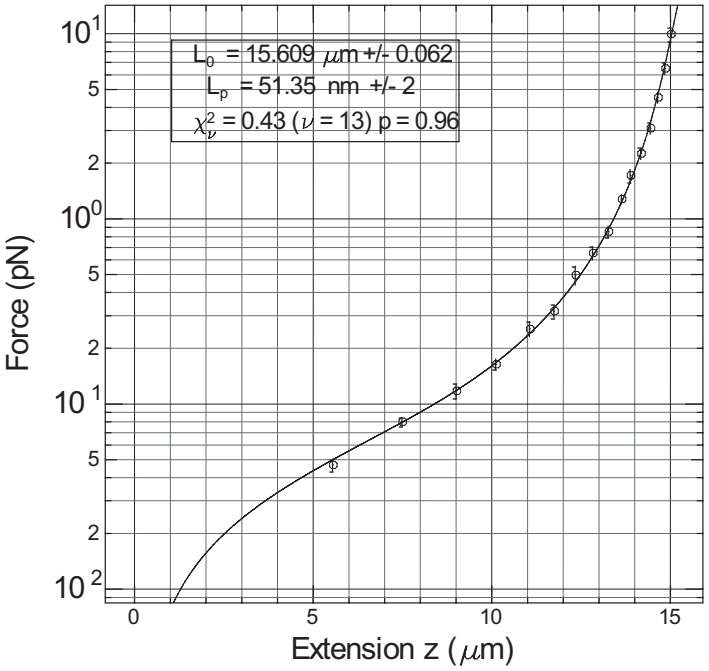

FIGURE 3. Force extension curves of a dsDNA molecule [14].

high compared to common man-made polymers (with $\xi \sim 1 - 2$ nm) because the base stacking at the molecule's core stiffens it. Using this value of ξ, we can estimate the mean radius R_0 of the *E. coli* chromosome: $R_0 = \sqrt{2L\xi} \simeq 10$ μm, (L being the length of the DNA, $\simeq 1$ mm). The comparison of this value to the typical *E. coli* size of 1 μm suggests that the cell must have more efficient ways to compact its DNA. This is indeed achieved by specific DNA-compacting proteins (e.g., condensins) and by supercoiling the molecule.

3.2. Twisting dsDNA

The behavior of DNA under torsion can be explored with magnetic tweezers by simply rotating the magnets and thereby the bead tethered by a dsDNA. At low twist, the DNA's extension is not affected significantly by the torsion. However when the number of turns imposed on the molecule is large enough it buckles under the torsional load. Additional turns applied to the molecule make it writhe and form plectonemic loops, Fig. 4. Thus its extension decreases linearly with the applied number of turns, n. The partitioning of the excess linking number ΔLk (a topological constant here equal to n) between writhe (plectonemes) and twist (change of the helical pitch) plays a key role in major cellular processes, such as

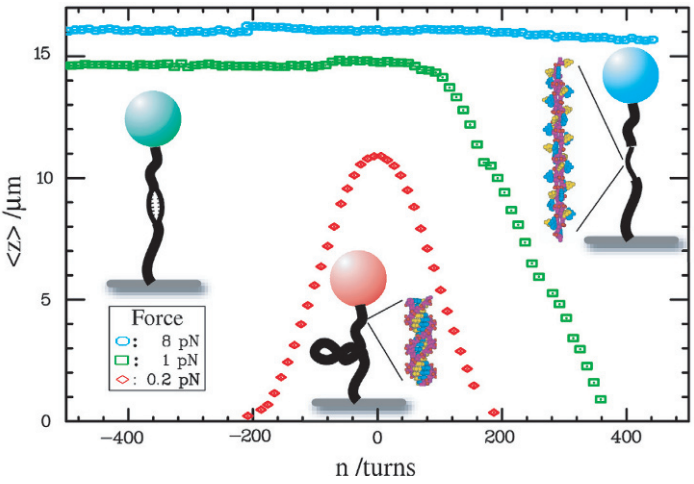

FIGURE 4. DNA twisting at various forces. At low forces (red), as the molecule is over- or underwound its extension decreases identically by forming left- or right-handed plectonemes. At intermediary forces (green), negatively supercoiled DNA denatures, while left-handed plectonemes can still be observed for positive supercoiling. At high forces (blue), positively supercoiled DNA undergoes a transition to an inside-out structure called P-DNA [13].

DNA compaction, replication or transcription. The formation of plectonemes is observed symmetrically under positive and negative torsion, as long as the stretching force is held below a (salt dependent) critical force, typically $F \sim 0.5$ pN. However above this force, the critical torque for denaturation is smaller than the critical torque for buckling Γ_c (which increases as $\Gamma_c \sim F^{1/2}$). In this case, a negatively supercoiled DNA will respond to a large unwinding by denaturing rather than by forming plectonemic loops [17].

3.3. Stretching ssDNA

The elastic behavior of ssDNA, unlike that of dsDNA, strongly depends on the salt conditions and the chain's nucleotide content. It cannot be fitted by a simple elastic polymer model such as the WLC model. First ssDNA is much more flexible than dsDNA: its persistence length ($\xi_{\mathrm{ssDNA}} \sim 1.6$ nm) is about 30 times smaller. Therefore, the electrostatic repulsion between the charged phosphates on its backbone cannot be neglected (as they are for dsDNA), since they are screened over a Debye length that is similar to ξ_{ssDNA}. Second, ssDNA is a somewhat peculiar polymer: because of the possibility of pairing between the bases along its backbone, it is able to form hairpin structures at low forces, which are highly sequence- and salt-dependent. All these effects can be incorporated (with some approximations)

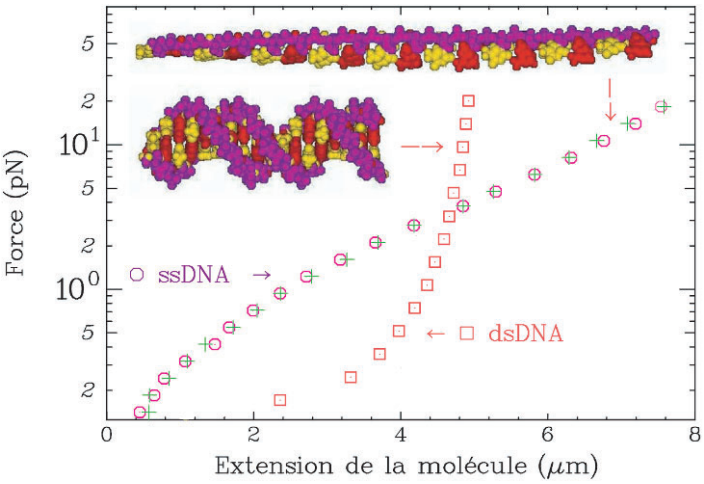

FIGURE 5. Force extension curves of single stranded (green and magenta points) and double stranded (blue points) DNA. The dsDNA data was fitted to a WLC model (blue line) with persistence length $\xi = 52$ nm. The ssDNA data show that the molecule is shorter than dsDNA when force is smaller than 5pN and longer above.[14].

in a Monte Carlo (MC) simulation of a chain under tension. These simulations turn out to nicely describe the behavior of ssDNA over a large range of forces and ionic strengths [14]. Even though a complete theoretical understanding of the elastic behavior of ssDNA is still lacking, the experimental evidence clearly shows that (except near $F \sim 5$ pN) ssDNA and dsDNA have different extensions. As we shall see below this difference can be used to monitor the action of enzymes such as helicases or DNA-polymerases that transform dsDNA into ssDNA or vice-versa.

3.4. Unzipping DNA

Many DNA substrates may be studied using magnetic tweezers. Let us discuss one which will be of interest when studying the replication fork. It consists of a single stranded DNA molecule having a partial palindromic sequence in its center. This palindromic part of the molecule spontaneously folds forming a double stranded DNA molecule closed at one end by a short loop while the two non-complementary parts form a fork (see Fig. 6A). Using biochemistry, we modify the two ends of the DNA molecule attaching biotin at one extremity and digoxigenin at the other. Beads incubated with such DNA molecules are next inserted into the magnetic tweezers chamber. To test whether a magnetic bead has a DNA molecule attached we increase the stretching force until 15 pN, the force required to unzip the molecule (see Fig. 6 B). At that force the hydrogen bonds between base pairs are broken and the extension of the molecule abruptly increases. Each time a base pair opens,

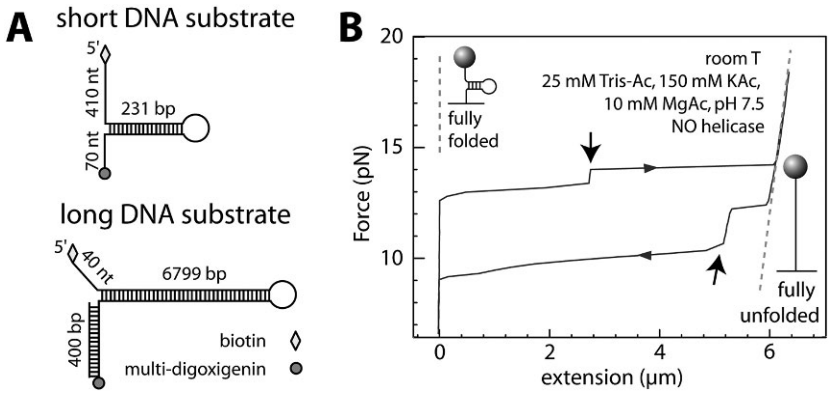

FIGURE 6. (A) Single stranded DNA molecules having a palindromic sequence. This sequence leads to the formation of a hairpin structure: the molecule refolds and presents a dsDNA structure. The biotin molecule binds this molecule on the streptavidin coated bead, while the digoxigenin at the other end of the molecule links to the glass substrate. When a force is applied it pulls apart the hairpin in an unzipping action. Two DNA substrates have been studied which differ in their lengths (231 bp and 6799 bp) and GC contents (32% and 42% respectively).

(B) Typical force vs. extension curve observed for the long DNA hairpin. As the force is increased to 14 pN, the molecule abruptly extends, and finally reaches its full length 6 μm. Refolding of the DNA molecule occurs at a lower force (F $\approx$ 11 pN). Unfolding and refolding transitions display intermediates (arrows), which corresponds to metastable positions of the fork along the hairpin sequence.

the extension increases by approximately 1 nm, as expected from single strand DNA elasticity.

When the molecule is fully open, it may refold if the force is lowered. However, this process is controlled by a critical step involving the refolding of the loop in the middle of the palindromic sequence. This loop formation requires a fluctuation having a significant energy to bring in contact base pairs which are separated. The time needed to overcome this critical step diverges as the force increases close to the unzipping force. Thus there is a substantial hysteresis in the molecule refolding as shown in Fig. 6.

4. Study of the Replisome

In the cell, DNA replication is carried out by a multiprotein complex known as the replisome. Replisomes from different organisms vary in size and complexity. For example, only four proteins are needed to assembly the bacteriophage T7 replisome [18], whereas tens of proteins are required in eukaryotes [19]. Despite the differences in the number of proteins involved, many components of the replisome are functionally and structurally conserved from organism to organism. Studies in prokaryotic and viral systems have contributed greatly to our present understanding of DNA replication [20].

One of the model systems used to study DNA replication is the bacteriophage T4 replisome. The bacteriophage T4 presents a simple yet interesting replisome having eight proteins, a number small enough to be handled and sufficiently large compared with the seven different activities of the replisome. These eight proteins together have been shown to reconstitute in vitro leading and lagging strand DNA synthesis [20].

4.1. The T4 replisome components

The leading and lagging strand templates are copied by two holoenzyme complexes, each composed of the polymerase (gp43) and the clamp (gp45) [21]. The clamp protein is loaded by the clamp loader complex (gp44/62) in an ATP-dependent fashion [22, 23]. DNA polymerases can only synthesize nascent DNA in the 5′ to 3′ direction; therefore, the leading strand holoenzyme may copy the DNA template continuously, while the lagging strand holoenzyme must copy the DNA template in the opposite direction from the fork movement. This process can only be done sequentially in short segments known as Okazaki fragments approximately 1 kb in size. The primosome is a subassembly acting in front of the replisome composed of a hexameric helicase (gp41) that unwinds dsDNA by translocating along the lagging strand template in the 5′ to 3′ direction [24] and an oligomeric primase (gp61) that synthesizes pentaribonucleotide primers at 5-GTT and 5-GCT sequences to initiate repetitive Okazaki fragment synthesis [25, 26]. In the presence of single-stranded DNA binding protein (gp32), which coats the ssDNA produced by the helicase [27], the primosome requires a helicase accessory protein (gp59) for efficient loading [28, 29].

The work presented here focuses on the study of the enzymes of the T4 replisome, and the interactions between them. In particular, we have investigated two sub-assemblies of the replisome: the primosome and the holoenzyme. The primosome is the assembly of the helicase and the primase and it is responsible for unwinding the DNA and initiation of Okazaki fragments. The holoenzyme which copies the DNA is the complex formed by the polymerase and the clamp, and it requires the clamp loader to be efficiently loaded. Leading strand synthesis is achieved by combining holoenzyme and helicase activities.

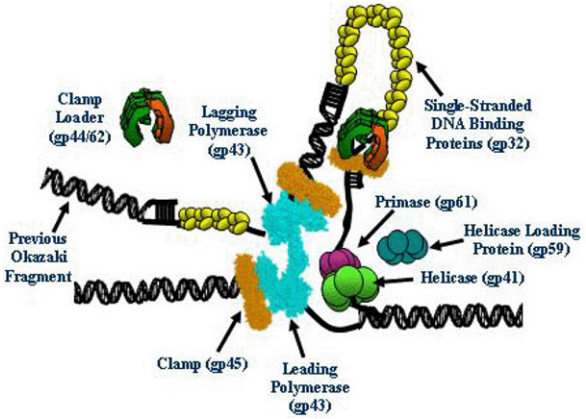

FIGURE 7. Sketch of the replisome around a DNA replication fork. The gp41 helicase opens the DNA and gp61 is the primase that synthesizes a small RNA primer required for initiation of Okazaki fragment synthesis. On both strands, the DNA is copied by the gp43 polymerase which stability is enhanced by the gp45 clamp. The helicase, the primase and the polymerase have each a special protein complex which helps their loading on the DNA substrate. The single stranded binding protein gp32 covers the single stranded DNA molecule that appears transiently in this process.

4.2. A simple replication fork

The replisome as presented in Fig. 7 is a fascinating but complex molecular object. Observing the activity of all its components at once at the single molecule might be hard and results difficult to interpret. Our strategy consists of first studying individual proteins. Once the behaviour of each component is well characterized, we can start studying protein sub-assemblies within the replisome to get insight into its functioning. Finally by progressively increasing the number of proteins we aim to build up the full replisome.

We have prepared a simplified version of the replication fork which consists of a single stranded DNA molecule forming a hairpin (the DNA molecule used in the unzipping assay presented previously). Experiments were carried out by tethering a DNA hairpin between a glass surface and a magnetic bead (Fig. 8) Different DNA substrates were used with variable duplex lengths (from 231 bp up to 6.8 kbps). We use these templates in our magnetic tweezers setup. Using one micron bead, the force may reach 20 pN.

4.3. Helicase, polymerase and replisome assays

The basis of the assay is the following: either the activity of isolated proteins such as gp41 helicase and gp43 polymerase or the activity of the full replisome will

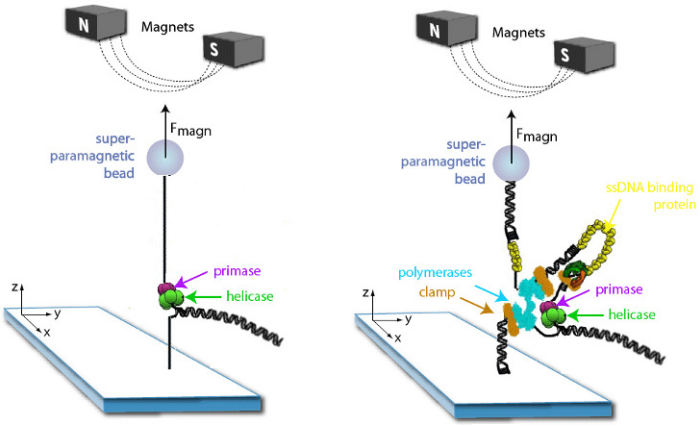

FIGURE 8. Sketch of different steps in the replisome study. On the left, a simple DNA fork is unwound by the helicase alone or associated with the primase. On the right, the full replisome unwinds and duplicates the two strands of the DNA hairpin. In both cases, the extension of the molecule is used to follow in real time the motion of the enzymes. The force applied on the bead is kept below 11 pN ensuring that the changes in DNA extension are the result of enzymatic activity of proteins on the DNA and not mechanical manipulation.

induce the unwinding of the hairpin. Thus their activity can be detected as an increase in the end-to-end distance of the DNA molecule observed as a change in the distance between the bead and the surface (Fig. 8).

We initially characterize the mechanical unfolding of the hairpin construct in the absence of proteins. Mechanical unfolding resulting in an extension of the DNA molecule occurs at a typical range force of 14–17 pN depending on the substrate and displays a marked hysteresis as seen on Fig. 6. Typically at forces of 12 ± 1pN the hairpin is stably folded for the duration of a typical experiment. Therefore below 12 ± 1 pN of force, any unfolding observed in the presence of proteins results from their activity. Indeed in absence of any helicase and polymerase, the extension of the DNA molecule remains constant at the level corresponding to the folded hairpin.

After this calibration, the DNA hairpin is held at a constant force below the unfolding transition force and a buffer containing the proteins under study is injected into the experimental chamber while the extension of the molecule is recorded over time. Any change in extension is thus due to an interaction of the proteins with the DNA (unwinding, polymerization, DNA looping, dissociation, or translocation on ssDNA).

5. Characterizing the helicase activity

The gp41 helicase is active as an hexameric ring [30] that encircles ssDNA and unwinds the DNA with 5′ to 3′ polarity [31]. Within the full replisome is able to promote DNA unwinding at rates of 300–400bp/s [32, 33]. Here we have studied its unwinding and translocation activity at the single molecule level.

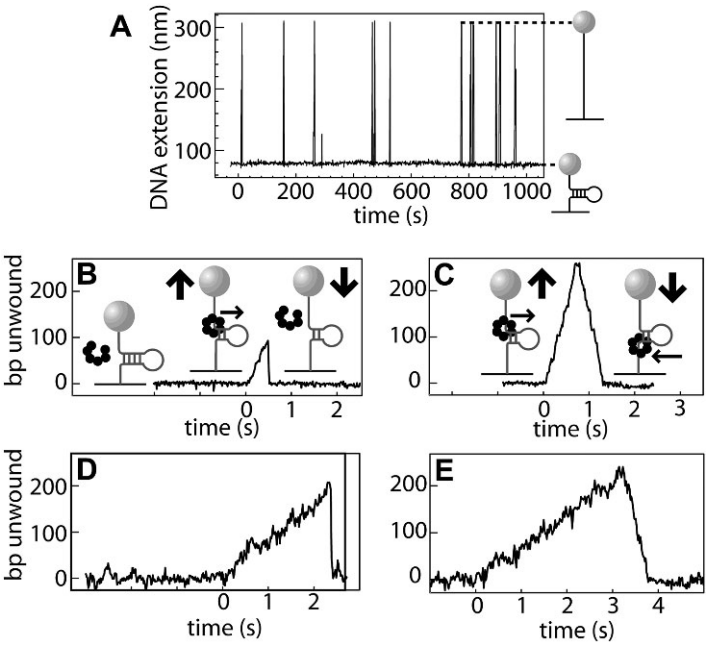

FIGURE 9. Gp41 unwinds the hairpin substrate in bursts. A) Typical recording of the molecule extension versus time over 20 minutes. Most of the time the hairpin is closed but the helicase is active in short bursts. This signal demonstrates that we are in a single molecule regime. B), C), D), E) close view on the unwinding events. Two kinds of events are seen: some with fast falling edge B) and D) and those with slower falling edge. B) and C) are recorded in saturating ATP conditions whereas D) and E) are recorded in condition where ATP is limited resulting in a decreased enzyme rate.

5.1. gp41 unwinding rate measurement

As gp41 and ATP are added into the chamber, we observe short events displaying a transient increase of DNA extension (Fig. 9A)). Between these events, the measured length of the DNA molecule corresponds to the folded state of the hairpin. The slope of the DNA extension time trace during these events (i.e., the unwinding velocity) depends on the ATP concentration (see below). Thus these events

result from helicase-catalyzed transient unwinding of the duplex. The time duration of each event is much shorter than the time between events, which guarantees that each event results from the activity of a single helicase complex. The length increase (in nm) we observe can be readily translated into base pairs (bp) at a given force using the measured ssDNA extension vs. force curve in Fig. 5. This conversion factor is calibrated against the full length of the hairpin, measured as the maximal length of the unwinding events.

Two types of events are observed. The first type consists of a slowly rising edge followed by a rapidly falling edge (Fig. 9B) and C)). The length of these events is variable, distributed between zero and full DNA extension. In contrast with the ATP-dependent slope of the rising edge, the falling edge displays a steep, ATP-independent slope. This means that whereas the rising edge is gp41-controlled, the falling edge is not. As a consequence, the rising edge must correspond to gp41 unwinding the duplex, whereas the falling edge must correspond to the spontaneous re-annealing of the two strands. It is highly unlikely that the two strands re-hybridize around the helicase. We therefore conclude that the first type of event corresponds to gp41 unwinding the duplex, then dissociating from its DNA substrate, allowing the two DNA strands to re-anneal, refolding the hairpin completely.

The second type of event displays a slowly rising edge until the maximum DNA extension (i.e., fully unwound hairpin) followed by a slowly falling edge (Fig. 9D) and E)). These events all display full-length unwinding of the duplex. Both the rising and falling rates are dependent on the ATP concentration (although they are not necessarily equal, see Fig. 9E)). The slowly rising edge displays the same slope as the rising edge in the first type of event. We therefore conclude that it corresponds to gp41 unwinding the entire duplex. The falling edge must also correspond to gp41 activity because it is ATP dependent as well. It is highly unlikely that the falling edge is due to the presence of a second helicase since the probability of coincident binding of two helicases at low concentration is negligible, or that the helicase switches directionality at the center of the hairpin (previous experiments have shown that gp41 translocates with a 5′ to 3′ polarity [31]). It is also unlikely that gp41 could switch strands as reported for other helicases [34, 35], expect such events to occur randomly during unwinding and not only in situations with a fully unfolded hairpin. We therefore conclude that this type of event corresponds to the helicase unwinding the entire duplex and then translocating further on the ssDNA, thus blocking the spontaneous, rapid rehybridization of the two separated strands. As the helicase moves on the ssDNA, the fork is able to slowly close in its wake. Thus, the falling edge corresponds to the gp41 translocation-limited rezipping of the opened hairpin.

The unwinding rate v_U can be measured from the slope of the rising edge. We define the rezipping rate v_Z as the slope of the slowly falling edge. The rezipping velocity is ATP-concentration dependent (typically a few 100 bp/s) and can be readily distinguished from the fast, ATP-concentration independent spontaneous

rehybridization rate (typically a few 1000 bp/s). Whereas the unwinding rate increases with increasing force, the rezipping rate does not depend on the applied force (compare Fig. 9B vs. 9D; Fig. 9C vs. 9E).

5.2. gp41 rezipping rate is equal to its ssDNA translocation rate

During the rezipping phase, the enzyme translocates on ssDNA, while the fork closes in its wake. Is this situation different from gp41 translocating alone on ssDNA? The fork closing behind the enzyme might alter the enzyme translocation rate in two possible, but not mutually exclusive ways: first, the pairing energy gained by the fork while it is closing might provide an effective driving force to the translocating helicase; and second, the mere presence of the fork in the vicinity of gp41 might affect its velocity.

We addressed the first point by measuring the gp41 rezipping rate v_Z as a function of force. At low force ($F \approx 3$pN), the folded hairpin is highly stable; therefore, the potential driving force exerted by the fork should be the greatest. In contrast, when approaching the mechanical unfolding transition ($F \approx 12$ pN), the effective driving force should approach zero since the paired and unpaired forms of the hairpin are equally stable at the transition. Therefore, one would expect significant changes in the driving force between 3 and 12 pN that should reflect on v_Z. We find that the rezipping rate v_Z does not depend on the force exerted (compare Fig. 9C and 9E; Fig. 10A). Therefore, we conclude that the pushing action of the closing fork due to the energy gain upon base-pairing is negligible.

To address the influence of the presence of the fork behind gp41, we performed the following experiment: we increased the force to a value close to the unfolding transition. In this regime, the folded hairpin is stable on the timescale of the experiment; however, if previously unfolded, the spontaneous rehybridization of the two strands does not take place immediately, but after a fraction of a second. We then recorded gp41 unwinding events. In addition to the two main types of events described above, we observed a third type (Fig. 10B). After a careful evaluation of the other potential interpretations for these events, we dismissed them and concluded that these events correspond to a single enzyme unwinding dsDNA (i) and continuing to translocate on ssDNA, first without any fork behind it (ii and iii), then with the fork closing in its wake (iv) (Fig. 10C). We can measure the rezipping rate during these events as the slope of the extension time trace during phase (iv). In contrast, the translocation of the enzyme on the stretched ssDNA does not change its extension; however, we can estimate this rate as the ratio of the distance traveled divided by the time the hairpin remains unfolded ($\delta L/\delta t$ on Fig. 10C, (ii)/(iii)). We then compared the rates of translocation on ssDNA with or without a fork closing behind the helicase. In the conditions explored ($F > 7$ pN; 0.5 mM $\leq$ [ATP] $\leq$ 5 mM) the mean rates are similar (Fig. 10D) differing by only 5% (S.D. 20% $N = 10$ events).

We therefore conclude that the rezipping rate is equal to the ssDNA translocation rate. As a consequence, we can measure the dsDNA unwinding rate and the ssDNA translocation rate under the exact same conditions to quantify how

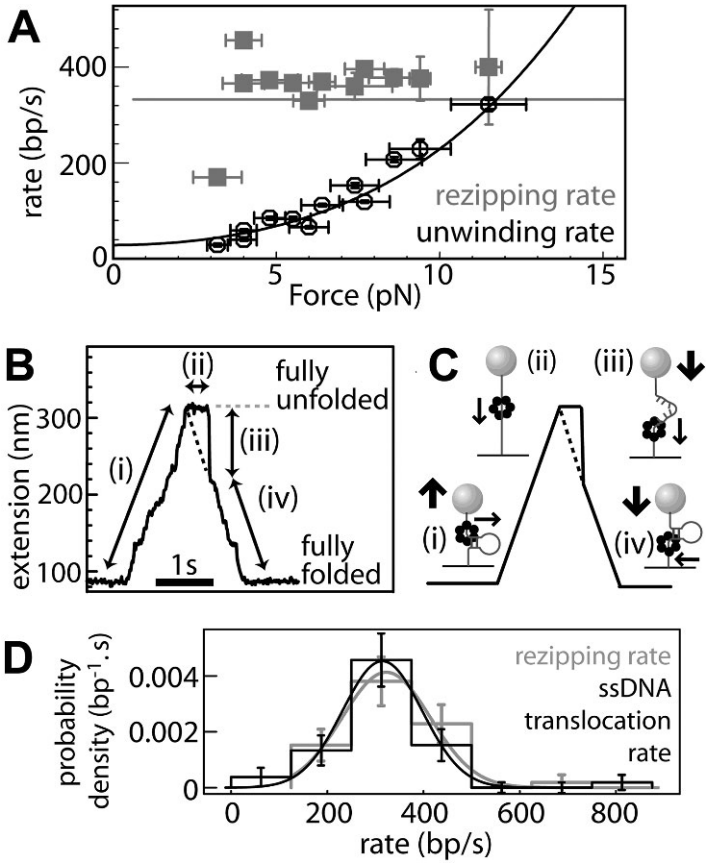

FIGURE 10. Third type of gp41 unwinding events occurring when the force is approaching the unzipping force. In this situation, once the hairpin is open, it refolds after some latency (typically one second). During that time the gp41 helicase travels on single stranded DNA. When the hairpin finally refolds, the refolding fork progresses very rapidly until it bumps into the helicase. Then, the hairpin closing is controlled by gp41 translocation. We find that the gp41 rezipping rate equals its ssDNA translocation rate.

gp41 slows down while unwinding dsDNA as compared to when it translocates on ssDNA. These measurements, performed as a function of force and ATP concentration, provide us with a set of data amenable to test various helicase mechanisms.

5.3. ssDNA translocation does not involve cooperative ATP hydrolysis

We first characterized the ssDNA translocation rate dependency on ATP. For each ATP concentration, we obtained the ssDNA translocation rate as the average of

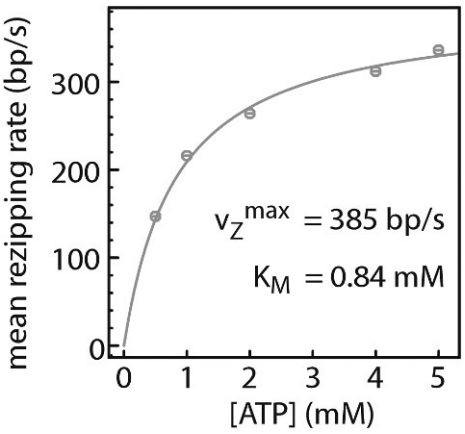

FIGURE 11. The rezipping rate versus the concentration of [ATP] follows a first-order Michaeli-Menten law. The rezipping rate increases linearly with the ATP concentration; at low value it saturates when [ATP] approaches the mM concentration. This rezipping rate is independent of the force applied on the hairpin.

the force-independent rezipping rates (Fig. 3). The resulting ssDNA translocation velocity vs. ATP concentration curve was fit to the Michaelis-Menten equation, $\langle |vZ| \rangle = v_Z \max[ATP]/(Km + [ATP])$, with a maximum velocity (v_Z max) of 400 ± 10 bp/s and Km of 1.1 ± 0.1 mM. The observed non-sigmoidal kinetics rule out a translocation mechanism involving simultaneous ATP hydrolysis by the six helicase monomers, but cannot distinguish between independent or cooperative ATP binding. Based on this result, we have modeled gp41 translocation on ssDNA involving a reversible ATP binding step followed by an irreversible translocation event (Fig. 13A)).

5.4. gp41 a passive helicase

Next, we measured the dsDNA unwinding rate v_U as a function of applied force and ATP (Fig. 12). The unwinding rate increases continuously with increasing force and ATP concentration. The maximum unwinding velocity measured at the critical force where the hairpin is marginally stable ($F \approx 12$pN) agrees with the translocation velocity on ssDNA (Fig. 10A) at the same ATP concentration.

We have represented these results using a simple global model for helicase activity on ssDNA and dsDNA [36]. We assume that the enzyme first binds ATP reversibly and that translocation is coupled to ATP hydrolysis. In the case of ssDNA translocation, the enzyme step size is n bp and occurs with rate k_+ (Fig. 13A)). In the case of dsDNA unwinding (Fig. 13B)), the fork must open by n bp prior to translocation. The kinetics of fork opening/closing depend on the

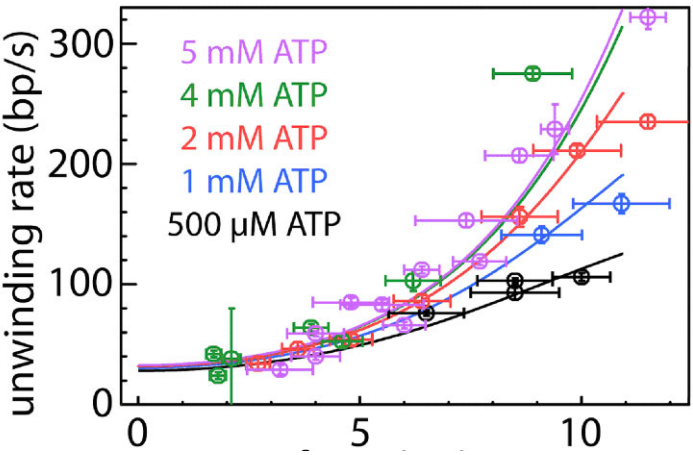

FIGURE 12. The unzipping rate of the gp41 helicase versus force at various [ATP] concentration. This rate corresponds to the velocity of the helicase when unwinding the dsDNA. Notice that this rate depends very strongly on the force applied to the hairpin as well as the [ATP] concentration. A fit to the force dependence is compatible with an exponential suggesting that the rate may be described by an Arrhenius process.

force exerted to open the hairpin and the active/passive character of the helicase. Finally, translocation by n bases takes place with the same rate k_+ as on ssDNA.

The active/passive nature of the helicase is introduced into the model through the fork opening and closing rates, α and β respectively, following a recent model [37, 38]. Briefly, if the enzyme is passive, the opening/closing kinetics of the fork are unaffected by the presence of the helicase. In contrast, an active helicase directly destabilizes the double helix. As a result, α and β depend on the position of the enzyme relative to the fork. When the enzyme is at the fork, the opening step is favored over the closing one. This is modeled by lowering the energy of unpairing at the fork (i.e., the equilibrium constant α/β) by a fixed amount when the enzyme is within n bp of the fork. The amount of energy devoted by the enzyme to the destabilization of the junction constitutes a measure of the active character of the enzyme. We have assumed that the base pairing energy is homogeneous, thus neglecting sequence effects. To preserve generality, we use a simple version of the model assuming that destabilization by the helicase occurs on the range of its step size and neglecting activation barrier position effects. We have been able to determine that the gp41 mechanism was mostly passive [36], the energy of the helicase involved in fork destabilization being equal to 0.15 k_BT, while that involved in melting one base pair is $\approx 2k_BT$.

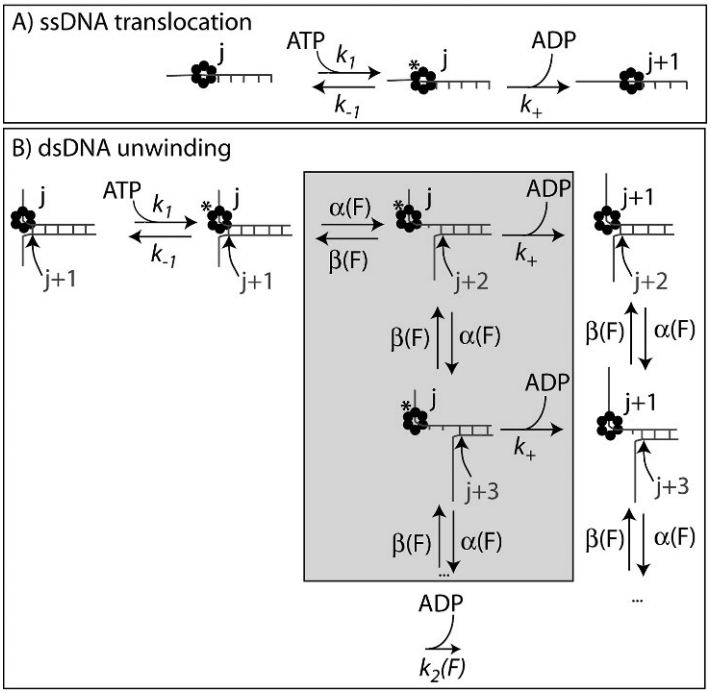

FIGURE 13. Models describing the various states involved during the gp41 helicase translocation.

A) when the substrate is only ssDNA, the motion is only dependent on the ATP binding and hydrolysis.

B) when unwinding a real dsDNA the mechanism involves more states.

In the passive model, after ATP binding, the spontaneous opening of the DNA fork upon thermal fluctuations offers the helicase an opportunity to quickly move forward. In the active model the helicase destabilizes the DNA fork and opens it by melting the base pairing of the nucleotide $j + 1$ at the fork. All those processes may be described by appropriate chemical rate constants k_i.

6. Behaviour of the primosome: coupling activity of the helicase and the primase

Here we focus on the study of the primosome and the interactions between the helicase and primase during primer synthesis. The primosome is known to play a crucial role in coupling leading and lagging strand DNA synthesis: the helicase unwinds the DNA for the leading strand holoenzyme and the primase repetitively primes the lagging strand for Okazaki fragment synthesis by the lagging strand holoenzyme. The two proteins clearly form a complex since both proteins enhance

the activity of the other [25, 39, 40]; however the helicase translocates 5′ to 3′ on the lagging strand and the primase must travel in the opposite direction (3′ to 5′) in order to synthesize an RNA primer.

6.1. Models of primosome behavior during primer synthesis

Three different models are possible for the coupling activities of the helicase and the primase (see Fig. 14). In the pausing model the helicase stops to allow the primase to synthesize a primer. The unwinding and the leading strand synthesis are then interrupted each time that a new primer is synthesized. This is the behavior observed in the T7 bacteriophage replisome [41]. In the disassembly model one or more subunits of primase dissociate from the hexameric helicase during priming, allowing the unwinding and leading strand synthesis to occur continuously. However new primase subunits might need to be recruited at each cycle of Okazaki

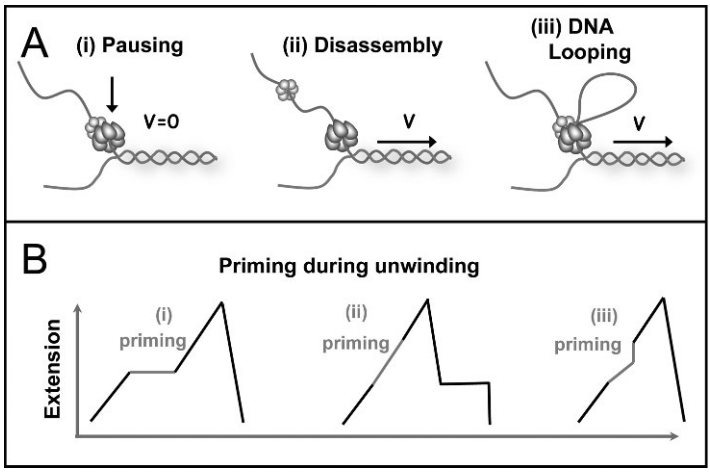

FIGURE 14. (A) Schematic representation of three possible models for helicase and primase interaction during primer synthesis:
(i) in the pausing model the helicase and primase temporarily stop translocating during priming;
(ii) in the disassembly model the primase dissociates from the helicase to synthesize a primer while the helicase continues unwinding DNA;
(iii) in the DNA looping model the primosome remains intact and DNA unwound during priming forms a loop.
(B) Schematic representation of the real-time DNA extension traces expected for each of the three models.

fragment synthesis. Trapping experiments with an inactive primase protein have shown that the gp61 primase is distributive, suggesting that in the T4 system a new primase subunit may be recruited with initiation of each Okazaki fragment [42]. Finally, in the looping model the primosome remains intact during priming by looping the DNA that is being unwound by the helicase. After priming, the primosome can transfer the primer directly or indirectly to the lagging strand polymerase and release the lagging strand loop. This looping mechanism allows the helicase to continuously unwind the DNA but without dissociating from the primase.

6.2. Two priming mechanisms

We have performed experiments with both the gp41 and gp61 primase to investigate how these two enzymes couple their activities and motions. In the absence of rNTPs (a situation in which priming cannot occur), the results are indistinguishable from those obtained with the helicase alone (see Fig. 15): the enzymatic events

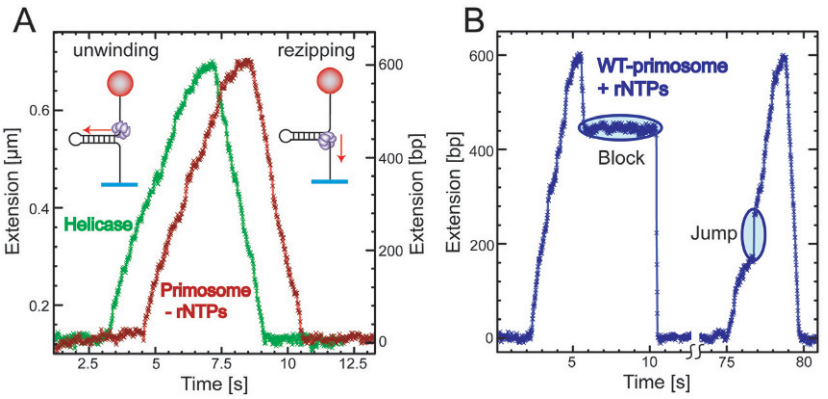

FIGURE 15. (A) Experimental traces corresponding to the gp41 helicase activity (green) and the wild-type primosome activity (red) on the S1 hairpin in the absence of rNTPs (B) Examples of two new features, blocks in hairpin reannealing and jumps in extension during unwinding, observed in experimental traces from wild-type primosome activity on a 600bps hairpin in the presence of 1 mM rNTPs.

start with a rising edge that is associated to the unwinding activity and end with a falling edge corresponding to the ssDNA translocation activity, followed by the rezipping of the hairpin. The unwinding and translocation velocity measured respectively from the unwinding and rezipping phases coincides with those measured in the experiments with the helicase alone. In contrast, in the presence of rNTPs

the enzymatic events present two new features: (i) the rezipping signal is strongly altered by the presence of blocks; (ii) once in a while a sudden extension increase (jump) is observed during the unwinding edge (see Fig. 15). These new features, blocks and jumps, are only observed in the presence of rNTPs and their frequency depends on the rNTP concentration [43]. As a result, the observed blocks during rezipping and jumps during unwinding are signatures of the priming activity of the primosome.

Using DNA substrates with specially designed sequences (showing available recognition priming sites only along one strand) we have established that priming can only occur during unwinding in our experimental configuration [43]. Probably priming during rezipping is inhibited by the reannealing of the hairpin behind the primosome, a situation which is also unnatural in a normal DNA replication fork where the DNA unwound by the helicase would be coated with ssDNA binding protein gp32. Therefore, the two different priming signatures (jumps during unwinding and blocks during rezipping) we observe are likely the result of two different priming mechanisms being employed by the primosome.

6.3. Primosome does not pause but disassembles

If the T4 primosome stopped during priming, this would result in the presence of pauses in the DNA unwinding traces. Long periods of no change in the DNA extension during unwinding were rare and their frequency was independent of the rNTP concentration, showing that they were not a signature of the priming activity. Moreover, these pauses occurred at the GC rich regions, suggesting that they corresponded to the slowing down of the helicase when encountering regions of high DNA stability. We then conclude that the T4 primosome does not pause during priming. In contrast, when rNTPs were present, long periods of no change in the DNA extension were frequently observed during the rezipping phase of the experimental traces. The frequency of such blocks increased upon rNTP concentration and their position along the sequence was correlated with the position of the priming sites in the lagging strand available during unwinding (see Fig. 16).

Overall these results show that the blocks observed during the rezipping phase are related to the priming activity during unwinding. Moreover the presence of blocks is predicted by the disassembly model (see Fig. 14). In that model during priming the primase dissociates from the helicase without altering the unwinding activity. The synthesized primer and/or some primase units might remain bound to the DNA, blocking the reannealing of the hairpin during the rezipping phase (see Fig. 16). The blocks in DNA rehybridization could be caused by the pentaribonucleotide primer itself, dissociated primase subunit(s), or a complex of the primase subunit(s) with the primer bound to the DNA hairpin. Several experiments were performed to investigate the nature of these blocks. Results suggest that blocks are generated by the primer/primase complex [43].

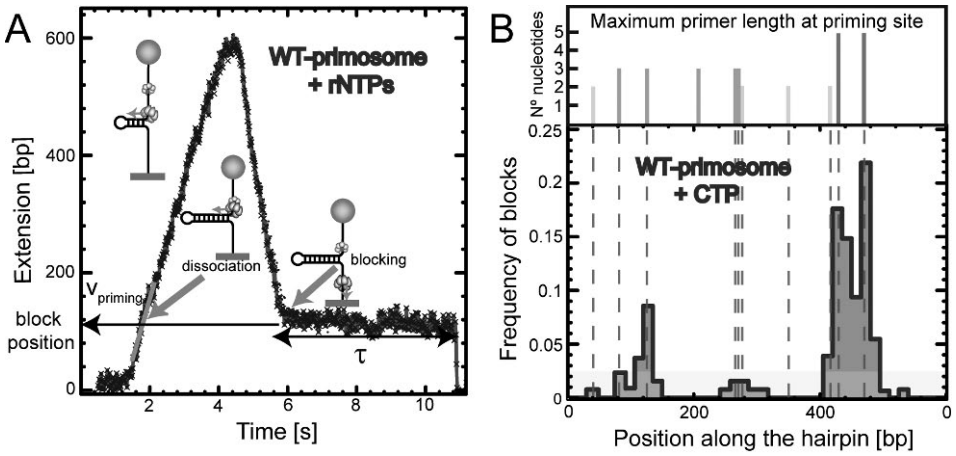

FIGURE 16. (A) Experimental trace displaying characteristics of the primosome disassembly model. The unwinding velocity during primer synthesis, the position of the priming site, and the lifetime of the block in hairpin rehybridization are indicated.

(B) Distribution of blocks plotted against the corresponding position along the hairpin substrate measured with wild-type primosome in the presence of CTP and ATP from 345 blocking events. The location of the priming sites available on the 5′ strand are indicated by dashed gray lines. The uniform light yellow distribution represents primase binding randomly along the DNA hairpin and not specifically at priming sites. The maximum primer length that may be synthesized at each priming site at the given rNTP conditions is shown in the upper panel.

6.4. Primosome activity by DNA looping

The other type of priming events, jumps during unwinding, can be explained neither by the disassembly nor by the pausing model, but by the DNA looping model. In this model, during priming the helicase continuously unwinds the DNA without dissociating from the primase. The unwound DNA in the lagging strand is then looped and released once priming is over. The release of an ssDNA loop that is formed during priming should provide a sudden increase of the molecular extension (see Fig. 14B). This signature is observed on the second type of priming events (see Fig. 15), revealing that priming can be carried out not only by primosome disassembly (which generates blocks during rezipping) but also by DNA looping (identified with extension jumps). During loop formation only one of the two strands of the unwound DNA contributes to the elongation of the measured molecular extension (see Fig. 17). Accordingly the apparent DNA unwinding velocity immediately prior to a sudden increase in the DNA extension is smaller than

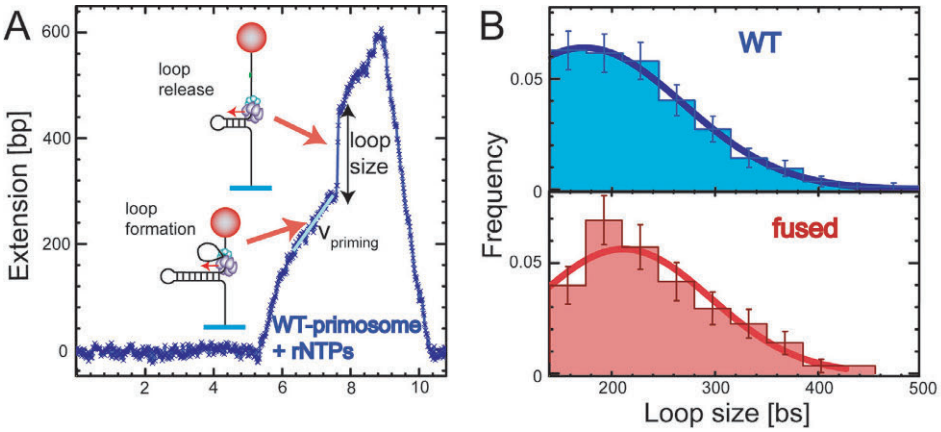

FIGURE 17. Experimental trace displaying characteristics of the DNA looping model. The unwinding velocity during primer synthesis and the loop size are indicated. Distribution of the DNA loop size for wild-type primosome (blue) and fused primosome (red) from 71 and 42 priming events involving loop formation, respectively. A minimum loop size of 140 nucleotides was used as a cutoff. Histograms are fit to a Gaussian function yielding a mean DNA loop size of 170 ± 20 and 210 ± 20 nucleotides for wild-type and fused primosome, respectively.

the DNA unwinding velocity when no looping occurs (see Fig. 17A). In particular its mean value is one-half of the mean DNA unwinding velocity [43]. This indicates that the primosome continues to unwind the DNA at a constant rate regardless of whether it is synthesizing a primer and consequently forming a DNA loop. As shown in Fig. 17B, the size of the loop follows a Gaussian distribution with a mean value of 250 nucleotides. Considering a mean unwinding velocity of 220 bp/s, the average time involved in loop formation and release is about 1 s. This value is consistent with the priming rate of 1 primer per second per replisome, which has been measured in bulk experiments [44].

Priming by DNA looping is infrequent, less than ten times less frequent than priming by primosome disassembly (see Fig. 18B). We then conclude that the primase processivity is very low in our experimental conditions: the primase mostly dissociates from the helicase during priming and hence the primosome rarely remains intact. In this latter case, disassembly of the primosome is prevented by DNA looping. Interestingly, experiments with a primosome consisting of a fused primase-helicase protein [43] works exclusively through a DNA looping model. In these experiments, in the absence of rNTPs, the detected activity is similar to the wild-type-gp41 activity. As rNTPs are added, the enzymatic events show the presence of jumps in extension during the unwinding phase (see Fig. 18A). In contrast to the wild-type experiments, the loops are frequently observed, the frequency being ten times larger than in the wild-type case (see Fig. 18B).

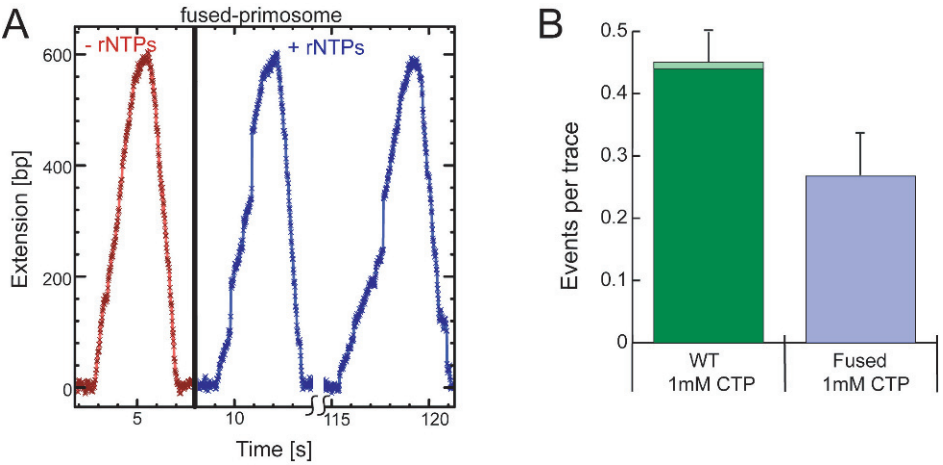

FIGURE 18. (A) Experimental traces corresponding to the fused primosome activity in absence (red) and presence of rNTPs (blue).
(B) Stacked histogram of the frequency of blocks in hairpin reannealing (dark green or blue) and jumps in extension during unwinding (light green or blue) measured in experiments with wild-type (green) and fused (blue) primosome in the presence of CTP on a 600 bps hairpin.
The frequency is calculated as the number of events per enzymatic trace, where an enzymatic trace is defined as a trace demonstrating complete unwinding and rezipping. The number of enzymatic traces analyzed for each condition is 447 and 169 in order.

6.5. Force does not hamper loop formation

When a pulling force is applied to stretch DNA, the primosome must work against it to form a loop during priming. We have performed low force experiments in order to investigate whether the applied force is preventing loop formation and/or favoring primosome disassembly. At low pulling force the signal to noise ratio is lower because the extension of ssDNA is short and the fluctuations in extension are large. 5 pN is the lowest force to which we can work and keep a good spatial resolution. Comparison between the results obtained at 9pN and 5pN with the wild-type-primosome show that the force does significantly affect neither the frequency of loop formation nor the frequency of the primase dissociation [43]. These results show that primosome disassembly and subsequent low primase processivity are not artifacts of our experimental approach, but they rather are an intrinsic property of the T4 wild-type-primosome. However, as suggested by recent bulk experiments [45], in the context of the full replisome other proteins might control the partitioning of these two mechanisms, preventing primosome disassembly thereby increasing primase processivity.

7. DNA synthesis

The gp43 is a monomeric polymerase that catalyzes the template-directed incorporation of dNTPs into the nascent DNA in both leading and lagging strand synthesis. However, leading and lagging strand synthesis require the presence of other replisomal proteins. In particular, only gp43 and gp41 are needed for leading strand synthesis [32] whereas the full replisome must be assembled for lagging strand synthesis. Nevertheless, the polymerase can perform chain elongation on ssDNA templates without gp41. Gp43 alone is not very efficient, but together with the three T4 polymerase accessory proteins (gp44/62 and gp45) becomes a highly processive enzyme [46]. The complex formed by the polymerase and the gp45 clamp, called the holoenzyme, is assembled and loaded by the gp44/62 clamp-loader [22, 23]. The holoenzyme alone can also carry out strand displacement activity on dsDNA templates, but its leading strand synthesis rate (10bp/s) is about 30 times slower than when gp41 is present [32, 33].

7.1. Measuring strand displacement synthesis and chain extension activity on ssDNA

The DNA substrates to study polymerase activity are the same as those used for the helicase and primosome assays: DNA hairpins of different lengths (from 1,2 to 7Kbp) aiming to mimic a replication fork. Since gp43 requires a DNA or RNA primer to start the polymerization reaction, the different DNA hairpins have a dsDNA tail at the 3′ end (see Fig. 19A). The latter can be used as a primer allowing the polymerase to initiate leading strand synthesis. Interestingly, these DNA substrates allow us to study not only strand displacement polymerase activity but also the activity on ssDNA. The first part of the synthesis corresponds to strand displacement activity, since the polymerase needs to displace the lagging strand in order to extend the dsDNA tail primer. Moreover, in the absence of lagging strand synthesis a second phase is possible. The latter corresponds to the polymerase reaching the end of the hairpin and copying the rest of the ssDNA substrate (see Fig. 19B). The strand displacement phase should produce an increase in the substrate extension, corresponding to the gain of one bp on the 3′ tail and one ssDNA base on the 5′ tail for each base added. The second phase, corresponding to the conversion of ssDNA to dsDNA, might have a different signature depending on the force applied. ssDNA is longer than dsDNA above 5pN and shorter below (see Fig. 5). Therefore the polymerase activity on ssDNA should result in an increase on extension at high forces (above 5pN) and a decrease on extension at low forces (below 5pN), as shown in Fig. 19B.

7.2. Polymerase and holoenzyme activities

By injecting gp43 and NTPs into the chamber, some polymerase activity could be detected at high enough forces (higher than 7pN) (see green trace in Fig. 20). By using the previously measured elasticity of ssDNA and dsDNA molecules (see Fig. 5) we can estimate the rates of DNA synthesis. The polymerization rate either during strand displacement or during primer extension on ssDNA was much

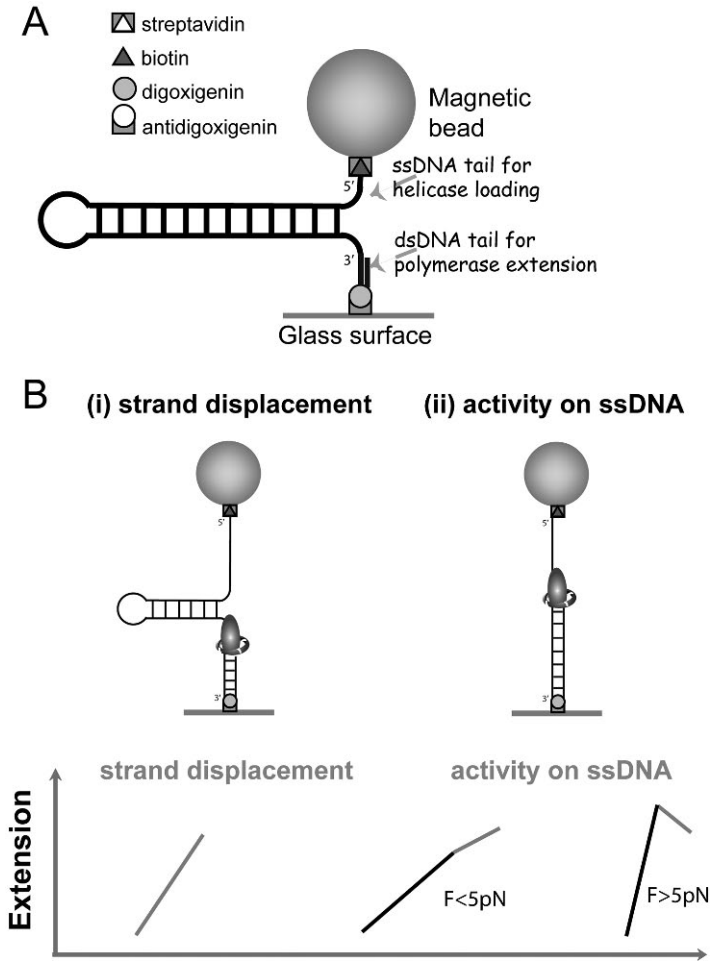

FIGURE 19. (A) Schematic representation of the DNA hairpin substrate used in polymerase assays, having a 5′-biotinylated ssDNA tail, and a 3′-digoxigenin labeled dsDNA tail. The DNA hairpin is specifically attached to the magnetic bead coated with streptavidin and to the glass surface treated with anti-digoxigenin antibody.

(B) Two phases of polymerase activity can be studied. The first phase corresponds to the strand displacement activity and can be identified with the initial increase in DNA extension. The second phase corresponds to the DNA chain extension on ssDNA and it can be identified with the final increase (decrease) in DNA length at forces larger (smaller) than 5pN.

lower than the replication rate of the full replisome measured in bulk experiments [32, 33]. Moreover, long pauses were frequently observed, suggesting that the processivity of the enzyme was very low (few bases). In the presence of the clamp and clamp loader the rates measured in the two phases of polymerization (strand displacement and synthesis on ssDNA template) were much higher, but still lower than the 300–400bp/s expected for replication fork advance [32, 33]. The rate during strand displacement was extremely sensitive to the value of the applied force, its value changing by two orders of magnitude when varying the force from 10pN to 4pN (see blue traces in Fig. 20).

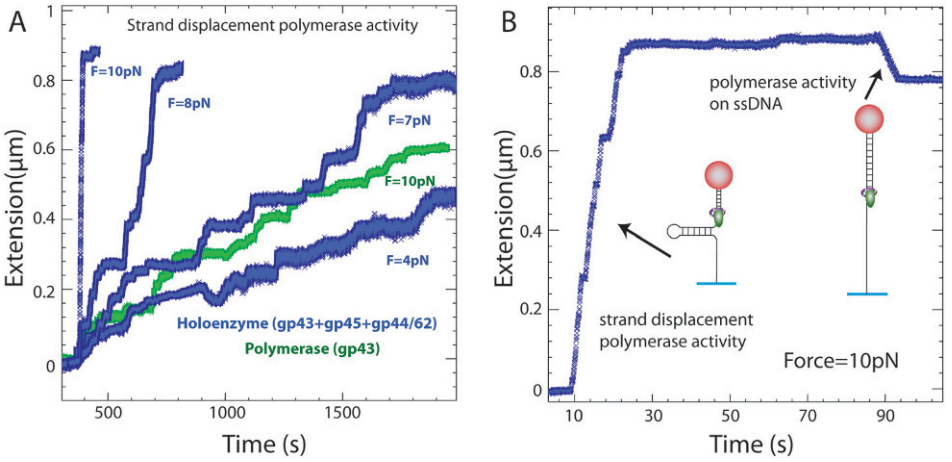

FIGURE 20. (A) Experimental traces corresponding to the strand displacement activity of the gp43 polymerase (green) and holoenzyme (blue) in presence of 500 μM NTPs. Results for the gp43 polymerase are obtained at 10pN of applied force. Different trajectories for the holoenzyme correspond at different forces, ranging from 4pN to 10pN.
(B) Trace corresponding to the full synthesis of the DNA substrate, containing the strand displacement phase and the ssDNA activity phase, catalyzed by the holoenzyme at 10pN of applied force.

The work required to open a bp at a given force F is given by $W = \Delta G - \int_0^F x(f)df$, where ΔG is the base pair energy and $x(f)$ is the extension of 2 nucleotides of ssDNA stretched by a force f. The work W corresponds to the energy barrier that the polymerase needs to overcome for incorporating one base during strand displacement activity. Accordingly, we find that higher forces result in larger polymerization rates. Thus we conclude that the force applied to the ends of the molecule helps the progress of the polymerase by destabilizing the base pair at the fork and decreasing the energy barrier for polymerase advance. On the contrary,

the rate of polymerase activity on ssDNA was force-independent at the range of forces studied (between 4pN and 16pN).

7.3. Leading strand synthesis: coupling helicase and polymerase activities

Coupled helicase and polymerase activity to perform leading strand synthesis was observed in the presence of holoenzyme, helicase, ATP and dNTPs (see Fig. 21A). In general, better activity was observed at low forces (between 2pN and 5pN). At high forces, most of the time the two enzymes worked in uncoupled mode (traces show separate helicase and polymerase activity, see Fig. 21B). As expected the polymerization rate observed in the coupled gp41-gp43 activity was independent of the applied force and agrees with the values of the replication rate measured in bulk assays [32, 33]. Interestingly, at the range of forces where coupled activity is observed (between 2 and 7pN) the measured polymerization rate is higher than that of the helicase or the holoenzyme alone. Moreover pauses are observed very rarely, suggesting that the processivity of the gp41-gp43 complex is very high (larger than 1kbp). In other words, the coupling between these two enzymes (direct or indirect) enhances both helicase and polymerase activities.

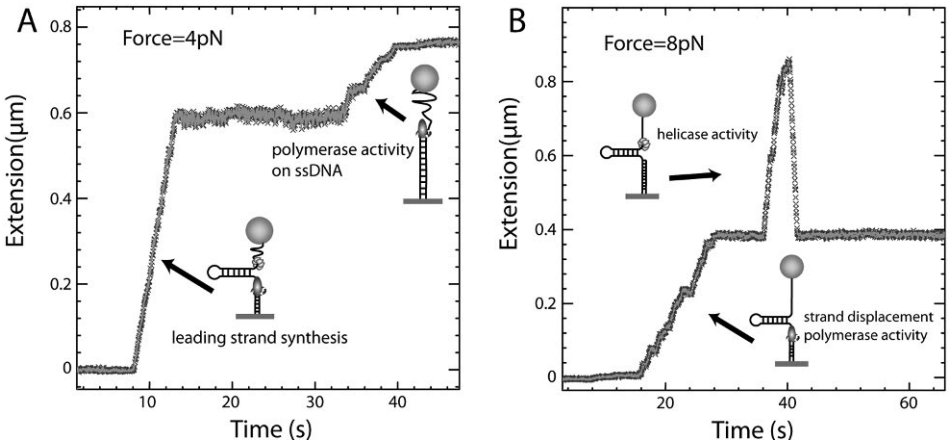

FIGURE 21. (A) Experimental trace corresponding to the leading strand synthesis carried out by the helicase and holoenzyme in the presence of ATP and NTPs and at 4pN of applied force.
(B) Experimental trace showing the uncoupled activity of the helicase and polymerase observed at high forces.

8. Conclusions

DNA replication is a complex process involving a large number of proteins. In this paper, we have used magnetic tweezers to investigate the replisome of the T4 bacteriophage. The T4 replisome is formed by eight different proteins that work in a very coordinated fashion in order to copy the T4 genome at high speed (300bp/s) and with a high processivity (larger than the size of the genome, 180Kbp). Our approach does not allow us to directly visualize the different proteins of the replisome but only to measure their overall activity as a change in the conformation of the DNA molecule that is being replicated. How from these measurements can one obtain information about the functioning of the replisome? Can one investigate the interaction between the different replisomal proteins that allow the progress of the replication fork and coordinate the DNA synthesis in the leading and lagging strands? Our strategy consists of first characterizing the activities of the different replisomal proteins separately. Next the behaviour of sub-assemblies of different parts of the replisome is investigated. In this way we attempt to build up the full replisome by increasing, step by step, the complexity of the system studied.

The activities of the gp41 helicase and the gp43 polymerase alone on a DNA hairpin have been extensively characterized. Both enzymes work fast and processively only at high force. In contrast, at low force their activity is more than 10 times slower than the rate of movement of the replication fork as measured in bulk assays [32, 33]. Comparison of the experimental results with models have shown that gp41 unwinds DNA as a passive helicase [36]; that is it does not actively destabilize the double helix but it works as an ssDNA translocase trapping the spontaneous opening fluctuations of the fork (3–5). These results show that both helicase and polymerase need other replisomal partners in order to reach their full speed.

We have next studied the primosome, formed by the helicase and primase, which is responsible for DNA unwinding and initiation of Okazaki fragments. Our results show that the T4 primosome continuously unwinds the DNA duplex while allowing for primer synthesis through a primosome disassembly or a DNA looping mechanism [43]. The activity of the holoenzyme, responsible for the processive DNA polymerization, can also be observed when the polymerase, clamp and clamp loader are studied together. Their speed and processivity are larger than those of the polymerase alone but still much lower (especially at low force) than those expected by the full replisome. Interestingly, efficient leading strand synthesis is observed when the holoenzyme and helicase are brought together at low force. The coupling between polymerase and helicase enhances both unwinding and polymerization activities, since the measured rate of synthesis at low forces is much higher than either the unwinding rate of the helicase or the polymerization rate of the holoenzyme alone. Addition of the primase and the single-stranded binding protein might allow us to form the full replisome and study the coordination between leading and lagging strand synthesis.

In this paper we have seen how one of the new tools of single molecule manipulation (magnetic tweezers) can be applied to the study of the enzymes involved

in DNA replication. The level of precision and detail of these experiments is often unmatched by bulk assays. These techniques allow one to generalize to a large class of enzymes the approach applied successfully and for many years to the study of ion channels. We have hereby only described one aspect of recent single molecule studies, those involving their manipulation. Another equally exciting and powerful approach is using single molecule fluorescence and fluorescence resonant energy transfer (FRET) to monitor the motion of a single enzyme on its substrate [47] and its internal conformational changes [48] with nanometer accuracy and millisecond time resolution [49]. Combining both approaches [50] will provide new opportunities for single molecule enzymology, where all (or most) of the parameters characteristic of a single molecular motor will be measured simultaneously (its rate, processivity, step-size, work done and number of ATP molecules consumed per cycle [51]). The characterization of the dynamic feature of an enzyme together with its static crystallographic data should provide an (almost) complete picture of its mechanism.

Acknowledgment

We thank our collaborators on the presented works: M.M. Spiering, S.J. Benkovic. This work was supported by grants from HFSP, ANR, and the EEC under the "BioNanoSwitch" program.

References

[1] C. Bustamante, S.B. Smith, J. Liphardt and D. Smith, *Single-molecule studies of DNA mechanics*, Curr. Op. Structural Biology **10** (2000), 279–285.

[2] T.R. Strick, M.-N. Dessinges, G. Charvin, N.H. Dekker, J.-F. Allemand, D. Bensimon, and V. Croquette, *Stretching of macromolecules and proteins*, Rep. Prog. Phys. **66** (2003), 1–45.

[3] G. Lia, D. Bensimon, V. Croquette, J.F. Allemand, D. Dunlap, D.E.A. Lewis, S. Adhya, and L. Finzi, *Supercoiling and denaturation in gal repressor-heat unstable nucleoid protein (hu)-mediated dna looping*, Proc. Natl. Acad. Sci. (USA) **100** (2003), 11373–11377.

[4] J. Liphardt, B. Onoa, S.B. Smith, I. Tinoco Jr., and C. Bustamante, *Reversible unfolding of single RNA molecules by mechanical force*, Science **292** (2001), 733–737.

[5] J.F. Marko and E.D. Siggia, *Driving proteins off DNA using applied tension*, Biophys. J. **73** (1997), 2173–2178.

[6] A. Engel and H.E. Gaub and D.J. Müller, *Atomic force microscopy: A forceful way with single molecules*, Curr. Biol. **9** (1999), pp. R133–R136.

[7] E. Evans and K. Ritchie, *Dynamic Strength of Molecular Adhesion Bonds*, Biophysical Journal **72** (1997), pp. 1541–1555.

[8] P. Cluzel, A. Lebrun, C. Heller, R. Lavery, J.-L. Viovy, D. Chatenay and F. Caron, *DNA: an extensible molecule*, Science **271** (1996), pp. 792–794.

[9] S.B. Smith, L. Finzi and C. Bustamante, *Direct Mechanical Measurements of the Elasticity of Single DNA Molecules by using Magnetic Beads*, Science **258** (1992), pp. 1122–1126.

[10] S. Chu, *Laser manipulation of atoms and particles*, Science **253** (1991), pp. 861–866.

[11] J.-F. Allemand, T. Strick, V. Croquette, and D. Bensimon, *Twisting and stretching single dna molecules*, Prog. Biophys. Molec. Biol. **74** (2000), 115–140.

[12] F. Gittes and C.F. Schmidt, *Signals and noise in micromechanical measurements*, Methods in Cell Biology **55** (1998), 129–156.

[13] J.-F. Allemand, D. Bensimon, R. Lavery, and V. Croquette, *Stretched and overwound DNA form a Pauling-like structure with exposed bases*, Proc. Natl. Acad. Sci. USA **95** (1998), 14152–14157.

[14] M.-N. Dessinges, B. Maier, Y. Zhang, M. Peliti, D. Bensimon, and V. Croquette, *Stretching ssdna, a model polyelectrolyte*, Phys. Rev. Lett. **89** (2002), 248102.

[15] J.F. Marko and E. Siggia, *Statistical mechanics of supercoiled DNA*, Phys. Rev. E **52(3)** (1995), 2912–2938.

[16] C. Bouchiat, M.D. Wang, S.M. Block, J.-F. Allemand, T.R. Strick, and V. Croquette, *Estimating the persistence length of a worm-like chain molecule from force-extension measurements*, Biophys. J. **76** (1999), 409–413.

[17] T. Strick, J.-F. Allemand, D. Bensimon, and V. Croquette, *The behavior of supercoiled DNA*, Biophys. J. **74** (1998), 2016–2028.

[18] C.C. Richardson, Cell **33** (1983), 315–317.

[19] S.P. Bell, and A. Dutta, *DNA replication in eukaryotic cells*, Annu. Rev. Biochem. **71** (2002), 333–374.

[20] S.J. Benkovic, A.M. Valentine, and F. Salinas, *Replisome-mediated DNA replication*, Annu. Rev. Biochem. **70** (2001), 181–208.

[21] C.F. Morris, N.K. Sinha, and B.M. Alberts, *Reconstruction of bacteriophage T4 DNA replication apparatus from purified components: rolling circle replication following de novo chain initiation on a single-stranded circular DNA template*, Proc. Natl. Acad. Sci. USA **72** (1975), 4800–4804.

[22] C.C. Huang, J.E. Hearst, and B.M. Alberts, *Two types of replication proteins increase the rate at which T4 DNA polymerase traverses the helical regions in a single-stranded DNA template*, J. Biol. Chem. **256** (1981), 4087–4094.

[23] B.F. Kaboord, and S.J. Benkovic, *Accessory proteins function as matchmakers in the assembly of the T4 DNA polymerase holoenzyme*, Curr. Biol. **5** (1995), 149–157.

[24] C.C. Liu, and B.M. Alberts, *Characterization of the DNA-dependent GTPase activity of T4 gene 41 protein, an essential component of the T4 bacteriophage DNA replication apparatus*, J. Biol. Chem. **256** (1981), 2813–2820.

[25] D.M. Hinton, and N.G. Nossal, *Bacteriophage T4 DNA primase-helicase. Characterization of oligomer synthesis by T4 61 protein alone and in conjunction with T4 41 protein*, J. Biol. Chem. **262** (1987), 10873–10878.

[26] J. Yang, J. Xi, Z. Zhuang, and S.J. Benkovic, *The oligomeric T4 primase is the functional form during replication*, J. Biol. Chem. **280** (2005), 25416–25423.

[27] P.D. Chastain, 2nd, A.M. Makhov, N.G. Nossal, and J. Griffith, *Architecture of the replication complex and DNA loops at the fork generated by the bacteriophage t4 proteins*, J. Biol. Chem. **278** (2003), 21276–21285.

[28] J. Barry, and B. Alberts, *Purification and characterization of bacteriophage T4 gene* 59 *protein. A DNA helicase assembly protein involved in DNA replication*, J. Biol. Chem. **269** (1994), 33049–33062.

[29] K.D. Raney, T.E. Carver, and S.J. Benkovic, *Stoichiometry and DNA unwinding by the bacteriophage T4* 41:59 *helicase*, J. Biol. Chem. **271** (1996), 14074–14081.

[30] F. Dong, E.P. Gogol, P.H. von Hippel, J. Biol. Chem. **270** (1995), 7462–7473.

[31] M. Venkatesan, L.L. Silver, and N.G. Nossal, J. Biol. Chem. **257** (1982), 12426–34.

[32] F. Dong, S.E. Weitzel, P.H. von Hippel, Proc. Natl. Acad. Sci. U S A **93** (1996), 14456–14461.

[33] F. Salinas, and S.J Benkovic, Proc. Natl. Acad. Sci. U S A **97** (2001), 7196–7201.

[34] M.N. Dessinges, T. Lionnet, X.G. Xi, D. Bensimon, and V. Croquette, *Single molecule assay reveals strand switching and enhanced processivity of uvrd*, Proc. Natl. Acad. Sci. U S A **101** (2004), 6439–44.

[35] D. S., L., B. Johnson, B.Y. Smith, S.S. Patel, and M.D. Wang, Cell **129** (2007), 1299–1309.

[36] T. Lionnet, M.M. Spiering, S.J. Benkovic, D. Bensimon, and V. Croquette, *Real-time observation of bacteriophage T4 gp*41 *helicase reveals an unwinding mechanism*, Proc. Natl. Acad. Sci. USA **104** (2007), 19790–19795.

[37] M.D. Betterton, and F. Julicher, Phys. Rev. Lett. **91** (2003), 258103.

[38] M.D. Betterton, and F. Julicher, Phys. Rev. E Stat. Nonlin. Soft Matter Phys. **71** (2005), 011904.

[39] R.W. Richardson, and N.G. Nossal, *Characterization of the bacteriophage T4 gene* 41 *DNA helicase*, J. Biol. Chem. **264** (1989), 4725–4731.

[40] T.A. Cha, and B.M. Alberts, *Effects of the bacteriophage T4 gene* 41 *and gene* 32 *proteins on RNA primer synthesis: coupling of leading- and lagging-strand DNA synthesis at a replication fork*, Biochemistry **29** (1990), 1791–1798.

[41] J.B. Lee, R.K. Hite, S.M. Hamdan, X.S. Xie, C.C. Richardson, and A.M. van Oijen, Nature **439** (2006), 621–624.

[42] M.A. Trakselis, R.M. Roccasecca, J. Yang, A.M. Valentine, and S.J. Benkovic, J. Biol. Chem. **278** (2004), 49839–49849.

[43] M. Manosas, M.M. Spiering, Z. Zhuang, S.J. Benkovic, and V. Croquette, unpublished.

[44] A.M. Valentine, F.T. Ishmael, V.K. Shier, and S.J. Benkovic, Biochemistry **40** (2001), 15074–15085.

[45] S.W. Nelson, R. Kumar, and S.J. Benkovic, *RNA primer handoff in bacteriophage T4 DNA replication: The role of single-stranded DNA binding protein and polymerase accessory proteins*, J. Biol. Chem. **283** (2008), 22838–22846.

[46] T.A. Cha, and B.M. Alberts, J. Biol. Chem. **264** (1989), 12220–12225.

[47] A. Yildiz, J.N. Forkey, S.A. McKinney, T. Ha, Y.E. Goldman, and P.R. Selvin, *Myosin v walks hand-over-hand: single fluorophore imaging with* 1.5 *nm localization*, Science **300** (2003), 2061–2065.

[48] X. Zhuang, L.E. Bartley, H.P. Babcock, R. Russel, T. Ha, D. Herschlag, and S. Chu, Science **288**(2000), 2048–2051.

[49] S. Weiss, *Fluorescence spectroscopy of single biomolecules*, Science **283** (1999), 1676–1683.

[50] T. Funatsu, Y. Harada, M. Tokunaga, K. Saito, and T. Yanagida, *Imaging of single fluorescent molecules and individual ATP turnovers by single myosin molecules in aqueous solution*, Nature **374** (1995), 555–559.

[51] A. Ishijima, H. Kojima, T. Funatsu, M. Tokunaga, H. Higuchi, H. Tanaka, T. Yanagida, Cell **92** (1998), 161–171.

M. Manosas, T. Lionnet, E. Praly, D. Fangyuan,
J.-F. Allemand, D. Bensimon and V. Croquette
LPS, ENS
UMR 8550 CNRS
24, rue Lhomond
75231 Paris Cedex 05, France
e-mail: Vincent.Croquette@lps.ens.fr

Evolution of Biological Complexity

Raymond E. Goldstein

Abstract. It is a general rule of nature that larger organisms are more complex, at least as measured by the number of distinct types of cells present. This reflects the fitness advantage conferred by a division of labor among specialized cells over homogeneous totipotency. Yet, increasing size has both costs and benefits, and the search for understanding the driving forces behind the evolution of multicellularity is becoming a very active area of research. This article presents an overview of recent experimental and theoretical work aimed at understanding this biological problem from the perspective of physics. For a class of model organisms, the Volvocine green algae, an emerging hypothesis connects the transition from organisms with totipotent cells to those with terminal germ-soma differentiation to the competition between diffusion and fluid advection created by beating flagella. A number of challenging problems in fluid dynamics, nonlinear dynamics, and control theory emerge when one probes the workings of the simplest multicellular organisms.

1. Introduction

One of the most fundamental issues in evolutionary biology is the transition from unicellularity to multicellularity, in which basic questions concern the fitness advantages conferred by increasing size and specialization [1, 2, 3, 4, 5]. To put this question in perspective, consider the data shown in Fig. 1, originally presented by Bell and Mooers [6] and discussed more recently by Bonner [3]. Unicellular organisms, which of course do all the functions of life with one cell type, reside at the lower left corner of this graph, while humans, with approximately 210 distinct cell types and 10^{14} cells, are at the upper right. Clearly, there is a general trend that organisms with larger total numbers of cells have more cell types, but there are wide variations among the different groups of organisms, and one would be hard-pressed to look for some precise mathematical scaling in this data. Instead, let us look at the most elementary steps along the path toward biological complexity: the transition from single cell organisms to those with just two distinct cell types.

B. Duplantier and V. Rivasseau (eds.), *Biological Physics*, Progress in Mathematical Physics 60,
DOI 10.1007/978-3-0346-0428-4_6,

Not surprisingly for microorganisms living in an aqueous environment, many of the key biological processes involved with this transition involve transport and mixing, for the efficient exchange of nutrients and metabolites with the environment is one of the most basic features of life [7]. In the conventional biological view, diffusion dominates over transport by fluid advection, as quantified by the Péclet number [8]

$$Pe = \frac{UL}{D} \ , \tag{1}$$

where U is a characteristic fluid velocity, L is a typical length scale, and D is the molecular diffusion constant of interest (typically 10^{-5} cm^2/s for small molecules such as oxygen, and varying inversely with size). The low Pe number world is most appropriate to small individual organisms such as bacteria [9], where $L \sim 10^{-4}$ cm and $U \sim 10^{-3}$ cm/s, so $Pe \sim 10^{-2}$. Such is generally not the case for multicellular organisms whose size L and swimming speed U are considerably larger. In a nutshell, this presentation concerns the relationship between advection and evolutionary transitions to multicellularity – what might be termed "Life at High Péclet Numbers."

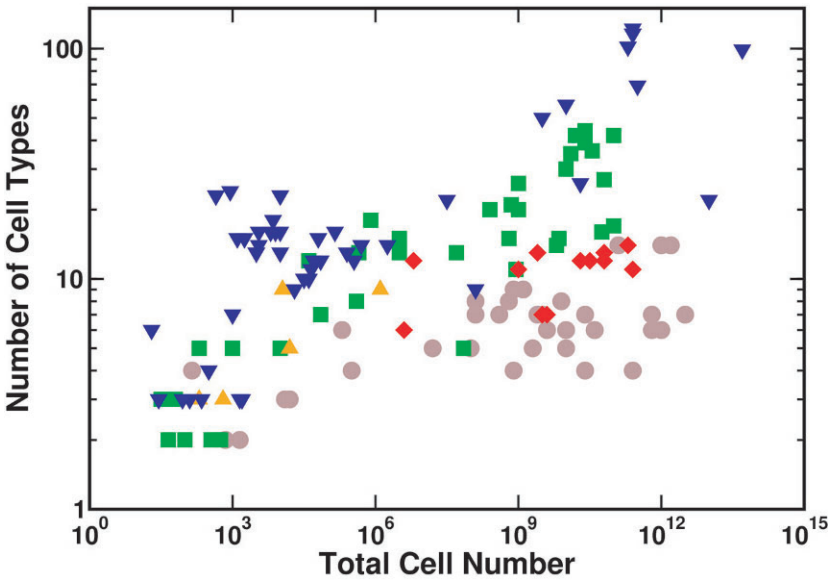

FIGURE 1. Scaling of the number of distinct cell types with total number of cells in various organisms. Data include amoebas, ciliates and brown seaweeds (brown), green algae and plants (green), red seaweeds (red), fungi (orange), and animals (blue). Adapted from Bells and Mooers [6] and Bonner [3].

2. *Volvox* and its relatives as model organisms

Long after he made his great contributions to microscopy and started a revolution in biology, Antony van Leeuwenhoek peered into a drop of pond water and discovered one of nature's geometrical marvels [10]. This was the freshwater alga which, years later, in the very last entry of his great work on biological taxonomy, Linneaus named *Volvox* [11] for its characteristic spinning motion about a fixed body axis. In van Leeuwenhoek's drawing (Fig. 2) we see that *Volvox* is a spherical colonial green alga with thousands of surface cells and daughter colonies inside the spheroid. His microscopy was insufficient to determine that *Volvox* swims by means of two beating flagella on each of the surface cells. We now know that those flagella are nearly identical to the cilia in our lungs. Indeed they are one of the most highly conserved structures in biology, a testament to the importance of fluid dynamics in life at all scales.

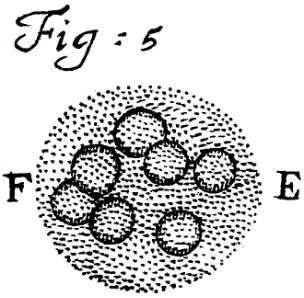

FIGURE 2. Figure 5 from van Leeuwenhoek's article on *Volvox* from 1700 [10]

Over a century ago, Weismann [12] suggested that a set of organisms related to *Volvox*, known as the Volvocine algae, can serve as a model lineage for study of the transition from unicellular to multicellular organisms, an argument amplified more recently by Kirk [13]. This suitability derives from the fact that this *extant* lineage (Fig. 3) displays varying colony size, structure, and specialization into the two fundamental cell types: vegetative (soma) and reproductive (germ). The species include unicellular *Chlamydomonas reinhardtii* (A), undifferentiated *Gonium pectorale* (B) and *Eudorina elegans* (C), soma-differentiated *Pleodorina californica* (D), germ-soma differentiated *Volvox carteri* (E), *V. aureus* (F), and even larger (e.g., *V. gigas* with a radius of 1 mm). In the multicellular forms from *Volvox* upward in size the *Chlamydomonas*-like somatic cells are at the surface of a transparent, spherical extracellular matrix (ECM), with their two outward-oriented flagella conferring motility, while the reproductive cells/daughter colonies are sequestered on the inside of the ECM. A central question in the study of this lineage is: *What are the driving forces which led to the scale of* ~ 150 μm *for the onset of germ-soma differentiation?*

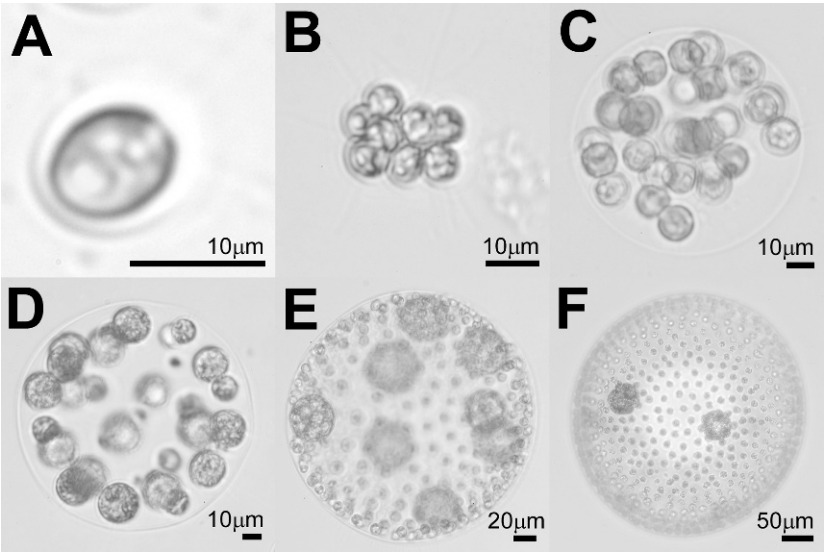

FIGURE 3. Volvocine species [22].

Although the precise relationships among species are not fully resolved in the Volvocales, it is known that *Volvox* species with increased cell specialization do not have a single origin – they have evolved several times, independently, from quite different ancestors [14, 15, 16, 17]. Lineages exhibiting the different developmental programs (details of cell division) [18] are interspersed with each other and with non-*Volvox* species, indicating that they have also evolved several times independently. Supporting this evidence for ease of evolutionary transitions is the underlying genetic architecture responsible for the separation of germ and soma, which does not involve many genetic steps [19]. Only two mutations are required to transform *V. carteri* into a mutant (*V. carteri glsA*$^-$*/regA*$^-$) with morphological and life-history features similar to those of *Eudorina* colonies with no cellular differentiation [20]. In short, the Volvocales comprise a group of closely related lineages with different degrees of cell specialization which seem to represent "alternative stable states" [21].

The tremendous range of size presented by these species, their common structural element of biflagellated somatic cells, and their most elementary differentiation beyond a critical size suggest that they would allow us to deconstruct scaling laws in self-propulsion, fluid mixing, and metabolism which may help explain the evolutionary driving forces which led to multicellularity. In the laboratory, *Volvox* is typically grown on a 48-hour lifecycle (Fig. 4). Populations can be rather precisely synchronized, so that large numbers are available at any given time in a well-defined life cycle stage, allowing for good statistical sampling of the properties during growth.

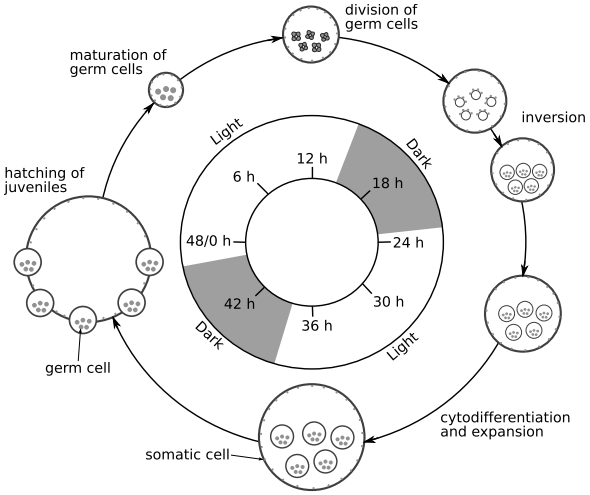

FIGURE 4. The 48 hour life cycle of *Volvox*, adapted from Kirk [13].

Volvox is also amenable to precise quantitative study of its fluid mechanics, using techniques from physiology. For instance, glass micropipettes familiar from *in vitro* fertilization, can be used to hold individual colonies under the microscope so that the flow fields produced by their collective flagellar beating can be mapped. Figure 5 shows an example of such a flow field, which shows clearly the existence of a (fixed) colonial axis, the flow along the surface being primarily from anterior to posterior. The flagella beat with a slight tilt, producing the force that makes the colony spin about its axis. In Fig. 5 we also observe that the characteristic length scale of these flows is comparable to the colony radius, and hence up to a fraction of a millimeter. The typical fluid velocities can reach nearly 1 mm/s, leading to Péclet numbers in the several hundreds, as anticipated above.

3. The advection-diffusion problem

For these organisms, basic considerations point to an intrinsic bottleneck to nutrient uptake by diffusion alone [22, 23, 24]. For a spherical absorbing colony of radius R in a *quiescent* fluid medium, taking up a nutrient from a diffusional steady state concentration profile $C(r) = C_\infty\,(1 - R/r)$, where C_∞ is the concentration far away, the diffusional current I_d of nutrients is linear in the radius: $I_d = 4\pi D C_\infty R$. In contrast, the metabolic requirements of surface somatic cells will scale as $I_m = 4\pi R^2 \beta$, where β is the consumption rate per unit area. Clearly, there is a bottleneck radius $R_b = DC_\infty/\beta$ beyond which metabolic needs cannot be met by diffusion alone. Our estimates [23] suggest that this length scale is close to that at which the Volvocales display germ-soma differentiation ($\sim$ 150 μm).

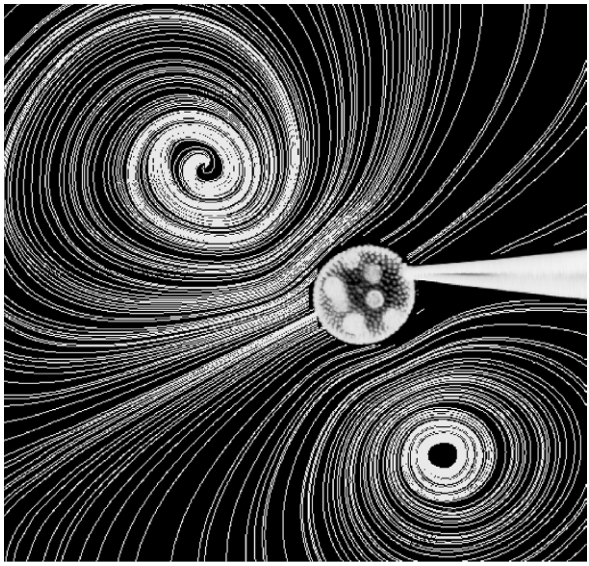

FIGURE 5. *Volvox* held on a micropipette, with streamlines visualized by particle-imaging-velocimetry. Diameter of colony is ~ 500 μm.

Since there are species much larger, there must be a means to increase nutrient acquisition accordingly. Indeed, we have recently established that the lineage covers a very broad range of Péclet numbers, from below unity at the single cell level, to vastly greater for colonies composed of thousands of cells. These large Péclet numbers arise from fluid flows driven by the coordinated action of tens, hundreds, or even thousands of flagella on the surface of these colonies, and imply metabolic dynamics fundamentally different from those limited by passive diffusion.

The concentration of a molecular species is governed by the equation

$$C_t + \mathbf{u} \cdot \nabla C = D\nabla^2 C \ , \tag{2}$$

for a solute concentration C in the presence of a fluid velocity field $\mathbf{u}$, with suitable boundary conditions. The key nontrivial point here is that $\mathbf{u}$ is a self-generated flow field deriving from the complex flagellar dynamics. The exchange rates of such a scalar for large Péclet numbers were derived by Acrivos and Taylor [25] for the related problem of heat transfer from a solid sphere in a flow that is uniform far from the sphere, where it was found that the current scales as $\sim RPe^{1/3}$ for $Pe \gg 1$. The fractional exponent arises from a (thermal) boundary layer that hugs the sphere ever more tightly at higher velocities, thereby increasing the local thermal gradient and thus the heat flux. This particular scaling law is not directly applicable to the uptake problem of a solute because the boundary conditions for a flagellated alga are quite different from that of a solid sphere. Subsequent work by Magar, Goto, and Pedley [26, 27] and by us [23] showed

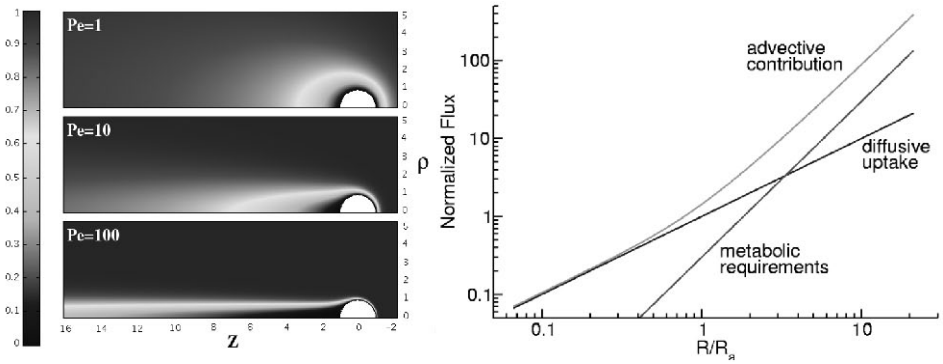

FIGURE 6. Results of finite-element computations of scalar concentration around an absorbing colony in flow at various Péclet numbers, showing boundary layer formation. (right) metabolite fluxes as a function of radius [23].

that the alternative boundary conditions of either prescribed tangential velocity or prescribed tangential force distribution change the scaling law for the current of nutrients to $RPe^{1/2}$. The question then becomes: How does the self-generated fluid velocity scale with size? In a simple model for *Volvox* swimming [23], flagellar dynamics are summarized by a time-averaged tangential force per unit area f exerted on the fluid. This model predicts a characteristic flow velocity

$$U \sim \frac{\pi f R}{8\eta} \ , \tag{3}$$

where η is the fluid viscosity. Under this scaling, the Pe number grows with size as $UR \sim R^2$, and the uptake rate becomes $RPe^{1/2} \sim R^2$, bypassing the diffusional bottleneck (Fig. 6). This increase in nutrient uptake due to fluid flow driven by flagella serves not only to remove the diffusive bottleneck, but also to provide an evolutionary driving force for transitions to multicellularity. As seen in Fig. 6b, there is a nutrient uptake enhancement *per somatic cell* that arises from the collective flow. This increase is a very steep function of size for radii spanning from that of *Chlamydomonas* up to 100–200 μm, the rough scale of germ-soma differentiation. One might say that this is socialism at work (!) – everyone stirs the fluid and everyone benefits.

4. Allometric scaling of flagella-driven flows

Because it is spherical, *Volvox* is an ideal organism for studies of biological fluid dynamics, being an approximate realization of Lighthill's "squirmer" model [28] of self-propelled bodies having a specified surface velocity. As mentioned above, such models have elucidated nutrient uptake at high Péclet numbers [26, 27, 23] by single organisms, and they have also illustrated pairwise hydrodynamic interactions between them [29]. Volvocine algae may also be used to study *collective* dynamics

of self-propelled objects [30], complementary to bacterial suspensions (*E. coli, B. subtilis*) exhibiting large-scale coherence in thin films [31] and bulk [32].

We have investigated the scaling laws for flagella-driven flows in the Volvocales. Two allometric relations are key; (i) the fluid velocity (or swimming speed) of a colony as it grows and its somatic cells move further apart, and (ii) those velocities at a given somatic cell density as a function of colony diameter. Studies of a range of species over their life cycles yield data sets from which scaling laws can be tested.

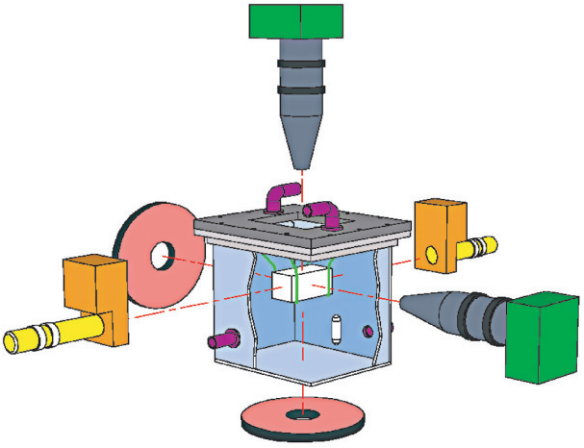

FIGURE 7. Schematic drawing of dual-view tracking apparatus [33]. The outer chamber (light blue, lid and flange in grey) contains a water bath, fed through inlets and outlets (purple), and mixed with a magnetic stir bar (white) driven by a motor external to the tank (not shown). The sample chamber (white) is suspended by stainless steel holders (light green), and illuminated by annular LED arrays (red). Microorganisms are visualized with two long-working-distance microscopes (dark gray) equipped with CCD cameras (dark green). Phototactic stimulus is provided by two LED and lens assemblies (yellow), and controlled by shutters (orange).

The experimental methods are by now quite standard. *Volvox carteri* f. *nagariensis* EVE strain were grown axenically in Standard Volvox Medium [34] in diurnal growth chambers with sterile air bubbling, in a daily cycle of 16 h in cool white light ($\sim$ 4000 lux) at 28° C and 8 h in the dark at 26° C. Swimming was studied in a dual-view system (Fig. 7) [33], consisting of two identical assemblies, each a CCD camera (Pike 145B, Allied Vision Technologies, Germany) and a long-working distance microscope (InfiniVar CMS-2/S, Infinity Photo-Optical, Colorado). Dark-field illumination used 102 mm diameter circular LED arrays (LFR-100-R, CCS Inc., Kyoto) with narrow bandwidth emission at 655nm, to

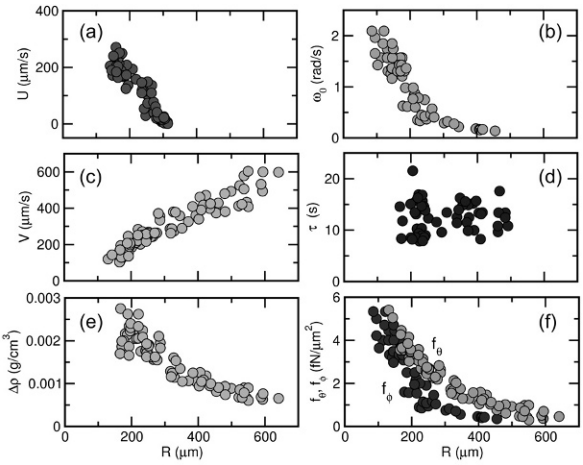

FIGURE 8. Swimming properties of *V. carteri* as a function of radius. (a) upswimming speed, (b) rotational frequency, (c) sedimentation speed, (d) reorientation time, (e) density offset, and (f) components of average flagellar force density.

which *Volvox* is insensitive [35]. Thermal convection induced by the illumination was minimized by placing the $2 \times 2 \times 2$ cm sample chamber, made from microscope slides held together with UV-curing glue (Norland), within a stirred, temperature-controlled water bath. Particle imaging velocimetry (PIV) studies (Dantec Dynamics, Skovelund, Denmark) showed that the r.m.s convective velocity within the sample chamber was $\lesssim 5$ μm/s.

From a theoretical point of view, four aspects of *Volvox* swimming are of interest, each arising, in the far field, from a distinct singularity of Stokes flow: (i) negative buoyancy (Stokeslet), (ii) self-propulsion (stresslet), (iii) bottom-heaviness (rotlet), and spinning (rotlet doublet). During the 48 hour life cycle, the number of somatic cells is constant; only their spacing increases as new ECM is added to increase the colony radius. This slowly changes the speeds of sinking, swimming, self-righting, and spinning, allowing exploration of a range of behaviors. The upswimming velocity U was measured with side views in the dual-view apparatus. *Volvox* density was determined by arresting self-propulsion through transient deflagellation with a pH shock [36], and measuring sedimentation. The settling velocity $V = 2\Delta\rho g R^2/9\eta$, with g the acceleration of gravity and η the fluid viscosity, yields the density offset $\Delta\rho = \rho_c - \rho$ between the colony and water. Bottom-heaviness implies a distance ℓ between the centers of gravity and geometry, measured by allowing *Volvox* to roll off a guide in the chamber and monitoring the axis inclination angle θ with the vertical, which obeys $\zeta_r \dot{\theta} = -(4\pi R^3 \rho_c g \ell/3) \sin\theta$, where $\zeta_r = 8\pi\eta R^3$

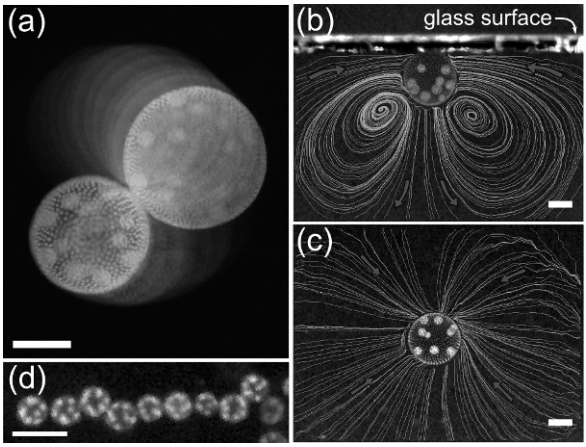

FIGURE 9. Waltzing of *V. carteri*.
(a) Top view. Superimposed images taken 4 s apart, graded in intensity.
(b) Side, and
(c) top views of a colony swimming against a coverslip, with fluid streamlines. Scales are 200 μm.
(d) A linear *Volvox* cluster viewed from above (scale is 1 mm).

is the rotational drag coefficient, yielding a relaxation time $\tau = 6\eta/\rho_c g\ell$ [37]. The rotational frequencies ω_o of free-swimming colonies were obtained from movies taken from above, using germ cells/daughter colonies as markers.

Figure 8 shows the four measured quantities (U, V, ω_o, τ) and the deduced density offset $\Delta\rho$. In the simplest model [23], locomotion derives from a uniform force per unit area $\mathbf{f} = (f_\theta, f_\phi)$ exerted by flagella tangential to the colony surface. Balancing the net force $\int dS\, \mathbf{f} \cdot \hat{\mathbf{z}} = \pi^2 f_\theta R^2$ against the Stokes drag and negative buoyancy yields $f_\theta = 6\eta(U+V)/\pi R$. Balancing the flagellar torque $\int dS\, R\hat{\mathbf{r}} \times \mathbf{f} \cdot \hat{\mathbf{z}} = \pi^2 f_\phi R^3$ against viscous rotational torque $8\pi\eta R^3\omega_o$ yields $f_\phi = 8\eta\omega_o/\pi$. These components are shown in Fig. 8f, where we used a linear parameterization of the upswimming data (Fig. 8a) to obtain an estimate of U over the entire radius range. The force density f_θ corresponds to several pN per flagellar pair [23], while the smallness of f_ϕ is a consequence of the $\sim 15^\circ$ tilt of the beating plane with respect to the colonial axis [38, 39].

These data provide a wealth of information on the physics of multicellular flagellar beating, and also provide the foundation for understanding some intriguing *collective* behavior of colonies. One such example is shown in Fig. 9. Here we see two colonies that have swum up to the ceiling of the experimental chamber

and orbit about each other in a "hydrodynamic bound state" [40]. This configuration arises from the "infalling" of two colonies initially some distance apart at the ceiling. Their remarkable mutual attraction arises from hydrodynamic interactions that are induced by the presence of the no-slip wall [41]. As each of the colonies spins about its axis it induces a short-range lubrication force on the other, slowing its motion and thereby producing a torque that leads to the orbiting motion. The fact that *Volvox* are bottom-heavy confers stability to this arrangement. A quantitative theory of the formation and dynamics of this bound state has been developed [40], making use of the extensive data in Fig. 8.

Hydrodynamic bound states, such as those described here, may have biological significance. When environmental conditions deteriorate, *Volvox* colonies enter a sexual phase of spore production to overwinter. Field studies show that bulk *Volvox* concentrations n are < 1 cm^{-3} [42], with male/female ratio of $\sim 1/10$, and ~ 100 sperm packets/male. Under these conditions, the mean encounter time for females and sperm packets is a substantial fraction of the life cycle. The hard sphere mean free path $\lambda = 1/\sqrt{2}n\pi(R + R_{sp})^2 \times 10/100$, with $R = 150$ μm for females, and $R_{sp} = 15$ μm for sperm packets, is $\lambda > 1$ m, implying a mean encounter time > 3 h. This suggests that another mechanism for fertilization must be at work, with previous studies having excluded chemoattraction in this system [43]. At naturally occurring concentrations, more than one *Volvox* may partake in the waltzing bound state, leading to long linear arrays (Fig. 9d). In such clusters, formed at the air-water interface, the recirculating flows would decrease the encounter times to seconds or minutes, clearly increasing the chance of sperm packets finding their intended target.

5. Phototactic steering

Another benchmark feature of the multicellularity exhibited by the Volvocales is their ability to perform accurate phototaxis, despite lacking a central nervous system to control the flagella beat dynamics. The accepted view of phototaxis [13] is that the light intensity measured by the photoreceptor of each individual somatic cell controls the beat dynamics of its flagella (with strong beating at low light levels, weaker beating at high intensity). Much as plants grow toward light by elongating more on the dark side, this stronger beating on the dark side leads to phototaxis, although these responses to darkness and light are themselves transient. Of course, the persistent rotation of *Volvox* constantly brings new cells in and out of the dark and light sides, yielding a continuous modulation of the light response.

Since there have been no systematic simultaneous studies of phototactic trajectories and beat dynamics to quantify this process, we have begun to investigate these motions in detail. The dual-view tracking system is particularly useful in this regard, and has allowed us to obtain the preliminary data in Fig. 10. With this synchronization and the known relationship between light intensity, orientation,

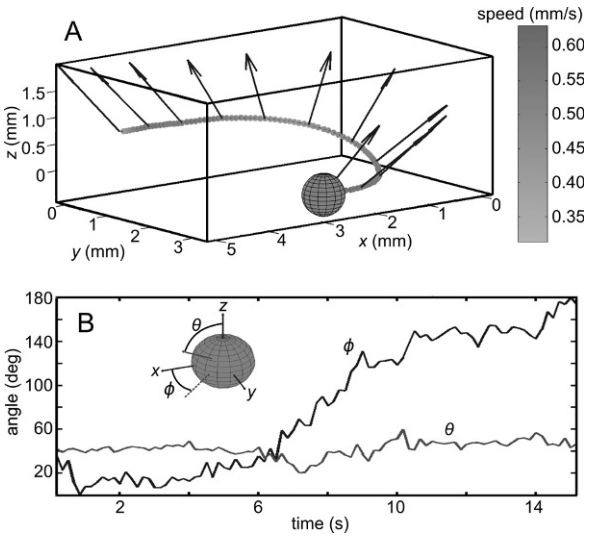

FIGURE 10. A phototactic turn of *Volvox barberi*.

(a) The positional and orientational measurements are illustrated by vectors indicating the body axis, and swimming-speed-dependent coloration of the track. To initiate the 180° change swimming direction, the light initially was from the right along the x-axis and then changed to come from the left. Gravity is directed along the negative z-direction. Sphere represents initial position along the track.

(b) Evolution of the body axis during the phototactic turn is described in terms of two angles θ and ϕ.

and flagellar beat patterns, the central mathematical questions which we aim to answer are both direct and inverse; Do the rules which are believed to connect light intensity to beat patterns lead to phototaxis as observed? What is the class of local rules relating light intensity to beat dynamics which produce phototaxis? Is there an optimum strategy?

6. Flagellar synchronization

As noted long ago [44], coordinated beating of *Volvox* flagella is found in species with and those without cytoplasmic connections between somatic cells. This fact implicates hydrodynamic interactions in synchronization. Such interactions also appear to underlie the generation of metachronal waves on ciliates; in neither system has synchronization been adequately explained theoretically or quantified

experimentally, although there is a growing body of work exploring the hydrodynamic origins [45, 46]. *Volvox* provides an excellent system to study this phenomenon, because of its ease of manipulation and visualization and the ability to sweep through a range of flagella lengths using the deflagellation technique mentioned earlier.

The ability to obtain high-resolution information on flagellar beating is illustrated in Fig. 11, where we see the two flagella on a single somatic cell of *Volvox* held on a micropipette. Imaging at up to 2000 video frames/sec allows a clear analysis of the waveform and precise measurement of the phase relationship between the two flagella.

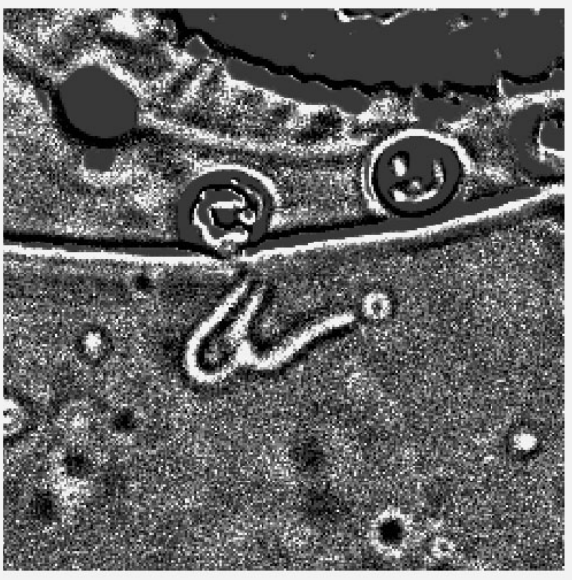

FIGURE 11. *Volvox* somatic cell flagella, imaged at 2000 frames per second. Image has been background-subtracted to enhance contrast.

One of the glaring lacunae in the theory of flagellar dynamics is a deep understanding of the synchronization of molecular motors via hydrodynamic interactions. A theory of synchronization has to be built from two main components: the hydrodynamic interactions between the moving objects (flagella) and the biochemical networks controlling the molecular motors which drive them. A point of reference for all such modeling is G.I. Taylor's well-known work on the hydrodynamic interactions between waving sheets in a viscous fluid [47], in which was solved the low Reynolds number fluid flow between two sheets undulating with specified traveling waves. It was found that the rate of viscous dissipation

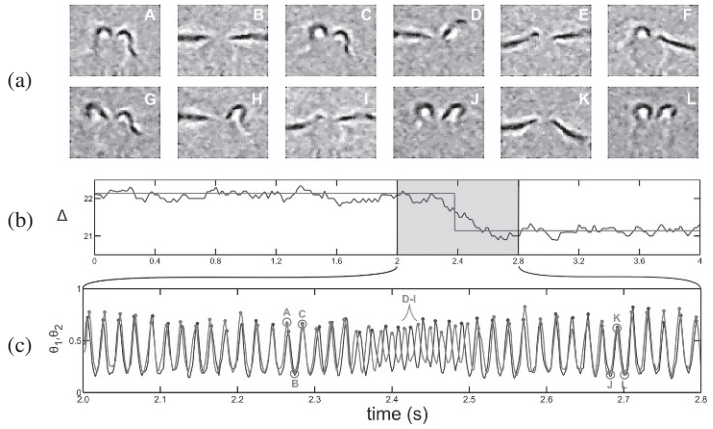

FIGURE 12. Phase slip in the beating of the two flagella of *Chlamydomonas*.
(a) Individual movie frames.
(b) Oscillatory signals obtained by local sampling of the image intensity near the flagella.
(c) Phase difference between the two flagellar beats.

of energy was minimized when the two sheets undulated in phase. However, minimization of dissipation is not a dynamical principle with which to determine the state of a system. In the absence of a microscopic description of how the internal mechanism which produces the traveling wave responds to forces and torques from the adjacent sheet, this question can not be answered.

The experimental situation is, however, becoming clearer. In recent work we have succeeded in tracking the flagellar beating dynamics of individual *Chlamydomonas* cells over thousands of beats, again with the help of the micromanipulation and imaging methods developed for *Volvox*. Historically [48], high-speed imaging of flagellar beating over periods of 1–2 s have shown that the two flagella of intact cells beat in synchrony most of the time. Occasionally it has been found that there is an extra beat of one of the flagella, and very rarely one finds unsynchronized flagella displaying beat frequency differences of 10–30%. These different behaviors have been assumed to reflect variations between individual cells.

We have now shown [49] that an individual *Chlamydomonas* cell can exhibit stochastic transitions back and forth between the states of synchrony and asynchrony. In the synchronous state, the two flagella beat in phase for a period of time which is exponentially distributed with a mean of several seconds, interrupted by "phase slips" of either sign. One such phase slip (or extra beat) is shown in Fig. 12. The statistics of these phase slips are consistent with a very simple model of coupled phase oscillators in the presence of noise, allowing one to extract from the dynamics a good estimate of the intrinsic frequency difference between the

two flagella in the phase-locked state. That difference is found to be a few percent. In the asynchronous state there is a clear phase difference of the magnitude known previously. This suggests strongly that the frequency difference between the flagella is dynamically regulated by the cell.

In addition, very recent experiments have shown that a consequence of this alternation between synchronous and asynchronous beating is the generation of a random walk in the trajectory of the cell. This, in turn, leads to diffusive behavior in a population of cells. In this sense, these findings show that there is a eukaryotic equivalent of the run-and-tumble locomotion well-known for peritrichously flagellated bacteria (e.g., *E. coli*) which swim by the rotation of helical flagella. The full implications of this finding for the life of these protists remains to be determined.

7. Conclusions

This overview has highlighted a number of challenging problems at the intersection of biology, physics, and mathematics that are motivated by the dynamics of multicellularity. From understanding phototaxis of a multicellular flagellated protist to the synchronized beating of flagella coupled through hydrodynamics, much needs to be understood before we will have a clear picture of the evolutionary transition from unicellular to multicellular organisms.

Acknowledgment

This overview highlights work done in collaboration with an extended group of physicists, applied mathematicians, and biologists: C.A. Solari, J.O. Kessler, R.E. Michod, M.B. Short, S. Ganguly, K. Drescher, I. Tuval, M. Polin, K. Leptos, T.J. Pedley, and T. Ishikawa. I am very grateful for support from the National Science Foundation, the Department of Energy, the Biotechnology and Biological Sciences Research Council, the Engineering and Physical Sciences Research Council, and the Schlumberger Chair Fund.

References

[1] J. Maynard Smith and E. Száthmary, *The Major Transitions in Evolution*, Freeman: San Francisco, 1995.

[2] J.T. Bonner, J. Biosci. **28** (2003), 523–528.

[3] J.T. Bonner, Evolution **58** (2004), 1883–1890.

[4] K.J.Niklas, *Plant Allometry*, University of Chicago Press: Chicago, IL, 1994.

[5] N. King, Develop. Cell **7** (2004), 313–325.

[6] G. Bell and A.O. Mooers, Biol. J. Linn. Soc. **60** (1997), 345.

[7] K.J. Niklas, Annals of Botany **85** (2000), 411–438.

[8] E. Guyon, J.P. Hulin, L. Petit, and C.D. Mitescu, Physical Hydrodynamics, Oxford University Press: Oxford, 2001.

[9] H.C. Berg and E.M. Purcell, Biophys. J. **20** (1977), 193–219.

[10] A. van Leeuwenhoek, Phil. Trans. Roy. Soc. **22** (1700), 509.

[11] C. Linneaus, *Systema Naturae*, 10th ed. (Holmiae, Impensis Laurentii Salvii, 1758), p. 820.

[12] A. Weismann, *Essays on Heredity and Kindred Biological Problems*, Oxford, Clarendon Press, 1892.

[13] D.L. Kirk, *Volvox: Molecular-genetic origins of multicellularity and cellular differentiation*, Cambridge University Press: Cambridge, 1998.

[14] A.W. Coleman, Proc. Natl. Acad. Sci. (USA) **96** (1999), 13892–13897.

[15] H. Nozaki, N. Ohta, H. Takano, and M.M. Watanabe, J. Phycology **35** (1999), 104–112.

[16] H. Nozaki, Biología **58** (2003), 425–431.

[17] H. Nozaki, F.D. Ott, and A.W. Coleman, J. Phycol. **42** (2006), 1072–1080.

[18] A.G. Desnitski, Eur. J. Protist., **31** (1995), 241–247.

[19] D.L. Kirk, Ann. Rev. Gen. **31** (1997), 359–380.

[20] L.W. Tam and D.L. Kirk, Development **112** (1991), 571–580.

[21] A. Larson, M.M. Kirk, D.L. Kirk, Mol. Biol. Evol. **9** (1992), 85–105.

[22] C.A. Solari, S. Ganguly, J.O. Kessler, R.E. Michod, and R.E. Goldstein, Proc. Natl. Acad. Sci. (USA) **103** (2006), 1353–1358.

[23] M.B. Short, C.A. Solari, S. Ganguly, T.R. Powers, J.O. Kessler, and R.E. Goldstein, Proc. Natl. Acad. Sci. (USA) **103** (2006), 8315–8319.

[24] C.A. Solari, J.O. Kessler, and R.E. Michod, Am. Nat. **167** (2006), 537–554.

[25] A. Acrivos and T.D. Taylor, Phys. Fluids **5** (1962), 387–394.

[26] V. Magar, T. Goto and T.J. Pedley, Q. J. Mech. Appl. Math. **56** (2003), 65–91.

[27] V. Magar and T.J. Pedley, J. Fluid Mech. **539** (2005), 93–112.

[28] M.J. Lighthill, Commun. Pure Appl. Math. **5** (1952), 109.

[29] T. Ishikawa and M. Hota, J. Exp. Biol. **209** (2006), 4452; T. Ishikawa, M.P. Simmonds, and T.J. Pedley, J. Fluid Mech. **568** (2006), 119.

[30] T. Ishikawa and T.J. Pedley, Phys. Rev. Lett. **100** (2008), 088103; T. Ishikawa, J.T. Locsei, and T.J. Pedley, J. Fluid Mech. **615** (2008), 401.

[31] X.-L. Wu and A. Libchaber, Phys. Rev. Lett. **84** (2000), 3017; A. Sokolov, *et al.*, Phys. Rev. Lett. **98** (2007), 158102.

[32] C. Dombrowski, *et al.*, Phys. Rev. Lett. **93** (2004), 098103.

[33] K. Drescher, K. Leptos, and R.E. Goldstein, Rev. Sci. Instrum. **80** (2009), 014301.

[34] D.L. Kirk and M.M. Kirk, Dev. Biol. **96** (1983), 493.

[35] H. Sakaguchi and K. Iwasa, Plant Cell Physiol. **20** (1979), 909.

[36] G.B. Witman, *et al.*, J. Cell Biol. **54** (1972), 507.

[37] T.J. Pedley and J.O. Kessler, Ann. Rev. Fluid Mech. **24** (1992), 313.

[38] H.J. Hoops, Protoplasma **199** (1997), 99.

[39] K. Drescher, R.E. Goldstein, and I. Tuval, Proc. Natl. Acad. Sci. (USA) 107, 11171 (2010).

[40] K. Drescher, K. Leptos, I. Tuval, T. Ishikawa, T.J. Pedley, and R.E. Goldstein, Phys. Rev. Lett. 102, 168101 (2009).

[41] J.R. Blake, Proc. Camb. Phil. Soc. **70** (1971), 303–310.
[42] F. DeNoyelles, Jr., Ph.D. thesis, Cornell Univ. (1971).
[43] S.J. Cogging, *et al.*, J. Phycol. **15** (1979), 247.
[44] J.D.F. Hiatt and W.G. Hand, J. Protozool. **19** (1972), 488–489.
[45] A. Vilfan and F. Jülicher, Phys. Rev. Lett. **96** (2006), 058102.
[46] B. Guirao and J.-F. Joanny, Biophys. J. **92** (2007), 1900–1917.
[47] G.I. Taylor, Proc. Roy. Soc. A **209** (1951), 447–461.
[48] U. Rüffer and W. Nultsch, Cell. Mot. **7** (1987), 87; **15** (1990), 162; **18** (1991), 269; **41** (1998), 297.
[49] M. Polin, I. Tuval, K. Drescher, J.P. Gollub, and R.E. Goldstein, Science 325, 487 (2009).

Raymond E. Goldstein
Department of Applied Mathematics and Theoretical Physics
Centre for Mathematical Sciences
University of Cambridge
Wilberforce Road
Cambridge CB3 0WA, UK
e-mail: R.E.Goldstein@damtp.cam.ac.uk

Conscious and Nonconscious Processes: Distinct Forms of Evidence Accumulation?

Stanislas Dehaene

Abstract. Among the many brain events evoked by a visual stimulus, which ones are associated specifically with conscious perception, and which merely reflect nonconscious processing? Understanding the neuronal mechanisms of consciousness is a major challenge for cognitive neuroscience. Recently, progress has been achieved by contrasting behavior and brain activation in minimally different experimental conditions, one of which leads to conscious perception whereas the other does not. This chapter reviews briefly this line of research and speculates on its theoretical interpretation. I propose to draw links between evidence accumulation models, which are highly successful in capturing elementary psychophysical decisions, and the conscious/nonconscious dichotomy. In this framework, conscious access would correspond to the crossing of a threshold in evidence accumulation within a distributed *global workspace*, a set of recurrently connected neurons with long axons that is able to integrate and broadcast back evidence from multiple brain processors. During nonconscious processing, evidence would be accumulated locally within specialized subcircuits, but would fail to reach the threshold needed for global ignition and, therefore, conscious reportability.

An experimental strategy for exploring consciousness

Although the nature of consciousness remains a formidable problem, Lionel Naccache and I argue that it can be approached through behavioral and brain-imaging methods:

> The cognitive neuroscience of consciousness aims at determining whether there is a systematic form of information processing and a reproducible class of neuronal activation patterns that systematically distinguish mental states that subjects label as *conscious* from other states (Dehaene and Naccache 2001).

In that respect, identifying the neural bases of consciousness need not be any more difficult than, say, identifying that of other states of mind (e.g., face percep-

B. Duplantier and V. Rivasseau (eds.), *Biological Physics*, Progress in Mathematical Physics 60,
DOI 10.1007/978-3-0346-0428-4_7, © Springer Basel AG 2011

tion or anger). Bernard Baars (1989) outlined a simple *contrastive method* which, in his own terms, consists simply in contrasting pairs of similar events, where one is conscious but the other is not. Baars noted that in the last forty years, experimental psychology and neuropsychology have identified dozens of contrasts relevant to consciousness. Examples include normal vision versus blindsight; extinguished versus seen stimuli in patients with hemineglect; masked versus nonmasked visual stimuli; habituated versus novel stimuli; accessed versus nonaccessed meanings of ambiguous stimuli; distinctions within states of consciousness (sleep, coma, wakefulness, arousal); voluntary versus involuntary actions; or even explicit problem solving versus implicit *incubation*.

In this chapter, I focus on the masking paradigm, perhaps the simplest and most productive situation in which to study conscious access in normal subjects. During masking, a target visual stimulus is flashed briefly on a computer screen. It can be followed or preceded by a *mask*: another visual stimulus is presented at the same screen location or just nearby. Under the right conditions, presentation of the mask erases the perception of the target stimulus, and subjects report that they are no longer able to see it. Yet the target stimulus still induces behavioral priming effects and brain activation patterns which correspond to nonconscious or *subliminal* (below threshold) processing. Focusing on what types of processing can occur under subliminal masking conditions, and what additional processes unfold once the stimulus is unmasked, can thus shed considerable light on the nature of conscious access.

How do we measure whether conscious access occurred?

As mentioned above, once an appropriate paradigm such as masking is available, studying the cerebral correlates of conscious access need not be more difficult than, say, studying face perception. In both cases, one correlates brain activity with the presence or absence of the relevant aspect of the stimulus (face vs. nonface stimulus, or conscious vs. nonconscious perception). What is special about conscious access, however, is that it is defined solely in subjective terms. Thus, Lionel Naccache and I have argued:

> The first crucial step is *to take seriously introspective phenomenological reports.* Subjective reports are the key phenomena that a cognitive neuroscience of consciousness purports to study. As such, they constitute primary data that need to be measured and recorded along with other psychophysiological observations (Dehaene and Naccache 2001).

Increasingly, therefore, consciousness research relies on subjective reports as a defining criterion. Ideally, one should measure the extent of conscious perception on every single trial, possibly using a graded scale to capture even fine nuances of the percept (Del Cul et al. 2007; Sergent et al. 2005; Sergent and Dehaene 2004). For an identical objective stimulus, one may then contrast the brain activation observed when it is or is not subjectively seen.

The emphasis on subjective reporting goes against a long tradition in psychophysics and experimental psychology, which has emphasized the need for objective criteria based on signal-detection theory. According to this tradition, a masked stimulus is accepted as being subliminal only if performance on some direct task of stimulus perception falls to chance level (zero d-prime). There are several difficulties associated with this objective definition, however. First, it tends to overestimate conscious perception, as there are many conditions in which subjects perform better than chance, and yet deny perceiving any stimulus. Second, it requires accepting the null hypothesis of chance-level performance; usually d-prime never quite drops to zero, and whether it is significant or not depends merely on the number of trials dedicated to its measurement. Finally, performance can be at chance level for some tasks, but not others. Does above-chance performance on the former tasks count as evidence of conscious perception, or merely of subliminal processing? The issue seems unsolvable unless we have a good theory of which tasks can only be performed at a conscious level, and thus constitute appropriate objective measures of conscious access, and which tasks can operate under subliminal conditions.

By focusing first and foremost on subjective reports, we can avoid this somewhat Byzantine discussion of what constitutes a good subliminal stimulus. It is an empirical fact that, when subjects rate a stimulus subjectively as having been seen consciously, a major transition occurs such that the stimulus also becomes available for a variety of objective tasks. For instance, Figure 1 shows data from a masking paradigm (Del Cul et al. 2007) where subjects were asked, on every trial, to perform two tasks on a masked digit: (a) a subjective task of rating the stimulus visibility; (b) an objective, forced-choice task of deciding whether the stimulus was larger or smaller than 5. As the interval between the target and mask increased, both subjective and objective performance increased in a nonlinear sigmoidal manner. Both sigmoids allowed for the definition of a threshold (placed at the inflection point). We found that these subjective and objective definitions of the consciousness threshold were virtually identical and highly correlated between subjects. Furthermore, both were degraded jointly in patients with schizophrenia or multiple sclerosis (Del Cul et al. 2006; Reuter et al. 2007). Interestingly, below this threshold, the objective and subjective tasks could be dissociated, as there was a proportion of trials in which objective performance remained higher than chance, although subjects denied subjective perception.

In view of such results, the following operational definitions of conscious and nonconscious processing may be proposed. First, on a single-trial basis, priority should be given to subjective reports in defining what constitutes a *conscious* trial. Second, when averaging across trials, the threshold for conscious access may be identified with the major nonlinearity that occurs in both subjective and objective performance as the stimulus is progressively unmasked. Third, the presence of nonconscious processing can be inferred whenever objective performance departs from subjective reports; for instance, by remaining above-chance in a region of stimulus space where subjective reports fall to zero.

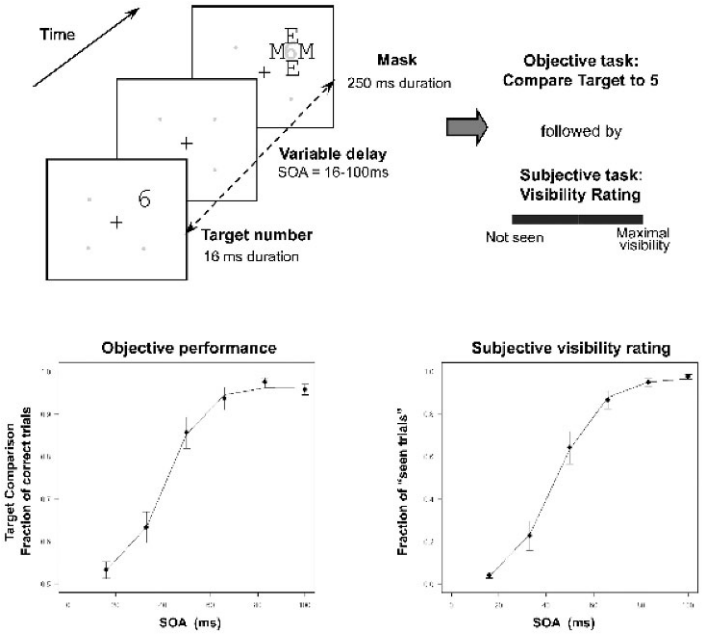

FIGURE 1. Example of a masking paradigm where objective and subjective measures concur to define a threshold for perceptual consciousness (after Del Cul et al. 2007). A digit is flashed at one of four parafoveal locations and is followed after a variable delay by a surrounding letter mask (top left panel). On each trial, participants are asked to perform an objective task (decide if the digit is larger or smaller than 5) and a subjective task (rate the stimulus visibility). Both measures concur: performance is low at short delays, but suddenly jumps to a high value above a threshold delay (around 50 ms). This method thus defines a range of *subliminal* (below-threshold) stimuli. SOA = stimulus onset asynchrony.

The latter hypothesis lies at the heart of the *dissociation method*, which has been used by many others to separate conscious and nonconscious processing. For instance, masking conditions can be found that create a U-shaped curve for subjective perception as a function of target-mask interval. Other aspects of performance, such as response time and brain activity patterns, vary monotonically with the same stimulus parameter, thus clearly reflecting nonconscious stimulus processing (Haynes et al. 2005; Vorberg et al. 2003).

Subliminal processing and evidence accumulation models

A broad array of research has focused on the issue of the depth of subliminal processing of masked visual stimuli: to what extent is a masked stimulus that is reported subjectively as *not seen* processed in the brain? Here I present only

a brief overview of this line of research (for a broader review, see Kouider and Dehaene 2007). The main goal is to examine these data in relation to models of decision making by evidence accumulation, which have proven highly successful in mathematical modeling of chronometric and neurophysiological data from simple psychophysical decisions (e.g., Laming 1968; Link 1992; Smith and Ratcliff 2004; Usher and McClelland 2001; Gold and Shadlen, 2002).

For the sake of concreteness, one such accumulation model is presented in Figure 2. This particular model was shown to capture much of what is known about simple numerical decisions and their neural bases (Dehaene 2007). While many variants can be proposed (see Smith and Ratcliff 2004), this model incorporates mechanisms that are generic to a variety of psychophysical tasks. To illustrate this, consider the task of deciding if a number, presented either as a set of dots or as an Arabic numeral, is smaller or larger than 10. The model assumes the following steps:

1. Visual perception of the stimulus.
2. Semantic coding along the appropriate dimension (here, numerosity).
3. Categorization of the incoming evidence in relation to the instructions. This is achieved by separating this continuum into pools of units, each favoring a distinct response (here, units preferring numbers larger than 10 and units preferring numbers smaller than 10).
4. Computation of a log likelihood ratio (logLR), a quantity which estimates the likelihood that response R1 or R2 is correct, given the sensory evidence.
5. Stochastic accumulation of the logLR over a period of time, until a threshold amount is obtained in one direction or the other.
6. Emission of a motor response when the threshold is exceeded.

Models of this form have been shown to capture the details of chronometric data, including the shape of response time (RT) distributions and speed-accuracy tradeoffs. Within the context of conscious versus nonconscious computation, a key question is: Which of the model's mechanisms can operate under subliminal conditions, and which cannot?

Subliminal perception

Extensive research has demonstrated that a subliminal masked stimulus can be processed at the perceptual level. The main support comes from the repetition priming experiment, in which a subliminal prime is shown to facilitate the subsequent processing of an identical stimulus presented as a target. Priming is evidenced behaviorally as a reduction of response time on repeated trials compared to nonrepeated trials and neurally as a reduction in the amount of evoked brain activity (repetition suppression).

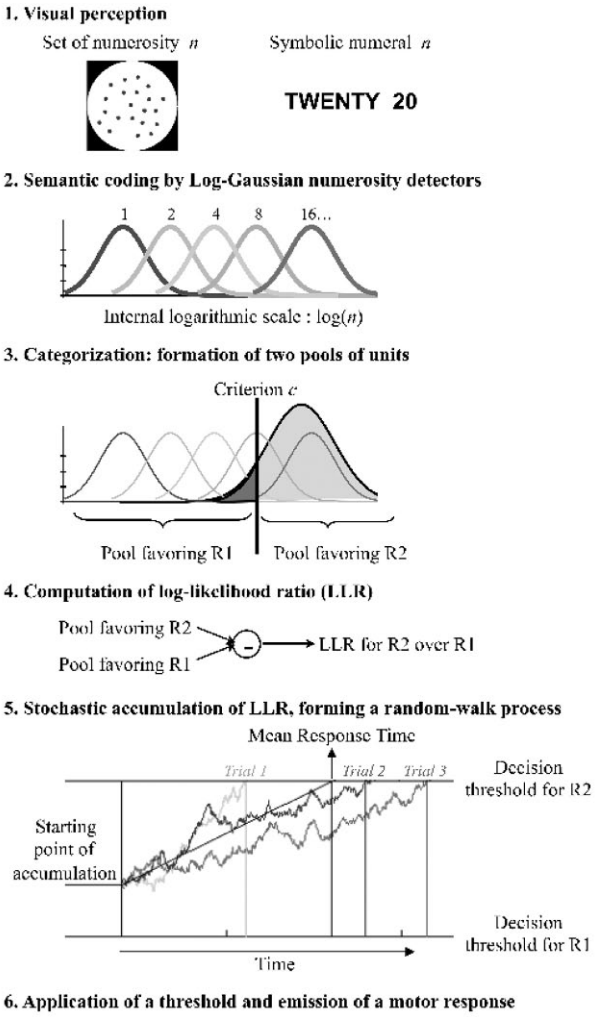

FIGURE 2. Proposed theoretical model of decision making in an objective numerical comparison task (for a full mathematical exposition, see Dehaene 2007). Subjects first encode each input number as a random variable on an internal continuum (top). The decision mechanism consists in accumulating evidence by adding up the log likelihood ratios (logLRs) for or against each of the two possible responses provided by successive samples of the random variable (middle). As a result, each trial consists in an internal random walk of the accumulated logLR (bottom). A response is emitted whenever the random walk reaches one of two response thresholds. Evidence reviewed in the present chapter suggests that all stages of the model can begin to operate in the absence of consciousness.

Repetition priming indicates that a subliminal stimulus can be registered perceptually. As illustrated in Figure 3, however, priming can occur at multiple levels. In extrastriatal cortex, priming is sensitive to the repetition of the exact same stimulus. In more anterior sectors of fusiform cortex, priming is more abstract and can resist a change in surface format, for example, when the same word is presented in upper case or lower case (Dehaene et al. 2001).

Subliminal semantic processing

At an even more abstract level, semantic subliminal priming has been observed, for example, in the left lateral temporal cortex for synonym words such as sofa/couch (Devlin et al. 2004) or for Japanese words presented in Kanji and Kana notations (Nakamura et al. 2005). Likewise, numerical repetition priming has been observed in bilateral intraparietal cortex when number words are presented in Arabic or word notations (Naccache and Dehaene 2001a). These observations have been confirmed by detailed behavioral studies (Naccache and Dehaene 2001b; Reynvoet et al. 2002). In terms of the model presented in Figure 2, they suggest that subliminal primes can partially bias the level of semantic coding.

The reality of subliminal semantic processing is confirmed by several empirical findings. Subliminal words can evoke an N400 component of the event related potential, which depends on their semantic relation to a previously presented word (Kiefer 2002; Kiefer and Brendel 2006). Subliminal words that convey an emotion (e.g., rape, shark) can cause an activation of the amygdala (Naccache et al. 2005), and the threshold for their conscious perception is lowered, indicating that they receive distinct processing even prior to conscious access (Gaillard, Del Cul et al. 2006).

In many of these cases, brain activation evoked by a subliminal stimulus is much reduced compared to the activation evoked by the same stimulus under conscious perception conditions (Dehaene et al. 2001). However, there are some cases in which a full-blown activation can be observed in the absence of conscious perception. In early visual areas, even heavily masked stimuli can produce essentially unchanged event-related responses in both fMRI (Haynes et al. 2005) and ERPs (Del Cul et al. 2007). In higher visual areas, large nonconscious responses have been observed under conditions of light masking, where invisibility is due to distraction by a secondary task (e.g., the attentional blink paradigm). Even a late ($\sim$ 400 ms) and abstract semantic event such as the N400 can be largely (Sergent et al. 2005) or even fully (Luck et al. 1996) preserved during the attentional blink.

Subliminal accumulation of evidence towards a decision

Dehaene et al. (1998) and Leuthold (Leuthold and Kopp 1998) first showed that a subliminal stimulus can bias a decision all the way down to the response programming level. The paradigm used by Dehaene et al. (1998) is illustrated in Figure 3c,

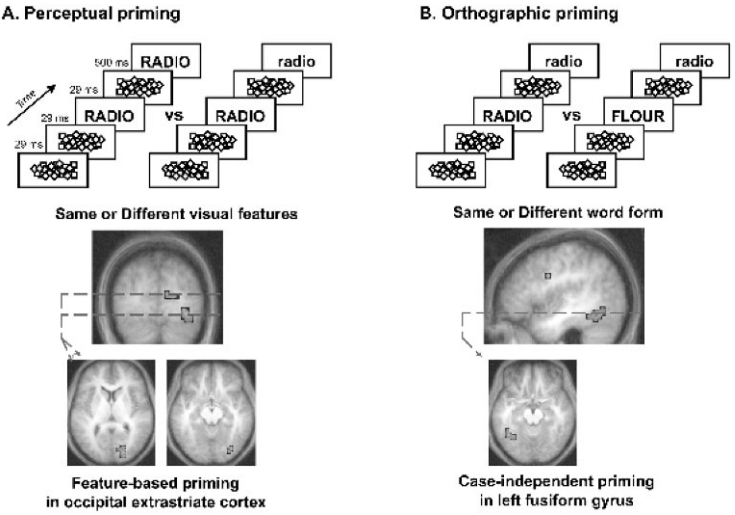

FIGURE 3. Brain imaging evidence for nonconscious processing at multiple levels of word and digit processing. All experiments rely on the priming method (Naccache and Dehaene 2001a), which consists in examining whether a subliminal prime can modulate the processing of a subsequent conscious target. The nature of the prime-target relation changes the site of modulation of brain activation:

(a) shared low-level visual features cause perceptual priming in extrastriate occipital cortex;
(b) case-independent orthographic priming of words occurs in the left occipitotemporal *visual word form area* (Dehaene et al. 2001b).

d. Subjects had to categorize numbers as being larger or smaller than 5 by pressing a right- or left-hand button (the response mappings were assigned randomly and switched in the middle of the experiment). Unknown to the participants, a subliminal number was presented prior to each target. A congruity effect was observed: on congruent trials, where the prime fell on the same side as the target (e.g., 9 followed by 6, both being larger than 5), responses were faster than on incongruent trials where they fell on different sides of 5 (e.g., 1 followed by 6). This effect could be measured by fMRI and ERP recordings of the motor cortex as a partial accumulation of motor bias towards the response side elicited by the prime.

Thus, activation evoked by an unseen prime can propagate all the way down to the motor level. Within the context of the model presented in Figure 2, this implies that semantic coding of the stimulus, categorization by application of arbitrary instructions, and response selection by evidence accumulation can all proceed, at least in part, without conscious perception. Research by Vorberg et al. (2003) supports this conclusion well. Using primes shaped as arrows pointing left or right, Vorberg et al. showed that the behavioral priming effect increased monotonically with the time interval separating the prime from the mask (while conscious

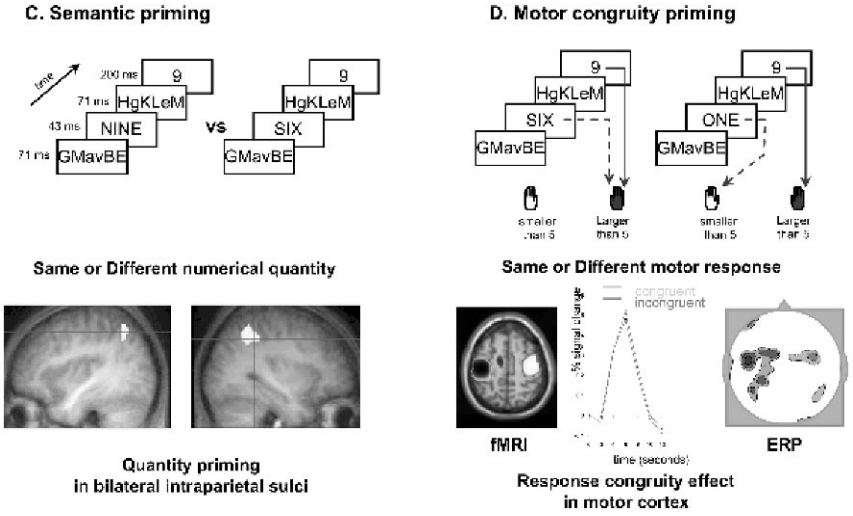

FIGURE 3. (continued)

(c) Repetition of a number, in Arabic or verbal notation, causes semantic priming in bilateral intraparietal sulci (Naccache and Dehaene 2001a);

(d) congruence of the motor responses associated with the prime and target modulates motor cortex activity, as if motor representations accumulate partial evidence from the prime before accumulating the main evidence arising from the target (Dehaene et al. 1998).

prime perception was either absent or followed a nonmonotonic, U-shaped curve). Those results, presented in Figure 4, can be captured mathematically using an evidence accumulation model similar to the one presented in Figure 2. The Vorberg et al. model supposes that the various response alternatives are coded by leaky accumulators which receive stochastic input: first from the prime, then from the target. The accumulators add up sensory evidence until a predefined threshold is reached, after which a response is emitted. Mathematical analysis and simulations show that this model can reproduce the empirical observation of a bias in response time. At long SOAs, the model predicts that primes can also induce a high error rate, especially if the response threshold is a relatively low prediction which is empirically supported by the data.

Role of instruction and attention in subliminal processing

Subliminal processing was previously thought to be automatic and independent of attention. In recent years, however, several effects from top-down modulation on subliminal processing have been identified.

Modulation by instructions

Task instructions readily alter the fate of subliminal stimuli. As just described, masked primes can elicit instruction-dependent activation in the motor cortex (Dehaene et al. 1998; Eimer and Schlaghecken 1998; Leuthold and Kopp 1998; Vorberg et al. 2003). Even details of the instructions provided to subjects, such as whether they are told that the targets consist of all numbers 1 through 9 or just the numbers 1, 4, 6 and 9, can affect subliminal priming (Kunde et al. 2003). Though still debated, those results suggest that the arbitrary stimulus-response mappings conveyed by conscious instructions can also apply to nonconscious stimuli. As noted above, within the framework of evidence accumulation models, this implies that an entire instruction set, reflected in how the stimulus is categorized and mapped onto responses, can be partially applied to a nonconscious stimulus.

Modulation by executive attention

Within-task changes in executive attention also seem to impact on subliminal processing. For instance, Kunde et al. (2003) studied the *Gratton effect*, a strategic increase in executive control which follows Stroop interference trials. The effect is such that, if on trial $n-1$ subjects experience a cognitive conflict due to a Stroop-incongruent trial, then on trial n the Stroop effect is reduced, as if subjects somehow regain stronger control over the task (perhaps by focusing attention more tightly around the time of the target). Kunde et al. manipulated the consciousness of the conflict by presenting, on each trial, a subliminal or supraliminal prime followed by a conscious target. They observed that the Gratton effect could only be induced by a conscious trial (i.e., the conflict at trial $n-1$ had to be a conscious conflict). Once established, however, the increase in control applied to both subliminal and supraliminal trials: the effect of conflict at trial n was diminished, whether or not this conflict was consciously perceived. This suggests that executive attention, once modified by a conscious stimulus, can have an impact on subsequent subliminal processing.

Modulation of subliminal priming by temporal attention

An impact of temporal attention on subliminal processing was demonstrated by Naccache et al. (2002) in a numerical masked priming paradigm. They showed that subliminal priming was present when subjects could attend to the time of presentation of the prime-target pair, but vanished when stimuli could not be temporally attended. Kiefer and Brendel (2006) observed a similar effect in an experiment investigating the N400 potential elicited by masked words. Unseen masked words elicited a much larger N400 when they were temporally attended than when they were not.

In terms of evidence accumulation models, temporal attention effects may relate to the little-studied issue of how the accumulators are reset and opened. To

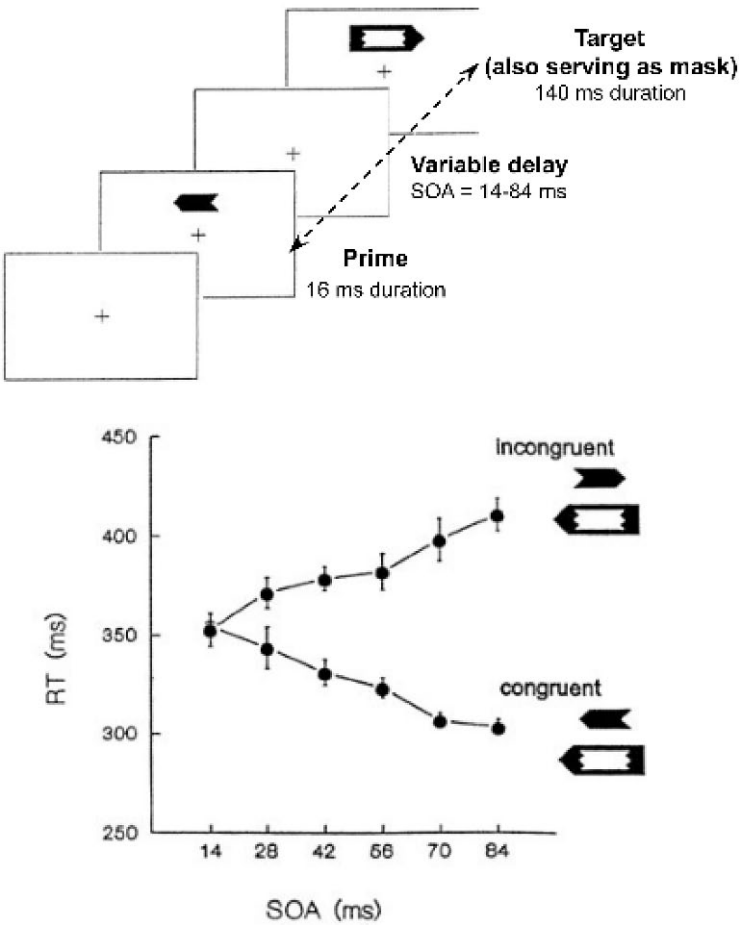

FIGURE 4. Evidence suggesting a partial accumulation of evidence from a nonconscious prime during a simple sensorimotor task (after Vorberg et al. 2003). Subjects classify target arrows as pointing right or left, while a masked prime also points left or right. A linear priming effect is seen: as the prime-target delay increases, congruent primes induce a monotonic speed-up of response times, while incongruent primes cause a monotonic slowing down. The slope of the effect is such that the difference in response time (RT) is essentially equal to the prime-target delay (SOA = stimulus onset asynchrony), suggesting that evidence is being continuously accumulated, first from the prime, then from the target.

operate optimally, the accumulators must be emptied before each trial, and evidence must only be accumulated once the stimulus is actually present. The above effects can be interpreted as showing that semantic and decision-related evidence arising from subliminal primes fails to be accumulated whenever it is presented

outside of the temporal window when the target is expected. Alternatively, if accumulated, it is reset to zero and therefore cannot bias target processing.

Modulation by spatial attention

Kentridge et al. (1999, 2004) first reported that blindsight patient GY could use consciously perceived cues to enhance unconscious processing of visual targets. When a target was presented in his scotoma region, patient GY responded more quickly and accurately when it was validly cued by a consciously perceptible arrow pointing to it, than when he was invalidly cued. In both cases, he still claimed that he could not see the target. Modulation of subliminal priming by spatial attention was also observed in normal subjects (Lachter et al. 2004; Marzouki et al. 2007).

In summary, task preparation includes many different components, including attention to the relevant stimulus parameter (e.g., number) and to the likely location and presentation time of the stimulus, as well as preparation of a stimulus-response mapping and setting of executive-level parameters (e.g., response threshold). Evidence suggests that essentially all of these task-preparation components, once prepared for a conscious target, apply as well to a nonconscious target.

Recent evidence for extended subliminal processing

Recently, subliminal research has gone one step further and asked whether task-preparation processes themselves can be primed subliminally. The central issue is whether processes traditionally associated with a *central executive* system can also unfold in the absence of consciousness.

Pessiglione et al. (2007) demonstrated that one aspect of task setting-motivation could be cued subliminally. Prior to each trial of a force-generation task, subjects were presented with conscious information about the amount of money they could earn on the subsequent trial: one penny or one pound. Unknown to them, each conscious monetary cue was preceded by a subliminal image which could be congruent or incongruent with the conscious image. This subliminal information modulated the subject's motivation, as evidenced by a modulation of both the applied force and the amount of activation of a bilateral ventral pallidal region known to convey reward anticipation information.

In a similar line of research, Mattler (2003) presented a series of experiments in which a square or diamond shape successively cued increasingly abstract aspects of the task: response finger, response hand, stimulus modality (auditory or visual), or the requested task (pitch or timbre judgment). For instance, in one experiment, subjects heard a variable sound which, if preceded by a square, had to be judged for its timbre and, if preceded by a diamond, had to be judged for its pitch. Unknown to the subject, each instruction cue was preceded by a masked prime which could be congruent or incongruent with the cue. Response times were systematically shorter on congruent trials and this effect increased with the prime-mask interval in

a manner which was dissociated from the U-shaped curve for conscious perception. Thus, even task selection seemed to be biased by a subliminal cue.

Unfortunately, Mattler's (2003) results could also be interpreted as a conflict at a purely visual level of cue identification; that is, the measure response time included components of cue identification, task selection, and task execution, and the observed priming might have arisen from the perceptual component alone. To demonstrate firmly that a subliminal prime could affect task selection, Lau and Passingham (2007) resorted to functional imaging. They selected tasks of phonological versus semantic judgment on visual words that are associated with broadly different cortical networks. Using a design similar to Mattler's, they then showed that not only the response time but the entire task-related network was modulated up or down as a function of whether the subliminal prime was congruent or incongruent with the task information provided by the visible cue. This subliminal task-cueing effect was not sufficient to reverse the conscious task cue, but it did yield an increase in subjects' error rates.

One last paradigm of relevance to the present discussion was developed by van Gaal et al. (2007). They showed that a subliminal cue could fulfill the role of a *stop signal* requiring subjects to interrupt their ongoing response to a main task. Unconscious stop signals yielded a minuscule but still significant slowing down of response time and increase in errors. Thus, subliminal stimuli can trigger the first hints of a task interruption.

How can one interpret such high-level priming effects? One possibility is that, even at the *central executive* level, task selection and task control processes continue to operate according to rules of evidence accumulation, which can be biased by subliminal priming. According to the model illustrated in Figure 2, subjects select a motor response by forming two pools of units: those accumulating evidence for response R1 and those accumulating evidence for response R2. Perhaps the *central executive* consists of nothing but similar decision mechanisms organized in a control hierarchy (Koechlin et al. 2003). At a higher level, similar evidence accumulation processes would be involved in the selection of one of two tasks, T1 and T2. Those accumulators would accrue evidence provided by conscious cues, but also by subliminal cues. Sigman and Dehaene (2006) presented precisely such a model of task selection in a dual-task context. They showed how the time to select which task to perform added a variable duration to the overall response time which could be captured well by an accumulator model. It remains to be seen whether these ideas can be extended to an entire hierarchy of interacting decision systems, as proposed, for example, by Koechlin et al (2003).

Limits to subliminal processing

Given this wealth of evidence which indicates that subliminal processing can extend to a high cognitive level, one may reasonably ask if there are any limits to subliminal processing. Are there mental processes that can be executed only

once conscious perception has occurred? This question naturally arises in relation to the evolutionary role of consciousness. Although the evidence remains fragmentary, several mental operations can be associated speculatively with conscious-level processing.

Durable and explicit information maintenance

Priming experiments show that subliminal information tends to be short-lived: after about 500 ms, priming effects typically cease to be detectable (Greenwald et al. 1996; Mattler 2005). To bridge delays of a few seconds, information is thought to be stored in working memory by active populations of neurons, particularly in prefrontal cortex. When information reaches this working memory stage, Dehaene and Naccache (2001) have suggested that it is always consciously accessible. The work of Kunde et al. (2003), reviewed above, fits nicely with this conclusion, since it shows that only the conscious variables of trial $n - 1$ can be carried out to trial n. Similar evidence is provided by the trace-conditioning paradigm, in which conditioning across a temporal gap only occurs if subjects report being aware of the relations among the stimuli (Clark et al. 2002). Additional supporting data has been reviewed by Dehaene and Naccache (2001). Altogether, the evidence points to a crucial role of consciousness in bridging information across a delay.

Global access and novel combinations of operations

Consciousness has been suggested to play an essential role in the expression of novel behaviors that require putting together evidence from multiple sources (e.g., by confronting evidence spread across several trials). For instance, Merikle et al. (1995) studied subjects' ability to control inhibition in a Strooplike task as a function of the conscious perceptibility of the conflicting information. Subjects had to classify a colored target string as green or red. Each target was preceded by a prime, which could be the word GREEN or RED. In this situation, the classical Stroop effect occurred: responses were faster when the word and color were congruent than when they were incongruent. However, when the prime-target relations were manipulated by presenting 75% of incongruent trials, subjects could take advantage of the predictability of the target from the prime to become faster on incongruent trials than on congruent trials, thus inverting the Stroop effect. Crucially, this strategic inversion occurred only when the prime was consciously perceptible. No strategic effect was observed when the word prime was masked (Merikle et al. 1995) or fell outside the focus of attention (Merikle and Joordens 1997). Here, only the classical, automatic Stroop effect prevailed. Thus, the ability to inhibit an automatic stream of processes and to deploy a novel strategy depended crucially on the conscious availability of information.

This conclusion may need to be qualified in the light of recent evidence, reviewed above, that is, task switching or task stopping can be modulated partially

by subliminal cues (Lau and Passingham 2007; Mattler 2003; van Gaal et al. 2007). Note, however, that this evidence was always obtained under conditions of highly routinized performance. Subjects performed hundreds of trials with consciously perceived task cues before the same cues, presented subliminally, began to affect task choice. This is very different from the rapid deployment of novel strategies that, presumably, can only be deployed under conscious conditions.

Intentional action

As noted by Dehaene and Naccache (2001), the spontaneous generation of intentional behavior may constitute a third property specifically associated with conscious perception. It is noteworthy that, in all of the above priming tasks, although subliminal primes modulate the response time to another conscious stimulus, they almost never induce a full-blown behavior in and of themselves. Only on a very small proportion of trials do subliminal primes actually cause overt responses. When they do, such trials are typically labeled as unintended errors by the subject (and by the experimenter).

As a related example, consider the case of blindsight patients (Weiskrantz 1997). Some of these patients, even though they claim to be blind, show an excellent performance in pointing to objects. As noted by Dennett (1992) and Weiskrantz (1997), a fundamental difference with normal subjects, however, is that blindsight patients never spontaneously initiate any visually guided behavior in their impaired field. Good performance can be elicited only by forcing them to respond to stimulation.

In summary, nonconscious stimuli do not seem to reach a stage of processing at which information representation enters into a deliberation process that supports voluntary action with a sense of ownership. If they do reach this stage, it is only with a trickle of activation that modulates decision time but does not determine the decision outcome.

Cerebral bases of conscious and nonconscious computations

The hypothesis that conscious information is associated with a second stage of processing that cannot be deployed fully for subliminal stimuli meshes well with recent experiments that have directly compared the brain activation evoked by conscious versus nonconscious stimuli. Many such experiments have been performed with fMRI, and they converge to suggest that, relative to a masked stimulus, an unmasked stimulus is amplified and gains access to high levels of activation in prefrontal and parietal areas (Dehaene et al. 2006; Dehaene et al. 2001; Haynes et al. 2005; for review and discussion, see Kouider et al. 2007). Most relevant to the present discussion are time-resolved experiments using ERPs or MEG that have followed the processing of a stimulus in time as it crosses or does not cross the threshold for conscious perception. My colleagues and I have performed such

experiments under conditions in which invisibility was created either by masking (Del Cul et al. 2007; see also Koivisto et al. 2006; Melloni et al. 2007; van Aalderen-Smeets et al. 2006) or by inattention during the attentional blink (Gross et al. 2004; Kranczioch et al. 2003; Sergent et al. 2005). In both cases, we were able to analyze a subset of trials in which the very same stimulus was presented, but was or was not consciously perceived according to subjective reports.

The results were highly convergent in coarsely separating two periods of stimulus processing. During the first 270 ms, brain activation unfolded in an essentially unchanged manner whether or not the stimuli were consciously perceived. Strong visual activation was seen, quickly extending to the ventral temporal visual pathway. In the case of the attentional blink, the nonconscious activation extended even further in time, with very strong left lateral temporal activity around 400 ms plausibly associated with semantic-level processing (see also Luck et al. 1996). However, around 270 ms, an important divergence occurred, with a sudden surge of additional activation being observed on conscious trials only. Over a few tens of milliseconds, activation expanded into bilateral inferior and dorsolateral frontal regions, anterior cingulate cortex, and posterior parietal cortex. As shown in Figure 5, this activity was reduced drastically on nonconscious trials: only short-lived activation was seen, quickly decaying towards zero about 500 ms after stimulus presentation. By contrast, activation seemed to be amplified actively on conscious trials.

The parsing of brain activation into two stages – early activation by subliminal stimuli, followed by late global amplification and reverberation – seems to be a generic phenomenon that can be observed in various stimulus modalities, by a variety of methods, and in multiple species. Thus Victor Lamme and collaborators (2002), using electrophysiological recordings in macaque area V1, have distinguished early feed-forward versus late feedback responses. They found that only the latter were sensitive to attention and reportability. Using intracranial electrodes in human epileptic patients, my team has obtained evidence for a similar division in human subjects during subliminal versus conscious word reading (Gaillard, Naccache et al. 2006; Naccache et al. 2005). In many electrodes, subliminal words evoked only a first peak of activation whereas conscious words evoked a similar but magnified peak followed by a sustained period of activation.

To give yet a third example, Nieuwenhuis et al. (2001) used ERPs in humans to track error detection and compensation processes. When subjects made an undetected erroneous saccade, an early error-related negativity was observed over mesial frontal electrodes, presumably reflecting a nonconscious triggering of an anterior cingulate system for error detection. However, only when the error was detected consciously was this early waveform amplified and followed by a massive P3-like waveform associated presumably with the expansion of activation into a broader cortical and subcortical network.

A global workspace model of conscious access

Jean-Pierre Changeux and I have suggested that these global self-amplifying properties of brain activation during conscious access can be accounted for by the concept of a *global workspace* (Dehaene and Changeux 2005; Dehaene and Naccache 2001; Dehaene et al. 2003). This model, which has been backed up with explicit computer simulations of realistic thalamo-cortical networks, supposes that access to consciousness again corresponds to a form of accumulation of activation within a recurrently connected network. However, this accumulation is postulated to occur, not just locally, but within a highly distributed set of columns coding for the same object within distinct brain areas. These columns are interconnected in a reciprocal manner by distinct cortical *workspace neurons* with long-distance axons. As a result, an entire set of distributed brain areas can function temporarily as a single integrator, with a strong top-down component such that higher association areas send supportive signals to the sensory areas that first excited them.

Computer simulations show that such a network, when stimulated by a brief pulse of activation, presents complex dynamics with at least two distinct stages. In the first stage, activation climbs up the thalamo-cortical hierarchy in a feed-forward manner. As it does, the higher levels send increasingly stronger top-down amplification signals. If the incoming signal is strong enough, then at a certain point a dynamic threshold is crossed and activation becomes self amplifying and increases in a nonlinear manner. During this second stage, the whole distributed assembly coding for the stimulus at multiple hierarchical levels then *ignites* into a single synchronously activated state. In peripheral neurons, this creates a late second peak of sustained firing. The corresponding brain state is illustrated schematically in Figure 6.

Why would this global brain state correspond to conscious access? Computer simulations show that once stimulus-evoked activation has reached highly interconnected associative areas, two important changes occur:

1. The activation can now reverberate for a long time period, thus holding information on-line for a duration essentially unrelated to the initial stimulus duration.
2. Stimulus information represented within the global workspace can be propagated rapidly to many brain systems.

We argue that both properties are characteristic of conscious information processing. As noted above, the information can be maintained in time, buffered from fast fluctuations in sensory inputs, and can be shared across a broad variety of processes including evaluation, verbal report, planning, and long-term memory (Baars 1989).

Anatomically, the model postulates that workspace neurons are particularly dense in prefrontal, parietal, and anterior cingulate cortices, thus explaining why these regions are recurrently found to be associated with conscious access across various paradigms and modalities (Dehaene et al. 2006). However, according to the model, workspace neurons are also present to variable degrees in essentially

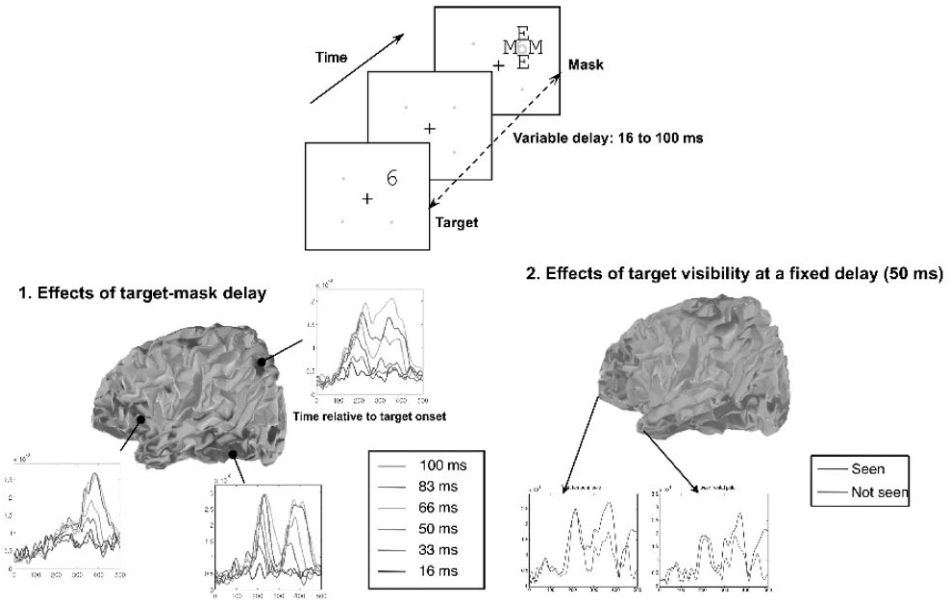

FIGURE 5. Changes in brain activity associated with crossing the threshold for conscious perception during masking (after Del Cul et al. 2007). The paradigm is described in Figure 1, and involves varying the delay between a digit and the subsequent mask. Event-related potentials are recorded with a 128-channel electrode net and reconstructed on the cortical surface with BrainStorm software. As the delay increases, thus rendering the stimulus increasingly visible, activation increases monotonically in posterior areas, then a threshold effect is seen. The late part of the activation (beyond 270 ms) suddenly increases nonlinearly in a sigmoidal manner once the delay exceeds a critical value which coincides with the threshold value for conscious perception. This nonlinear activation is highly global and occurs simultaneously in inferior and anterior prefrontal cortex as well as in posterior parietal and ventral occipito-temporal cortices. Even when the delay is fixed, the same results are seen when sorting the individual trials into seen versus not-seen (bottom panel): there is a clear separation between an initial period where activation is identical for seen and not-seen trials, and a later period (> 270 ms) where activation suddenly re-increases globally on seen trials.

all of the cortex, thus permitting essentially any active cortical contents to be brought together into a single brain-scale assembly. Indeed, it would seem likely that this long-distance network has been subject to a particular selective pressure in humans. A number of recent observations support this possibility, including (a) the disproportionate increase of prefrontal white matter volume in our species (Schoenemann et al. 2005), (b) the massive increase in dendritic branching and spine density in prefrontal cortex across the primate lineage (Elston 2003); and

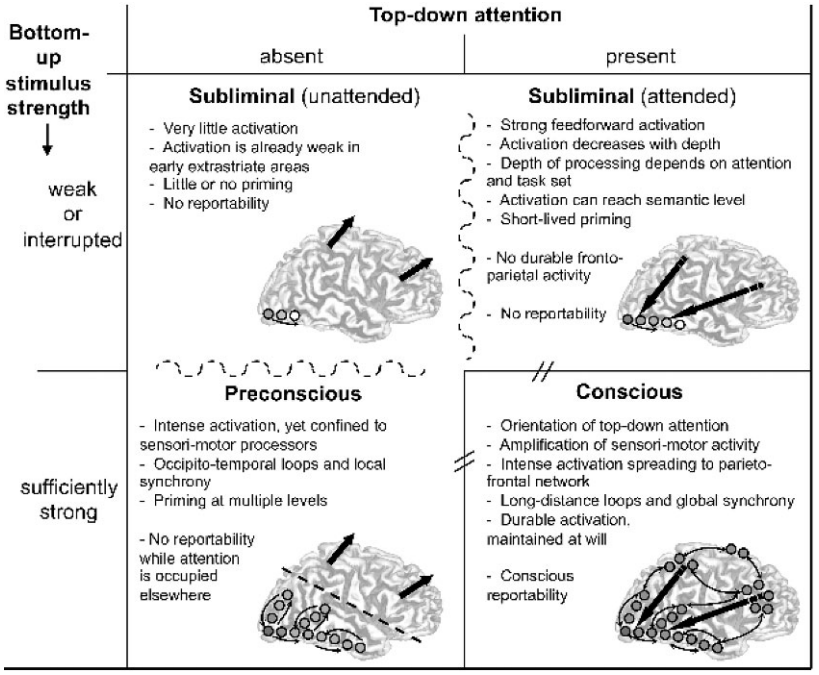

FIGURE 6. Theoretical proposal of a distinction between brain states of subliminal, preconscious, and conscious processing (after Dehaene et al. 2006). Conscious processing occurs when the accumulated stimulus-evoked activation exceeds a threshold and evokes a dynamic state of global reverberation (*ignition*) across multiple highlevel cortical areas forming a *global neuronal workspace*, particularly involving prefrontal, cingulate and parietal cortices (bottom right). These areas can maintain the information on-line and broadcast it to a variety of other processors, thus serving as a central hub for global access to information. Subliminal processing corresponds to a data-limited situation where only a trickle of partial evidence is able to propagate through specialized cerebral networks, yet without reaching a threshold for global ignition and thus without global reportability (top line). The orientation and depth of subliminal processing may nevertheless depend on the top-down state of attention (top right). A distinct nonconscious state, preconscious processing, corresponds to a resource-limited situation where stimulus processing is blocked at the level of the global neuronal workspace while it is temporarily occupied by another task. A preconscious stimulus may be temporarily buffered within peripheral sensory areas and later accessed by the fronto-parietal system once it is released by its distracting task. In this case, information switches from nonconscious to conscious.

(c) the presence in anterior cingulate cortex of large projection neurons (*spindle cells*) seemingly unique to humans and great apes (Nimchinsky et al. 1999).

Accounting for subliminal processing

The proposed workspace architecture separates, in a first minimal description, two computational spaces, each characterized by a distinct pattern of connectivity. Subcortical networks and most of the cortex can be viewed as a collection of specialized and automatized processors, each attuned to the processing of a particular type of information via a limited number of local or medium-range connections that bring to each processor the *encapsulated* inputs necessary to its function. On top of this automatic level, we postulate a distinct set of cortical workspace neurons characterized by their ability to send and receive projections to many distant areas through long-range excitatory axons, thus allowing many different processors to exchange information.

Can this model explain observations on subliminal processing? According to the proposed model, subliminal processing corresponds to a condition of specialized processing without global information accessibility (see Figure 6). A subliminal stimulus is a stimulus that possesses sufficient energy to evoke a feed-forward wave of activation in specialized processors, but it has insufficient energy or duration to trigger a large-scale reverberating state in a global network of neurons with long-range axons. As explained above, simulations of a minimal thalamocortical network (Dehaene and Changeux 2005) indicate that such a nonlinear self-amplifying system possesses a well-defined dynamic threshold. While it has been observed that activation exceeding a threshold level grows quickly into a full-scale ignition, a slightly weaker activation propagates forward, sometimes all the way into higher areas. It, however, loses its self-supporting activation and dies out quickly. Subliminal processing would correspond to the latter type of network state.

Let us examine briefly how this schematic model may account for the data reviewed in the preceding sections. We have seen that a masked visual stimulus that is not consciously reportable is nevertheless processed at multiple levels, including visual but also semantic, executive, and motor levels. These observations mesh well with the notion of an ascending wave of feed-forward activation that begins to accumulate within decision systems, but does not lead to a full-blown activation crossing the response threshold. Recent theorizing suggests that local neural assemblies recurrently interconnected by glutamatergic synapses with a mixture of AMPA and NMDA receptors can operate as accumulators of evidence (Wong and Wang 2006). The global workspace model suggests that such multiple integrators can operate in parallel during subliminal processing, each integrating evidence for or against their preferred stimulus. In priming experiments, where a subliminal stimulus is followed by a supraliminal target, this partial accumulation of evidence evoked by the prime would shift the baseline starting level of these accumulators, thus creating priming effects in response time, determined primarily by the congruity of the prime and target.

As long as the prime-based accumulation remains subthreshold, and therefore fails to trigger a global recurrent assembly, there is nothing in the global workspace

model that prevents subliminal processing from occurring at any cognitive level, including higher-level control processes. However, the model predicts that only the most specialized processors, tightly attuned to the stimulus, should be capable of activating strongly to a subliminal stimulus. This prediction meshes well with the narrow localized activation measured by fMRI and intracranial recordings in response to subliminal words and digits (Dehaene et al. 2001; Naccache and Dehaene 2001a; Naccache et al. 2005). Note that, under the model's hypotheses, subliminal processing is not confined to a passive spreading of activation, independent of the subject's attention and strategies, as previously envisaged. On the contrary, which-ever task and attentional set are prepared consciously, it can serve to orient and amplify the processing of a subliminal stimulus, even if its bottom-up strength remains insufficient for global ignition. This aspect of our model agrees with the many top-down influences on subliminal processing that have been observed experimentally.

Finally, the model predicts correctly that subliminal activation may be very strong within the first 100–300 ms after stimulus presentation, but progressively dies out in the next few hundreds of milliseconds as time elapses and as the stimulus reaches higher levels of representation. Such a decay of subliminal activation, both in time and in cortical space, has indeed been observed experimentally with high-density recordings of event-related potentials (Del Cul et al. 2007; see Figure 5). It can explain why only small behavioral influences of subliminal stimuli are measurable at higher cognitive levels (van Gaal et al. 2007; Mattler 2003), and why most if not all subliminal priming effects decay to a nonmeasurable level once the prime-target interval exceeds 500 ms (Mattler 2005). Only very rarely are subliminal effects seen beyond the range of a few seconds. My colleagues and I have suggested that when they do (Gaillard et al. 2007), it may be because the subliminal stimulus has caused structural changes (e.g., changes in synaptic efficacy) rather than it being due to lingering brain activity.

A distinct state of preconscious processing

Simulations of the global workspace have revealed that global workspace ignition can also be prevented in a different manner, suggesting a distinct state of nonconscious processing that we have proposed to call preconscious (or potentially conscious, or P-conscious). Contrary to subliminal processing, where the incoming stimulus itself does not have enough energy or duration to trigger a suprathreshold reverberation of activation, preconscious processing corresponds to a neural process that potentially carries enough activation for conscious access, but is temporarily blocked from activating the global workspace due to its transient occupancy by another stimulus. Simulations have shown that such a competitive interaction for global access can occur when two stimuli are presented in short succession, in a paradigm akin to the *attentional blink*. The first target (T1) creates

a global workspace ignition, but while this global state is occurring, lateral inhibition prevents a second target (T2) from entering the workspace. Essentially, the global workspace acts as a central bottleneck (Chun and Potter 1995; Pashler 1994) whose occupancy by T1 deprives the T2-evoked neural assembly from its top-down support. The corresponding postulated brain state is illustrated schematically in Figure 6.

Computer simulations (Dehaene and Changeux 2005) suggest that during preconscious processing, T2 activation is blocked sharply at the central level; it can, however, be quite strong at peripheral levels of processing. It may excite resonant loops within medium-range connections that may maintain the representation of the stimulus temporarily active in a sensory buffer for a few hundreds of milliseconds. As a result, a preconscious stimulus is literally on the brink of consciousness and can compete actively for conscious access with other stimuli, including the currently conscious one. Furthermore, although temporarily blocked, a preconscious stimulus may later achieve conscious access once the central workspace is freed. This aspect of the model may correspond to the empirical observation of a *psychological refractory period* in behavioral dual-task performance (Pashler 1984; Sigman and Dehaene 2005), in which one task is put on hold while another task is being processed. The model assumes that the key difference between the psychological refractory period and attentional blink phenomena is the possibility of a lingering of T2-induced activation in peripheral circuits. T2 may never gain access to conscious processing if its preconscious representation is erased prior to the orienting of top-down attention (as achieved by masking in the attentional blink paradigm).

At present, only a few studies have examined brain activity during states where conscious access is prevented by top-down attentional competition, such as the attentional blink (for review, see Marois and Ivanoff 2005). Time resolved experiments suggest that the initial activation by an unseen T2 can be very strong and essentially indistinguishable from that evoked by a conscious stimulus during a time window of about 270 ms (Sergent et al. 2005). The attentional blink then creates a sudden blocking of part of the activation starting around 270 ms, particularly in inferior prefrontal cortex (Sergent et al. 2005), and a global state of fronto-parietal synchrony indexed by the scalp P3 and by evoked oscillations in the beta range is prevented from occurring (Gross et al. 2004; Kranczioch et al. 2003). Other fMRI experiments also point to a distributed prefronto-parietal network as the main locus of the bottleneck effect in competition paradigms, consistent with the global workspace model (Dux et al. 2006; Kouider et al. 2007).

Conclusion: Conscious access as a solution to von Neumann's problem?

The purpose of this chapter was to survey the rich cognitive neuroscience literature on nonconscious processing and to establish links with evidence accumulation models. The main generalizations that I have proposed to draw from these observations are the following:

1. *Subliminal processing* corresponds to a state of partial accumulation of evidence within multiple sensory, semantic, executive, and motor networks, yet without reaching a full-blown decision threshold.
2. Nonconscious processing can also occur in a distinct state of *preconscious processing*, where evidence accumulation can proceed normally within posterior sensory and semantic networks while being blocked from accessing anterior networks due to competition with another attended mental representation.
3. *Conscious access* is associated with the crossing of a dynamic threshold beyond which the stimulus activation reverberates within a global frontoparietal network. The sensory representation of the stimulus can thus be maintained online and be used for higher-level executive processes, such as reasoning and decision making.

I end with a final speculative note on one of the possible functions of consciousness in evolution. In his 1958 book, *The Computer and the Brain*, von Neumann asked how a biological organ such as the brain, where individual neurons are prone to errors, could perform multistep calculations. He pointed out that in any analogical machine, errors accumulate at each step so that the end result quickly becomes imprecise or even useless. He therefore suggested that the brain must have mechanisms that discretize the incoming analogical information, much like the TTL or CMOS code of current digital chips is based on a distinction of voltages into high (between 4.95 and 5 volts) versus low (between 0 and 0.05 volts).

Tentatively, I surmise that the architecture of the *conscious workspace* may have evolved to address von Neumann's problem. In the human brain, one function of conscious access would be to control the accumulation of information in such a way that information is pooled in a coherent manner across the multiple processors operating preconsciously and in parallel, and a discrete categorical decision is reached before being dispatched to yet other processors. By pooling information over time, this global accumulation of evidence would allow the inevitable errors that creep up during analog processing to be corrected or at least to be kept below a predefined probability level. Many decision models already postulate such an accumulation of evidence within local brain systems such as the oculo-motor system (see Gold and Shadlen, 2002). The role of the conscious global workspace would be to achieve such accumulation of evidence in a unified manner across multiple distributed brain systems and, once a single coherent result has been obtained, to dispatch it back to essentially any brain processor as needed by the current task. This architecture would permit the execution of a multistep mental

algorithm through successive, consciously controlled steps of evidence accumulation followed by result dispatching. The latter proposal is consistent with recent findings from the *psychological refractory period* paradigm, where response time in a dual-task situation was shown to result from a temporal succession of multiple non-overlapping stochastic accumulation periods (Sigman and Dehaene 2005, 2006).

While clearly speculative and in need of further specification, the proposed architecture seems to combine the benefits of two distinct computational principles: massive parallel accumulation of evidence at a nonconscious level, followed by conscious broadcasting of the outcome permitting the operation of the human brain as a slow serial *Turing machine*.

References

[1] B.J. Baars, *A Cognitive Theory of Consciousness*, Cambridge, MA: Cambridge Univ. Press (1989).

[2] M.M. Chun and M.C. Potter, *A two-stage model for multiple target detection in rapid serial visual presentation*, J. Exp. Psychol.: Hum. Perc. Perf. **21**(1) (1995), 109–127.

[3] R.E. Clark, J.R. Manns and L.R. Squire, *Classical conditioning, awareness, and brain systems*, Trends Cogn. Sci. **6**(12) (2002), 524–531.

[4] S. Dehaene, *Symbols and quantities in parietal cortex: Elements of a mathematical theory of number representation and manipulation*, In: Sensorimotor Foundations of Higher Cognition, ed. P. Haggard and Y. Rossetti. Oxford: Oxford Univ. Press, in press (2007).

[5] S. Dehaene and J.P. Changeux, *Ongoing spontaneous activity controls access to consciousness: A neuronal model for inattentional blindness*, PLoS Biol. **3**(5) (2005), e141.

[6] S. Dehaene, J.P. Changeux, L. Naccache, J. Sackur and C. Sergent, *Conscious, preconscious, and subliminal processing: A testable taxonomy*, Trends Cogn. Sci. **10**(5) (2006), 204–211.

[7] S. Dehaene and L. Naccache, *Towards a cognitive neuroscience of consciousness: Basic evidence and a workspace framework*, Cognition **79** (2001), 1–37.

[8] S. Dehaene, L. Naccache, L. Cohen, D.L. Bihan, J.F. Mangin et al., *Cerebral mechanisms of word masking and unconscious repetition priming*, Nat. Neurosci. **4**(7) (2001), 752–758.

[9] S. Dehaene, L. Naccache, G. Le Clec'H, E. Koechlin, M. Mueller et al, *Imaging unconscious semantic priming*, Nature **395** (1998), 597–600.

[10] S. Dehaene, C. Sergent and J.P. Changeux, *A neuronal network model linking subjective reports and objective physiological data during conscious perception*, Proc. Natl. Acad. Sci. **100** (2003), 8520–8525.

[11] A. Del Cul, S. Baillet and S. Dehaene, *Brain dynamics underlying the non-linear threshold for access to consciousness*, PLoS Biol. **5**(10) (2007), e260.

[12] A. Del Cul, S. Dehaene and M. Leboyer. *Preserved subliminal processing and impaired conscious access in schizophrenia*, Arch. Gen. Psychiatry **63**(12) (2006), 1313–1323.

[13] D.C. Dennett, *Consciousness Explained*, London: Penguin (1992).

[14] J.T. Devlin, H.L. Jamison, P.M. Matthews and L.M. Gonnerman, *Morphology and the internal structure of words*, Proc. Natl. Acad. Sci. **101**(41) (2004), 14,984–14,988.

[15] P.E. Dux, J. Ivanoff, C.L. Asplund and R. Marois, *Isolation of a central bottleneck of information processing with time-resolved fMRI*, Neuron **52**(6) (2006), 1109–1120.

[16] M. Eimer and F. Schlaghecken, *Effects of masked stimuli on motor activation: Behavioral and electrophysiological evidence*, J. Exp. Psychol.: Hum. Perc. Perf. **24**(6) (1988), 1737–1747.

[17] G.N. Elston, *Cortex, cognition and the cell: New insights into the pyramidal neuron and prefrontal function*, Cerebral Cortex **13**(11) (2003), 1124–1138.

[18] R. Gaillard, L. Cohen, C. Adam, S. Clémenceau, M. Baulac et al., *Subliminal words durably affect neuronal activity*, Neuroreport **18**(15) (2007), 1527–1531.

[19] R. Gaillard, A. Del Cul, L. Naccache, F. Vinckier, L. Cohen et al., *Nonconscious semantic processing of emotional words modulates conscious access*, Proc. Natl. Acad. Sci. **103**(19) (2006), 7524–7529.

[20] R. Gaillard, L. Naccache, P. Pinel, S. Clemenceau, E. Volle et al., *Direct intracranial, fmri, and lesion evidence for the causal role of left inferotemporal cortex in reading*, Neuron **50**(2) (2006), 191–204.

[21] Gold, J.I., and Shadlen, M.N. (2002). *Banburismus and the brain: decoding the relationship between sensory stimuli, decisions, and reward*, Neuron, **36**(2), 299–308.

[22] A.G. Greenwald, S.C. Draine and R.L. Abrams, *Three cognitive markers of unconscious semantic activation*, Science **273**(5282) (1996), 1699–1702.

[23] J. Gross, F. Schmitz, I. Schnitzler, K. Kessler, K. Shapiro et al., *Modulation of long-range neural synchrony reflects temporal limitations of visual attention in humans*, Proc. Natl. Acad. Sci. **101**(35) (2004), 13,050–13,055.

[24] J.D. Haynes, J. Driver and G. Rees, *Visibility reflects dynamic changes of effective connectivity between V1 and fusiform cortex*, Neuron **46**(5) (2005), 811–821.

[25] R.W. Kentridge, C.A. Heywood and L. Weiskrantz, *Attention without awareness in blindsight*, Proc. Roy. Soc. Lond. **B 266**(1430) (1999), 1805–1811.

[26] R.W. Kentridge, C.A. Heywood and L. Weiskrantz, *Spatial attention speeds discrimination without awareness in blindsight*, Neuropsychologia **42**(6) (2004), 831–835.

[27] M. Kiefer, *The N400 is modulated by unconsciously perceived masked words: Further evidence for an automatic spreading activation account of N400 priming effects*, Brain Res. Cogn. Brain Res. **13**(1) (2002), 27–39.

[28] M. Kiefer and D. Brendel, *Attentional modulation of unconscious* automatic *processes: Evidence from event-related potentials in a masked priming paradigm*, J. Cogn. Neurosci. **18**(2) (2006), 184–198.

[29] E. Koechlin, C. Ody and F. Kouneiher, *The architecture of cognitive control in the human prefrontal cortex*, Science **302**(5648) (2003), 1181–1185.

[30] M. Koivisto, A. Revonsuo and M. Lehtonen, *Independence of visual awareness from the scope of attention: An electrophysiological study*, Cereb. Cortex **16**(3) (2006), 415–424.

[31] S. Kouider and S. Dehaene, *Levels of processing during non-conscious perception: A critical review of visual masking*, Phil. Trans. Roy. Soc. Lond. B, **362**(1481) (2007), 857–875.

[32] S. Kouider, S. Dehaene, A. Jobert and D. Le Bihan, *Cerebral bases of subliminal and supraliminal priming during reading*, Cereb. Cortex **17**(9) (2007), 2019–2029.

[33] C. Kranczioch, S. Debener and A.K. Engel, *Event-related potential correlates of the attentional blink phenomenon*, Brain Res. Cogn. Brain Res. **17**(1) (2003), 177–187.

[34] W. Kunde, A. Kiesel and J. Hoffmann, *Conscious control over the content of unconscious cognition*, Cognition **88**(2) (2003), 223–242.

[35] J. Lachter, K.I. Forster and E. Ruthruff, *Forty-five years after Broadbent* (1958)*: Still no identification without attention*, Psychol. Rev. **111**(4) (2004), 880–913.

[36] D.R.J. Laming, *Information Theory of Choice-Reaction Times*, London: Academic Press (1968).

[37] V.A. Lamme, K. Zipser and H. Spekreijse, *Masking interrupts figure-ground signals in V1*, J. Cogn. Neurosci. **14**(7) (2002), 1044–1053.

[38] H.C. Lau and R.E. Passingham, *Unconscious activation of the cognitive control system in the human prefrontal cortex*, J. Neurosci. **27**(21) (2007), 5805–5811.

[39] H. Leuthold and B. Kopp, *Mechanisms of priming by masked stimuli: Inferences from event-related potentials*, Psychol. Sci. **9** (1998), 263–269.

[40] S.W. Link, *The Wave Theory of Difference and Similarity*, Hillsdale, NJ: Lawrence Erlbaum (1992).

[41] S.J. Luck, E.K. Vogel and K.L. Shapiro, *Word meanings can be accessed but not reported during the attentional blink*, Nature **383**(6601) (1996), 616–618.

[42] R. Marois and J. Ivanoff, *Capacity limits of information processing in the brain*, Trends Cogn. Sci. **9**(6) (2005), 296–305.

[43] Y. Marzouki, J. Grainger and J. Theeuwes, *Exogenous spatial cueing modulates subliminal masked priming*, Acta Psychol. **126**(1) (2007), 34–45.

[44] U. Mattler, *Priming of mental operations by masked stimuli*, Perc. Psychophys. **65**(2) (2003), 167–187.

[45] U. Mattler, *Inhibition and decay of motor and nonmotor priming*, Perc. Psychophys. **67**(2) (2005), 285–300.

[46] L. Melloni, C. Molina, M. Pena, D. Torres, W. Singer et al., *Synchronization of neural activity across cortical areas correlates with conscious perception*, J. Neurosci. **27**(11) (2007), 2858–2865.

[47] P.M. Merikle and S. Joordens, *Parallels between perception without attention and perception without awareness*, Conscious Cogn. **6**(2–3) (1997), 219–236.

[48] P.M. Merikle, S. Joordens and J.A. Stolz, *Measuring the relative magnitude of unconscious influences* Conscious. Cogn. **4** (1995), 422–439.

[49] L. Naccache, E. Blandin and S. Dehaene, *Unconscious masked priming depends on temporal attention*, Psychol. Sci. **13** (2002), 416–424.

[50] L. Naccache and S. Dehaene, *The Priming Method: Imaging Unconscious Repetition Priming Reveals an Abstract Representation of Number in the Parietal Lobes*, Cereb. Cortex **11**(10) (2001a), 966–974.

[51] L. Naccache and S. Dehaene, *Unconscious semantic priming extends to novel unseen stimuli*, Cognition **80**(3) (2001b), 215–229.

[52] L. Naccache, R. Gaillard, C. Adam, D. Hasboun, S. Clémenceau et al., *A direct intracranial record of emotions evoked by subliminal words*, Proc. Natl. Acad. Sci. **102** (2005), 7713–7717.

[53] K. Nakamura, S. Dehaene, A. Jobert, D. Le Bihan and S. Kouider, *Subliminal convergence of Kanji and Kana words: Further evidence for functional parcellation of the posterior temporal cortex in visual word perception*, J. Cogn. Neurosci. **17**(6) (2005), 954–968.

[54] S. Nieuwenhuis, K.R. Ridderinkhof, J. Blom, G.P. Band and A. Kok, *Error related brain potentials are differentially related to awareness of response errors: Evidence from an antisaccade task*, Psychophys. **38**(5) (2001), 752–760.

[55] E.A. Nimchinsky, E. Gilissen, J.M. Allman, D.P. Perl, J.M. Erwin et al., *A neuronal morphologic type unique to humans and great apes*, Proc. Natl. Acad. Sci. **96**(9) (1999), 5268–5273.

[56] H. Pashler, 1984. *Processing stages in overlapping tasks: Evidence for a central bottleneck*, J. Exp. Psychol.: Hum. Perc. Perf. **10**(3) (1984), 358–377.

[57] H. Pashler, 1994. *Dual-task interference in simple tasks: Data and theory*, Psychol. Bull. **116**(2) (1994), 220–244.

[58] M. Pessiglione, L. Schmidt, B. Draganski, R. Kalisch, H. Lau et al., *How the brain translates money into force: A neuroimaging study of subliminal motivation*, Science **316** (2007), 904–906.

[59] F. Reuter, A. Del Cul, B. Audoin, I. Malikova, L. Naccache et al., *Intact subliminal processing and delayed conscious access in multiple sclerosis*, Neuropsychologia **45**(12) (2007), 2683–2691.

[60] B. Reynvoet, M. Brysbaert and W. Fias, *Semantic priming in number naming*, Qtly. J. Exp. Psychol. **55**(4) (2002), 1127–1139.

[61] P.T. Schoenemann, M.J. Sheehan and L.D. Glotzer, *Prefrontal white matter volume is disproportionately larger in humans than in other primates*, Nat. Neurosci. **8**(2) (2005), 242–252.

[62] C. Sergent, S. Baillet and S. Dehaene, *Timing of the brain events underlying access to consciousness during the attentional blink*, Nat. Neurosci. **8**(10) (2005), 1391–1400.

[63] C. Sergent and S. Dehaene, *Is consciousness a gradual phenomenon? Evidence for an all-or-none bifurcation during the attentional blink*, Psychol. Sci. **15**(11) (2004), 720–728.

[64] M. Sigman and S. Dehaene, *Parsing a cognitive task: A characterization of the mind's bottleneck*, PLoS Biol. **3**(2) (2005), e37.

[65] M. Sigman and S. Dehaene, *Dynamics of the Central Bottleneck: Dual-task and task uncertainty*, PLoS Biol. **4**(7) (2006), e220.

[66] P.L. Smith and R. Ratcliff, *Psychology and neurobiology of simple decisions* Trends Neurosci. **27**(3) (2004), 161–168.

[67] M. Usher and J.L. McClelland, 2001. *The time course of perceptual choice: The leaky, competing accumulator model*, Psychol. Rev. **108**(3) (2001), 550–592.

[68] S.I. van Aalderen-Smeets, R. Oostenveld and J. Schwarzbach, *Investigating neurophysiological correlates of metacontrast masking with magnetoencephalography*, Adv. Cogn. Psychol. **2**(1) (2006), 21–35.

[69] S. van Gaal, K.R. Ridderinkhof, W.P.M. van den Wildenberg and V.A. Lamme, *Exploring the boundaries of unconscious processing: Response inhibition can be triggered by masked stop-signals*, J. Vision **7**(9) (2007), 425.

[70] J. von Neumann, 1958. *The Computer and the Brain*, London: Yale Univ. Press (1958).

[71] D. Vorberg, U. Mattler, A. Heinecke, T. Schmidt and J. Schwarzbach, *Different time courses for visual perception and action priming*, Proc. Natl. Acad. Sci. **100**(10) (2003), 6275–6280.

[72] L. Weiskrantz, *Consciousness Lost and Found: A Neuropsychological Exploration*, New York: Oxford Univ. Press (1997).

[73] K.F. Wong and X.J. Wang, *A recurrent network mechanism of time integration in perceptual decisions*, J. Neurosci. **26**(4) (2006), 1314–1328.

Stanislas Dehaene
Inserm-CEA Cognitive Neuroimaging Unit
NeuroSpin center, CEA/SAC/DSV/I2BM
Bât 145, Point Courrier 156
F–91191 Gif/Yvette, FRANCE
e-mail: stanislas.dehaene@cea.fr